UNIVERSIDAD DE MÁLAGA

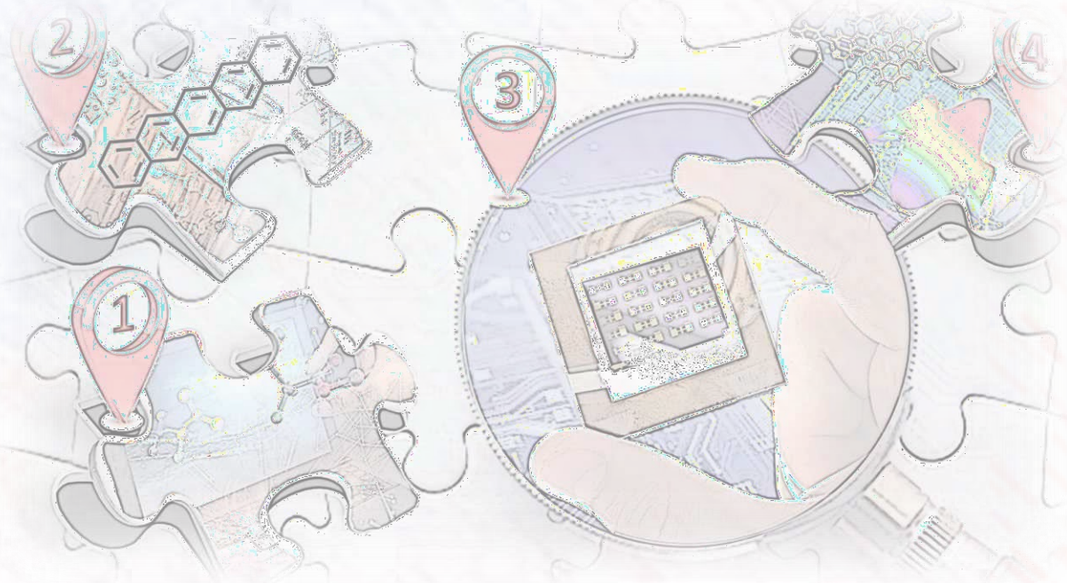

TESIS DOCTORAL

Sergio Gámez Valenzuela

Málaga, 2023

Towards the rational design and characterization of organic semiconductors by a combined experimental and theoretical approach: from small molecules to polymers

UNIVERSIDAD DE MÁLAGA

Sergio Gámez Valenzuela 2023 TESIS DOCTORAL

Towards the rational design and characterization of organic semiconductors by a combined experimental and theoretical approach: from small molecules to polymers

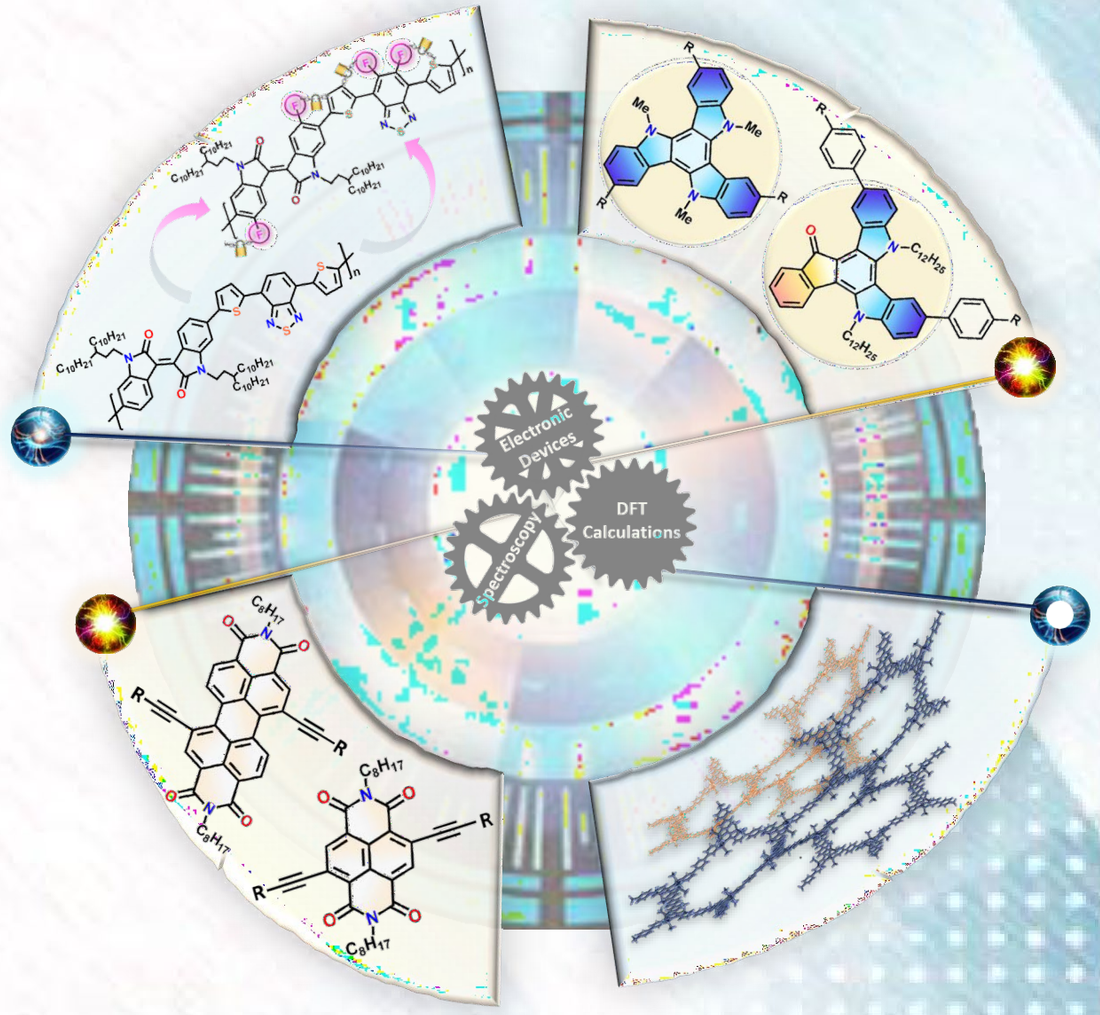

Sergio Gámez Valenzuela

TESIS DOCTORAL 2023

DIRECTORES: María del Carmen Ruiz Delgado y Rocío Ponce Ortiz

Doctorado en Química y Tecnologías Químicas. Materiales y Nanotecnología

Departamento de Química Física, Facultad de Ciencias, Universidad de Málaga

AUTOR: Sergio Gámez Valenzuela

http://orcid.org/0000-0002-2690-2331

EDITA: Publicaciones y Divulgación Científica. Universidad de Málaga

DECLARACIÓN DE AUTORÍA Y ORIGINALIDAD DE LA TESIS PRESENTADA PARA OBTENER EL TÍTULO DE DOCTOR

D. **Sergio Gámez Valenzuela**, estudiante del programa de doctorado en **Química Y Tecnologías Químicas, Materiales Y Nanotecnología** de la Universidad de Málaga, autor de la tesis, presentada para la obtención del título de doctor por la Universidad de Málaga, titulada: "**Towards the rational design and characterization of organic semiconductors by a combined experimental and theoretical approach: from small molecules to polymers**".

Realizada bajo la tutorización de Dña. **María del Carmen Ruiz Delgado** y dirección de Dña. **María del Carmen Ruiz Delgado** Y Dña. **Rocío Ponce Ortiz**,

Declaro que:

La tesis presentada es una obra original que no infringe los derechos de propiedad intelectual ni los derechos de propiedad industrial u otros, conforme al ordenamiento jurídico vigente (Real Decreto Legislativo 1/1996, de 12 de abril, por el que se aprueba el texto refundido de la Ley de Propiedad Intelectual, regularizando, aclarando y armonizando las disposiciones legales vigentes sobre la materia), modificado por la Ley 2/2019, de 1 de marzo. Igualmente asumo, ante a la Universidad de Málaga y ante cualquier otra instancia, la responsabilidad que pudiera derivarse en caso de plagio de contenidos en la tesis presentada, conforme al ordenamiento jurídico vigente.

En Málaga, a 27 de marzo de 2023

Fdo.: **Sergio Gámez Valenzuela** Doctorando	Fdo.: **María del Carmen Ruiz Delgado** Tutora
Fdo.: **María del Carmen Ruiz Delgado** y **Rocío Ponce Ortiz** Directoras de tesis	

Edificio Pabellón de Gobierno. Campus El Ejido. 29071
Tel.: 952 13 10 28 / 952 13 14 61 / 952 13 71 10
E-mail: doctorado@uma.es

UNIVERSIDAD DE MÁLAGA

Dña. **María del Carmen Ruiz Delgado** y Dña. **Rocío Ponce Ortiz**, ambas como Profesoras Titulares del Departamento de Química-Física de la Universidad de Málaga,

Certifican:

Que la memoria presentada por **Sergio Gámez Valenzuela** bajo el título "**Towards the rational design and characterization of organic semiconductors by a combined experimental and theoretical approach: from small molecules to polymers**" para optar al título de Doctor en Ciencias Químicas por la Universidad de Málaga, ha sido realizada bajo nuestra dirección en los laboratorios del Departamento de Química Física de la Universidad de Málaga.

Considerando que constituye una investigación de alta calidad en el campo de la ciencia de materiales, se autoriza mediante este escrito su presentación y defensa como Tesis Doctoral en la Facultad de Ciencias de la Universidad de Málaga.

Y para que así conste, firman el presente certificado en Málaga a 27 de marzo de 2023.

Fdo.: Dña. **María del Carmen Ruiz Delgado**

Fdo.: Dña. **Rocío Ponce Ortiz**

UNIVERSIDAD DE MÁLAGA

Dña. **María del Carmen Ruiz Delgado** y Dña. **Rocío Ponce Ortiz**, ambas como Profesoras Titulares del Departamento de Química-Física de la Universidad de Málaga y directoras de la tesis doctoral de **Sergio Gámez Valenzuela** bajo el título "***Towards the rational design and characterization of organic semiconductors by a combined experimental and theoretical approach: from small molecules to polymers***" para optar al título de Doctor en Ciencias Químicas por la Universidad de Málaga,

Certifican:

Que el artículo que avala la tesis doctoral de **Sergio Gámez Valenzuela**:

Gámez-Valenzuela, S.; Comi, M.; Rodríguez González, S.; Ruiz Delgado, M. C.; Al-Hashimi, M.; Ponce Ortiz, R., The fluorination effect: importance of backbone planarity in achieving high performance ambipolar field effect transistors. Journal of Materials Chemistry C, 2023, *Accepted*. (DOI https://doi.org/10.1039/D2TC05073K)

No ha sido utilizado en tesis doctorales anteriores, ni será utilizado en ocasiones venideras con el mismo fin.

Y para que así conste, firman el presente certificado en Málaga a 27 de marzo de 2023.

Fdo.: Dña. **María del Carmen Ruiz Delgado**

Fdo.: Dña. **Rocío Ponce Ortiz**

UNIVERSIDAD DE MÁLAGA

D. **Juan Carlos Otero Fernández de Molina**, Catedrático de Universidad y Director del Departamento de Química Física de la Universidad de Málaga,

Certifica:

Que la Tesis Doctoral titulada "**Towards the rational design and characterization of organic semiconductors by a combined experimental and theoretical approach: from small molecules to polymers**" constituye la memoria que presenta D. **Sergio Gámez Valenzuela** para optar al título de Doctor en Ciencias Químicas por la Universidad de Málaga, y ha sido realizada bajo la dirección de las Doctoras Dña. **María del Carmen Ruiz Delgado** y Dña. **Rocío Ponce Ortiz**, en el Departamento de Química Física de la Universidad de Málaga.

Y para que así conste, firmo el presente certificado en Málaga a 27 de marzo de 2023.

Fdo.: D. **Juan Carlos Otero Fernández de Molina**

El desarrollo de esta memoria significa que se acerca el momento de cerrar una de las etapas más enriquecedoras que he vivido, resultado de un sinfín de acontecimientos relacionados no solo con lo académico, sino también con lo personal. Algunos pensarán que, llegado a este punto, agradecer a las personas partícipes de ello "es lo de menos", pero por mucho que me esfuerce no creo encontrar palabras suficientes para agradecer todo lo recibido tal y como se merece. En un intento de ello, esta parte va dedicada a todas esas personas que se han ganado el estar de algún modo en esta memoria.

Para comenzar, me gustaría dedicar estas primeras líneas a mis directoras Mari Carmen y Rocío. Aunque seis años trabajando juntos no se puedan resumir en un párrafo, si tuviera que elegir dos palabras para referirme a vosotras creo no equivocarme al hablar de "admiración y respeto". Admiración, por ser un claro ejemplo de mujeres con una gran brillantez para hacer ciencia y, más importante aún, la pasión con la que la trasmitís a nuevas generaciones. Por otro lado, hablo de respeto refiriéndome a los valores que me habéis demostrado a lo largo de este periodo, durante el cual han sido muchos los consejos y palabras de aliento recibidas tanto en lo profesional como en lo personal. A vosotras os debo muchas cosas, pero sobre todo, os doy gracias por dedicarme tiempo aun cuando no lo teníais y por la gran dedicación que habéis puesto en mi formación. Por ello, si bien cuando agradecemos a alguien lo que ha hecho es darle a entender que realmente valió la pena su esfuerzo, quiero que sepáis que estoy orgulloso de lo que he aprendido en esta etapa y del trabajo que he realizado gracias a vosotras.

Hago un alto en el camino para agradecer también a Víctor y Teo por abrirme las puertas del grupo y darme la oportunidad de iniciarme en el mundo científico de la mejor forma posible. Quiero hacer especial mención a Víctor, al que además de sus tertulias espectroscópicas (papel y boli en mano), le debo de agradecer su apoyo constante y cercanía durante todos estos años.

Sin duda, parte de los mejores recuerdos que me llevo de estos años han sido gracias a compañeros con los que he compartido algún que otro café, risas, viajes y sobre todo,

largas jornadas de trabajo. Quiero agradecer a María por tenderme la mano desde el primer momento, estar siempre dispuesta a ayudar y levantarme el ánimo en tantas ocasiones. Debo de reconocer María, que he perdido la cuenta de los cafés que te debo… No puedo olvidarme tampoco de todos los momentos compartidos con Rafa, el cual me llevó "al lado oscuro" con sus seminarios de química computacional, ni toda la ayuda prestada por Iratxe dentro y fuera del laboratorio, teniendo siempre un buen consejo.

Gracias también al resto de "jóvenes quifiqueros", en especial a Fran, Fernando, Sara y Guzmán por todas las risas que hemos compartido juntos. A Alexandra, por su amistad y energía que han hecho que las horas pasen de una forma más agradable. Gracias, Cristina y Zafra, por aguantarme desde mi inicio con los "plásticos". Estoy seguro de que sabéis la deuda de gratitud que os tengo, pues nunca habéis dejado de enseñarme, aconsejarme e intentar sacarme una sonrisa en malos momentos. A Beloqui, al cual le doy las gracias por demostrarme en tan poco tiempo su gran calidad científica y más importante aún, humana. Es una pena haber compartido solo parte de esta etapa con un "tío tan cremasso" como tú. Gracias Samara y Sergio, por hacer que los días de laboratorio y despacho sean amenos a la par que productivos. Sois un claro ejemplo de constancia y entrega. En el ámbito personal os doy las gracias por la amistad que hemos forjado, donde nunca olvidaré aquellas noches de juegos de mesa, fiestas de disfraces y tardes de "tortitas" entre un sinfín de planes más. A Raúl y Abel les doy las gracias por estos años juntos que no se pueden resumir en unas líneas. Gracias por hacer que cada día tenga una anécdota digna de contar, por ser la alegría del grupo y, sobre todo, por demostrarme el valor de la amistad.

Por último, quiero agradecer a la persona con la que no solo he tenido el placer de compartir los años de grado, sino también 6 años de "pecera". Es por ello, por lo que la señorita Badia se merece un punto aparte. Entramos juntos al departamento y hemos ido "de la mano" durante todo este tiempo, en el cual me has demostrado ser una gran científica, compañera y amiga. Gracias por ser mi mayor confidente, tenderme siempre la mano cuando la necesitaba y hacerme ver el lado positivo de las cosas constantemente. Estoy seguro de que recordaré siempre esta etapa con una sonrisa y en gran parte, es gracias a ti.

No puedo olvidarme del resto de personas del Departamento, los cuales me han hecho sentir como en casa desde el primer momento y de los que me llevo muy buenos recuerdos. Gracias a todos.

Me gustaría agradecer a las profesoras Berta Gómez-Lor, del Instituto de Ciencia de los Materiales de Madrid (ICMM) y María Pilar Prieto, de la Universidad de Castilla la Mancha, así como al profesor Mohammed Al-Hashimi, de la Universidad de Texas (Qatar) por proporcionarme los compuestos estudiados en esta Tesis Doctoral.

Mi agradecimiento también al grupo del Prof. José Ignacio Martínez del ICMM por hacer que mi estancia en Madrid no solo fuese fructífera científicamente hablando, sino que también lo fuese en el ámbito personal. Nunca olvidaré aquellas "barritas energéticas" con vermut postpartido, los miércoles de tarta o los meetings de grupo de los que tanto he aprendido. *Likewise, one of the best experiences of these years is the time in Stuttgart. Thank Prof. Sabine for giving me the opportunity to work in your lab and introduce me to the field of electrochemistry and nonlinear optic behaviors. I am extremely grateful to my labmates of "IPOC" as well as to the Prof. Belén Villacampa for making the lab days more bearable.*

Por último, fuera del ámbito científico, doy mi más sincero agradecimiento a familiares y amigos. Quiero hacer especial mención a mis padres, a los que les dedico todo el esfuerzo que hay detrás de estas páginas. Gracias por confiar siempre en mí y por inculcarme que no hay más camino sino la perseverancia y el trabajo para conseguir cualquier objetivo que me proponga. Para el final he dejado a mi principal apoyo durante esta etapa. Estas palabras van dedicadas a ti Rocío, por todo el apoyo que me diste cuando veía el "vaso medio vacío", por entender que la ciencia carece de horario, por creer siempre en mí y por soportar la distancia que egoístamente he impuesto en ocasiones. Por todo ello, puedo decir que este trabajo tiene un pedacito de ti.

Gracias a todos, de corazón.

*Si he logrado **ver más lejos**,*

ha sido porque he subido

*a **hombros de gigantes**.*

(Isaac Newton)

Contents Page

Contents **Page**

Contents **Page**

Contents Page

Contents Page

1 Introduction

Table of contents

In plain decline of Roman empire, during the second expedition to Britain, Julius Caesar wrote in book V of De Bello Gallico, "All Britons paint themselves with woad, which grows wild and produces a blue dye. This gives them a terrifying appearance in battle".[1] The term woad is the common name of a flowering plant also known as indigo plant, which is the source of the blue dye after which it was named.[2, 3] At the molecular level, indigo dye is an organic (carbon based) material composed by two 3-indolinone units covalently linked through a double CC bond, resulting on a planar π-conjugated structure due to the presence of distinctive O···H non-covalent interactions (Figure 1.1).

Figure 1.1. Scheme of the evolution in the application of indigo ((E)-[2,2'-biindolinylidene]-3,3'-dione), together with its chemical structure.

Eventually, the demand for indigo exceed natural production and therefore, new synthetic alternatives have been developed until now.[4, 5] In fact, it is presumable that some of you are using synthetic indigo dye in an unknown way while reading this doctoral thesis, since several thousand tons per year are used on the coloration of denim cloth and blue jeans.[6] Furthermore, taking advantage of its π-conjugated nature, indigo was satisfactory tested in 2012 as semiconducting active layer in organic electronic devices, such as Organic Field Effect Transistors (OFETs).[7] To date, molecular design and device engineering strategies have been put forward to improve device performances, with new indigo-derivatives rendering around four order of magnitude higher OFETs performance compared to those of the reported in 2012, affording the opportunity to modulate materials properties toward specific device functions.[8]

As reflected by this historical background, we can assume that the great evolution in the application of π-conjugated organic materials has gone hand in hand with the knowledge of their properties. Thus, the quest of structure-property guidelines is an important aspect to take into account for the optimal application of these materials in optoelectronic devices as well as to design new derivatives that improve the properties and applications of the existing ones.

As the reader might have surely noticed in this brief historic background, concepts such as "semiconducting character" or "π-conjugation" unavoidably have appeared when talking about organic compounds because of their close relationship. For that, the introduction will first outline some general aspect about these two terms, then describe how them can be fine-tuned by structural modifications and finally, we will consider the function of π-conjugated materials in materials science, for example as active component in devices.

1.1. Semiconducting character in π-conjugated organic materials

Electrical conductivity can be described in its simpler extension as the ability of a material to transport electric current. The way this electrical conduction works, and the properties derived from it, can be explained in first instance by an elementary quantum mechanics point of view of Hückel Molecular Orbitals (HMO) theory.[9, 10] For this purpose, the two simplest linear organic molecules with alternating single and double CC bonds, 1,3-butadiene and 1,3,5-hexatriene, will be described in the following.

On the basis of the Linear Combination of Atomic Orbitals (LCAO) approach, when carbon atoms join together to form 1,3-butadiene and 1,3,5-hexatriene, their atomic orbitals come closer to spatially overlap. At this stage the orbitals hybridize, that is, one 2s-orbital combines with only two of the three available 2p-orbitals to form three new and identical sp^2 hybrid sigma-orbitals arranged in a trigonal coplanar structure around each carbon atom. The remaining unhybridized 2p orbitals, usually denoted $2p_z$, are orthogonal to the plane of the sp^2 molecular framework and they are responsible of π-bonding due to the presence of one free electron (or π-electron) for each $2p_z$ orbital.

Within the HMO approach, it is possible to predict the *bond order* between two adjacent atoms i and j (P_{ij}), a magnitude of significant importance that represents the contribution of the π-bond on the molecular structure. In view of the predicted data for 1,3-butadiene (Figure 1.2) the essence of the π-conjugation is described in a simple way, since CC bond between atoms 1 and 2 (or 3 and 4) is not a pure double bond (in that case, P should be equal to the unit), and the CC bond between atoms 2 and 3 is not a pure single bond (where P should be zero). Thus, the calculated bond orders suggest that the π-electrons are delocalized over the sp^2 framework as a consequence of the p_z orbitals overlap, through which electrons can freely move. This is just the definition of π-conjugation, which is defined by the IUPAC Gold Book as "*not localized π-bonding between two atoms: instead, each link has a 'fractional double bond character' or bond order*".[11]

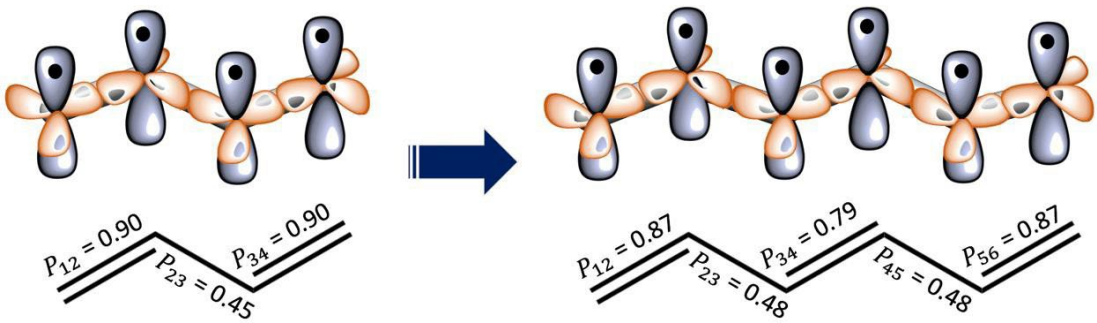

Figure 1.2. Schematic illustration of the sp^2 hybrid and $2p_z$ atomic orbitals of 1,3-butadiene (left) and 1,3,5-hexatriene (right) molecules. The calculated *bond orders* between adjacent atoms are also shown.

It is important to note that, even more pronounced is the effect predicted in 1,3,5-hexatriene, where the innermost CC bond between atoms 3 and 4 present the lowest P value within the double bonds. Therefore, the calculated bond order suggests that as long as each contiguous atom in a chain has an available p_z atomic orbital, the system enhances its π-conjugation. To further insight into this, the energies and wavefunctions of the molecular orbitals involved on the π-system can be also calculated assuming the HMO theory. In view of the results plotted in Figure 1.3, it is clear that an additional double bond in the conjugated system brings the Highest Occupied (HOMO) and Lowest Unoccupied Molecular

Orbitals (LUMO) closer together, reducing the energy difference between them (namely *energy gap*) as a consequence of a higher number of π-π overlapped molecular orbitals which enhance the electronic delocalization along the structure. Therefore, the energy required to promote one electron from HOMO to LUMO progressively decrease on going from ethylene to 1,3,5-hexatriene, shifting the absorption maximum to higher wavelengths.[12] As a result, it has been demonstrated that optoelectronic properties of polyene-based system can be modulated by fine-tunning its π-conjugation degree.[13]

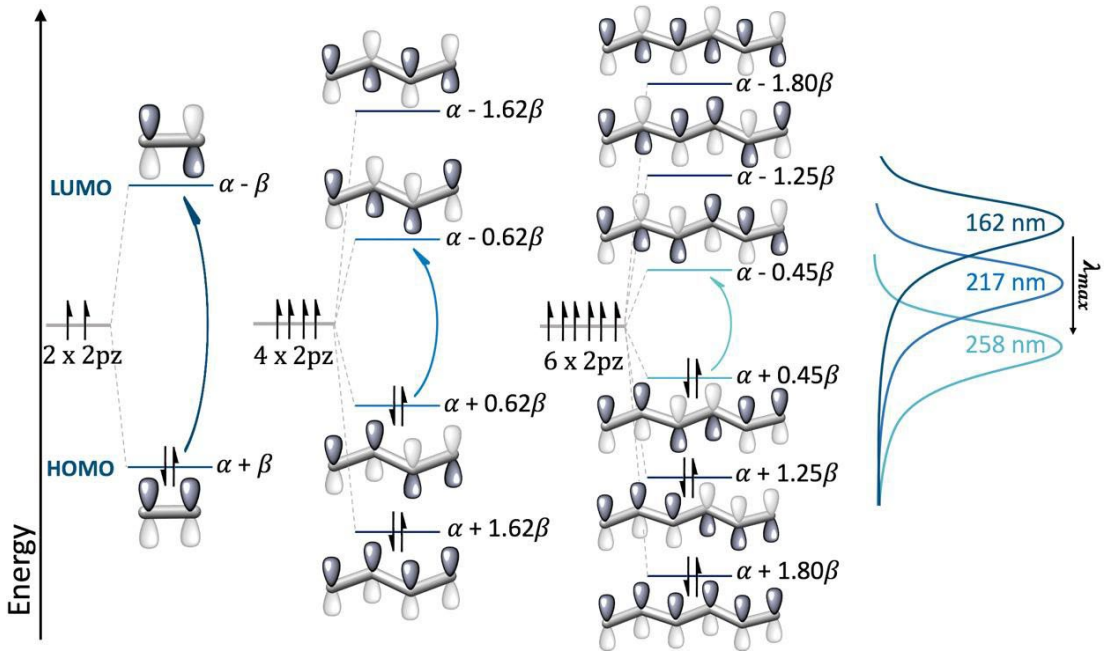

Figure 1.3. Pictorial representation of Hückel molecular orbitals energy diagram evolution by lengthening the oligomer size, together with its respective red-shifted maximum absorption wavelength. Molecular orbital wavefunctions with the different signs of the orbital lobes being depicted as different colors are also shown. Please, note that α and β, namely Coulomb and resonance integrals respectively, are parameters introduced by Hückel that can be evaluated empirically by fitting the theory to experimental results.

Similarly, when a large number of carbon atoms come together to form highly extended covalent systems, such as graphite, numerous adjacent levels so close in energy look like a continuum, producing both valence (analogous to previously mentioned HOMO)

and conduction (analogous to LUMO) bands separated by a band gap. This opens the scenario to the discussion of the effect that the band gap width plays on the electrical conductivity of the materials, which can be classified as insulators, metals or semiconductors (Figure 1.4).

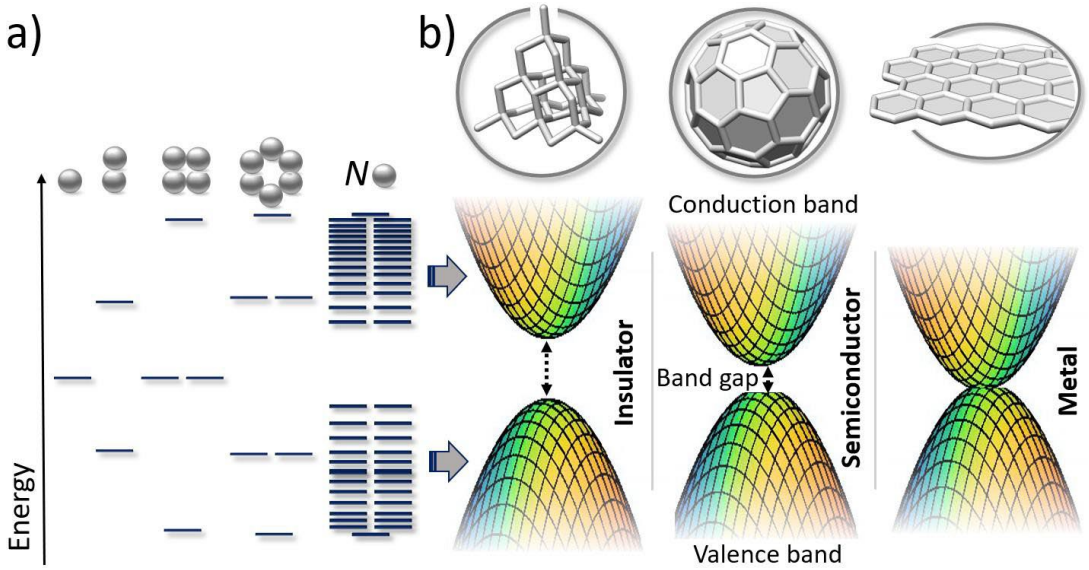

Figure 1.4. (a) Hypothetical schematic representation of a large number of carbon atoms coming together to form different carbon-based materials, demonstrating formation of the electronic band structure. Since *N* is a very large number in a macroscopic crystal, the adjacent levels are energetically close together, effectively forming a continuous energy band. (b) Comparison of characteristic energy bands for insulator (diamond), semiconductor (fullerene) and metal (graphene) materials.

Taking the different allotropes of carbon atom as example, natural diamond shows a large band gap between the completely filled valence and empty conduction band which avoid the electron-hopping between them, resulting on an insulator nature with null electrical conductivity ($\sigma < 10^{-8}$ Scm^{-1}). In marked contrast, electrons in graphene can move freely since metals or more accurately semi-metals have not energy gap between the two bands as a consequence of the overlap between them. These materials are characterized by an electrical conductivity higher than 10^{3} Scm^{-1}.[14] Finally, under certain conditions the inherent small band gap of fullerene makes possible the electron-hopping to the conduction

band, but not with the same easiness as they do in conductors. For example, it has been demonstrated that an external electrical field can effectively tune both the injection and accumulation of charges in this material, providing high conductivity in OFETs devices. In consequence, electrical conductivity between those of metals and insulators (10^{-8} Scm^{-1} <σ < 10^{3} Scm^{-1}) can be measured, classifying fullerene as a semiconducting material.[15, 16]

However, from a strict point of view, the molecular solid nature of organic semiconductors precludes transport of electric charges along delocalized bands like in its inorganic counterpart, except in exceptional cases of ultrapure single crystals at very low temperature.[17, 18]

1.2. Charge transport mechanism operating in organic semiconductors

Unlike inorganic semiconductors, where all the atoms are covalently bonded together forming a highly crystalline three-dimensional solid with a strong overlapping of the atomic orbitals which in turn allows the charge transport along highly delocalized bands, the order of molecular solids is determined by non-covalent intermolecular interactions between molecules.[19, 20] Taking into account the weakness of these interactions, the solid structure of an organic semiconductor is subjected to statistical changes on the distances and orientations between molecules (positional disorder) leading to variable molecular environment for each molecule, and thus different energy levels.[21, 22] As a result, charge carriers (charged particles that generate an electric current when moving) in organic semiconductors are usually localized over spatially and energetically distributed energy levels that define a Density of States (DOS), as showed in Figure 1.5, determined by either gaussian[23] [1.1] or purely exponential[24] [1.2] functions:

$$g(\varepsilon) = \frac{N}{\sigma\sqrt{2\pi}} exp\left(-\frac{\varepsilon^2}{2\sigma^2}\right) \qquad [1.1] \qquad g(\varepsilon) = \frac{N}{\sigma} exp\left(\frac{\varepsilon}{\sigma}\right) \qquad [1.2]$$

where σ is the energy scale of the DOS, while ε and N are the energy and the concentration of randomly distributed localized states, respectively.

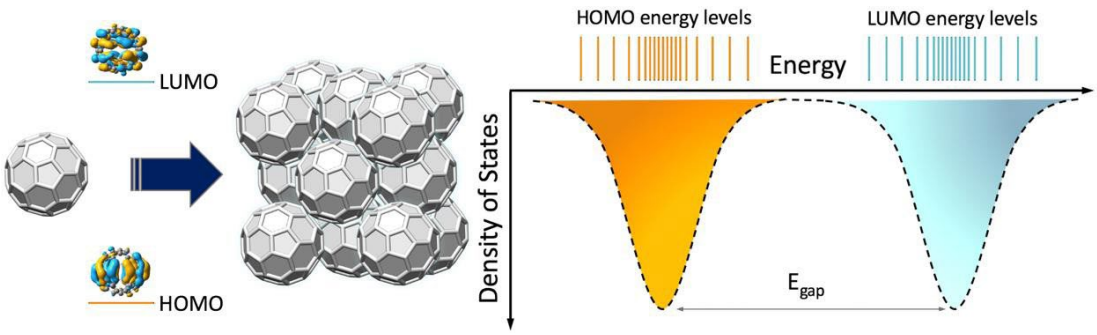

Figure 1.5. A hypothetical example of the density of states diagram for a generic organic semiconductor as a function of HOMO and LUMO energy levels. Fullerene is shown on the left as an example.

Before going in detail into the transport mechanism which will be expanded below, let me to stop here to briefly explain the first critical process that affects the electronic devices functioning: the charge carrier injection at the semiconductor-electrode interface. There are two types of charge carriers responsible of semiconducting properties in organic materials: (i) Negatively charged *electron* particles, which are generated and transported through LUMO energy levels population of the semiconductor. (ii) Effective particles known as *holes* with positive charge, interpreted as electron vacancies in the HOMO energy levels resulting from either one electron excitation or electron transfer process with an electrode.[25, 26] Depending on the type of charge carriers predominantly transported, semiconductors can be further sub-categorized as p-type or n-type for holes and electron-transporting materials, respectively. Another kind of semiconductors, known as ambipolar materials, can combine both electron and hole charge carriers as a consequence of simultaneously electron and hole injection from electrodes.[27]

As can be inferred by looking Figure 1.6, the position of the work function of the electrode (W_F) relative to the HOMO/LUMO levels of the semiconductor can, in principle, determine if a material operates as p-type, n-type, or ambipolar. In fact, W_F of the electrode aligns with the HOMO (LUMO) energy levels for p-type (n-type) organic semiconductors, whereas ambipolar transport requires that W_F lies in between the HOMO and LUMO levels

in order to reduce the injection barrier (ϕ_B) and thus, allowing that holes/electrons can be injected/extracted to localized states into the bulk at accessible applied electric fields.

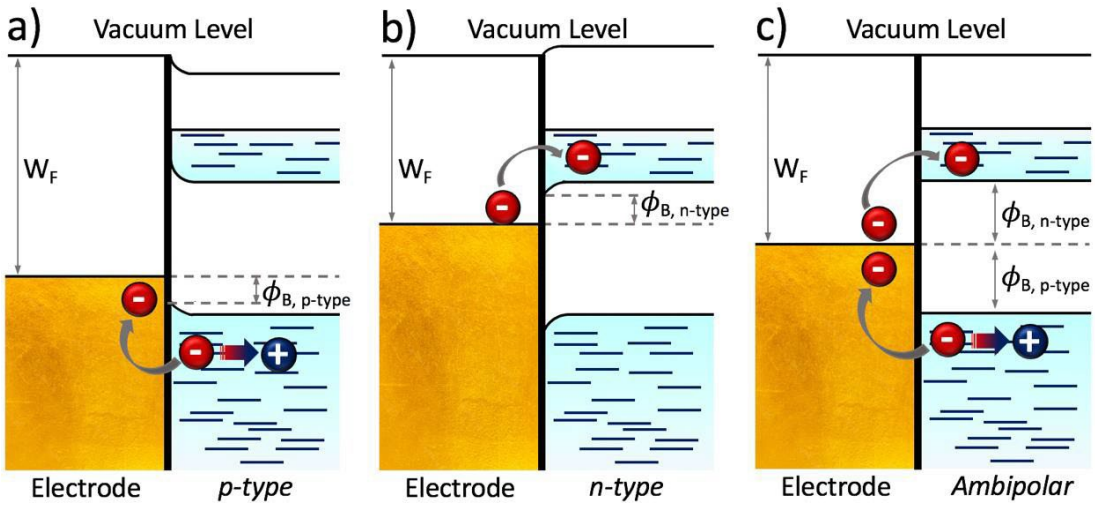

Figure 1.6. Scheme of (a) holes and (b) electrons injection into the HOMO and LUMO orbitals of p-type and n-type semiconductors, respectively. (c) Electrodes with W_F in between the HOMO and LUMO levels can facilitate ambipolar transport. The ϕ_B as the difference between W_F and the corresponding semiconductor energy level is also shown.

Nevertheless, ϕ_B is influenced by many complex effects, including the formation of interface dipoles and charge transfer between interfaces brought into contact, which make almost impossible to predict the energy level alignment at the electrode/semiconductor interface given only W_F and semiconductor HOMO/LUMO levels.[28]

Once the charge carriers responsible of electrical conductivity have been injected into the semiconducting material, we aim at exploring the following question: How do charge carriers move through the semiconducting material and what parameters control that? In this sense, the answer can be found on the "*hopping*" mechanism, which assumes that at the microscopic level the charge carriers randomly "hop" from one localized state to another associated to an adjacent molecule due to thermally activated effects that permit to overcome the energy barrier. Therefore, each "*hop*" is taken as an energetically activated electron transfer (ET) process between two adjacent molecules, as illustrated in Figure

1.7.[29-31] Usually, hopping mechanism in disordered materials can be interrupted by charge trapping, that is, situations where charge carriers are located in isolated energy levels which have not adjacent levels with a similar energy in a nearby molecule, leading to shallow or deep traps (depending on the deviation with respect the center of the DOS) from which charge carriers can release by energy or definitively get trapped stopping its contribution to charge transport, respectively.[32, 33]

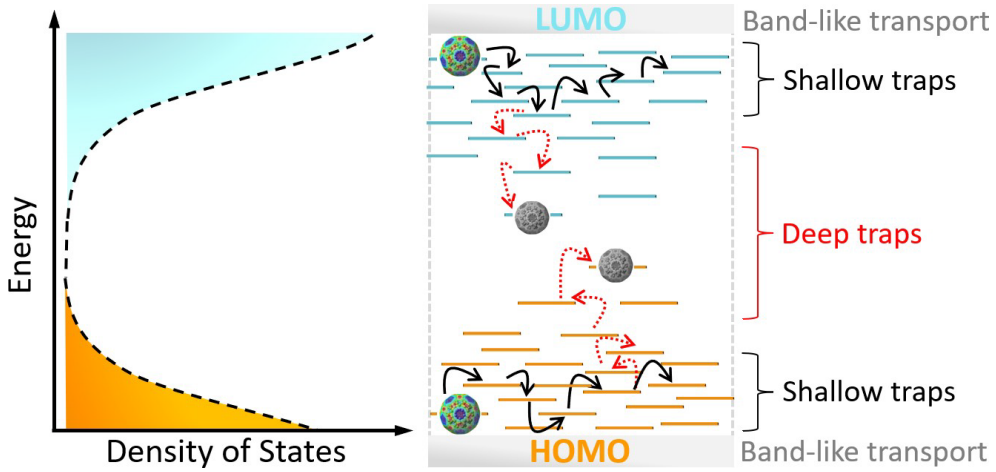

Figure 1.7. Illustration of *hopping* electron transport mechanism over spatially and energetically distributed energy levels. Charge trapping effects are also considered.

In this context, the main contribution to the electron transfer theory comes from R. A. Marcus, whose first formulation of the theory in 1956 drove him to the Nobel Prize in Chemistry in 1992.[34, 35] For Marcus, the inspiration to develop his theory was a work of W. F. Libby in which Franck-Condon principle was applied to explain why electron transfer reactions between pairs of small cations in aqueous solution are relatively slower than those involving larger ions.[36] In this sense, Marcus proposed that the missing ingredient to explain the different rate of these reactions is the dramatic variations in the chemical structure of the reactants, which is thermally activated by the reorganization of the surroundings that create the geometrically favorable situation prior to the electron transfer. Given that electron transfer in solution has much in common with the theory of the "polaron", which

is defined as an electron moving in a medium and carrying with it a polarized atmosphere, Marcus theory has been significantly refined and extended to address electron transfer processes in solids. In fact, about 20 years ago, Brédas et al. first proposed to use semiclassical Marcus theory to describe the charge transport process in organic semiconductors,[37, 38] describing the electron transfer hopping rate (K_{ET}) as:

$$K_{ET} = \frac{4\pi^2}{h}\frac{1}{\sqrt{4\pi K_B T}} t^2 exp\left(-\frac{(\lambda_i + \lambda_o)}{4k_B T}\right) \quad [1.3]$$

Where h and K_B are the Planck and Boltzmann constants respectively, T is the temperature, λ is the reorganization energy and t is the transfer integral. It is important to highlight that this theory is applicable when vibrational mode energies are significantly smaller than the thermal energy available and t is considerably shorter than λ,[39] in which case the electronic transport is essentially controlled by two parameters: (i) t, which reflects the degree of intermolecular interactions between HOMOs or LUMOs of nearest-neighbor molecular pairs and the (ii) λ term, which describes the strength of the electron-phonon (vibration) coupling at both intra- and intermolecular levels, denoted as λ_i and λ_o respectively. λ_i is reliably associated with the energetic cost of the conformational molecular changes needed to the acceptance or release of charge carriers, while λ_o reflects the external response of the environment surrounding the molecules involved in the charge transfer process. In solid state, λ_o is usually much smaller than λ_i, therefore it can be neglected to consider only λ_i.[40] With these considerations in mind, Equation 1.3 reveals that efficient charge transfer processes within a hopping regime require large transfer integrals and small reorganization energies.[41, 42] These two parameters are closely associated to the molecular structure and the solid-state packing.

This fact points up that the new area of molecular electronics depends critically on the understanding and the control of the electron transfer in and between molecules. Since the spirit of the present thesis is digging into the structure-property relationships of organic semiconductors, it can be considered mandatory to approach how structural changes at both intra- and intermolecular levels can fine-tune the charge-transport properties of a

specific material, in order to rationally manipulate them for their final implementation in devices. When it comes to complex structure-property relationships, an important requirement in developing high-performance optoelectronic devices involves the design of π-conjugated systems with an optimal charge carrier ability,[43] whose clues are presented in the next sections.

1.3. π-conjugation tuning at the intramolecular level

Taking the OFETs as a representative example of electronic device, since the first polymer and small molecule-based transistors were reported in 1986 and 1989 respectively,[44, 45] tremendous progress has been made on the development of "the perfect system", with OFET devices rapidly improving performance records year after year (Figure 1.8).[46-49] In fact, in the 1980s the mobility (the ability of charges to move under an applied electric field) of the first reported organic semiconductor was of around 10^{-5} $cm^2V^{-1}s^{-1}$, while in 2020 the values of single crystal small molecules have increased up to 48 and 28 $cm^2V^{-1}s^{-1}$ for hole and electron transport, respectively.[50, 51]

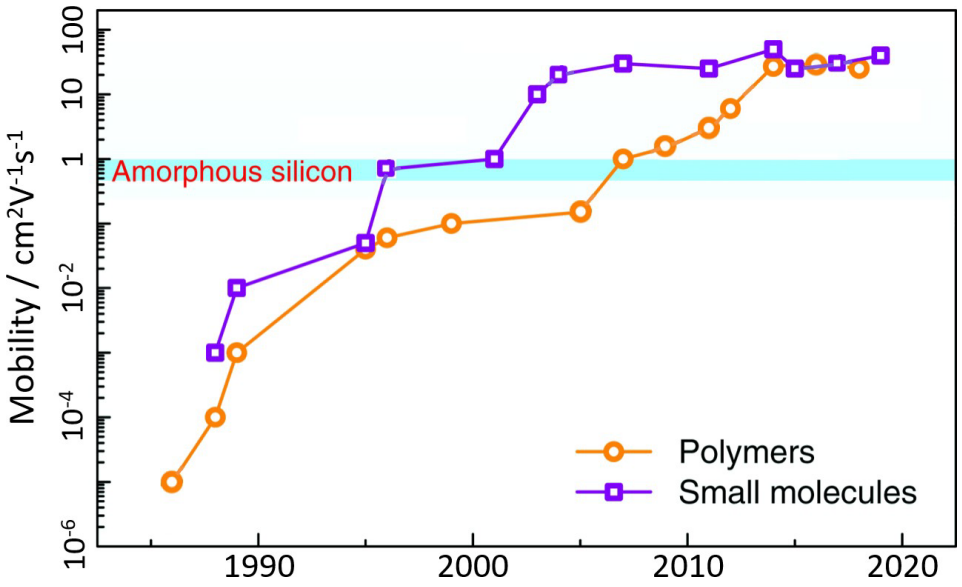

Figure 1.8. Statistical relationship between the charge carrier mobilities of reported small molecules and polymer-based semiconductors and their report date, from 1980 to 2020.

In the next subsections, we review the key milestones that have been made in terms of design criteria over the last 30 years, outlining the molecular design strategies that have, over time, been behind these successes, rather than focus on specific/highest reported mobilities. Considering that polymers consist of several conjugated small units which dictate the processability and optoelectronic properties of the final materials and given that both small molecules and polymers share the same design criteria to obtain high performance organic semiconductors, we mainly discuss the case of small molecules to provide the readers with the historic research route.

1.3.1. From twisted to planar π-conjugated systems

Since all the materials proposed to study in this thesis are based on cyclic and/or heterocyclic units covalently linked, we firstly discuss the simplest oligoarylene derivative: the biphenyl molecule (**1** in Figure 1.9), which consists of two phenyl rings almost perpendicularly connected to each other through a CC single bond, due to the steric hindrance caused by the hydrogen atoms of adjacent rings.[52] This molecular arrangement has physical consequences, such as a π-conjugation disruption between the two adjacent phenyls rings induced by a negligible orbital overlapping. In fact, almost identical absorption maxima (at around 256 nm) can be found on the UV-Vis absorption spectra of benzene and biphenyl molecules, confirming that both phenyl rings of biphenyl act as independent units without apparent π-conjugation between them.[53] Likewise, α-sexithiophene, which supposes the first ever OFET based on a small molecule, shows a backbone conformation strongly dependent on the rotational freedom of the single bonds connecting the thiophene rings.[54] It is, therefore, an invaluable prerequisite for conjugation that conjugated systems are planar (or nearly so), in which case, "side-on" orbital overlap between line-up adjacent π-orbitals takes place.[55, 56]

To address this issue, molecular materials with two or more fused rings have attracted considerable attention in the emerging area of organic electronics, as the combination of conformationally blocked and rigid molecular structures as well as optimum π-orbital

overlapping may lead to practical applications.[57] Similar to strategies presented by Müllen and coworkers in the 1990s for minimizing the mutual distortion between phenyl rings in poly(*p*-phenylene),[58, 59] totally coplanar 9H-fluorene (compound **2** of Figure 1.9) and pyrene (compound **3** of Figure 1.9) π-systems can be obtained via formation of methylene and doubly ethene-bridged biphenyl bridges.[60] Note that pyrene can be considered as two fused naphthalene (compound **4** of Figure 1.9) moieties, which is the simplest polycyclic aromatic hydrocarbon.

Thereby, the lowest energy transition of diluted chloroform solutions containing these samples greatly red shift on going from the non-fused biphenyl molecule (255 nm) to the fused fluorene (301 nm), naphthalene (312 nm), or pyrene (349 nm) analogous, corroborating that fused rings is a useful strategy to enhance the overall π-conjugation of the system.[61-63] In addition, these planar and rigid backbones give rise to lower λ values since the molecular geometry undergoes less changes on going from the charged to the neutral state (see Figure 1.10), which result in enhanced intramolecular charge transport.[64, 65]

However, reducing the torsional disorder along the molecular backbone can not only be achieved by covalently linking aromatic units into fused moieties. Another technique is based on the introduction of noncovalent intramolecular conformational locks to control the rotation and enforce the planarity of the conjugated backbones.[66] Indeed, free rotation of sigma bonds can be restricted by X···Y (Y = O, N, halide) noncovalent interactions by taking advantage of electron interactions between the lone pair electrons of Y and the antibonding orbitals of the heteroatom X inserted to the cycle.[67-69] The two most prominent building blocks illustrating this strategy are the electron-deficient isoindigo (IIG, named as **5** in Figure 1.9) and diketopyrrolopyrrole-based systems with flanking phenyl rings (DPP, named as **6** in Figure 1.9), where favorable oxygen-hydrogen interactions lead to highly coplanar systems with reduced torsional disorder along the molecular backbone.[70-73]

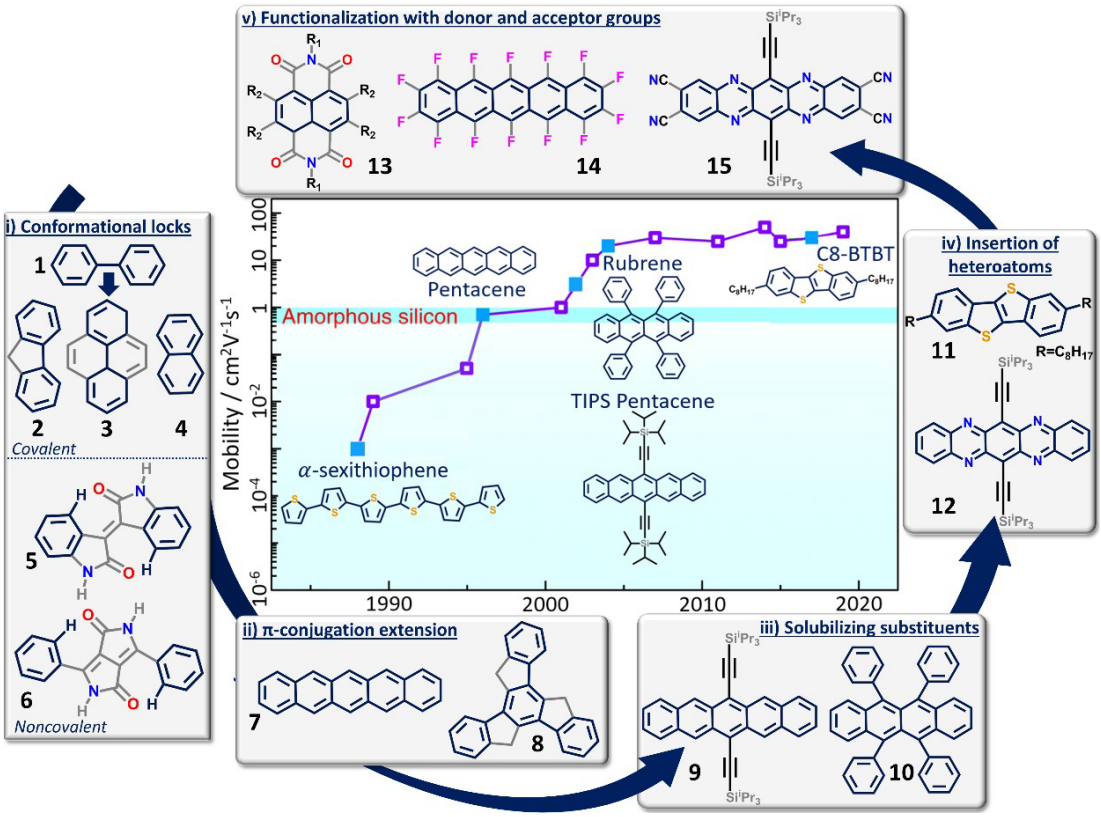

Figure 1.9. Time-evolution of small molecule based OFETs performance. Some milestone progresses are labeled out.

1.3.2. π-conjugation extension

As anticipated in the previous section, another successful strategy toward enhanced semiconducting properties is lengthening the π-framework. Taking the above-mentioned fused-rings molecules as building blocks, extended condensed derivatives of considerable interest for optoelectronic applications can be obtained. For instance, closely related with naphthalene, when the focus is on highly π-conjugated semiconductors with fused rings, it is unavoidable to think in pentacene (compound **7** of Figure 1.9). In fact, since hole mobility of OFETs based on pentacene films was beyond that of amorphous silicon (0.5-1 $cm^2V^{-1}s^{-1}$) in 1997,[74] this molecule is considered as the fused system par excellence, being the precursor of the most important p-type building-blocks synthesized to date, as we will see below. The clearly improved electronic delocalization along the molecular backbone of

pentacene when compared with naphthalene is evidenced by the absorption maxima red shifts experimentally observed when the system gets larger (from 312 to 380 nm on going from naphthalene to pentacene), as a consequence of the HOMO-LUMO gap narrowing going from -4.3 eV for naphthalene to -2.1 eV for pentacene.[75, 76] Additionally, the extensive conjugated structure benefits the intramolecular delocalization of charge carriers, giving rise to lower reorganization energies compared to the naphthalene counterpart (see Figure 1.10).

It is worth to mention that π-conjugation extension is not limited to follow a linear direction as observed in pentacene. In fact, fluorene can be used as building block for the design of three-armed star-shaped molecules such as truxene (compound **8** of Figure 1.9), which can be considered as three fluorene units that share a fused aromatic ring. Compared with the linear system commonly used, star-shaped molecules offer a number of advantages when used in optoelectronic devices, including the ability to show multifunctionality in a single molecule.[77] The effective electron delocalization along the three fluorenone arms confers this molecule a narrower energy gap (determined by a red-shifted of the longest wavelength of 43 nm) with respect the parent fluorene as well as successful semiconducting characteristics for solution processable OFETs, displaying hole mobilities of up to 10^{-3} $cm^2V^{-1}s^{-1}$.[78]

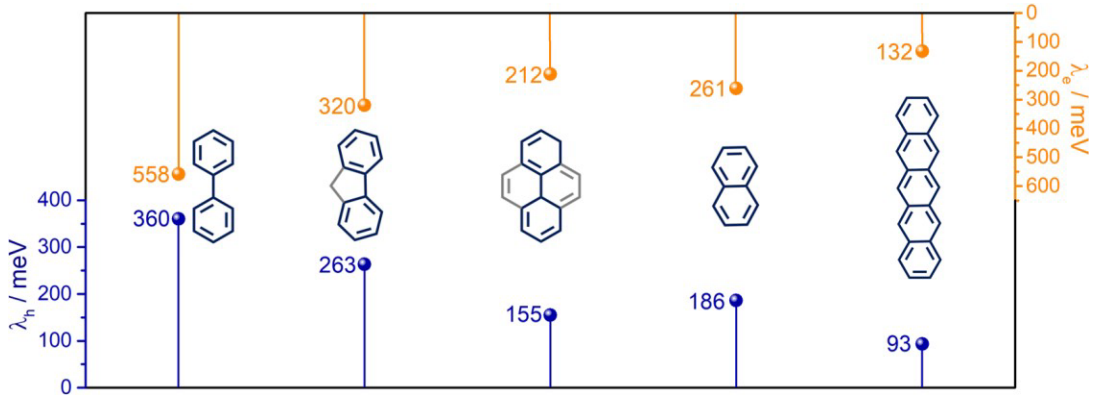

Figure 1.10. Theoretically calculated (B3LYP/6-31G** level) hole (blue) and electron (orange) reorganization energies for some oligoarylene derivatives.

Although mobilities exceeding those of amorphous silicon were already obtained at this point of the historic research route, some issues still need to be addressed to improve the applicability of these materials. On one hand, low-lying HOMO levels make these systems notably vulnerable to the oxidation by exposing oxygen. On the other hand, rigid highly π-conjugated molecules are generally poorly soluble in most common solvents due to their strong intermolecular π-interactions and the lack of flexible chains. These considerations open the scenario to the design of new highly-performance organic semiconductors meeting the environmental stability and easy processability standards required for the high throughput manufacturing of devices, which is discussed in the next two sections.

1.3.3. Insertion of solubilizing substituents

To guarantee sufficient solubility of the material and thus improve the processability of organic semiconductors in solution, solubilizing lateral substituents are usually introduced in the π-conjugated skeleton. In this sense, the search of solution processable pentacene derivatives has led to the discovery of several new materials.[79-84] Examples include the introduction of triisopropylsilylethynyl groups to the pentacene, which drive us to the second breakthrough (compound **9** of Figure 1.9). For TIPS-pentacene, solution deposition yielded devices with hole mobility up to 2 $cm^2V^{-1}s^{-1}$,[80] suggesting the material is able to form highly crystalline films, with the lateral chains leading to soluble materials without disturbance of the conjugated system. Even more remarkable is the case of rubrene (compound **10** of Figure 1.9), in which arylation in peri-positions of tetracene (linear acene composed of four fused benzene rings) resulted in single crystal based OFETs with mobilities up to 15 $cm^2V^{-1}s^{-1}$.[85] However, low mobility thin film OFETs (in most cases less than that of amorphous silicon) were recorded as a consequence of the poor film quality, which was attributed to an inefficient molecular packing caused by the mutual distortion of the phenylene units.[86, 87] Therefore, on the basis of the above considerations it is of crucial importance that the incorporation of lateral groups helps to solubilize the conjugated

material without altering the molecular planarity and, thus, the intramolecular π-orbital delocalization.

1.3.4. Insertion of heteroatoms

The pursue of environmentally stable materials has driven research to design new π-conjugated systems invulnerable to oxidation by exposing oxygen. A commonly used strategy to accomplish that is the use of sulfur-rich systems owing to the following characteristics: (i) conjugated systems with sulfur atoms have been shown to be environmentally stable and robust in nature,[88, 89] and (ii) they offer a great ability to improve the extent of intermolecular π-π overlap in the solid state as a result of multiple short intermolecular S···S contacts, being both factors of crucial importance to achieve effective semiconducting materials.[90, 91] In this context, Takimiya and coworkers demonstrated that incorporation of fused thiophenes into oligoacene frameworks is an efficient strategy to overcome the instability of pentacene, proposing 2,7-Dioctyl[1]benzothieno[3,2-b][1]benzothiophene (**C8-BTBT-C8** listed as compound **11** in Figure 1.9) as a new promising semiconductor, which placed us on the last breakthrough of this historic route.[92] In fact, **C8-BTBT-C8** shows larger mobility compared to pentacene (higher than 31 $cm^2V^{-1}s^{-1}$ for single-crystalline thin films) in addition to a significantly improved solution processability and stability to oxidation, with device characteristics preserved for more than 200 days without any significant change. From a supramolecular point of view, the excellent electrical properties of **C8-BTBT-C8**-based OFET devices can be attributed to the existence of bidimensional semiconducting channels with strong intermolecular overlap.[93] As a result, **C8-BTBT-C8** has been taken as model to design new organic semiconductors.[94-96]

Interestingly, depending on the heteroatom used, the charge transport properties of these organic semiconductors can be modulated going from p-type to n-type or ambipolar characteristics. For example, the substitution of sp^2 carbon atoms by N in the conjugated

skeleton of TIPS-pentacene (compound **12** of Figure 1.9) leads to electron-transport properties with mobilities of 13 $cm^2V^{-1}s^{-1}$ for semicrystalline thin films.[97, 98]

On the basis of all the aforementioned data, it has been evidenced that the vast majority of organic semiconductors favor hole-transport whereas electron or ambipolar transporting materials are rarer and, in general, still lag behind its p-type counterparts.[99] An explanation to this can be found on the difficulty of designing organic semiconductors whose LUMO energy level is close to the work function of the used electrodes (like Au and Pt), which is a basic requirement to have an efficient charge injection from the electrode to the organic layer. Simply speaking, the work functions of the most common electrode materials are very high and thus, more suitable for the injection of holes into the HOMO of the organic semiconductor. Furthermore, compared to holes, electrons are more easily trapped as a result of the oxidative environment in which we live.[100] In order to match the LUMO energy level of the organic semiconductor with the work function of the electrode, tuning the energy levels of organic materials by chemical functionalization of the molecular structure with electron donor and acceptor groups is a widely used strategy, as described below.

1.3.5. Functionalization with donor and acceptor groups

Nowadays, precise engineering of both HOMO and LUMO energy levels of π-conjugated systems is critical and therefore, it has become one of the main research topics in the field. In general, the linear extension of the π-conjugation tends to both raise the HOMO and lower the LUMO making the system both easier to oxidize and reduce, as previously discussed. Such strategy has been employed to design ambipolar materials into which both hole and electrons can be injected. If one desires to preferentially lower the energy of the LUMO, the substitution of the π-conjugated framework with electron withdrawing groups, is a reasonable strategy. In contrast, the insertion of electron-rich groups preferentially increase the energy of the HOMO with a lower effect on the LUMO (Figure 1.11).[101] As a representative example, substitution of two sets of π-accepting

dicarboximide groups at the peri-positions of naphthalene molecule renders a more extended oligoarylene system named as naphthalene diimide (NDI), which can exhibit electron mobilities as high as 6.2 $cm^2V^{-1}s^{-1}$ (compound **13** of Figure 1.9).[102] In addition, further functionalization at both N atoms of the imide groups and naphthalene core with acceptor units (cyano, nitro, etc.) pull electron density away from the core of the π-system by mesomeric effect, essentially lowering the energy of the LUMO and facilitating electron injection.[103, 104] Another approach to make a conjugated system more electron deficient is by the insertion of inductive electron withdrawing groups such as halides. Such substitution directly affects the polarisation of the σ-orbitals and effectively lowers the electron density at the nuclei of the attached atoms in the π-systems, resulting in a stabilization of both HOMO and LUMO. In this context, respectable electron mobilities can be extracted from benchmark p-type semiconductors such as pentacene, as long as strongly electron-withdrawing groups such as F groups are introduced to the conjugated framework (compound **14** of Figure 1.9).[105]

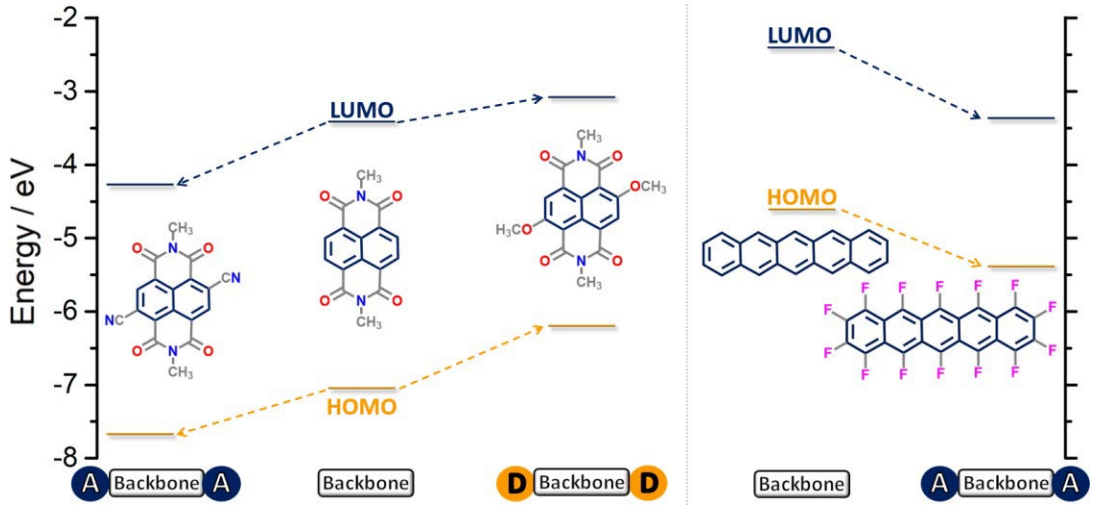

Figure 1.11. Schematic representation of the HOMO and LUMO energy levels modulation by insertion of either electron-rich or electron withdrawing groups to the NDI (left) and pentacene (left) cores. The HOMO and LUMO energy values have been predicted by using DFT calculations at the B3LYP/6-31G** level of theory.

Note that this donor-acceptor concept was firstly introduced by Wynberg in 1992 as an excellent approach to design polymers constituted by alternating electron-deficient (acceptor) and electron-rich (donor) repeating units.[106] For instance, the HOMO of the polymer will depend strongly on the donor, while its LUMO will localize fundamentally in the acceptor group. Consequently, the HOMO-LUMO gap of these D-A polymers can be modulated according to the choice of the donor and acceptor moieties, in addition to the appropriate functionalization of the conjugated backbone through the insertion of peripheral substituents.

1.4. From small molecules to polymers

Compared to small molecules, the application of conjugated polymers in commercial electronic devices as well as the further understanding of structure–property relationships remain challenging due to some of their inherent disadvantages. For example, (i) the traditional synthesis methods for semiconducting polymers lead to the presence of high polydispersity, which significantly hinders the purification of polymers due to the uncertainty of molecule weight. This fact produces batch-to-batch variations undesirable for commercial applications. In addition, (ii) intra and interchain entanglements usually provide less ordered materials with low degree of crystallinity, limiting its charge transport properties. Finally, (iii) thermal evaporation methods, which are widely used in the deposition of organic small molecules, can no longer be used in polymers.

However, despite these limitations, organic semiconducting polymers are considered attractive candidates for future applications in lightweight and foldable electronic devices,[107] due to its potential low-temperature solution processing ability (which allow large scale production applicable to building circuits) and the excellent capacity to modulate its electronic and mechanical properties by adjusting the substituents or monomeric building blocks.[108, 109] In fact, thanks to the discovery of novel polymers and the improvements of device fabrication, most recent reports on semiconducting polymer implemented in OFETs have highlighted device performance on par with the best small

molecules.[89, 110, 111] As a representative example, it is worth to mention the thienoisoindigo-naphthalene-based conjugated polymer reported by Yang, Noh and coworkers in 2014 (**PTIIG-Np** in Figure 1.12), which exhibited hole mobility up to 14 $cm^2V^{-1}s^{-1}$ from a simple coating processing.[112] Likewise, Yan and coworkers reported in 2009 one of the first examples of stable, printable and high-performance electron-transporting polymer-based OFETs fabricated with an naphthalene-bis(dicarboximide) polymer (**NTCDI** in Figure 1.12). Electron mobilities up to 0.85 $cm^2V^{-1}s^{-1}$ were recorded.[113] These findings show that both high performance p-type and n-type donor-acceptor polymers with mobilities exceeding the benchmark value of amorphous silicon semiconductor have now been achieved, which suppose a major step towards commercialization of polymer-based circuit technologies.

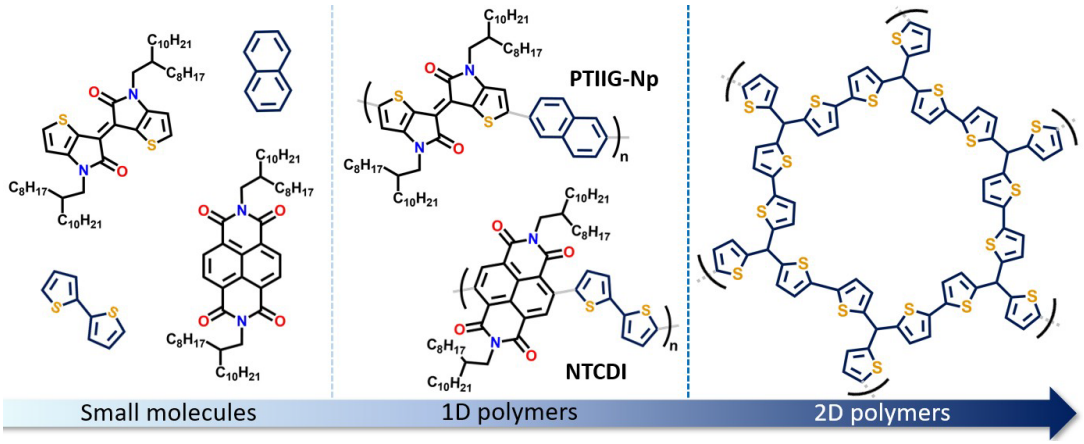

Figure 1.12. Representative examples of: small molecules, linear (1D) polymers and bidimensional (2D) polymer.

Curiously, it has been demonstrated that the charge transport pathway of these linear polymers take place along the molecular chains rather than through the π-π stacking direction, leading to a considerable anisotropy between intrachain and interchain directions.[114-116] In this context, expanding the polymer dimensionality towards two (or even three) dimensions architectures has emerged as an effective way to exploit the dominant intrachain charge transport. For example, large-area bidimensional covalent organic framework (COFs) materials built from the precise periodic in-plane integration of

building blocks through covalent bonds (as show in Figure 1.12, right) have demonstrated to be isotropic materials with higher in plane mobility.[117] The correct selection of the building blocks is a critical step on the formation of this kind of polymers, since the required topology, optical and electronic properties of the resulting polymer will depend on it.[116, 118-121]

In view of those considerations, we conclude that the π-conjugation of semiconducting materials clearly depends on molecular structural factors, such as planarity, effective conjugation length and the presence of the attached substituent groups, among others.[101] Nevertheless, the charge transport ability of organic semiconductors is not exclusively determined by the properties of the individual molecules that compose them, but also its spatial arrangement in the solid is a crucial aspect that must be investigated in order to obtain molecular materials with outstanding performances in electronic devices.[38, 122]

1.5. Importance of intermolecular interactions

The good overlap between molecular orbitals of adjacent molecules is an indispensable prerequisite to obtain an efficient migration of electric charge within a semiconductor, being this greatly conditioned by the degree of ordering of the organic molecules in the material. In this context, it is possible to distinguish three types of molecular packing depending on the molecular order in the solid state: high-order crystalline, partial-order polycrystalline and disorder amorphous states (see Figure 1.13). In a crystalline solid, the molecules that constitute it are perfectly arranged in a periodic network by the effect of intermolecular interactions such as hydrogen bonds or by cooperative effects of Van der Waals forces. As a consequence of the weak nature of these interactions, various molecular environments can coexist in the solid state, leading to a polycrystalline solid formed by several crystalline domains with different orientations.[123] In this situation, even though the molecules are ordered within each crystalline domain, the overall periodicity of the solid is broken at the limit between different domains (named as grain boundaries). Finally, if the molecules that form the material are randomly distributed without any periodic pattern, the solid is considered to be amorphous.[124]

The different degree of molecular order in the solid state plays a key role on the macroscopic properties of the material. In fact, structural defects and grain boundaries in amorphous and polycrystalline molecular packing structures normally complicate the intrinsic charge transport properties, being thus desirable highly dense and ordered molecular packing motifs with minimal traps and defects.[125] This effect is evident by comparison of the electrical mobilities measured in disorder, partially ordered, and highly ordered films of pentacene (Figure 1.13), where variations by three to six orders of magnitude can be observed.

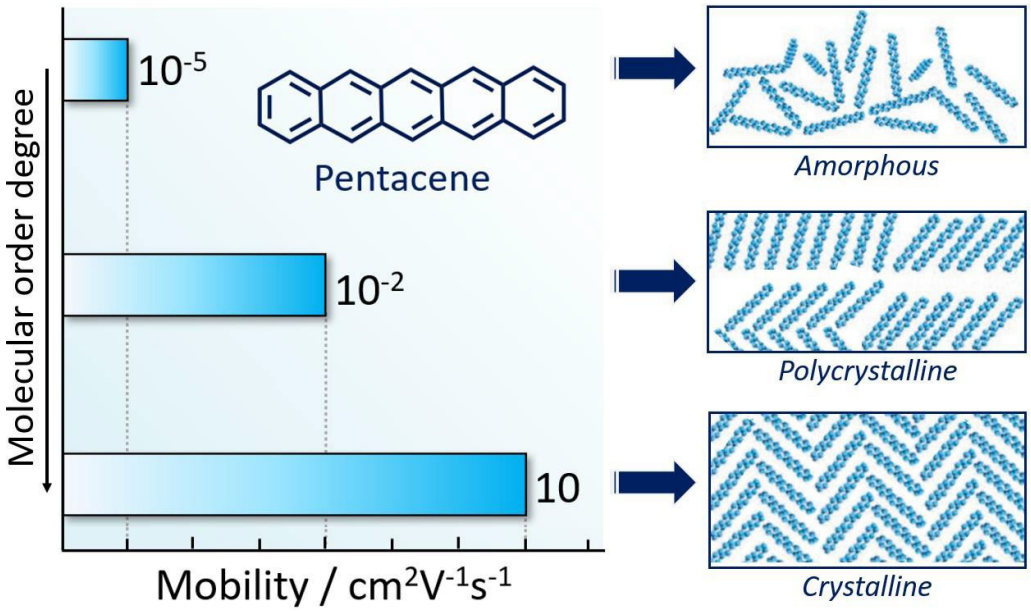

Figure 1.13. Evolution of OFET performance as a function of the molecular order for pentacene films.

In the case of amorphous films, low mobilities of around 10^{-5} $cm^2V^{-1}s^{-1}$ were measured in 1992.[126] Curiously, a notable mobility enhancement of three orders of magnitude was reported during the 1990s as a result of a higher control of the conditions under which pentacene molecules assemble to form the solid. In this sense, mobilities of 0.038 $cm^2V^{-1}s^{-1}$ were reported for devices based on polycrystalline pentacene films, whose structural characterization revealed the coexistence of two phases.[127, 128] Since mobility is very

sensitive to structure imperfections, the polycrystalline nature of these films limited the device performance due to the presence of grain boundaries that impede the carrier transport process. This consideration opened the scenario to think that better mobilities could be obtained in pentacene, provided that grain boundaries effects were minimized. In 2007, this issue was addressed when ultrapure single crystal films characterized by a herringbone pattern within the layers were obtained, showing charge-carrier mobility values around 15 $cm^2V^{-1}s^{-1}$ and thus, corroborating that defects free materials are desired to obtain high-mobility devices.[129]

Such characteristics highlight the importance of controlling the molecular packing by the correct material design and device optimization. In this regard, four typical molecular packing motifs can be found: herringbone packing motif without (style I in Figure 14) or with π–π overlap (style II in Figure 14) between adjacent molecules, and lamellar motifs with one (slipped in Figure 14) or two dimensional π–π stacking (bricklayer in Figure 14).[130] It should be noticed that different transporting routes can be seen along different orientations of the molecular packing motifs. As a result, structural anisotropy is unavoidable, with transfer integral along the direction of maxima π-π overlap being much larger than those along other directions.[131, 132] Therefore, it is of crucial importance the correct use of the structural isotropy for achieving high performance optoelectronic devices.[133-135]

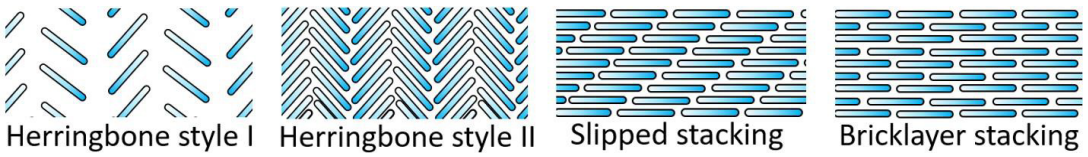

Figure 1.14. Illustration of the most important crystalline molecular packing styles.

Since the first organic semiconductor crystal was reported in the 1950s,[136] the understanding of how molecular packing affects charge transport has become a powerful tool for examining structure-property relationships, paving the way to the understanding of fundamental factors needed to achieve high performance devices. Thereby, in addition to the nature of the molecule itself (as seen on the previous section), optima molecular packing

motifs that increase the π-π stacking are considered the most efficient for transporting charge carriers.[41, 130, 137] The key point behind this philosophy is that if the molecules would adopt a more π-π stacking arrangement, the electronic coupling would be maximized due to enhanced π-π overlap between neighboring molecules and thus, the charge carrier mobility would also be improved.[122, 138] From this point of view, tremendous effort has been focused on achieving π-π stacking in two dimensions, being finally demonstrated that highly planar polyheteroaromatic systems help the formation of such packing motifs as a consequence of cooperative intermolecular interactions between heteroatoms that lead to a balanced bidimensional electronic structure.[138, 139] However, there exist molecules that have effective wavefunction overlap without extensive π-stacking and likewise cases of molecules with strong π-stacking but which a poor wavefunction overlap. These statements point out that one must not only consider simply the presence of π-stacking interactions to determine coupling but also the precise nature of that π-stacking.[42] To further complexity, it should be point out that although the addition of lateral substituents to the conjugated core does not necessarily contribute to charge transport directly, they can strongly modify the crystal packing of the organic semiconductors.[140, 141] For example, X-ray crystallography data of TIPS-pentacene reveals that this material stacks in a two-dimensional columnar array with significantly enhanced orbital overlap and reduced interplanar spacing compared to unsubstituted pentacene.[80]

Despite the difficulty in the investigation of charge transport in organic materials, after three decades of enormous research effort, the field of organic semiconductors has incredibly grown for next-generation optoelectronics applications.

1.6. Applications of organic semiconductors in electronics

Looking around us, electronic dominates the current word in which we live since most of our daily activities involve the use of optoelectronic devices. Different fundamental aspects such as the economy, leisure, health, personal relationships, etc. are closely related to technological progress. This close relationship, more and more dependent on each other,

makes mandatory the design and synthesis of new materials that improve the properties and applications of the existing ones. The quest of this objective requires an interdisciplinary scenario in which chemists, physicists, material scientists and engineers work together in the comprehension of new fascinating materials. Until now, this social need has been mainly satisfied with the use of inorganic materials mostly based on silicon. Nevertheless, its hard processability, high cost of the massive manufacturing of devices and difficult modulation of its electronic properties have been a turning point, making incompatible these materials for new social demands.[142, 143]

In this sense, organic semiconductors have emerged as an important class of materials for next-generation optoelectronics applications, offering interesting prospects for high throughput, low-cost and flexible electronic circuits which are often unreachable by the most common and widely used inorganic counterpart. Indeed, the organic optoelectronics can be considered a future alternative. There are several reasons for the incredibly rapid emergence of the organic optoelectronics in the past three decades: (i) facile structural synthesis and functionalization allowing fine tuning of electronic properties, solid-state packing and solubility among others; (ii) the presence of high mechanical flexibility which allows devices with low brittleness; (iii) economic processing by printing, which is beneficial for large-area industrial applications; (iv) possibility to be used in biologic systems (biocompatibility).[144-146] With these benefits and after three decades of enormous research effort, the field of organic optoelectronics has already reached the market. In fact, organic semiconductors have become widely used in the preparation of OLEDs (Organic Light-Emitting Diodes, displayed at the center of Figure 1.15) being specially common and widespread.[147] Likewise, other technologies are experiencing great development, such as photovoltaic cells (OPVs, displayed on the right of Figure 1.15)[148] and OFETs (displayed on the left of Figure 1.15).

It is important to highlight that in these next-generation optoelectronic devices, the efficiency of charge transport within the organic layer plays a key role. For example, in solar cells the charges created by photoexcitation of the active material must be efficiently

transported to the metallic contacts, where they are collected and stored under the form of electrical energy.[149] In light-emitting diodes, it is desirable that the injected holes and electrons from the electrodes have large and balanced charge transport characteristics to favor recombination processes in the bulk instead of electroluminescence quenching produced by charges recombination close to a metallic interface.[150] Another challenge is to develop materials displaying high hole and electron charge transport properties in field-effect architectures to design complex organic circuits.

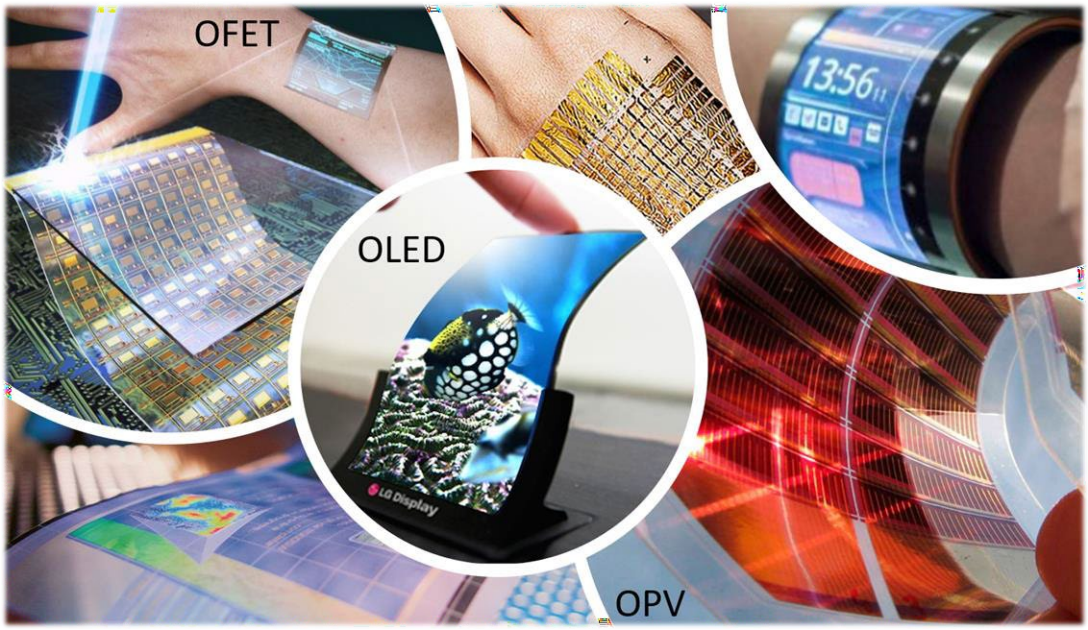

Figure 1.15. Some examples of electronic devices based on organic semiconductors. It is worth to highlight the cases of ultra-thin, flexible and transparent OFETs (top), commercialized high-resolution OLED screens (middle) and flexible as well as lightweight solar cells (bottom).

Since OFETs are a versatile platform for a quick examination of the electrical mobility of new semiconductors (which is essential, as previously discussed), most of the materials proposed to study in this thesis have been implemented in OFETs. A field-effect transistor can be defined as a type of electronic device that uses an external electric field to control the flow of current in the semiconducting channel. Thereby, they can act as signal-amplifiers, oscillators and logic switchers.

Simply speaking, an OFET is constituted of different layers assembled on a substrate: the organic semiconductor, the insulating layer (dielectric) and three terminal electrodes (the gate, source and drain electrodes). The operation of an OFET relies on the application of an electric potential at the gate electrode (V_{GS}) which generates an electric field causing the accumulation of charge carriers at the semiconductor-dielectric interface (left side of Figure 1.16). Once the charge carriers are accumulated, an applied electric potential between source and drain electrodes (V_{DS}) allows charge transport within the semiconducting layer and thus, a current (I_{DS}) is measured (right side of Figure 1.16). Note that the charge density in the transistor channel (and thus, I_{DS}) can be modulated by the magnitude of the applied field (V_{GS}), hence the "field-effect" terminology.

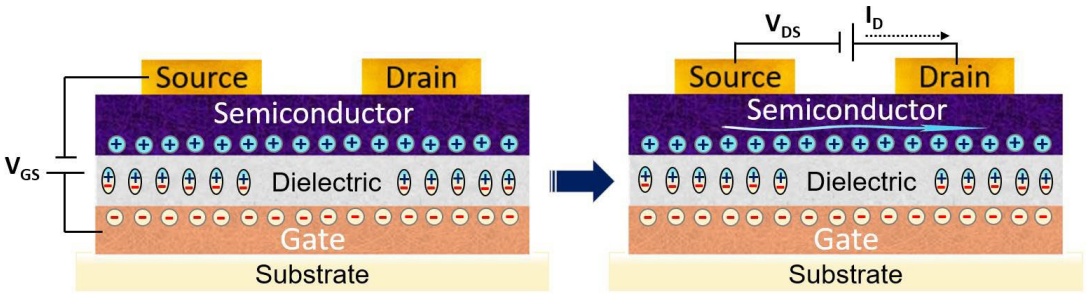

Figure 1.16. Schematic illustration of the operation of an OFET with p-type characteristics.

Given that usual transistors are now the fundamental building blocks of any electronic device, OFETs could be in the future the base for the next generation of organic circuits and this is the reason of the increasing interest in this research field.[138]

1.7. References

[1] Caesar, J.; Robertson, J. C.; Robertson, J. C., *De bello Gallico. Books V and VI*. W.J. Gage Co.: Toronto, 1894.

[2] Puchalska, M.; Połeć-Pawlak, K.; Zadrożna, I.; Hryszko, H.; Jarosz, M., Identification of indigoid dyes in natural organic pigments used in historical art objects by high-performance liquid chromatography coupled to electrospray ionization mass spectrometry. *Journal of Mass Spectrometry* **2004,** 39, (12), 1441-1449.

[3] Mohn, T.; Plitzko, I.; Hamburger, M., A comprehensive metabolite profiling of Isatis tinctoria leaf extracts. *Phytochemistry* **2009,** 70, (7), 924-934.

[4] Lei, T.; Wang, J.-Y.; Pei, J., Design, Synthesis, and Structure–Property Relationships of Isoindigo-Based Conjugated Polymers. *Accounts of Chemical Research* **2014,** 47, (4), 1117-1126.

[5] Bogdanov, A. V.; Musin, L. I.; Mironov, V. F., Advances in the synthesis and application of isoindigo derivatives. *ARKIVOC: Online Journal of Organic Chemistry* **2015,** 2015.

[6] Steingruber, E., Indigo and Indigo Colorants. In *Ullmann's Encyclopedia of Industrial Chemistry*.

[7] Irimia-Vladu, M.; Głowacki, E. D.; Troshin, P. A.; Schwabegger, G.; Leonat, L.; Susarova, D. K.; Krystal, O.; Ullah, M.; Kanbur, Y.; Bodea, M. A.; Razumov, V. F.; Sitter, H.; Bauer, S.; Sariciftci, N. S., Indigo - A Natural Pigment for High Performance Ambipolar Organic Field Effect Transistors and Circuits. *Advanced Materials* **2012,** 24, (3), 375-380.

[8] Shi, K.; Zhang, W.; Gao, D.; Zhang, S.; Lin, Z.; Zou, Y.; Wang, L.; Yu, G., Well-Balanced Ambipolar Conjugated Polymers Featuring Mild Glass Transition Temperatures Toward High-Performance Flexible Field-Effect Transistors. *Advanced Materials* **2018,** 30, (9), 1705286.

[9] Hückel, E., Zeitschrift für Physik. In 1931.

[10] Griffiths, D. J.; Schroeter, D. F., *Introduction to quantum mechanics*. Cambridge university press: 2018.

[11] Muller, P., Glossary of terms used in physical organic chemistry (IUPAC Recommendations 1994). *Pure and Applied Chemistry* **1994,** 66, (5), 1077-1184.

[12] Hesse, M.; Meier, H.; Zeeh, B., *Spectroscopic methods in organic chemistry*. Thieme/Houben-Weyl Series: 2008.

[13] Sun, H.; Autschbach, J., Electronic Energy Gaps for π-Conjugated Oligomers and Polymers Calculated with Density Functional Theory. *Journal of Chemical Theory and Computation* **2014,** 10, (3), 1035-1047.

[14] Novoselov, K. S.; Geim, A. K.; Morozov, S. V.; Jiang, D.; Zhang, Y.; Dubonos, S. V.; Grigorieva, I. V.; Firsov, A. A., Electric Field Effect in Atomically Thin Carbon Films. *Science* **2004,** 306, (5696), 666-669.

[15] De Bruin, M., Glossary of terms used in nuclear analytical chemistry (provisional). *Pure and Applied Chemistry* **1982,** 54, (8), 1533-1554.

[16] Yu, G.; Gao, J.; Hummelen, J. C.; Wudl, F.; Heeger, A. J., Polymer Photovoltaic Cells: Enhanced Efficiencies via a Network of Internal Donor-Acceptor Heterojunctions. *Science* **1995,** 270, (5243), 1789-1791.

[17] Tsurumi, J.; Matsui, H.; Kubo, T.; Häusermann, R.; Mitsui, C.; Okamoto, T.; Watanabe, S.; Takeya, J., Coexistence of ultra-long spin relaxation time and coherent charge transport in organic single-crystal semiconductors. *Nature Physics* **2017,** 13, (10), 994-998.

[18] Minder, N. A.; Ono, S.; Chen, Z.; Facchetti, A.; Morpurgo, A. F., Band-like electron transport in organic transistors and implication of the molecular structure for performance optimization. *Advanced Materials* **2012,** 24, (4), 503-508.

[19] Cornil, J.; Verlaak, S.; Martinelli, N.; Mityashin, A.; Olivier, Y.; Van Regemorter, T.; D'Avino, G.; Muccioli, L.; Zannoni, C.; Castet, F., Exploring the energy landscape of the charge transport levels in organic semiconductors at the molecular scale. *Accounts of Chemical Research* **2013,** 46, (2), 434-443.

[20] Ryno, S. M.; Risko, C.; Bredas, J.-L., Noncovalent interactions and impact of charge penetration effects in linear oligoacene dimers and single crystals. *Chemistry of Materials* **2016,** 28, (11), 3990-4000.

[21] Kaiser, W.; Albes, T.; Gagliardi, A., Charge carrier mobility of disordered organic semiconductors with correlated energetic and spatial disorder. *Physical Chemistry Chemical Physics* **2018,** 20, (13), 8897-8908.

[22] Okamoto, T.; Yu, C. P.; Mitsui, C.; Yamagishi, M.; Ishii, H.; Takeya, J., Bent-shaped p-type small-molecule organic semiconductors: a molecular design strategy for next-generation practical applications. *Journal of the American Chemical Society* **2020,** 142, (20), 9083-9096.

[23] Bässler, H., Charge transport in disordered organic photoconductors. A Monte Carlo simulation study. *Physica Status Solidi B (Basic Research);(Germany)* **1993,** 175, (1).

[24] Vissenberg, M.; Matters, M., Theory of the field-effect mobility in amorphous organic transistors. *Physical Review B* **1998,** 57, (20), 12964.

[25] Zhuiykov, S., *Nanostructured semiconductor oxides for the next generation of electronics and functional devices: properties and applications*. Woodhead Publishing: 2014.

[26] Jiang, R.; Zhu, R.; Li, Z. S., Designing Hole Transport Materials with High Hole Mobility and Outstanding Interface Properties for Perovskite Solar Cells. *ChemPhysChem* **2020,** 21, (16), 1866-1872.

[27] Edelman, K. R.; Holliday, B. J., Metal-Interrupted Perylene Diimide: Toward a New Class of Tunable n-Type Inorganic– Organic Hybrid Semiconductors. *Inorganic chemistry* **2010,** 49, (15), 6787-6789.

[28] Scott, J. C., Metal–organic interface and charge injection in organic electronic devices. *Journal of Vacuum Science & Technology A* **2003,** 21, (3), 521-531.

[29] Schön, J. H.; Kloc, C.; Batlogg, B., Universal crossover from band to hopping conduction in molecular organic semiconductors. *Physical Review Letters* **2001,** 86, (17), 3843.

[30] Haddon, R.; Siegrist, T.; Fleming, R.; Bridenbaugh, P.; Laudise, R., Band structures of organic thin-film transistor materials. *Journal of Materials Chemistry* **1995,** 5, (10), 1719-1724.

[31] Horowitz, G.; Hajlaoui, R.; Bourguiga, R.; Hajlaoui, M., Theory of the organic field-effect transistor. *Synthetic Metals* **1999,** 101, (1-3), 401-404.
[32] Zhu, X.; Wang, K.; He, J.; Zhang, L.; Yu, H.; He, D.; Hu, B., Exploring deep and shallow trap states in a non-fullerene acceptor ITIC-based organic bulk heterojunction photovoltaic system. *The Journal of Physical Chemistry C* **2019,** 123, (34), 20691-20697.
[33] Haneef, H. F.; Zeidell, A. M.; Jurchescu, O. D., Charge carrier traps in organic semiconductors: A review on the underlying physics and impact on electronic devices. *Journal of Materials Chemistry C* **2020,** 8, (3), 759-787.
[34] Marcus, R. A.; Sutin, N., Electron transfers in chemistry and biology. *Biochimica et Biophysica Acta (BBA)-Reviews on Bioenergetics* **1985,** 811, (3), 265-322.
[35] Marcus, R. A., Electron transfer reactions in chemistry. Theory and experiment. *Reviews of Modern Physics* **1993,** 65, (3), 599-610.
[36] Libby, W. F., Theory of electron exchange reactions in aqueous solution. *The Journal of Physical Chemistry* **1952,** 56, (7), 863-868.
[37] Malagoli, M.; Brédas, J., Density functional theory study of the geometric structure and energetics of triphenylamine-based hole-transporting molecules. *Chemical Physics Letters* **2000,** 327, (1-2), 13-17.
[38] Brédas, J. L.; Calbert, J. P.; da Silva Filho, D. A.; Cornil, J., Organic semiconductors: A theoretical characterization of the basic parameters governing charge transport. *Proceedings of the National Academy of Sciences* **2002,** 99, (9), 5804-5809.
[39] Shuai, Z.; Li, W.; Ren, J.; Jiang, Y.; Geng, H., Applying Marcus theory to describe the carrier transports in organic semiconductors: Limitations and beyond. *The Journal of Chemical Physics* **2020,** 153, (8), 080902.
[40] Yang, L.; Mao, J.; Yin, C.-Z.; Ali, M. A.; Wu, X.-P.; Dong, C.-Y.; Liu, Y.-Y.; Wei, Y.; Xie, L.-H.; Ran, X.-Q., A novel structure of grid spirofluorene: a new organic semiconductor with low reorganization energy. *New Journal of Chemistry* **2019,** 43, (20), 7790-7796.
[41] Vehoff, T.; Baumeier, B.; Troisi, A.; Andrienko, D., Charge transport in organic crystals: role of disorder and topological connectivity. *Journal of the American Chemical Society* **2010,** 132, (33), 11702-11708.
[42] Brédas, J.-L.; Beljonne, D.; Coropceanu, V.; Cornil, J., Charge-Transfer and Energy-Transfer Processes in π-Conjugated Oligomers and Polymers: A Molecular Picture. *Chemical Reviews* **2004,** 104, (11), 4971-5004.
[43] Coropceanu, V.; Cornil, J.; da Silva Filho, D. A.; Olivier, Y.; Silbey, R.; Brédas, J.-L., Charge Transport in Organic Semiconductors. *Chemical Reviews* **2007,** 107, (4), 926-952.
[44] Koezuka, H.; Tsumura, A.; Ando, T., Field-effect transistor with polythiophene thin film. *Synthetic Metals* **1987,** 18, (1-3), 699-704.
[45] Horowitz, G.; Fichou, D.; Peng, X.; Xu, Z.; Garnier, F., A field-effect transistor based on conjugated alpha-sexithienyl. *Solid State Communications* **1989,** 72, (4), 381-384.
[46] Paterson, A. F.; Singh, S.; Fallon, K. J.; Hodsden, T.; Han, Y.; Schroeder, B. C.; Bronstein, H.; Heeney, M.; McCulloch, I.; Anthopoulos, T. D., Recent progress in high-mobility organic transistors: a reality check. *Advanced Materials* **2018,** 30, (36), 1801079.
[47] Hu, P.; He, X.; Jiang, H., Greater than 10 cm2 V− 1 s− 1: A breakthrough of organic semiconductors for field-effect transistors. *InfoMat* **2021,** 3, (6), 613-630.

[48] Yan, Y.; Zhao, Y.; Liu, Y., Recent progress in organic field-effect transistor-based integrated circuits. *Journal of Polymer Science* **2022,** 60, (3), 311-327.

[49] Wang, C.; Zhang, X.; Dong, H.; Chen, X.; Hu, W., Challenges and emerging opportunities in high-mobility and low-energy-consumption organic field-effect transistors. *Advanced Energy Materials* **2020,** 10, (29), 2000955.

[50] Hamai, T.; Arai, S.; Hasegawa, T., Effects of tunneling-based access resistance in layered single-crystalline organic transistors. *Journal of Materials Research* **2018,** 33, (16), 2350-2363.

[51] Chu, M.; Fan, J. X.; Yang, S.; Liu, D.; Ng, C. F.; Dong, H.; Ren, A. M.; Miao, Q., Halogenated Tetraazapentacenes with Electron Mobility as High as 27.8 cm2 V− 1 s− 1 in Solution-Processed n-Channel Organic Thin-Film Transistors. *Advanced Materials* **2018,** 30, (38), 1803467.

[52] Johansson, M. P.; Olsen, J., Torsional barriers and equilibrium angle of biphenyl: reconciling theory with experiment. *Journal of Chemical Theory and Computation* **2008,** 4, (9), 1460-1471.

[53] Almasy, F.; Laemmel, H., Der Einfluss der Temperatur auf das Absorptionsspektrum des Diphenyldampfes im nahen Ultraviolett. Extinktionsmessungen zwischen 170 und 520° C. *Helvetica Chimica Acta* **1950,** 33, (7), 2092-2100.

[54] Horowitz, G.; Bachet, B.; Yassar, A.; Lang, P.; Demanze, F.; Fave, J.-L.; Garnier, F., Growth and characterization of sexithiophene single crystals. *Chemistry of Materials* **1995,** 7, (7), 1337-1341.

[55] Yuan, J.; Ford, M. J.; Zhang, Y.; Dong, H.; Li, Z.; Li, Y.; Nguyen, T.-Q.; Bazan, G. C.; Ma, W., Toward Thermal Stable and High Photovoltaic Efficiency Ternary Conjugated Copolymers: Influence of Backbone Fluorination and Regioselectivity. *Chemistry of Materials* **2017,** 29, (4), 1758-1768.

[56] Liu, B.; Wang, Y.; Sun, H.; Gámez-Valenzuela, S.; Yan, Z.; Feng, K.; Uddin, M. A.; Koh, C.; Zhou, X.; López Navarrete, J. T.; Ruiz Delgado, M. C.; Meng, H.; Niu, L.; Woo, H. Y.; Ponce Ortiz, R.; Guo, X., Backbone Configuration and Electronic Property Tuning of Imide-Functionalized Ladder-Type Heteroarenes-Based Polymer Acceptors for Efficient All-Polymer Solar Cells. *Advanced Functional Materials* **2022,** 32, (21), 2200065.

[57] Wu, W.; Liu, Y.; Zhu, D., π-Conjugated molecules with fused rings for organic field-effect transistors: design, synthesis and applications. *Chemical Society Reviews* **2010,** 39, (5), 1489-1502.

[58] Scherf, U.; Müllen, K., Polyarylenes and poly (arylenevinylenes), 7. A soluble ladder polymer via bridging of functionalized poly (p-phenylene)-precursors. *Die Makromolekulare Chemie, Rapid Communications* **1991,** 12, (8), 489-497.

[59] Kreyenschmidt, M.; Uckert, F.; Muellen, K., A new soluble poly (p-phenylene) with tetrahydropyrene repeating units. *Macromolecules* **1995,** 28, (13), 4577-4582.

[60] Griesbaum, K.; Behr, A.; Biedenkapp, D.; Voges, H. W.; Garbe, D.; Paetz, C.; Collin, G.; Mayer, D.; Höke, H., Hydrocarbons. *Ullmann's encyclopedia of industrial chemistry* **2000**.

[61] Weast, R. C., *CRC handbook of chemistry and physics Sixty-seventh edition*. CRC Press Inc: United States, 1986.

[62] Tsujimoto, K.; Ogasawara, R.; Kishi, Y.; Fujiwara, H., TTF–fluorene dyads and their M (CN) 2−(M= Ag, Au) salts designed for photoresponsive conducting materials. *New Journal of Chemistry* **2014,** 38, (1), 406-418.
[63] Yang, C.-H.; Guo, T.-F.; Sun, I. W., Highly efficient greenish blue-emitting organic diodes based on pyrene derivatives. *Journal of Luminescence* **2007,** 124, (1), 93-98.
[64] Prins, P.; Grozema, F.; Schins, J.; Patil, S.; Scherf, U.; Siebbeles, L., High intrachain hole mobility on molecular wires of ladder-type poly (p-phenylenes). *Physical Review Letters* **2006,** 96, (14), 146601.
[65] Wang, L.; Nan, G.; Yang, X.; Peng, Q.; Li, Q.; Shuai, Z., Computational methods for design of organic materials with high charge mobility. *Chemical Society Reviews* **2010,** 39, (2), 423-434.
[66] Huang, H.; Yang, L.; Facchetti, A.; Marks, T. J., Organic and polymeric semiconductors enhanced by noncovalent conformational locks. *Chemical Reviews* **2017,** 117, (15), 10291-10318.
[67] Huang, H.; Chen, Z.; Ortiz, R. P.; Newman, C.; Usta, H.; Lou, S.; Youn, J.; Noh, Y.-Y.; Baeg, K.-J.; Chen, L. X.; Facchetti, A.; Marks, T., Combining Electron-Neutral Building Blocks with Intramolecular "Conformational Locks" Affords Stable, High-Mobility P- and N-Channel Polymer Semiconductors. *Journal of the American Chemical Society* **2012,** 134, (26), 10966-10973.
[68] Takacs, C. J.; Sun, Y.; Welch, G. C.; Perez, L. A.; Liu, X.; Wen, W.; Bazan, G. C.; Heeger, A. J., Solar cell efficiency, self-assembly, and dipole–dipole interactions of isomorphic narrow-band-gap molecules. *Journal of the American Chemical Society* **2012,** 134, (40), 16597-16606.
[69] Dong, T.; Lv, L.; Feng, L.; Xia, Y.; Deng, W.; Ye, P.; Yang, B.; Ding, S.; Facchetti, A.; Dong, H., Noncovalent Se··· O conformational locks for constructing high-performing optoelectronic conjugated polymers. *Advanced Materials* **2017,** 29, (34), 1606025.
[70] Mauck, C. M.; Hartnett, P. E.; Margulies, E. A.; Ma, L.; Miller, C. E.; Schatz, G. C.; Marks, T. J.; Wasielewski, M. R., Singlet Fission via an Excimer-Like Intermediate in 3,6-Bis(thiophen-2-yl)diketopyrrolopyrrole Derivatives. *Journal of the American Chemical Society* **2016,** 138, (36), 11749-11761.
[71] Wei, X.; Zhang, W.; Yu, G., Semiconducting Polymers Based on Isoindigo and Its Derivatives: Synthetic Tactics, Structural Modifications, and Applications. *Advanced Functional Materials* **2021,** 31, (21), 2010979.
[72] Yang, J.; Wang, H.; Chen, J.; Huang, J.; Jiang, Y.; Zhang, J.; Shi, L.; Sun, Y.; Wei, Z.; Yu, G.; Guo, Y.; Wang, S.; Liu, Y., Bis-Diketopyrrolopyrrole Moiety as a Promising Building Block to Enable Balanced Ambipolar Polymers for Flexible Transistors. *Advanced Materials* **2017,** 29, (22), 1606162.
[73] Liu, Q.; Bottle, S. E.; Sonar, P., Developments of Diketopyrrolopyrrole-Dye-Based Organic Semiconductors for a Wide Range of Applications in Electronics. *Advanced Materials* **2020,** 32, (4), 1903882.
[74] Lin, Y. Y.; Gundlach, D. J.; Nelson, S. F.; Jackson, T. N., Stacked pentacene layer organic thin-film transistors with improved characteristics. *IEEE Electron Device Letters* **1997,** 18, (12), 606-608.

[75] Mazaki, Y.; Kobayashi, K., Synthesis of tetrathieno-acene and pentathieno-acene: UV-spectral trend in a homologous series of thieno-acenes. *Tetrahedron Letters* **1989,** 30, (25), 3315-3318.

[76] Leonardi, F., Self-Assembled Monolayers (SAMs) in Organic Field-Effect Transistors. **2014**.

[77] Goubard, F.; Dumur, F., Truxene: a promising scaffold for future materials. *RSC Advances* **2015,** 5, (5), 3521-3551.

[78] Sun, Y. M.; Xiao, K.; Liu, Y. Q.; Wang, J. L.; Pei, J.; Yu, G.; Zhu, D. B., Oligothiophene-Functionalized Truxene: Star-Shaped Compounds for Organic Field-Effect Transistors. *Advanced Functional Materials* **2005,** 15, (5), 818-822.

[79] Anthony, J. E.; Brooks, J. S.; Eaton, D. L.; Parkin, S. R., Functionalized pentacene: Improved electronic properties from control of solid-state order. *Journal of the American Chemical Society* **2001,** 123, (38), 9482-9483.

[80] Park, S. K.; Jackson, T. N.; Anthony, J. E.; Mourey, D. A., High mobility solution processed 6, 13-bis (triisopropyl-silylethynyl) pentacene organic thin film transistors. *Applied Physics Letters* **2007,** 91, (6), 063514.

[81] Sheraw, C. D.; Jackson, T. N.; Eaton, D. L.; Anthony, J. E., Functionalized pentacene active layer organic thin-film transistors. *Advanced Materials* **2003,** 15, (23), 2009-2011.

[82] Yu, X.; Zhou, N.; Han, S.; Lin, H.; Buchholz, D. B.; Yu, J.; Chang, R. P.; Marks, T. J.; Facchetti, A., Flexible spray-coated TIPS-pentacene organic thin-film transistors as ammonia gas sensors. *Journal of Materials Chemistry C* **2013,** 1, (40), 6532-6535.

[83] Niazi, M. R.; Li, R.; Qiang Li, E.; Kirmani, A. R.; Abdelsamie, M.; Wang, Q.; Pan, W.; Payne, M. M.; Anthony, J. E.; Smilgies, D.-M., Solution-printed organic semiconductor blends exhibiting transport properties on par with single crystals. *Nature Communications* **2015,** 6, (1), 1-10.

[84] Sakanoue, T.; Sirringhaus, H., Band-like temperature dependence of mobility in a solution-processed organic semiconductor. *Nature materials* **2010,** 9, (9), 736-740.

[85] Podzorov, V.; Menard, E.; Borissov, A.; Kiryukhin, V.; Rogers, J. A.; Gershenson, M. E., Intrinsic Charge Transport on the Surface of Organic Semiconductors. *Physical Review Letters* **2004,** 93, (8), 086602.

[86] Takahashi, T.; Takenobu, T.; Takeya, J.; Iwasa, Y., Ambipolar organic field-effect transistors based on rubrene single crystals. *Applied Physics Letters* **2006,** 88, (3), 033505.

[87] Seo, J.; Park, D.; Cho, S.; Kim, C.; Jang, W.; Whang, C.; Yoo, K.-H.; Chang, G.; Pedersen, T.; Moewes, A., Buffer layer effect on the structural and electrical properties of rubrene-based organic thin-film transistors. *Applied Physics Letters* **2006,** 89, (16), 163505.

[88] Lee, E. K.; Lee, M. Y.; Park, C. H.; Lee, H. R.; Oh, J. H., Toward environmentally robust organic electronics: approaches and applications. *Advanced Materials* **2017,** 29, (44), 1703638.

[89] Zhao, Z.; Yin, Z.; Chen, H.; Zheng, L.; Zhu, C.; Zhang, L.; Tan, S.; Wang, H.; Guo, Y.; Tang, Q., High-performance, air-stable field-effect transistors based on heteroatom-substituted naphthalenediimide-benzothiadiazole copolymers exhibiting ultrahigh electron mobility up to 8.5 cm V− 1 s− 1. *Advanced Materials* **2017,** 29, (4), 1602410.

[90] Sun, Y.; Tan, L.; Jiang, S.; Qian, H.; Wang, Z.; Yan, D.; Di, C.; Wang, Y.; Wu, W.; Yu, G., High-performance transistor based on individual single-crystalline micrometer wire of perylo [1, 12-b, c, d] thiophene. *Journal of the American Chemical Society* **2007,** 129, (7), 1882-1883.

[91] Wood, S.; Kim, J.-H.; Wade, J.; Park, J. B.; Hwang, D.-H.; Kim, J.-S., Systematic control of heteroatoms in donor–acceptor copolymers and its effects on molecular conformation and photovoltaic performance. *Journal of Materials Chemistry C* **2016,** 4, (34), 7966-7978.

[92] Ebata, H.; Izawa, T.; Miyazaki, E.; Takimiya, K.; Ikeda, M.; Kuwabara, H.; Yui, T., Highly soluble [1] benzothieno [3, 2-b] benzothiophene (BTBT) derivatives for high-performance, solution-processed organic field-effect transistors. *Journal of the American Chemical Society* **2007,** 129, (51), 15732-15733.

[93] Minemawari, H.; Yamada, T.; Matsui, H.; Tsutsumi, J. y.; Haas, S.; Chiba, R.; Kumai, R.; Hasegawa, T., Inkjet printing of single-crystal films. *Nature* **2011,** 475, (7356), 364-367.

[94] Nakayama, K.; Hirose, Y.; Soeda, J.; Yoshizumi, M.; Uemura, T.; Uno, M.; Li, W.; Kang, M. J.; Yamagishi, M.; Okada, Y., Patternable solution-crystallized organic transistors with high charge carrier mobility. *Advanced Materials* **2011,** 23, (14), 1626-1629.

[95] Soeda, J.; Uemura, T.; Okamoto, T.; Mitsui, C.; Yamagishi, M.; Takeya, J., Inch-size solution-processed single-crystalline films of high-mobility organic semiconductors. *Applied physics express* **2013,** 6, (7), 076503.

[96] He, P.; Tu, Z.; Zhao, G.; Zhen, Y.; Geng, H.; Yi, Y.; Wang, Z.; Zhang, H.; Xu, C.; Liu, J., Tuning the Crystal Polymorphs of Alkyl Thienoacene via Solution Self-Assembly Toward Air-Stable and High-Performance Organic Field-Effect Transistors. *Advanced Materials* **2015,** 27, (5), 825-830.

[97] Wang, C.; Liang, Z.; Liu, Y.; Wang, X.; Zhao, N.; Miao, Q.; Hu, W.; Xu, J., Single crystal n-channel field effect transistors from solution-processed silylethynylated tetraazapentacene. *Journal of Materials Chemistry* **2011,** 21, (39), 15201-15204.

[98] Xue, G.; Wu, J.; Fan, C.; Liu, S.; Huang, Z.; Liu, Y.; Shan, B.; Xin, H. L.; Miao, Q.; Chen, H., Boosting the electron mobility of solution-grown organic single crystals via reducing the amount of polar solvent residues. *Materials Horizons* **2016,** 3, (2), 119-123.

[99] Quinn, J. T. E.; Zhu, J.; Li, X.; Wang, J.; Li, Y., Recent progress in the development of n-type organic semiconductors for organic field effect transistors. *Journal of Materials Chemistry C* **2017,** 5, (34), 8654-8681.

[100] Chua, L.-L.; Zaumseil, J.; Chang, J.-F.; Ou, E. C. W.; Ho, P. K. H.; Sirringhaus, H.; Friend, R. H., General observation of n-type field-effect behaviour in organic semiconductors. *Nature* **2005,** 434, (7030), 194-199.

[101] Roncali, J., Molecular engineering of the band gap of π-conjugated systems: Facing technological applications. *Macromolecular Rapid Communications* **2007,** 28, (17), 1761-1775.

[102] Shukla, D.; Nelson, S. F.; Freeman, D. C.; Rajeswaran, M.; Ahearn, W. G.; Meyer, D. M.; Carey, J. T., Thin-Film Morphology Control in Naphthalene-Diimide-Based Semiconductors: High Mobility n-Type Semiconductor for Organic Thin-Film Transistors. *Chemistry of Materials* **2008,** 20, (24), 7486-7491.

[103] Röger, C.; Würthner, F., Core-tetrasubstituted naphthalene diimides: synthesis, optical properties, and redox characteristics. *The Journal of Organic Chemistry* **2007,** 72, (21), 8070-8075.
[104] Anthony, J. E.; Facchetti, A.; Heeney, M.; Marder, S. R.; Zhan, X., n-Type organic semiconductors in organic electronics. *Advanced Materials* **2010,** 22, (34), 3876-3892.
[105] Inoue, Y.; Sakamoto, Y.; Suzuki, T.; Kobayashi, M.; Gao, Y.; Tokito, S., Organic thin-film transistors with high electron mobility based on perfluoropentacene. *Japanese Journal of Applied Physics* **2005,** 44, (6R), 3663.
[106] Havinga, E.; Ten Hoeve, W.; Wynberg, H., A new class of small band gap organic polymer conductors. *Polymer Bulletin* **1992,** 29, (1), 119-126.
[107] Lin, Y.-C.; Chen, C.-K.; Chiang, Y.-C.; Hung, C.-C.; Fu, M.-C.; Inagaki, S.; Chueh, C.-C.; Higashihara, T.; Chen, W.-C., Study on intrinsic stretchability of diketopyrrolopyrrole-based π-conjugated copolymers with poly (acryl amide) side chains for organic field-effect transistors. *ACS Applied Materials & Interfaces* **2020,** 12, (29), 33014-33027.
[108] Bronstein, H.; Nielsen, C. B.; Schroeder, B. C.; McCulloch, I., The role of chemical design in the performance of organic semiconductors. *Nature Reviews Chemistry* **2020,** 4, (2), 66-77.
[109] Lei, T.; Cao, Y.; Zhou, X.; Peng, Y.; Bian, J.; Pei, J., Systematic investigation of isoindigo-based polymeric field-effect transistors: design strategy and impact of polymer symmetry and backbone curvature. *Chemistry of Materials* **2012,** 24, (10), 1762-1770.
[110] Yamashita, Y.; Hinkel, F.; Marszalek, T.; Zajaczkowski, W.; Pisula, W.; Baumgarten, M.; Matsui, H.; Müllen, K.; Takeya, J., Mobility exceeding 10 cm2/(V· s) in donor–acceptor polymer transistors with band-like charge transport. *Chemistry of Materials* **2016,** 28, (2), 420-424.
[111] Yang, J.; Zhao, Z.; Geng, H.; Cheng, C.; Chen, J.; Sun, Y.; Shi, L.; Yi, Y.; Shuai, Z.; Guo, Y.; Wang, S.; Liu, Y., Isoindigo-Based Polymers with Small Effective Masses for High-Mobility Ambipolar Field-Effect Transistors. *Advanced Materials* **2017,** 29, (36), 1702115.
[112] Kim, G.; Kang, S.-J.; Dutta, G. K.; Han, Y.-K.; Shin, T. J.; Noh, Y.-Y.; Yang, C., A Thienoisoindigo-Naphthalene Polymer with Ultrahigh Mobility of 14.4 cm2/V·s That Substantially Exceeds Benchmark Values for Amorphous Silicon Semiconductors. *Journal of the American Chemical Society* **2014,** 136, (26), 9477-9483.
[113] Yan, H.; Chen, Z.; Zheng, Y.; Newman, C.; Quinn, J. R.; Dötz, F.; Kastler, M.; Facchetti, A., A high-mobility electron-transporting polymer for printed transistors. *Nature* **2009,** 457, (7230), 679-686.
[114] Wang, S.; Kappl, M.; Liebewirth, I.; Müller, M.; Kirchhoff, K.; Pisula, W.; Müllen, K., Organic field-effect transistors based on highly ordered single polymer fibers. *Advanced Materials* **2012,** 24, (3), 417-420.
[115] Kim, J. H.; Lee, D. H.; Yang, D. S.; Heo, D. U.; Kim, K. H.; Shin, J.; Kim, H. J.; Baek, K. Y.; Lee, K.; Baik, H., Novel Polymer Nanowire Crystals of Diketopyrrolopyrrole-Based Copolymer with Excellent Charge Transport Properties. *Advanced Materials* **2013,** 25, (30), 4102-4106.
[116] Yao, Y.; Dong, H.; Liu, F.; Russell, T. P.; Hu, W., Approaching intra-and interchain charge transport of conjugated polymers facilely by topochemical polymerized single crystals. *Advanced Materials* **2017,** 29, (29), 1701251.

[117] Adjizian, J.-J.; Briddon, P.; Humbert, B.; Duvail, J.-L.; Wagner, P.; Adda, C.; Ewels, C., Dirac Cones in two-dimensional conjugated polymer networks. *Nature Communications* **2014,** 5, (1), 1-10.
[118] Xu, Y.; Jin, S.; Xu, H.; Nagai, A.; Jiang, D., Conjugated microporous polymers: design, synthesis and application. *Chemical Society Reviews* **2013,** 42, (20), 8012-8031.
[119] Huang, N.; Wang, P.; Jiang, D., Covalent organic frameworks: a materials platform for structural and functional designs. *Nature Reviews Materials* **2016,** 1, (10), 16068.
[120] Huang, N.; Zhai, L.; Coupry, D. E.; Addicoat, M. A.; Okushita, K.; Nishimura, K.; Heine, T.; Jiang, D., Multiple-component covalent organic frameworks. *Nature Communications* **2016,** 7, (1), 12325.
[121] Chen, X.; Geng, K.; Liu, R.; Tan, K. T.; Gong, Y.; Li, Z.; Tao, S.; Jiang, Q.; Jiang, D., Covalent Organic Frameworks: Chemical Approaches to Designer Structures and Built-In Functions. *Angewandte Chemie International Edition* **2020,** 59, (13), 5050-5091.
[122] Mas-Torrent, M.; Rovira, C., Role of Molecular Order and Solid-State Structure in Organic Field-Effect Transistors. *Chemical Reviews* **2011,** 111, (8), 4833-4856.
[123] Desiraju, G. R., Cryptic crystallography. *Nature materials* **2002,** 1, (2), 77-79.
[124] Li, S. S., Semiconductor Physical Electronics (Microdevices). *Softcover reprint of the original 1st ed* **1993**.
[125] Yao, Z.-F.; Wang, J.-Y.; Pei, J., Control of π–π stacking via crystal engineering in organic conjugated small molecule crystals. *Crystal Growth & Design* **2018,** 18, (1), 7-15.
[126] Horowitz, G.; Peng, X.-Z.; Fichou, D.; Garnier, F., Role of the semiconductor/insulator interface in the characteristics of π-conjugated-oligomer-based thin-film transistors. *Synthetic Metals* **1992,** 51, (1-3), 419-424.
[127] Brown, A.; Pomp, A.; de Leeuw, D. M.; Klaassen, D.; Havinga, E.; Herwig, P.; Müllen, K., Precursor route pentacene metal-insulator-semiconductor field-effect transistors. *Journal of Applied Physics* **1996,** 79, (4), 2136-2138.
[128] Dimitrakopoulos, C.; Brown, A.; Pomp, A., Molecular beam deposited thin films of pentacene for organic field effect transistor applications. *Journal of Applied Physics* **1996,** 80, (4), 2501-2508.
[129] Jurchescu, O. D.; Popinciuc, M.; Van Wees, B. J.; Palstra, T. T., Interface-controlled, high-mobility organic transistors. *Advanced Materials* **2007,** 19, (5), 688-692.
[130] Wang, C.; Dong, H.; Jiang, L.; Hu, W., Organic semiconductor crystals. *Chemical Society Reviews* **2018,** 47, (2), 422-500.
[131] Li, R.; Dong, H.; Zhan, X.; Li, H.; Wen, S.-H.; Deng, W.-Q.; Han, K.-L.; Hu, W., Physicochemical, self-assembly and field-effect transistor properties of anti-and syn-thienoacene isomers. *Journal of Materials Chemistry* **2011,** 21, (30), 11335-11339.
[132] Gámez-Valenzuela, S.; Benito-Hernández, A.; Echeverri, M.; Gutierrez-Puebla, E.; Ponce Ortiz, R.; Ruiz Delgado, M. C.; Gómez-Lor, B., Functionalized Crystalline N-Trimethyltriindoles: Counterintuitive Influence of Peripheral Substituents on Their Semiconducting Properties. *Molecules* **2022,** 27, (3), 1121.
[133] Benito-Hernández, A.; Pandey, U. K.; Cavero, E.; Termine, R.; García-Frutos, E. M.; Serrano, J. L.; Golemme, A.; Gómez-Lor, B., High Hole Mobility in Triindole-Based Columnar

phases: Removing the Bottleneck of Homogeneous Macroscopic Orientation. *Chemistry of Materials* **2013,** 25, (2), 117-121.

[134] Lee, S. S.; Loth, M. A.; Anthony, J. E.; Loo, Y.-L., Orientation-independent charge transport in single spherulites from solution-processed organic semiconductors. *Journal of the American Chemical Society* **2012,** 134, (12), 5436-5439.

[135] Irkhin, P.; Ryasnyanskiy, A.; Koehler, M.; Biaggio, I., Absorption and photoluminescence spectroscopy of rubrene single crystals. *Physical Review B* **2012,** 86, (8), 085143.

[136] Fielding, P.; Gutman, F., Electrical properties of phthalocyanines. *The Journal of Chemical Physics* **1957,** 26, (2), 411-419.

[137] Sutton, C.; Marshall, M. S.; Sherrill, C. D.; Risko, C.; Brédas, J.-L., Rubrene: The Interplay between Intramolecular and Intermolecular Interactions Determines the Planarization of Its Tetracene Core in the Solid State. *Journal of the American Chemical Society* **2015,** 137, (27), 8775-8782.

[138] Wang, C.; Dong, H.; Hu, W.; Liu, Y.; Zhu, D., Semiconducting π-Conjugated Systems in Field-Effect Transistors: A Material Odyssey of Organic Electronics. *Chemical Reviews* **2012,** 112, (4), 2208-2267.

[139] Xiao, K.; Liu, Y.; Qi, T.; Zhang, W.; Wang, F.; Gao, J.; Qiu, W.; Ma, Y.; Cui, G.; Chen, S., A highly π-stacked organic semiconductor for field-effect transistors based on linearly condensed pentathienoacene. *Journal of the American Chemical Society* **2005,** 127, (38), 13281-13286.

[140] Ruiz, C.; Arrechea-Marcos, I.; Benito-Hernández, A.; Gutierrez-Puebla, E.; Monge, M. A.; López Navarrete, J. T.; Ruiz Delgado, M. C.; Ortiz, R. P.; Gómez-Lor, B., Solution-processed N-trialkylated triindoles for organic field effect transistors. *Journal of Materials Chemistry C* **2018,** 6, (1), 50-56.

[141] Babel, A.; Jenekhe, S. A., Alkyl chain length dependence of the field-effect carrier mobility in regioregular poly (3-alkylthiophene) s. *Synthetic Metals* **2005,** 148, (2), 169-173.

[142] Keyes, R. W., Physical limits of silicon transistors and circuits. *Reports on Progress in Physics* **2005,** 68, (12), 2701.

[143] Thompson, S. E.; Parthasarathy, S., Moore's law: the future of Si microelectronics. *Materials Today* **2006,** 9, (6), 20-25.

[144] Jiang, C.; Chellappan, V.; Goh, W.; Zhang, J., Investigating coating method induced vertical phase distribution in polymer-fullerene organic solar cells. *Solar Energy Materials and Solar Cells* **2018,** 179, 241-246.

[145] Li, Y.; Sun, H.; Shi, Y.; Tsukagoshi, K., Patterning technology for solution-processed organic crystal field-effect transistors. *Science and Technology of Advanced Materials* **2014**.

[146] Sanda, S.; Nagase, T.; Kobayashi, T.; Takimiya, K.; Sadamitsu, Y.; Naito, H., High-performance didodecylbenzothienobenzothiophene-based top-gate organic transistors processed by spin coating using binary solvent mixtures. *Organic Electronics* **2018,** 58, 306-312.

[147] Jiang, Z.-Q.; Poriel, C.; Leclerc, N., Emerging organic electronics. *Materials Chemistry Frontiers* **2020,** 4, (9), 2497-2498.

[148] Albes, T.; Xu, L.; Wang, J.; Hsu, J. W.; Gagliardi, A., Origin of photocurrent in fullerene-based solar cells. *The Journal of Physical Chemistry C* **2018,** 122, (27), 15140-15148.
[149] Wong, W. W.; Singh, T. B.; Vak, D.; Pisula, W.; Yan, C.; Feng, X.; Williams, E. L.; Chan, K. L.; Mao, Q.; Jones, D. J., Solution processable fluorenyl hexa-peri-hexabenzocoronenes in organic field-effect transistors and solar cells. *Advanced Functional Materials* **2010,** 20, (6), 927-938.
[150] Ma, H.; Yip, H. L.; Huang, F.; Jen, A. K. Y., Interface engineering for organic electronics. *Advanced Functional Materials* **2010,** 20, (9), 1371-1388.

2 Goals

Goals

As can be seen in previous sections, charge transport process in organic materials is a complex topic which depends on many factors. This inherent complexity makes that, even nowadays, the charge transport mechanisms in organic semiconductors is not fully understood. Therefore, the main motivation for continuously designing and synthesizing new organic frameworks in the past few decades do not only include improving the optoelectronic characteristics and realizing novel functions, but also to better understand the complex structure-property relationships.

In this sense, the present Ph.D. Thesis is focused on the exhaustive physico-chemical investigation of organic semiconductors, from small molecules to one-dimensional or even two-dimensional polymers. Our aims in this perspective are two-fold: (i) On one hand, to have a detailed understanding of the effect that different structural modifications plays on the intramolecular π-electron delocalization characteristics of organic semiconductors. On the other hand, (ii) to analyze the consequences of these structural modifications on the supramolecular arrangement, a factor which determines the charge transport properties of the final materials.

To this purpose, we have performed a joint experimental and theoretical study that links a wide range of techniques such as UV-Vis absorption, fluorescence, electrochemistry, Raman and OFETs characterization with Density Functional Theory (DFT) calculations. The outcome of this study will help drawing the key structure–property–function relationships for the fundamental understanding of the charge transport behavior in these systems, and more generally, it will provide insights in to the design of new semiconductors for electronic applications.

With this goal in mind, the present Ph.D. Thesis has been divided in four main chapters according to the π-conjugated frameworks of the systems under study:

Chapter I: Role of peripheral substitution on the molecular order of disk-like semiconductors: the case of triindoles and diazatruxenones

In this first chapter, we became interested in the study of two families of triindole and diazatruxenone-based semiconductors functionalized at 3,8,13 positions with different peripheral groups (*i.e*. methoxy electron donor group or acetyl, nitrile and nitro electron-withdrawing groups). The particular aim of this chapter is to shed light on the influence that the electronic nature of the attached peripheral groups and the combination of electron rich and electron deficient segments in the same diazatruxenone scaffold exert on the electronic, supramolecular and semiconducting properties of these materials. Particularly, both series show a favorable synergy between their good intrinsic optoelectronic properties and its high tendency to self-assemble into one-dimensional superstructures, which can be dramatically modulated as a function of structural modifications. The synthesis of these disk-like semiconductors has been performed by the group of Prof. Berta Gómez-Lor Pérez from the Instituto de Ciencia de Materiales de Madrid (ICMM) and their chemical structures are depicted in Figure 2.1.

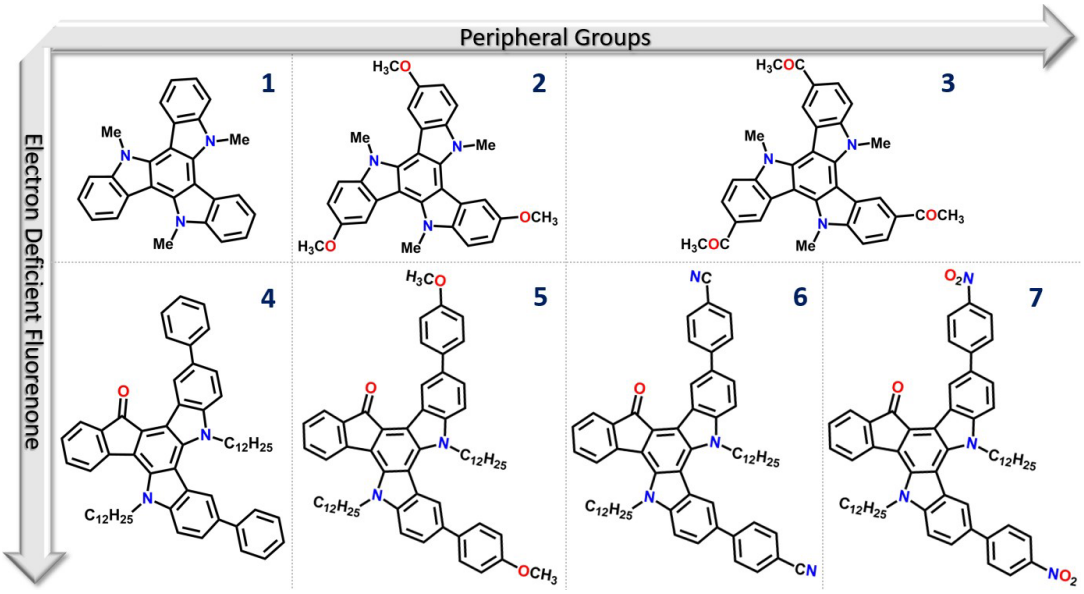

Figure 2.1. Chemical structures of triindole **1**–**3** (top) and diazatruxenone-based systems **4**–**7** (bottom) studied in Chapter I.

Chapter II: Untangling the optoelectronic properties of 2D-organic polymers

In this chapter, a series of 2D-conjugated polymers derived from C_3-symmetry π-conjugated building blocks have been investigated. To make clear the discussion of the results, this chapter has been divided in two blocks. In the first block, a combined experimental and theoretical approach was used to get a detailed understanding of the role that the different π-spacer group (phenylene or benzothiadiazole) and linkage position between the cores (*para* in **T2** or *meta* in **T3**) plays on the effectiveness of π-electron communication between the conjugated platforms, emphasizing on their ability for the detection of electron deficient nitroaromatics analytes (see Figure 2.2). The synthesis of these conjugated microporous polymers (CMPs) has been also performed by the group of Prof. Berta Gómez-Lor from the ICMM.

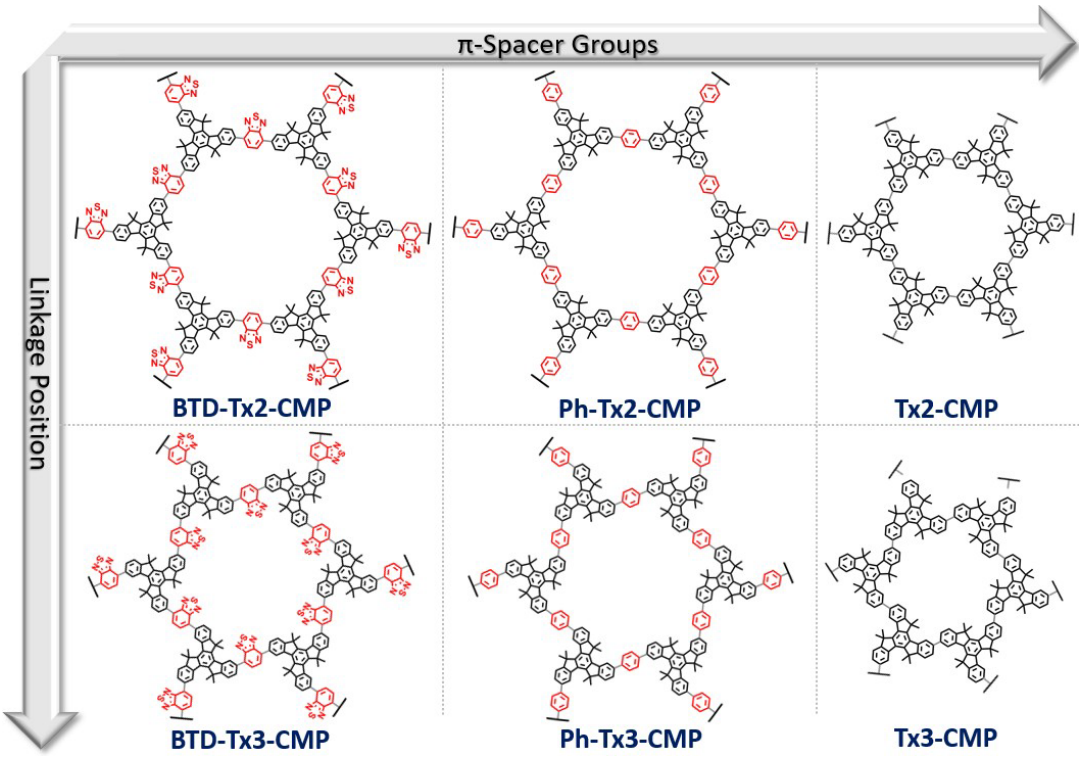

Figure 2.2. Idealized chemical structures of the conjugated microporous polymers studied in the first block of Chapter II.

Secondly, we performed a purely theoretical investigation of a total of 27 different 2D-conjugated polymers (Figure 2.3) with the ultimate goal of exploring how their the structural, electronic and charge-transport properties can be modulated by molecular engineering. For this purpose, we have explored three different chemical structural changes: (i) the nature of the building blocks (from truxene to trindole or truxenone), (ii) insertion of different π-spacers (phenylene to alkyne), (iii) the connecting mode (from *para* in **T2** to *meta* in **T3**) or (iv) the increased number of π-bridges from three units in **T2** and **T3** to six units in **T2,3**). This exhaustive and systematic study provides a powerful prefiltering protocol to select the most promising polymers towards different applications according to a targeted functionality.

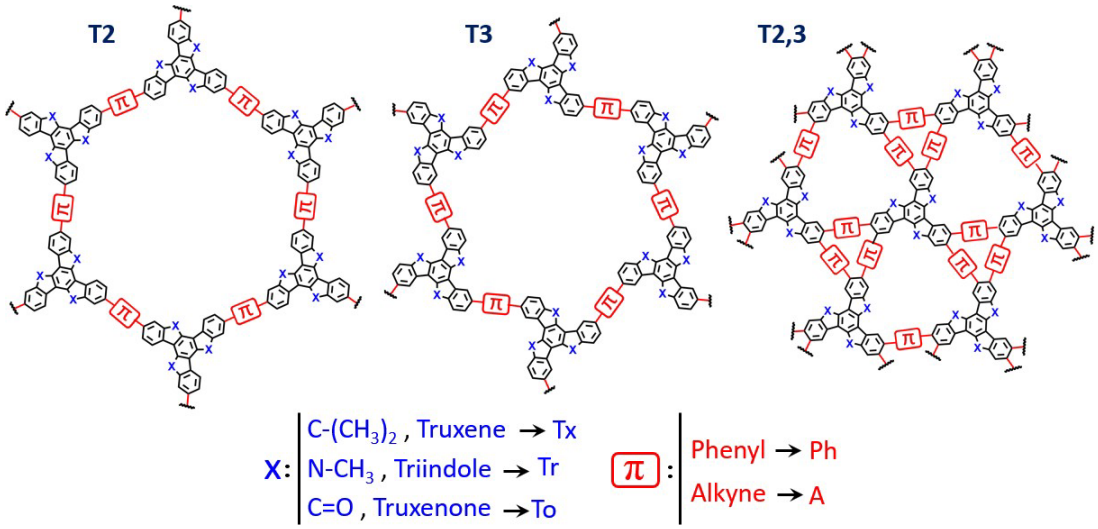

Figure 2.3. Idealized chemical structures of the conjugated 2D-polymers studied in the second block of Chapter II.

Chapter III: Extended π-conjugation effect of NDI and PDI-based semiconductors on n-type electrical properties

In the third chapter, we approach the investigation of the semiconducting properties of four D-π-A-π-D small molecules having **NDI** and **PDI** as central acceptor cores, and triphenylamine and phenylcarbazole donor groups laterally linked through ethynyl bonds. This study was motivated by the interest in exploring the effects of the π-conjugation extension (either via (i) the enlargement of the acceptor central core going from **NDI**- to **PDI**-based semiconductors or (ii) the lateral substitution with different electron rich conjugated groups) on the molecular structure, energy levels and supramolecular order of the resulting n-type materials. The syntheses of these **NDI**- and **PDI**-based semiconductors have been performed by the group of Prof. María Pilar Prieto from the University of Castilla-La Mancha and their chemical structures are depicted in Figure 2.4.

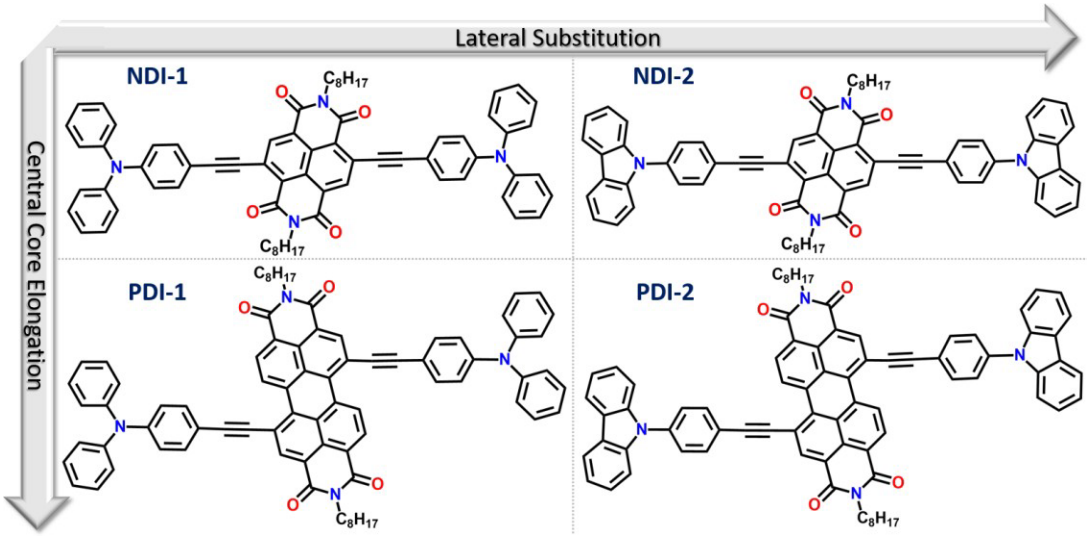

Figure 2.4. Chemical structures of NDI and PDI-based systems studied in Chapter III.

Chapter IV: Towards high performance ambipolar field effect transistors: the fluorination effect

In this final chapter, the importance of the planarity to achieve an effective π-electron delocalization is assessed. For this purpose, we have investigated a series of A-D-A´ copolymers composed of isoindigo (IIG) and benzothiadiazole (BTD) building blocks linked by a flanking thiophene ring, which have been subjected to a progressive fluorination process giving rise to four different copolymers with different degrees of fluorination and thus, different degrees of backbone planarization (Figure 2.5). The synthesis of these copolymers has been performed by the group of Prof. Mohammed Al-Hashimi from the Texas A&M University at Qatar. The main goal of this study lies on the analysis of the impact that fluorination of IIG and BTD units produces on the polymer structure, energy levels and intramolecular interactions, which can lead to different electrical performances. We hope that the results of this study pave the way to the control of the degree of backbone π-conjugation, intra and interchain interactions as well as thin-film morphologies, which are key aspects to design new derivatives with improved semiconducting performance.

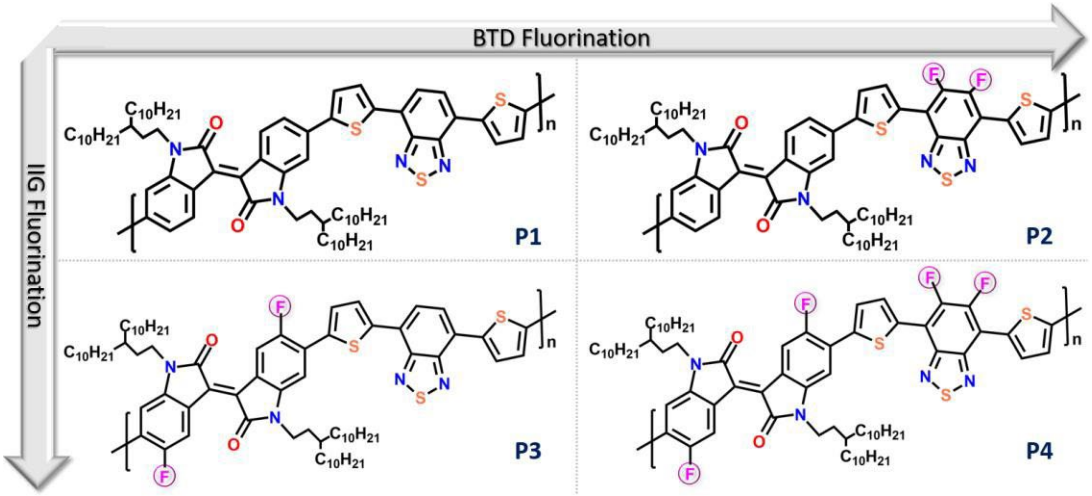

Figure 2.5. Chemical structures of semiconducting polymeric materials studied in Chapter IV.

3 Methodology

Table of contents

During the development of this thesis, a systematic study that combines experimental techniques and quantum chemical calculations has been carried out. As Figure 3.1 shows, this methodology can be divided in four key stages: (i) Firstly, the systems under study have been subjected to a spectroscopic and electrochemical characterization process in order to explore the optical and electronic properties of them. (ii) With this information, quantum chemical calculations have been performed not only to get deeper insights in the interpretation of the experimental results, but also to understand the physical and chemical behaviors responsible of the optoelectronic properties of the materials under study. (iii) Then, the systems that present promising optoelectronic properties have been implemented in electronic devices such as OFETs or sensors. (iv) Finally, the crystallinity and morphology of OFETs has been characterized to gain insight into the effect that the molecular packing plays on the charge transport process. In this chapter, the different techniques/methods used in each of these points will be described.

Figure 3.1. Scheme of the methodology employed during the development of this thesis.

3.1. Spectroscopic techniques

Spectroscopy is defined as a branch of science that studies the interaction between matter and the electromagnetic radiation. As a result of this interaction, detailed information about the structure and other chemical properties of atoms and molecules can be elucidated.[1, 2] According to the nature of the electromagnetic radiation, it generates different kinds of information on the chemical systems under study, giving rise to different kinds of spectroscopies (see Figure 3.2).

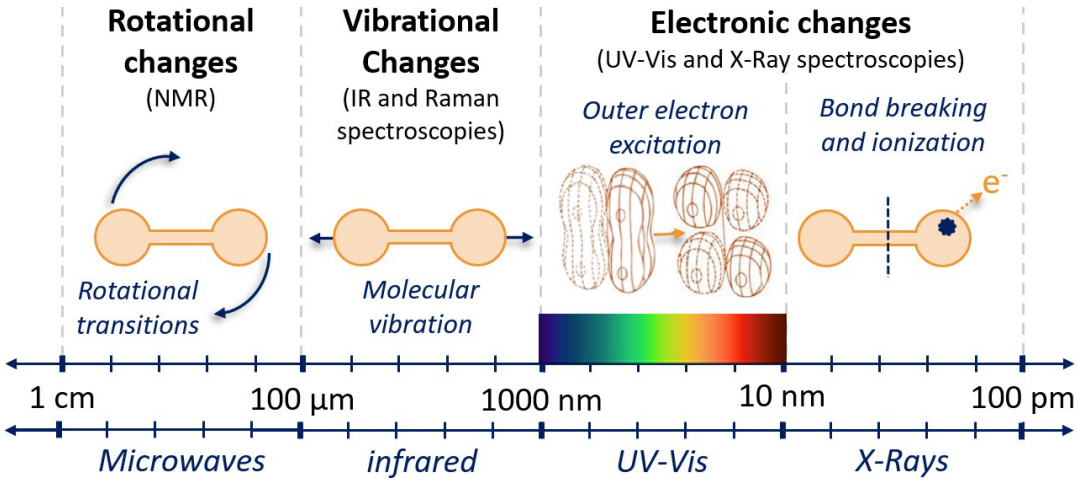

Figure 3.2. Representation of the different spectroscopies used in this thesis as a function of the employed electromagnetic radiation region for the sample excitation.

The elemental spectroscopic phenomenon involves the absorption (or emission) of a quantized radiation that carries the system from an initial energy state (E_0) to a final state (E_1). According to the Einstein equation ($\Delta E=h\upsilon$), the energy of the absorbed radiation must match the energy difference between the two involved states. As can be seen in Figure 3.3, attending to the different energy transitions that can take place between the energy levels of a molecular system, the main spectroscopies are: (i) electronic spectroscopy, when variations on the electronic function (purple arrows) are generated by an UV-Vis radiation, (ii) vibrational spectroscopy, when the vibrational function changes (grey arrow) by using an

infrared radiation or (iii) rotational spectroscopy, in which transitions between quantized rotational states (orange arrow) occur in the microwave and radiofrequency regions.

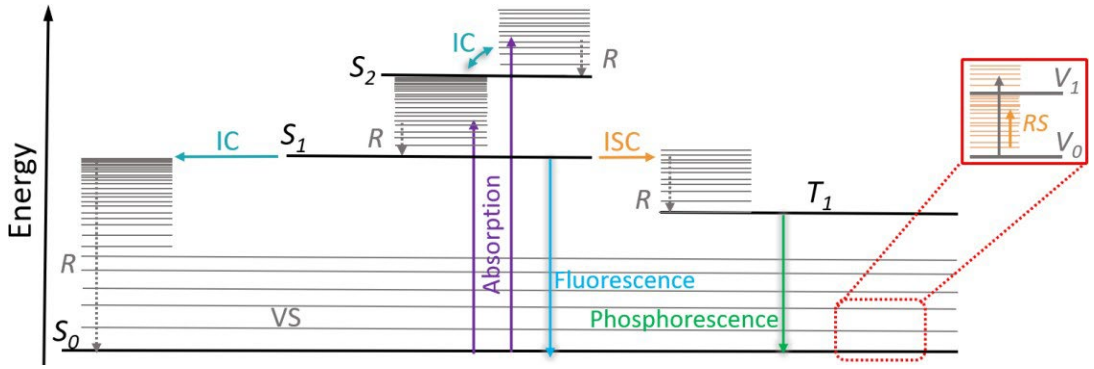

Figure 3.3. Representation of Jablonski diagram. Sn: singlet electronic states; Tn: triplet electronic states; VS: vibrational states; RS: rotational states; IC: internal conversion; ISC: intersystem crossing; R: thermal relaxation.

In this scenario, the spectroscopic techniques employed in the present thesis are electronic absorption, fluorescence emission and vibrational Raman spectroscopies, principally.

3.1.1. Electronic absorption spectroscopy

Electronic absorption spectroscopy uses an electromagnetic radiation in the UV-Vis-NIR region as source of excitation to promote a transition from the ground electronic state (S_0) to a singlet excited state (S_n). As a result of this electronic transition, an absorption band appear. Unlike atoms, the electronic transitions in molecular systems are associated with rotational and vibrational transits of similar but not identical energies. Thus, several of these spectral lines constitute a band with a vibronic structure. As previously discussed in the introduction section, analysis of these bands renders valuable information about the electronic delocalization degree in π-conjugated systems.

In this context, the electronic absorption spectra of disk-like molecules (Chapter I), porous polymers (Chapter II) and **NDI**- or **PDI**-based semiconductors (Chapter III) presented in this Thesis have been generally measured disolving the sample in CH_2Cl_2 solvent (Sigma-Aldrich/Merck, HPLC grade, 99.8%) at room temperature, with molar concentration in the range of 10^{-5}-10^{-6} mol/L. Several solvents were used for the solvatochromic experiments of **NDI**- or **PDI**-based semiconductors (*i.e.*, hexane, toluene, chloroform, tetrahydrofuran, dichloromethane, acetone and dimethylformamide). In the case of **P1**-**P4** polymers studied in Chapter IV, 10^{-4} M chlorobenzene solutions (Sigma-Aldrich/Merck, HPLC grade, 99.8%) were prepared. Electronic absorption of thin films was also carried out for these polymers. To perform these measurements, the previously prepared 10^{-4} M standard solutions in chlorobenzene were spin-coated on glass. The spectrophotometers employed in the electronic absorption measurements were:

- Agilent 8453 UV-Vis spectrophotometer, which used a deuterium lamp for the UV spectral range and a tungsten lamp for the visible and near-infrared (NIR) one. The Agilent spectrophotometer consists of 910 photodiodes, one for each nanometer, which allows very short registration times in a wavelength range of 190-1100 nm.

- Cary 5000 UV-Vis-NIR spectrophotometer with a wavelength range of 175-3300 nm and a spectral resolution of 1 nm. This equipment uses a light source of deuterium for the UV spectral region and a light source of tungsten halogen for the Vis-NIR region, together with a PbSmart NIR detector.

3.1.2. Fluorescence emission spectroscopy

As previously mentioned, the absorption of UV-Vis energy results in the formation of an excited electronic state of higher energy than the ground state. As can be seen in Figure 3.3, the excited state is unstable, therefore it will return to the fundamental electronic state by losing the excess energy either in a non-radiative or radiative way. In the former, the energy is dissipated without emission of electromagnetic radiation (vibrational relaxation,

internal conversion and intersystem crossing). On the other hand, in radiative processes the energy is dissipated through fluorescence (from a single excited state) or phosphorescence (from a triplet excited state) emission.

In this context, the fluorescence spectra of 10^{-5} M solutions of **NDI**- or **PDI**-based semiconductors in CH_2Cl_2 were recorded on an Edinburgh FLS920 fluorometer (Chapter III). This equipment uses a 450W Xe lamp as excitation source for steady-state measurements and a R2658P detector. Several solvents were used for the solvatochromic experiments of these samples (*i.e.*, hexane, toluene, chloroform, tetrahydrofuran, dichloromethane, acetone and dimethylformamide). On the other hand, fluorescence spectra of the porous polymers analyzed in Chapter II were recorded by the group of the Prof. Berta Gómez-Lor Pérez from the Instituto de Ciencia de Materiales de Madrid (ICMM). In this case, the emission spectra of 50 µg/ml suspensions of these polymers in CH_2Cl_2 were recorded on an Aminco SLM 8000 spectrophotometer.

3.1.3. Raman spectroscopy

As previously described, the light-matter interaction can be studied through absorption and emission processes. However, photons can also interact with samples and then be re-emitted from them. This re-emitted radiation is known as light scattering, and it constitutes the phenomenon in which Raman spectroscopy is based.

In this dispersive technique, the molecular system is excited at a determined frequency radiation which distorts the electron cloud around the nuclei (in other words, the molecular polarizability) forming a short-lived virtual state. It should be noted that the energy of the virtual state depends on the energy of the light source. At this point, the inherent instability of the virtual state makes the excited photon to be quickly reemitted without energy exchange (Rayleigh scattering) or with energy transfer from the photons to the molecule (Stokes Raman scattering) and viceversa (anti-Stokes Raman scattering). It has to be noted that Raman scattering is an unusual phenomenon since only one of 10^6-10^8 photons experiments an inelastic scattering.[3]

As a consequence of the large polarizability of π-conjugated systems generated by the alternant double and single CC bonds, two important characteristics can be found in Raman spectra: (i) high selectivity of some specific transitions, leading to simple spectra and (ii) an increasing intensity as well as a wavenumber downshift of selective Raman signals when lengthening the π-conjugation, particularly those related with the collective ECC (Effective Conjugation Coordinate) mode.[4, 5]

An important phenomenon that must be considered when selecting the laser excitation energy, is the resonant Raman effect. This effect is observed when the laser excitation energy is close to the energy of an electronic transition, resulting in an enhanced Raman scattering phenomenon as well as a selective intensification for the Raman activity of the chromophore responsible of the electronic transition. In this sense, resonant Raman spectroscopy allows the detection of specific molecules in more complex chemical systems.[6]

The vibrational Raman spectra shown in the following chapters were recorded in the solid state as bulk. Since different laser excitation wavelengths have been used (described below), the employed spectrometers are classified here in accordance with the presence or not of resonant effects:

- Out-of-Resonance FT-Raman spectra showed in Chapter I, Chapter II and Chapter IV were recorded by using an FT-Raman accessory kit (RamII) connected to a Bruker Vertex70 FT-IR interferometer. A continuous-wave Nd:YAG laser working at λ_{exc}=1064 nm was employed for excitation, while a germanium detector operating at liquid nitrogen temperature was used to collect the Raman scattering radiation in a back-scattering configuration (with an angle of 180˚ between the incident radiation and the scattered radiation). A spectral resolution of 4 cm^{-1} was used. In general, the power of the laser beam was kept at a level lower than 100 mW to conserve the sample stability. With respect the acquisition times, around 3000-4000 scans were averaged for each spectrum to optimize the signal-to-noise ratio.

- Resonance Raman spectra of Chapter IV at 532 and 473 nm laser excitation wavelengths were recorded by using a InVia Qontor Raman Confocal Microscope of Renishaw. This setup is equipped with different diffraction gratings optimized for Visible and Near IR and a Charge Couple Device (CCD) detector to collect the Raman scattering radiation in a back-scattering configuration with a spectral resolution of 1 cm^{-1}. On the other hand, Resonance Raman spectra with 633 nm laser excitations were recorded by using a Bruker Senterra dispersive Raman microscope equipped with a CCD detector thermoelectrically cooled to -65°C, a confocal microscope with a x40 objective and a neon lamp used for laser (Nd:YAG) calibration. This set up operates in a back-scattering configuration with a spectral resolution of 3-5 cm^{-1}. In all the cases, the power of the laser beam was kept between 0.2-2 mW to conserve the sample stability and acquisition times of 10 co-additions of 10 s were enough to obtain high signal-to-noise ratio.

3.2. Electrochemical characterization

Since feasible hole/electron injection from electrodes to the semiconducting active layer is an indispensable prerequisite for the design of electronic devices, the charge injection ability of the materials under study was evaluated by analyzing their charged species. Among the electrochemical techniques, in the development of this Thesis we have make use of cyclic voltammetry and spectroelectrochemistry.

3.2.1. Cyclic voltammetry

As first step, cyclic voltammetries (CV) of the systems under study were performed. This electrochemical technique allows the analysis of multistage redox processes by measuring the current intensity generated as a function of the applied potential to the working electrode with respect to a reference electrode. As a result, a cyclic process is obtained in which when oxidation or reduction processes appear, peaks are generated.

Considering that the most energetically accessible oxidation or reduction process should be associated with the participation of HOMO or LUMO orbitals, it is possible to predict the HOMO and LUMO energies from the potential at which the first oxidation and reduction processes take place, respectively.

In this thesis, CV experiments were performed on a BASi C3 Epsilon Voltammetry Cell Stand operating at room temperature under nitrogen atmosphere. The electrochemical measurements showed in Chapter I were carried out using CH_2Cl_2 solutions of triindoles **1**-**3** ($c=1x10^{-5}$ M) and diazatruxenonas **4**-**7** ($c=1x10^{-3}$ M) with the presence of a high excess of tetra-n-butylammonium hexafluorophosphate supporting electrolyte (0.1 M of BuN_4-PF_6, Sigma-Aldrich/Merck, 98%) at a scan rate 100 mV/s. A three electrode setup was used including a platinum working electrode, Ag/AgCl (3 M NaCl) reference electrode, and a platinum wire auxiliary electrode. All potentials were referenced to the ferrocene/ferrocenium redox couple (Fc/Fc^+) used as internal standard.

On the other hand, CV measurements of **P1**-**P4** polymers films (Chapter IV) were performed by the group of Prof. Mohammed Al-Hashimi from the Texas A&M University at Qatar, making use of CHI760E Voltammetry analyzer operating at room temperature under argon atmosphere. In this context, thin film cyclic voltammograms of copolymers **P1**-**P4** were recorded at a scan rate of 100 $mV{\cdot}s^{-1}$ in acetonitrile/0.1 M Bu_4NPF_6 as electrolyte, using a platinum disk working electrode, an Ag/AgCl reference electrode and a platinum wire auxiliary electrode. Polymer films were drop-casted from chlorobenzene solutions on the Pt working electrode (2 mm in diameter). All potentials were referenced to the Fc/Fc^+ redox couple used as internal standard.

In all the cases, the experimental HOMO and LUMO energy levels were estimated from the onsets of the first oxidation and reduction potentials referenced to Fc/Fc^+ respectively, according to the equation:

$$E_{HOMO/LUMO} = -[(E_{onse}^{ox/red} - E_{1/2}^{Fc/Fc+}) + 4.8\ eV] \quad [3.1]$$

Where 4.8 eV is the formal potential of Fc/Fc^+ with respect to zero vacuum level.

3.2.2. *In situ* UV-Vis absorption spectroelectrochemistry

It is widely known that spectroelectrochemistry is a very useful tool for the study of charged species of π-conjugated systems, since it provides a whole vision of the evolution of the absorption spectra in UV-Vis regions during applied potential variation. This technique provides valuable information from an electrochemical and spectroscopic point of view. On one hand, we can obtain molecular information related to the charged defects of the π-conjugated system from the evolution of the spectra. On the other hand, kinetic and thermodynamic information of the oxidative/reductive processes is obtained from the electrochemical signal.

In this context, the *in situ* evolution of the absorption spectra of **NDI** and **PDI**-based semiconductors studied in Chapter III upon progressive electrochemical reduction was recorded. To this end, 10^{-5} M solutions of **NDI** and **PDI**-based semiconductors in dichloromethane with the presence of a high excess of supporting electrolyte (0.1 M of BuN_4-PF_6, Sigma-Aldrich/Merck, 98%) was used as electrochemical medium. The diluted solution was introduced in an Optically Transparent Thin-Layer Electrochemical (OTTLE) cell positioned in the sample compartment of a Cary 5000 spectrophotometer. This spectroelectrochemical cell is based on a transparent thin-layer of quartz and three electrodes: a Pt gauze as the working electrode, a Pt wire as the counter electrode and an Ag wire as the pseudo-reference electrode. The potential was controlled with a C3 epsilon potentiostat from BASi.

3.3. Quantum chemical methods

According to modern science, matter is constituted essentially by elemental particles combined in different ways. Since elemental particles do not obey classic physics but quantum mechanics laws, the study of molecular systems is thus a quantum mechanics problem. In this context, quantum chemistry has emerged as a powerful tool to understand the structure-property relationships of a wide range of molecular systems and therefore, to guide the molecular design of new materials with potential applications in electronic devices. From a physical chemistry point of view, the main interest of quantum chemistry is to find approximate solutions of the time-independent Schrödinger equation (Equation 3.2), which allow to obtain the energy and related properties of any molecular system:

$$\hat{\mathrm{H}}\Psi = E\Psi \qquad [\mathbf{3.2}]$$

where $\hat{\mathrm{H}}$ is the Hamiltonian operator, Ψ stands for the wavefunction that contains all the information about the quantum system at hand and E is the value of the energy of the state described by Ψ. Focusing on the Hamiltonian operator, it can be formulated as:

$$\hat{\mathrm{H}} = -\frac{1}{2}\sum_{i=1}^{N}\nabla_i^2 - \frac{1}{2}\sum_{A=1}^{M}\frac{1}{M_A}\nabla_A^2 - \sum_{i=1}^{N}\sum_{A=1}^{M}\frac{Z_A}{r_{iA}} + \sum_{i=1}^{N}\sum_{j>1}^{N}\frac{1}{r_{ij}} + \sum_{A=1}^{M}\sum_{B>A}^{M}\frac{Z_A Z_B}{r_{AB}} \qquad [\mathbf{3.3}]$$

In the above equation, ∇_i^2 and ∇_A^2 involve the Laplacian operators with respect to the coordinates of the i^{th} electron and the A^{th} nucleus, respectively; M_A and Z_A are the mass and the atomic number of nucleus A, respectively; r_{iA} is the distance between the i^{th} electron and the A^{th} nucleus: r_{ij} is the distance between the i^{th} and the j^{th}electrons; and r_{AB} is the distance between the A^{th} and B^{th} nucleus. The first two terms correspond to the kinetic energy of electrons and nuclei, respectively. The third term represents the Coulomb attraction between electrons and nuclei, while the fourth and fifth terms stand for the repulsion between electrons and between nuclei, respectively.

However, the Schrödinger equation can only be solved exactly for the hydrogen atom (two-particle system), and therefore, it is necessary to introduce approximations which

allow one to deal with the study of molecular systems. Regarding to that, the Born-Oppenheimer approximation is of critical importance in quantum chemistry. [7] This approximation takes advantage of the significant difference between the masses of electrons and nuclei (which are much heavier than electrons and therefore, they move more slowly) to assume that the electronic and nuclear motions are independent. In this way, the separated electronic Hamiltonian $\hat{H}_{elec}$ has the expression:

$$\hat{H}_{elec} = -\frac{1}{2}\sum_{i=1}^{N}\nabla_i^2 - \sum_{i=1}^{N}\sum_{A=1}^{M}\frac{Z_A}{r_{iA}} + \sum_{i=1}^{N}\sum_{j>1}^{N}\frac{1}{r_{ij}} \qquad [3.4]$$

which has been simplified with respect to Equation 3.3 since the kinetic energy of nuclei is zero and the potential energy of nucleus-nucleus repulsion is merely a constant. Nevertheless, the last term related to interelectronic Coulomb repulsion (r_i^{-1}) significantly increases the difficulty to solve the electronic Schrödinger equation for a molecular system, being necessary further approximations. There are several methods in quantum chemistry, based on different mathematical approximations and degree of accuracy, which allow us to address this issue: (i) *ab initio* methods, which are based on quantum mechanics and do not use other data than the fundamental physical constants (*i.e.* speed of light, mass of electrons, Planck constant, the charge of nuclei, among others). Indeed, ab initio calculations solve approximately the Schrödinger equation by using rigorous mathematical approaches. (ii) Semi-empirical methods are characterized by introducing parameters obtained from experimental data, simplifying quantum-chemical calculations and reducing the computational cost. (iii) Density functional theory (DFT) methods, which constitute the approach used along this Thesis.

3.3.1. Density functional theory method

Nowadays, DFT is the most used method for electronic structure calculations in quantum chemistry and matter physics. One of the main reasons is that this methodology allows the study of molecular systems with a reasonable accuracy and a low computational

cost. In fact, the theoretical characterization and description of all the systems studied along this Thesis have been performed within this methodology. Thereby, theoretical calculations have been performed not only to get deeper insights in the interpretation of the experimental results, but also to understand the physical and chemical behaviors responsible of the optoelectronic properties of the materials under study. This method represents an alternative to the conventional *ab initio* methodology, and considers the ground state electron density ($\rho(r)$) as the key variable that contains all the information about a molecular system, and not the wavefunction as in *ab initio* methods.[8]

DFT as we know it today was born in 1964, when Hohenberg and Kohn published a decisive work in the Physical Review that proved the existence of a universal functional of the density.[9] The theorems published in this work constitute the major theoretical pillars on which modern DFT is supported. The first theorem states that "*any observable for a non-degenerated ground state of an N-electron system, including the energy, can be calculated, in principle exactly, from the electron density of the ground state*". Therefore, the energy of the ground state can be expressed as:

$$\mathrm{E}_0[\rho] = \int \rho(r).V_{Ne}\,\mathrm{d}r + F_{HK}[\rho] = E_{Ne}[\rho] + T[\rho] + E_{ncl}[\rho] + J[\rho] \qquad [3.5]$$

where the first term corresponds to nuclei-electron attraction and $F_{HK}[\rho]$ refers to the Hohenberg-Kohn functional, which contains the functionals for the kinetic energy ($T[\rho]$), the classical Coulomb part $J[\rho]$ and the non-classical contribution to the electron-electron repulsion ($E_{ncl}[\rho]$). Unfortunately, the explicit form for the $T[\rho]$ and $E_{ncl}[\rho]$ terms were unknown, so we had to wait just one more year, when Kohn and Sham proposed an ingenious method by which these functionals could be approached.[10] The Kohn-Sham approach is based on the HF method, in which the Slater determinant describes a fictitious non-interacting system that does not include electron-electron repulsion terms:

$$\Theta\,(\mathrm{x}_1, \mathrm{x}_2 \ldots \mathrm{x}_N) = (N!)^{-1/2} \begin{vmatrix} \varphi_1(\mathrm{x}_1) & \varphi_2(\mathrm{x}_1) & \cdots & \varphi_N(\mathrm{x}_1) \\ \varphi_1(\mathrm{x}_2) & \varphi_2(\mathrm{x}_2) & \cdots & \varphi_N(\mathrm{x}_2) \\ \vdots & \vdots & & \vdots \\ \varphi_1(\mathrm{x}_N) & \varphi_2(\mathrm{x}_N) & \cdots & \varphi_N(\mathrm{x}_N) \end{vmatrix} \qquad [3.6]$$

Where φ_i refers to the Kohn-Sham orbitals, which can be determined by the Kohn-Sham operator defined as $\hat{f}^{KS}$ (in parentheses):

$$\left(-\frac{1}{2}\nabla_1^2 + \int \frac{\rho(r_2)}{r_{12}} dr_2 + V_{xc}(r_1) - \sum_A^M \frac{Z_A}{r_{1A}}\right)\varphi_i = \left(-\frac{1}{2}\nabla_2 + V_{eff}(r_1)\right)\varphi_i = \varepsilon_i \varphi_i \quad [3.7]$$

In view of the Kohn-Sham equation, the key that connects the artificial system with the real one is the choose of one local potential ($V_{xc}(r)$) such that the density resulting from the summation of the moduli of squared Kohn-Sham orbitals exactly equals the ground state density of the real target system of interacting electrons:

$$\rho_s(r) = \sum_i^N |\varphi_i|^2 = \rho_0(r) \quad [3.8]$$

The $V_{xc}(r)$ potential emerges from the introduction of an exchange-correlation energy term (E_{xc}) to the ground state energy functional:

$$E_0[\rho] = E_{Ne}[\rho] + J[\rho] + T_s[\rho] + E_{xc}[\rho] \quad [3.9]$$

Since the exchange-correlation energy term ($E_{xc}[\rho]$) is the only one unknown, the Kohn-sham one-electron equations must be solved iteratively by applying the variational principle. For that, the starting point is a trial electron density usually calculated as a superposition of atomic densities. Then, a V_{xc} potential is computed from an approximate expression of E_{xc} and the initial density:

$$V_{xc} \equiv \frac{\delta E_{xc}}{\delta \rho} \quad [3.10]$$

With this information, the Kohn-sham equations are solved, obtaining as result an initial set of orbitals which is used to compute an improved density. This process is repeated until both the electron density and the ground state energy have converged within the thresholds chosen.

In the practice, there are different ways to approximate the undefined exchange-correlation functionals.: (i) the Local Density Approach (LDA) uses the uniform electron gas

model to obtain an approximate E_{xc} functional which only depends on the density at each point. (ii) In the Generalized Gradient Approximation (GGA), the non-homogeneity of the true electron density is considered making that the E_{xc} term depends not only on the localized density but also on the gradient of the density. This approach improves the resolution of several parameters (*i.e.* harmonic frequencies or equilibrium geometries) with respect to the LDA methods, although it fails in the description of weakly bounded systems. Therefore, the next step in sophistication of E_{xc} term was to add a dependence with the kinetic energy density resulting in meta-GGA functionals. (iii) Hybrid functionals incorporate a portion of exact exchange energy in the expression of E_{xc} as well as local and corrected gradient terms for the exchange and correlation energy. The development of hybrid functionals have marked a milestone for DFT, yielding high performances in the computation of equilibrium geometries, harmonic frequencies, thermochemistry test and charge densities, among others. These are the reasons why the DFT calculations showed in the present Thesis have been performed by using this kind of functionals, among which, it is worth to highlight:

- B3LYP functional, which will be the most widely used in this thesis. It combines the Becke's three-parameter exchange functional (B3) with the Lee-Yang-Parr (LYP) non-local correlation functional.[11, 12]
- The hybrid generalized gradient approximation PBE0 functional from Adamo, which uses 25% Hartree-Fock exchange and 75% DFT exchange. This functional is based on the pure functional of Perdew, Burke and Ernzerhof (PBE).[13]
- M06-2X functional, which is a hybrid meta-GGA functional of Truhlar and Zhao. It is well known that this functional gives reliable ground electronic state polarization when compared to X-ray structures and also accurate excited states dipole moments for a large variety of push-pull systems.[14]
- The latest functional from Head-Gordon and co-workers is the ωB97X-D functional, which includes a version of Grimme's D2 empirical dispersion. The molecular

geometries of longer systems were calculated with this functional to check the long-range correction effects on the optical and electronic properties.[15]

Note that except for ωB97X-D functional, the used functionals exhibit a local or semi-local dependence on the electronic density, failing in the description of non-covalent interactions. To avoid this situation, Grimme's dispersion correction D3 (which is essential to describe the intermolecular interactions) has been used to compute the trimeric models of Chapter I and the 2D-polymers of Chapter II.[16, 17]

The mathematical description of the orbitals has been computed with the split-valence double-zeta 6-31G** basis set,[18, 19] as implemented in the Gaussian 09[20] and Gaussian 16 programs.[21] In this basis set, the core orbitals are described by six primitive gaussian type orbitals (PGTOs), whereas the inner part of the valence orbitals is a contraction of three PGTOs and the outer part of the valence orbitals is represented by one PGTO. The double asterisk (also indicated as d,p) indicates that a single set of d- and p-type polarization functions have been added on heavier and hydrogen atoms, respectively.

Once the level of theory of the quantum chemical calculations performed along this Thesis has been defined, let me briefly explain how the study of the different properties have been approached.

3.3.1.1. Geometry optimizations

In all the calculations, large alkyl chains were replaced by methyl groups to reduce the computational cost. All geometrical parameters were allowed to vary independently apart from planarity of the rings, and no imaginary frequencies were observed, which ensures the finding of the global minimum energy. Ultrafine integration grid and tight convergence criteria were used. Molecular orbital topologies and dipole moments were directly obtained from the optimized geometries and were plotted using the ChemCraft 1.8 molecular modelling software.[22]

3.3.1.2. Aromatic parameters

The degree of aromaticity has been evaluated by computing the Nucleus-Independent Chemical Shifts (NICS) values at the geometrical centers of selected phenyl rings.[23, 24] In this work, this aromatic parameter has been computed at B3LYP/6-311++G(2df,p) level from the B3LYP/6-31G** optimized structures by using the gauge-independent atomic orbital (GIAO) method.[25] The GIAO method calculates the magnetic shielding tensor for each orbital contribution separately, and the sum of all orbital contributions gives the shielding tensor at the ring center.

3.3.1.3. Raman frequencies calculations

The theoretical treatment of molecular vibrations is considered an excellent example of the importance of theoretical chemistry to assist the interpretation of experimental data. In fact, the calculated normal modes and their corresponding intensities can be used to assign the Raman experimental peaks. Additionally, the analysis of the normal modes enables to explain the frequency shifts of some vibrational peaks within a family of molecules, which in turn can give important notions about the effective π-conjugation degree. On the basis of these considerations, vibrational frequencies calculations allow to establish important structure-property relationships as will be shown along the Thesis.

The calculation of Raman frequencies has been performed at the same level of theory previously used for geometry optimizations. In fact, all real positive vibrational frequencies confirm the minima energy of the optimized systems, as previously mentioned.

Although DFT has proven to be a powerful technique to simulate vibrational spectra of π-conjugated systems, the harmonic frequencies calculated at DFT level are usually uniformly scaled by using an adjustment of the theoretical force fields to disentangle experimental misassignments. The specific scale factor for each case under study is determined by comparison of the computed harmonic frequencies with respect the experimental frequencies ones. [26, 27] In this sense, scaling factors of 0.968, 0.954 and 0.971

were used for the Raman spectra of disk-shape molecules (Chapter I), porous polymers (Chapter II) and linear **P1**-**P4** polymers (Chapter IV), respectively. Finally, the theoretical spectra were obtained by convolution of the scaled frequencies and the Raman scattering activities with Gaussian functions (10 cm^{-1} width at the half-height). Vibrational eigenvectors were plotted using the ChemCraft 1.8 molecular modelling software.[22]

3.3.1.4. Simulations of electronic spectra

Up to now, DFT methods have been proved to be a powerful tool for the investigation of several properties. Nevertheless, DFT is based on a ground state theory within its original formulation. In 1984, Runge and Gross extended the DFT approach to deal with time-dependent phenomena such as the formation of excited states. This theory is known as the Time-Dependent DFT (TD-DFT).[28-30] Thanks to this theory, we have calculated the properties of the excited states for all the systems under study and, consequently, the electronic vertical transitions, allowing us to predict their electronic absorption spectra. In this context, absorption spectra were simulated through convolution of the vertical transition energies and oscillator strengths with Gaussian functions (0.3 eV width at the half-height) by using GaussSum 3.0 software.[31] These calculations have been performed at the same level of theory that previously used for geometry optimizations and frequency calculations.

3.3.1.5. Charge transport parameters

In this section, we have computed and presented in Chapter I the two key charge transport parameters which dictate the electron transfers rate within a semiclassical hopping mechanism: the intramolecular reorganization energy and the transfer integral.

Considering the former, this parameter reflects the structural changes of the molecules needed to accommodate a positive or negative charge (*i.e.*, hole (λ_h) or electron (λ_e) reorganization energy, respectively). The λ_e and λ_h values were computed directly from

the relevant points on the potential energy surfaces by means of a standard procedure reported in the literature.[32, 33] This approach needs the calculation of four-points:

$$\lambda_e = (E^*_0 - E_{-1}) + (E^*_{-1} - E_0) \qquad \lambda_h = (E^*_0 - E_{+1}) + (E^*_{+1} - E_0) \qquad [3.11]$$

where E_0 is the optimized ground state energy of the neutral molecule, E_{-1}/E_{+1} is the optimized energy of the anion/cation state, E^*_{-1}/E^*_{+1} is the energy of the neutral molecule at the anion/cation state geometry and E^*_0 is the energy of the anion/cation state at the optimized geometry of the neutral state.

On the other hand, the transfer integral parameter reflects the efficiency of the frontier molecular orbital coupling between neighboring molecular pairs. In this sense, hole transfer integrals (t_h) for cofacial dimers of triindoles **1** and **2** built from the X-ray determined structures at an intermolecular distance of 3.51 Å, were calculated at the B3LYP/6-31G** level by using the approach described by Valeev et al.[34] Since HOMO and HOMO-1 orbitals of these molecules are degenerated in energy, the t_h values were calculated as: $[(t_{HOMO.HOMO}{}^2 + t_{HOMO-1.HOMO-1}{}^2 + t_{HOMO-1.HOMO}{}^2 + t_{HOMO.HOMO-1}{}^2)/4]^{1/2}$. For the diazatruxenones **6** and **7**, t values for cofacial dimeric models in which molecules of the dimer are separated by 3.80 Å with an antiparallel dipole-dipole arrangement were also calculated.

3.3.1.6. Periodic calculations

In a step forward, we used periodic boundary conditions to obtain the geometry optimizations of the 2D-π-conjugated polymers investigated in Chapter II. For that purpose, the preliminary optimized dimeric models (at PBE0/6-31G** level) were considered as a reasonable starting point geometries towards the assembling of the whole periodic systems. Once the 2D-polymers were constructed, they were fully optimized (simultaneous lattice/cell and structure optimizations) with the QUANTUM EXPRESSO plane-wave DFT code.[35]

Within this implementation, the PBE0 functional [13] was used in addition to Grimme DFT-D3 corrections.[17] Ultra-soft pseudopotentials have been used for C, N, O and H atoms.[36, 37] The Brillouin zones have been sampled by means of optimal Monkhorst-Pack grids,[38] and the energy cutoff values have been tested to guarantee a full convergence in total energy and electronic density. Thereby, the one-electron wave-functions are expanded in a basis of plane-waves with an energy cutoff of 41 Ry for the kinetic energy and 260 Ry for electronic density.

Inter-layer distances were also fully-relaxed following the afore mentioned simultaneous lattice + structure relaxation protocol. In this sense, inter-layer cohesive energies between the 2D-layers were obtained in their both AA and AB stacking fashions as the difference between the total energies of the crystal bulks and the optimized corresponding single-layers.

Furthermore, the topologies of valence and conduction electronic states of the different 2D-polymers at the k-point have been plotted by using the VMD 1.9.3 program.[39] The same program has been used in order to represent the surface charge distributions of the resulting 2D-polymeric layers. All of them have been depicted with the same isosurface value (0.0003 e^-/Å) for the sake of comparison.

Finally, effective hole (m_h^*) and electron masses (m_e^*) have been evaluated from the top of the valence band and the bottom of the conduction band, respectively. To this purpose, the following expression has been used:

$$m^* = \hbar^2 \frac{\partial^2 E}{\partial K^2}^{-1} \qquad [3.12]$$

where the $E(K)$ function has been parametrized and fitted by a quadratic anharmonical expression $E(K) = a_0 + a_1 \cdot k + a_2 \cdot k^2$ within a close region to the band-gap k-point, with the rest of quantities in atomic units to obtain the effective masses directly in m_e units.

3.4. Implementation of semiconducting materials in OFETs

As mentioned in the introduction chapter, OFETs are a versatile platform for the direct examination of the electrical mobility of new semiconductors, which is essential in next-generation optoelectronic devices. Thereby, most of the materials proposed to study in this thesis have been implemented in OFETs.

3.4.1. Device configuration

Simply speaking, an OFET is constituted of different electrically active layers assembled on a substrate: the organic semiconductor, the gate dielectric and three terminal electrodes (gate, source and drain electrodes). According to the different position of the layers, OFETs can be classified into one of the following four device architectures: bottom gate-bottom contact (BG-BC, Figure 3.4a), bottom gate-top contact (BG-TC, Figure 3.4b), top gate-bottom contact (TG-BC, Figure 3.4c) and top gate-top contact (TG-TC, Figure 3.4d). Each of the four device architectures present advantages and disadvantages, so the one to be adopted is a direct consequence of its purpose.[40]

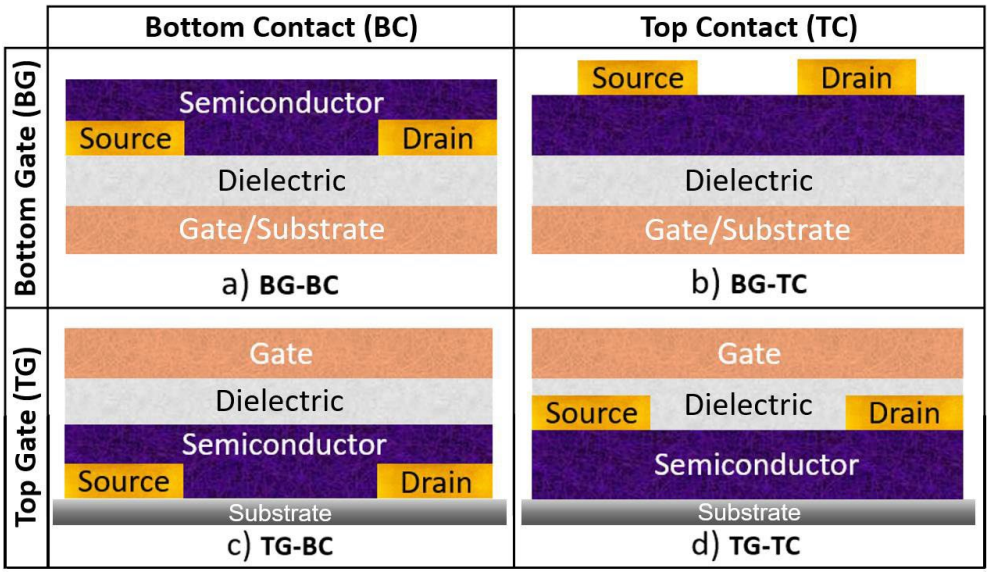

Figure 3.4. Schematic representation of OFET device configurations: (a) bottom gate-bottom contact, (b) bottom gate-top contact, (c) top gate-bottom contact and (d) top gate-top contact.

For instance, BG-BC devices allow for quick examination of new semiconductors because the insulating layer and the three terminal electrodes can be prefabricated, and therefore, the semiconductor is deposited in the final step of the process. However, this configuration fully exposes the semiconductor to ambient conditions which may accelerate degradation. In this sense, TG-BC and TG-TC configurations reduce environmental degradation of the semiconductor as the dielectric acts as an encapsulation layer, although the dielectric must be carefully chosen and deposited to preserve the integrity of the semiconductor layer. Regarding these configurations, the TC mode is probably more useful for obtaining high quality semiconducting layers than the BC configuration because the prefabricated electrodes in the latter can act as nucleation sites, leading to worse contact quality between the semiconductor and the source and drain electrodes.[41]

Based on these considerations, we used the bottom gate-top contact configuration on the development of this thesis, which is described in detail as follow.

3.4.2. Bottom gate-top contact (BG-TC) configuration

For the fabrication of field effect transistors in a standard bottom gate-top contact architecture, we followed the procedure shown in Figure 3.5. Commercially available highly-doped silicon wafers covered with a 300 nm thick thermally grown SiO_2 layer were used as gate electrode and dielectric layer, respectively. First the all, Si/SiO_2 substrates with dimensions of 2.5 x 1 cm were cut and double-cleaned in an ultrasonic bath with ethanol for 10 minutes, dried with a stream of N_2 and finally treated with UV-ozone (UVO CLEANER 342-220) for 10 minutes to eliminate any organic impurities (section *i* of Figure 3.5).

Nevertheless, this dielectric surface based on SiO_2 is hydrophilic, whereas most of organic materials are hydrophobic. To overcome this mismatch, surface functionalization with self-assembly monolayers is a widely used strategy to change the surface polarity from hydrophilic to hydrophobic, which can also facilitate the formation of well-ordered organic semiconductor layers as well as minimize the concentration of charge carrier trap states due to surface hydroxyl groups, resulting in enhanced charge carrier mobility and device

stability.[42, 43] In this sense, we have used hexamethyldisilane (HMDS) and octadecyltrichlorosilane (OTS) as self-assembling materials. The HMDS treatment is performed by exposing the cleaned silicon substrates to HMDS vapor at room temperature in a closed air-free container under argon atmosphere for a week. On the other hand, the surface functionalization with a self-assembled monolayer of OTS is carried out by immersion of the cleaned silicon substrates in a 3.0 mM humidity-exposed solution of OTS in hexane for 1 hour. After OTS deposition, the substrates are subsequently cleaned by sonication in hexane, acetone, and ethanol for 10 minutes each and then, dried with a stream of N_2 (section *ii* of Figure 3.5).

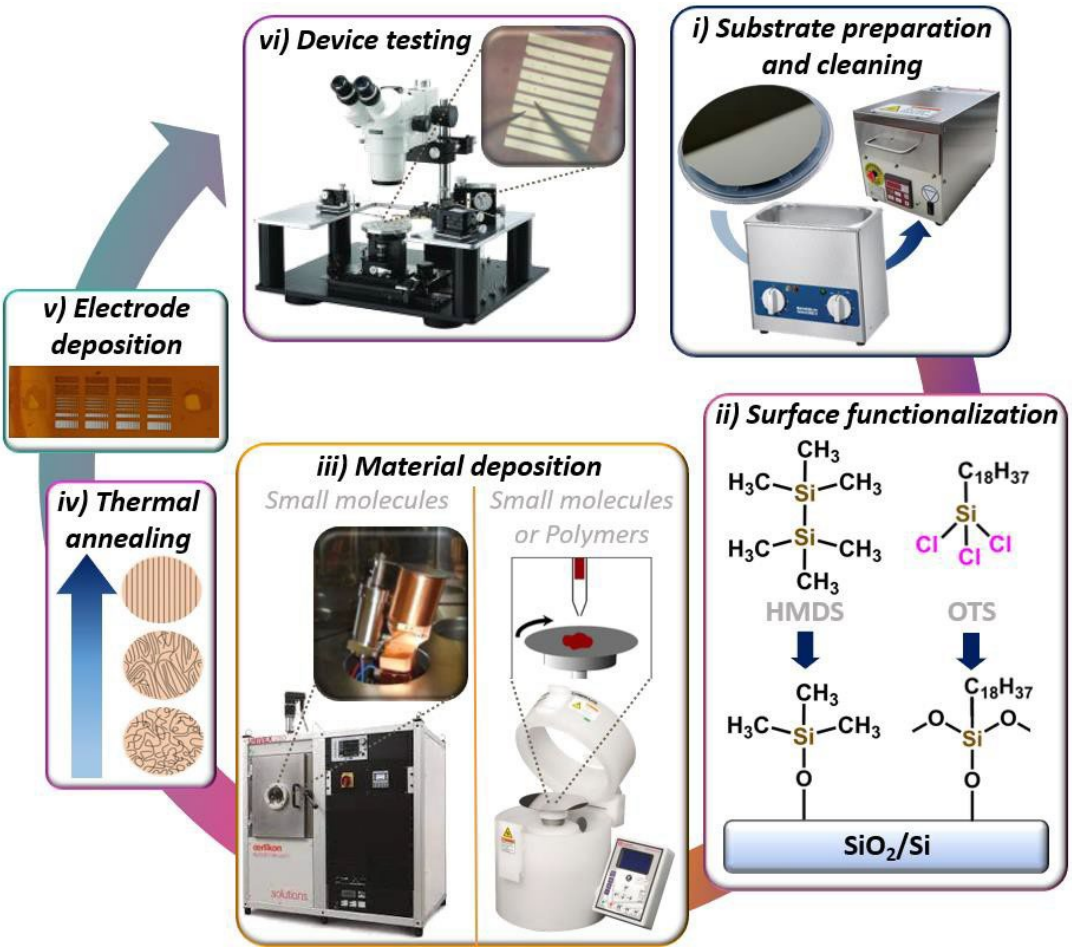

Figure 3.5. Different steps on the fabrication of BG-TC OFETs showed in this Thesis.

Once the dielectric surface has been functionalized, the semiconducting active materials are deposited by slow sublimation under vacuum conditions or solution-processed techniques. In the vacuum evaporation technique, the organic semiconductor is placed under vacuum (around 10^{-6} mbar) and heated to cause sublimation, followed by condensation on the substrate forming thin films. In our case, an OERLIKON UNIVEX 250 evaporator has been used to thermally deposit 50 nm (determined through a quartz microbalance) of disk-shape molecules **1**-**7** and **NDI**/**PDI**-based compounds of Chapter I and Chapter III, respectively. Among the main advantages of thermally deposited films, it is worth to highlight its excellent uniformity and reproducibility (controlled by monitoring the substrate temperature and the deposition rate) as well as its high purity due to the lack of solvents involved in the process or gases such as oxygen.[44] Nevertheless, this technique is mainly used for small-molecules and oligomeric semiconductors, not being applicable to polymers because they tend to decompose by cracking at high temperatures (section *iii* of Figure 3.5).

For polymers, solution processing techniques are mainly used since they do not need high deposition temperatures or high vacuum conditions. Among the different techniques used to deposit organic semiconductors from solution, the most used method in laboratories is “spin coating” due to its simplicity, thus not requiring sophisticated and expensive equipment. However, this technique requires organic semiconductors with good solubility in some common organic solvents. Translated to the case of the **P1**-**P4** polymers studied in Chapter IV, where a LAURELL TECHNOLOGIES WS-650MZ-23NPP spin-coater has been used, the “spin coating” method involves dropping a small portion of semiconductor solution (at a concentration of 5 mg/ml in tetrahydrofuran) onto the center of the substrate and spinning the substrate at high speeds (1500 rpm for 60 seconds). Then, the centripetal acceleration forces the solution to spread on the substrate, leaving it covered with a uniform thin film upon solvent evaporation. Interestingly, variations in the concentration of the solution, used solvent or working parameters of the spin coater (*i.e.* spin speed, time and acceleration) give rise to changes in the solvent evaporation rate during film formation,

which might result in different film microstructures and therefore, different OFET device performances (section *iii* of Figure 3.5).[45, 46]

The deposited organic active layers were subsequently subjected to a thermal annealing process to improve its molecular ordering and its crystallinity. Nevertheless, it should be noted that the same thermal annealing treatment does not work properly for all organic materials, and thus the annealing conditions should be fully optimized for each sample by systematically investigating the effect of the annealing condition on materials morphology and crystallinity, and on charge transport characteristics. In this context, disk-shaped molecules **1**-**3** and **NDI**/**PDI**-based compounds were deposited on preheated substrates at temperatures of 60, 80 and 90ºC, followed by annealing treatments at 120-150ºC for 2 hours. Likewise, annealing treatments at 100,150 and 200ºC for 2 hours were performed to thin-films based on **P1**-**P4** copolymers (section *iv* of Figure 3.5). We recommend readers to see Appendix 6.3, where the complete device optimization procedure is shown.

The last step in the fabrication of bottom-gate top-contact devices is the deposition of the source and drain electrodes. In this sense, although platinum and aluminum are also commonly used, gold is the most used metal as electrode for laboratory purposes due to its stability and inertness. Therefore, we have made use of the same OERLIKON UNIVEX 250 evaporator previously used for the deposition of the semiconducting materials to thermally evaporate 40 nm gold source and drain electrodes through shadow masks. The channel width of these masks (W) oscillates between 100 and 5000 µm, while the channel length varies from 10 to 100 µm (section *v* of Figure 3.5).

Finally, the devices were tested (section *vi* of Figure 3.5).

3.4.3. OFET operation and determination of device parameters

The operation of an OFET relies on the application of two electric potentials, one at the gate electrode (V_{GS}) and the other at the drain electrode (V_{DS}), while the source electrode

held at ground. For the following discussion, the OFET channel is assumed to be p-type, being the polarities simply reversed compared with its n-type counterpart. Starting from the situation where no V_{GS} is applied to an ideal p-type device, the device is "off" (left side of Figure 3.6).

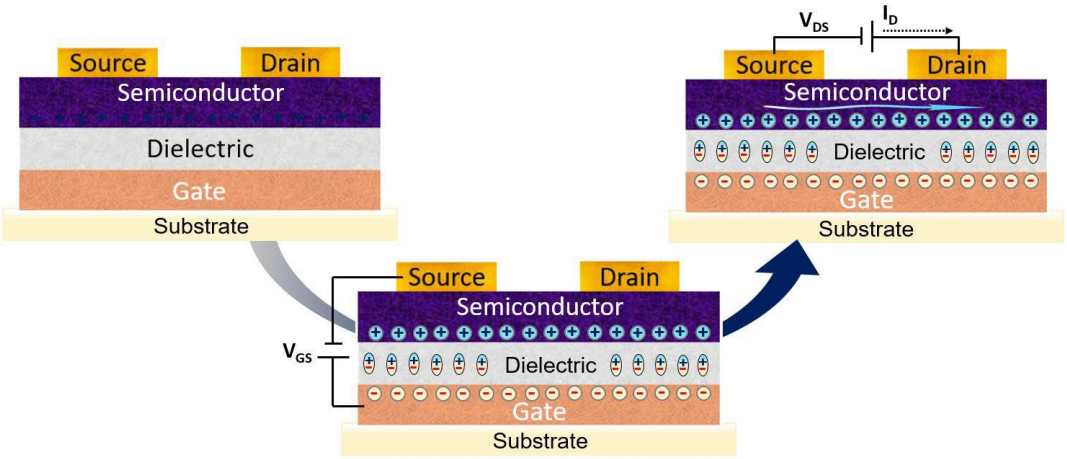

Figure 3.6. Schematic representation of the operation of an OFET with p-type characteristics.

However, an applied negative V_{GS} polarizes the dielectric causing the accumulation of holes charge carriers at the semiconductor-dielectric interface: in this situation, the transistor turns "on" (central part of Figure 3.6). It is important to mention that in a real device a small V_{GS} potential, known as the threshold voltage (V_T), is firstly required to fill charge traps at the semiconductor-dielectric interface before charge carriers are accumulated in the conduction channel. Once the charge carriers are accumulated, an applied negative V_{DS} forces them to move from the source to the drain electrode where the drain current (I_{SD}) is measured (right side of Figure 3.6). Note that the charge density in the transistor channel (and thus, I_{SD}) can be modulated by the magnitude of the applied field (V_{GS}), hence the "field-effect" terminology.

The operating mode of an OFET produces two typical curent-voltage curves, as shown in Figure 3.7.

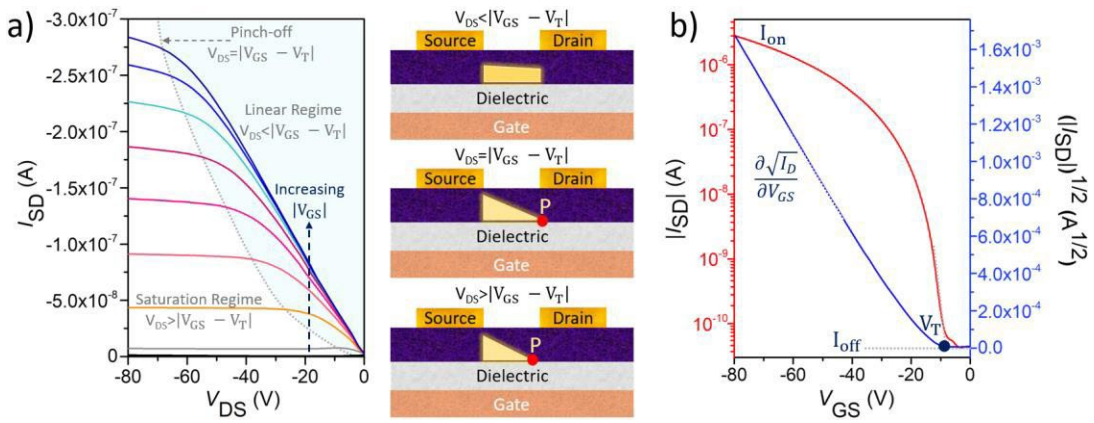

Figure 3.7. Representative (a) output and (b) transfer curves of a p-type OFET. The BG-TC structure with the conduction channel highlighted in yellow for the linear (top), pinch-off (middle) and saturation regimes (bottom) are also shown.

Figure 3.7a shows the well-known "output curves", which measure the evolution of I_D with increasingly negative V_{DS} values at determined V_{GS} voltages. As long as $V_{DS} < V_{GS} - V_T$, the current flowing along the transistor channel (I_{SD}) obeys the Ohm's law, in other words, the device operates in a linear regime in which I_{DS} increases linearly with V_{DS}. However, when V_{DS} magnitude is further increased until approaches that of V_{GS}, the shape of the conduction channel changes. At the critical point where $V_{DS} = V_{GS} - V_T$, the area near the drain electrode is depleted of free charge carriers and the channel becomes pinched off (point P in Figure 3.7a). Further increasing V_{DS} does not substantially increase the current since the device operates in saturation regime but leads to the growing of the depletion zone and therefore a slight shortening of the conduction channel.

On the other hand, Figure 3.7b displays an example of "transfer curve", which shows in red the evolution of I_{SD} on a logarithmic scale as a function of V_{GS} with V_{DS} held constant in the saturation regime. In blue, the same figure shows the dependence between the square-root I_{SD} value and V_{GS} by using the assumptions of conventional transistor formalism:

$$I_{SD}^{1/2} = \left(\frac{W}{2L} \cdot \mu \cdot C_{diel}\right)^{1/2} \cdot (V_{GS} - V_T) \qquad [3.13]$$

Where L is the channel length (being the distance between the source and drain electrodes), W is the channel width and C_{diel} is the capacitance per unit area of the insulator layer. Importantly, the main electrical parameters that characterize the performance of an OFET can be extracted from this curve (i) the field-effect mobility (μ), which measures how quickly charge carriers can move in response to an external electric field, is calculated from the slope of the blue line. (ii) The $I_{on/off}$ ratio which needs to be as high as possible, so the "on" state and the "off" state are clearly distinguishable. (iii) The V_T value, which is the minimum V_{GS} required to turn on the transistor, can be calculated by finding the intercept of I_{DS}=0 and the intersection with the X axis.[47]

In our case, OFET transfer and output curves were measured at ambient conditions by using an EB-4 Everbeing ProbeStation or under vacuum conditions (around 10^{-6} mbar) by using a customized probestation from Trinos Vacuum, both connected to a 4200-SCS/C Keithley semiconductor characterization system.

3.5. Morphological characterization of OFETs

The thin film morphology of organic semiconductors has an important influence in both injection and charge transport processes, which dictate the device operation. In fact, an efficient charge transport process requires of highly ordered and homogeneous films, in which the presence of large crystalline domains is accompanied by a good interconnection of them.[48, 49] On the basis of the above considerations, the microstructures of the semiconducting films, prepared under the optimal device fabrication conditions, were characterized via Grazing Incidence X-Ray Diffraction (GIXRD) and Atomic Force Microscopy (AFM):

- When a conventional X-ray diffraction analysis is performed on OFETs, it generally produces a week signal from the semiconducting layer and an intense signal from the substrate. One effective way to avoid this problematic is to perform the X-ray scanning with a fixed grazing angle of incidence, leading to the GIXRD version (see Figure 3.8a). Thereby, GIXRD technique renders valuable information about the

crystal structure, lattice parameters, and physical properties of thin films and coatings. From the operating point of view, the GIXDR data were recorded by using a Bruker D8 DISCOVER diffractometer that uses $CuK_{\alpha 1}$ radiation (λ= 1.5405 Å) to measure a range of 2θ values from 2 to 35º for 120 minutes. The diffracted beam is collected by a Scintillation detector.

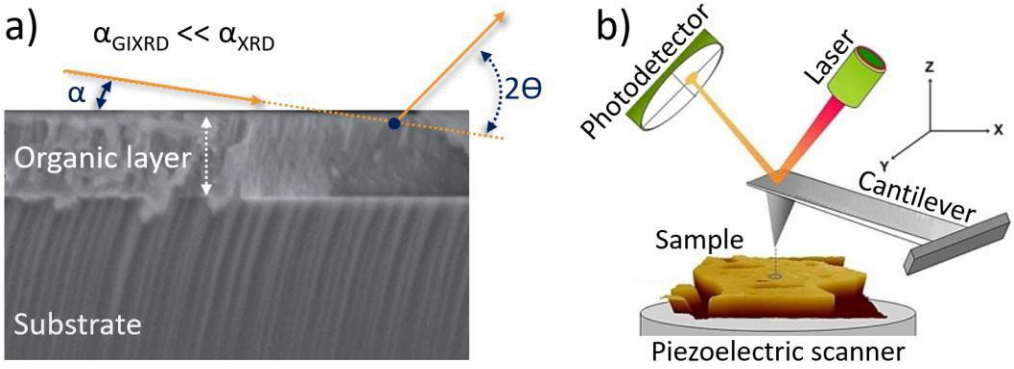

Figure 3.8. Representations of (a) GIXRD and (b) AFM characterization techniques.

- On the other hand, AFM was the chosen tool to obtain the surface root-mean-square (RMS) roughness values. This information is gathered by tapping the surface with a sharp tip integrated at the end of a flexible cantilever, whose movements are detected by a piezoelectric scanner in a highly accurate and precise way (see Figure 3.8b). In this Thesis, AFM images of the thin films were recorded by using a multimode atomic force microscope with a Nanoscope V Controller (Bruker Corporation, Billerica, MA, USA) working in tapping mode. Attractive/repulsive interactions between the tip and the sample are established with a separation in a range of 1-100 Å, depending on the vibration frequency of the cantilever.

3.6. References

[1] Harris, D. C.; Bertolucci, M. D., *Symmetry and spectroscopy: an introduction to vibrational and electronic spectroscopy*. Courier Corporation: 1989.

[2] Parson, W. W., *Modern optical spectroscopy*. Springer: 2007; Vol. 2.

[3] Smith, E.; Dent, G., *Modern Raman spectroscopy: a practical approach*. John Wiley & Sons: 2019.

[4] Castiglioni, C.; Tommasini, M.; Zerbi, G., Raman spectroscopy of polyconjugated molecules and materials: confinement effect in one and two dimensions. *Philosophical Transactions of the Royal Society of London. Series A: Mathematical, Physical and Engineering Sciences* **2004,** 362, (1824), 2425-2459.

[5] Lopez-Navarrete, J.; Tian, B.; Zerbi, G., Relation between effective conjugation, vibrational force constants and electronic properties in polyconjugated materials. *Solid State Communications* **1990,** 74, (3), 199-202.

[6] Efremov, E. V.; Ariese, F.; Gooijer, C., Achievements in resonance Raman spectroscopy: Review of a technique with a distinct analytical chemistry potential. *Analytica Chimica Acta* **2008,** 606, (2), 119-134.

[7] Born, M.; Oppenheimer, J. R., On the quantum theory of molecules. *Сборник статей к мультимедийному электронному учебно-методическому комплексу по дисциплине «физика атома и атомных явлений»/отв. ред. Шундалов МБ; БГУ, Физический факультет* **1927**.

[8] Szabo, A.; Ostlund, N. S., *Modern quantum chemistry: introduction to advanced electronic structure theory*. Courier Corporation: 2012.

[9] Hohenberg, P.; Kohn, W., Density functional theory (DFT). *Phys. Rev* **1964,** 136, B864.

[10] Kohn, W.; Sham, L. J., Self-Consistent Equations Including Exchange and Correlation Effects. *Physical Review* **1965,** 140, (4A), A1133-A1138.

[11] Lee, C.; Yang, W.; Parr, R. G., Development of the Colle-Salvetti correlation-energy formula into a functional of the electron density. *Physical Review B* **1988,** 37, (2), 785-789.

[12] Becke, A. D., Density-functional thermochemistry. III. The role of exact exchange. *The Journal of Chemical Physics* **1993,** 98, (7), 5648-5652.

[13] Perdew, J. P.; Burke, K.; Ernzerhof, M., Generalized Gradient Approximation Made Simple. *Physical Review Letters* **1996,** 77, (18), 3865-3868.

[14] Zhao, Y.; Truhlar, D. G., Density Functionals with Broad Applicability in Chemistry. *Accounts of Chemical Research* **2008,** 41, (2), 157-167.

[15] Chai, J.-D.; Head-Gordon, M., Long-range corrected hybrid density functionals with damped atom–atom dispersion corrections. *Physical Chemistry Chemical Physics* **2008,** 10, (44), 6615-6620.

[16] Grimme, S.; Antony, J.; Ehrlich, S.; Krieg, H., A consistent and accurate ab initio parametrization of density functional dispersion correction (DFT-D) for the 94 elements H-Pu. *The Journal of Chemical Physics* **2010,** 132, (15), 154104.

[17] Grimme, S., Semiempirical GGA-type density functional constructed with a long-range dispersion correction. *Journal of Computational Chemistry* **2006,** 27, (15), 1787-1799.

[18] Hehre, W. J.; Ditchfield, R.; Pople, J. A., Self—Consistent Molecular Orbital Methods. XII. Further Extensions of Gaussian—Type Basis Sets for Use in Molecular Orbital Studies of Organic Molecules. *The Journal of Chemical Physics* **1972,** 56, (5), 2257-2261.

[19] Francl, M. M.; Pietro, W. J.; Hehre, W. J.; Binkley, J. S.; Gordon, M. S.; DeFrees, D. J.; Pople, J. A., Self-consistent molecular orbital methods. XXIII. A polarization-type basis set for second-row elements. *The Journal of Chemical Physics* **1982,** 77, (7), 3654-3665.

[20] Frisch, M. J., Trucks, G.W., Schlegel, H.B., et al. , Gaussian 09 Revision C 01 *Wallingford* **2009**

[21] M. J. Frisch, G. W. T., H. B. Schlegel, G. E. Scuseria, M. A. Robb, J. R. Cheeseman, G. Scalmani, V. Barone, G. A. Petersson, H. Nakatsuji, X. Li, M. Caricato, A. V. Marenich, J. Bloino, B. G. Janesko, R. Gomperts, B. Mennucci, H. P. Hratchian, J. V. Ortiz, A. F. Izmaylov, J. L. Sonnenberg, D. Williams-Young, F. Ding, F. Lipparini, F. Egidi, J. Goings, B. Peng, A. Petrone, T. Henderson, D. Ranasinghe, V. G. Zakrzewski, J. Gao, N. Rega, G. Zheng, W. Liang, M. Hada, M. Ehara, K. Toyota, R. Fukuda, J. Hasegawa, M. Ishida, T. Nakajima, Y. Honda, O. Kitao, H. Nakai, T. Vreven, K. Throssell, J. A. Montgomery, Jr., J. E. Peralta, F. Ogliaro, M. J. Bearpark, J. J. Heyd, E. N. Brothers, K. N. Kudin, V. N. Staroverov, T. A. Keith, R. Kobayashi, J. Normand, K. Raghavachari, A. P. Rendell, J. C. Burant, S. S. Iyengar, J. Tomasi, M. Cossi, J. M. Millam, M. Klene, C. Adamo, R. Cammi, J. W. Ochterski, R. L. Martin, K. Morokuma, O. Farkas, J. B. Foresman, and D. J. Fox. , Gaussian 16, Revision B.01. *Gaussian, Inc., Wallingford CT,* **2016**.

[22] https://www.chemcraftprog.com, Chemcraft - graphical software for visualization of quantum chemistry computations.

[23] Schleyer, P. v. R.; Maerker, C.; Dransfeld, A.; Jiao, H.; van Eikema Hommes, N. J. R., Nucleus-Independent Chemical Shifts: A Simple and Efficient Aromaticity Probe. *Journal of the American Chemical Society* **1996,** 118, (26), 6317-6318.

[24] Zywietz, T. K.; Jiao, H.; Schleyer, P. v. R.; de Meijere, A., Aromaticity and Antiaromaticity in Oligocyclic Annelated Five-Membered Ring Systems. *The Journal of Organic Chemistry* **1998,** 63, (10), 3417-3422.

[25] Wolinski, K.; Hinton, J. F.; Pulay, P., Efficient implementation of the gauge-independent atomic orbital method for NMR chemical shift calculations. *Journal of the American Chemical Society* **1990,** 112, (23), 8251-8260.

[26] Jiménez-Hoyos, C. A.; Janesko, B. G.; Scuseria, G. E., Evaluation of range-separated hybrid density functionals for the prediction of vibrational frequencies, infrared intensities, and Raman activities. *Physical Chemistry Chemical Physics* **2008,** 10, (44), 6621-6629.

[27] Merrick, J. P.; Moran, D.; Radom, L., An evaluation of harmonic vibrational frequency scale factors. *The Journal of Physical Chemistry A* **2007,** 111, (45), 11683-11700.

[28] Runge, E.; Gross, E. K. U., Density-Functional Theory for Time-Dependent Systems. *Physical Review Letters* **1984,** 52, (12), 997-1000.

[29] Gross, E. K. U.; Kohn, W., Time-Dependent Density-Functional Theory. In *Advances in Quantum Chemistry*, Löwdin, P.-O., Ed. Academic Press: 1990; Vol. 21, pp 255-291.

[30] Heinze, H. H.; Görling, A.; Rösch, N., An efficient method for calculating molecular excitation energies by time-dependent density-functional theory. *The Journal of Chemical Physics* **2000,** 113, (6), 2088-2099.

[31] O'boyle, N. M.; Tenderholt, A. L.; Langner, K. M., cclib: A library for package-independent computational chemistry algorithms. *Journal of Computational Chemistry* **2008,** 29, (5), 839-845.

[32] Brédas, J.-L.; Beljonne, D.; Coropceanu, V.; Cornil, J., Charge-transfer and energy-transfer processes in π-conjugated oligomers and polymers: a molecular picture. *Chemical Reviews* **2004,** 104, (11), 4971-5004.

[33] Coropceanu, V.; Cornil, J.; da Silva Filho, D. A.; Olivier, Y.; Silbey, R.; Brédas, J.-L., Charge Transport in Organic Semiconductors. *Chemical Reviews* **2007,** 107, (4), 926-952.

[34] Senthilkumar, K.; Grozema, F. C.; Bickelhaupt, F. M.; Siebbeles, L. D. A., Charge transport in columnar stacked triphenylenes: Effects of conformational fluctuations on charge transfer integrals and site energies. *The Journal of Chemical Physics* **2003,** 119, (18), 9809-9817.

[35] Giannozzi, P.; Baroni, S.; Bonini, N.; Calandra, M.; Car, R.; Cavazzoni, C.; Ceresoli, D.; Chiarotti, G. L.; Cococcioni, M.; Dabo, I.; Dal Corso, A.; de Gironcoli, S.; Fabris, S.; Fratesi, G.; Gebauer, R.; Gerstmann, U.; Gougoussis, C.; Kokalj, A.; Lazzeri, M.; Martin-Samos, L.; Marzari, N.; Mauri, F.; Mazzarello, R.; Paolini, S.; Pasquarello, A.; Paulatto, L.; Sbraccia, C.; Scandolo, S.; Sclauzero, G.; Seitsonen, A. P.; Smogunov, A.; Umari, P.; Wentzcovitch, R. M., QUANTUM ESPRESSO: a modular and open-source software project for quantum simulations of materials. *Journal of Physics: Condensed Matter* **2009,** 21, (39), 395502.

[36] Rappe, A. M.; Rabe, K. M.; Kaxiras, E.; Joannopoulos, J. D., Optimized pseudopotentials. *Physical Review B* **1990,** 41, (2), 1227-1230.

[37] Mounet, N.; Marzari, N., First-principles determination of the structural, vibrational and thermodynamic properties of diamond, graphite, and derivatives. *Physical Review B* **2005,** 71, (20), 205214.

[38] Pack, J. D.; Monkhorst, H. J., "Special points for Brillouin-zone integrations"---a reply. *Physical Review B* **1977,** 16, (4), 1748-1749.

[39] Humphrey, W.; Dalke, A.; Schulten, K., VMD: Visual molecular dynamics. *Journal of Molecular Graphics* **1996,** 14, (1), 33-38.

[40] Bao, Z.; Locklin, J., *Organic field-effect transistors*. CRC press: 2018.

[41] Lamport, Z. A.; Haneef, H. F.; Anand, S.; Waldrip, M.; Jurchescu, O. D., Tutorial: Organic field-effect transistors: Materials, structure and operation. *Journal of Applied Physics* **2018,** 124, (7), 071101.

[42] DiBenedetto, S. A.; Facchetti, A.; Ratner, M. A.; Marks, T. J., Molecular self-assembled monolayers and multilayers for organic and unconventional inorganic thin-film transistor applications. *Advanced Materials* **2009,** 21, (14-15), 1407-1433.

[43] Yoon, M.-H.; Kim, C.; Facchetti, A.; Marks, T. J., Gate Dielectric Chemical Structure−Organic Field-Effect Transistor Performance Correlations for Electron, Hole, and Ambipolar Organic Semiconductors. *Journal of the American Chemical Society* **2006,** 128, (39), 12851-12869.

[44] Laudise, R.; Kloc, C.; Simpkins, P.; Siegrist, T., Physical vapor growth of organic semiconductors. *Journal of crystal growth* **1998,** 187, (3-4), 449-454.

[45] DeLongchamp, D. M.; Vogel, B. M.; Jung, Y.; Gurau, M. C.; Richter, C. A.; Kirillov, O. A.; Obrzut, J.; Fischer, D. A.; Sambasivan, S.; Richter, L. J., Variations in semiconducting

polymer microstructure and hole mobility with spin-coating speed. *Chemistry of Materials* **2005,** 17, (23), 5610-5612.

[46] Chen, J.; Shao, M.; Xiao, K.; Rondinone, A. J.; Loo, Y.-L.; Kent, P. R.; Sumpter, B. G.; Li, D.; Keum, J. K.; Diemer, P. J., Solvent-type-dependent polymorphism and charge transport in a long fused-ring organic semiconductor. *Nanoscale* **2014,** 6, (1), 449-456.

[47] Boudinet, D.; Le Blevennec, G.; Serbutoviez, C.; Verilhac, J.-M.; Yan, H.; Horowitz, G., Contact resistance and threshold voltage extraction in n-channel organic thin film transistors on plastic substrates. *Journal of Applied Physics* **2009,** 105, (8), 084510.

[48] Tsao, H. N.; Müllen, K., Improving polymer transistor performance via morphology control. *Chemical Society Reviews* **2010,** 39, (7), 2372-2386.

[49] Eckstein, B. J.; Melkonyan, F. S.; Wang, G.; Wang, B.; Manley, E. F.; Fabiano, S.; Harbuzaru, A.; Ponce Ortiz, R.; Chen, L. X.; Facchetti, A.; Marks, T. J., Processable High Electron Mobility π-Copolymers via Mesoscale Backbone Conformational Ordering. *Advanced Functional Materials* **2021,** 31, (15), 2009359.

4 Results and discussion

Table of contents

Chapter I:

Role of peripheral substitution on the molecular order of disk-like semiconductors: the cases of triindoles and diazatruxenones

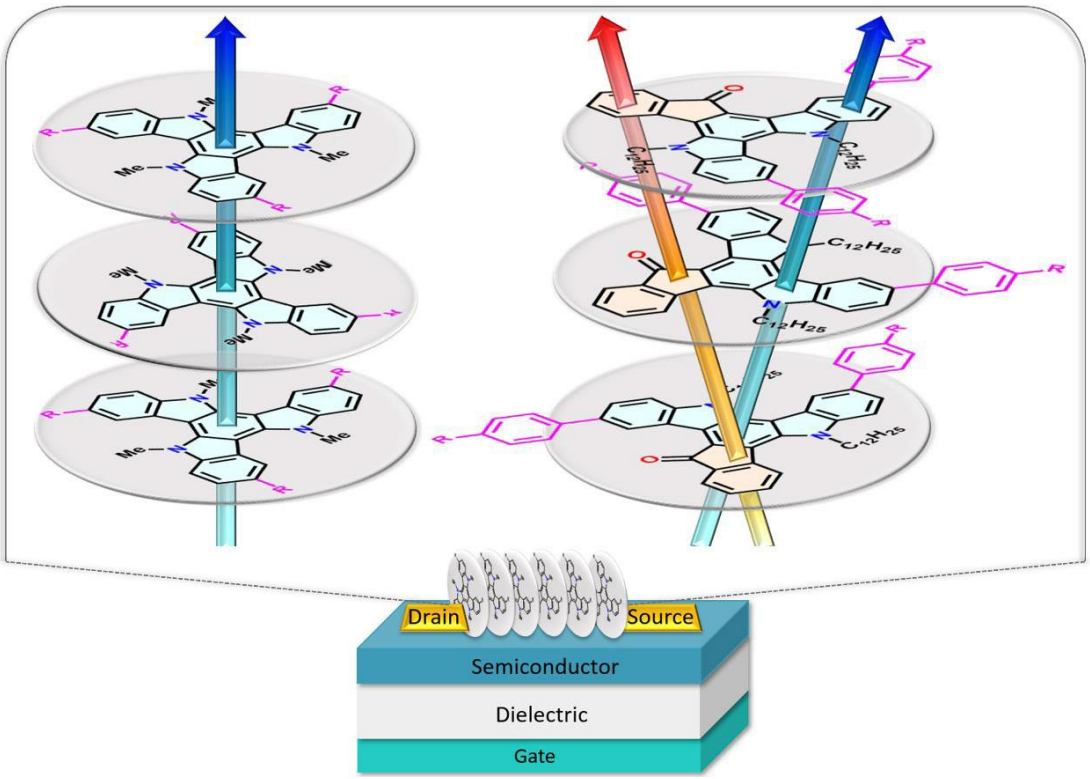

The most relevant results obtained in this study have given rise to publications 1 and 2 listed in Appendix 6.4:

1. **Gámez-Valenzuela, S**.; Benito-Hernández, A.; Echeverri, M.; Gutierrez-Puebla, E.; Ponce Ortiz, R.; Ruiz Delgado, M. C.; Gómez-Lor, B., Functionalized Crystalline N-Trimethyltriindoles: Counterintuitive Influence of Peripheral Substituents on Their Semiconducting Properties. Molecules **2022**, 27, (3), 1121-1135.

2. **Gámez-Valenzuela, S.**; Benito-Hernández, A.; Ponce Ortiz, P.; Golemme, A.; Termine, R.; Ruiz Delgado, M. C.; Gómez-Lor. B., Role of peripheral substitution on electronics and self-assembly of discotic semiconductors: the case of diazatruxenone. *In preparation.*

I.1. Introduction

In the search of efficient charge transport materials for flexible electronics, it is essential to achieve a favorable molecular spatial ordering in the semiconductor thin film since it involves charge transport as the main operation process, which is highly dependent on the electronic coupling between neighbouring units, and thus, on the intermolecular order.[1-3] In this line, disk-shaped molecules arouse a great interest as they have a strong tendency to self-assemble into column stacks when conveniently functionalized through the action of intermolecular interactions, offering a favorable pathway for charge carrier migration. Consequently, the correct design of this kind of semiconductors is usually a challenging task that requires a deep knowledge of the effects produced by the non-covalent interactions existing among the molecules, which are weak in nature and act cooperatively. Furthermore, electronic and spatial ordering changes can be induced by means of electronic factors. As example, peripheral substitution with electron donors in conjugated backbones such as methoxy groups, has been found to favor the self-assembly properties giving rise to highly ordered columnar stacks.[4]

In this context, we became interested in the electron-rich disk-like triindole system (*10,15-dihydro-5H-diindolo[3,2-a:30,20-c] carbazole*), which can be considered as three carbazole units that share the central fused aromatic ring (see Figure I.1a). This platform has been demonstrated to be a high performance self-assembling p-type organic semiconductor.[5, 6] Particularly, high hole mobilities above 2 $cm^2V^{-1}s^{-1}$ have been found on triindole-based materials as a result of the favorable synergy between their good intrinsic charge transport properties and its high tendency to self-assemble into one-dimensional superstructures providing an efficient path for charge transport.[7, 8]

Structurally related to triindole is truxenone. Using the same analogy as the one used to describe the triindole platform, truxenone can be considered as three fluorenone units sharing the central fused aromatic ring (see Figure I.1b), with the three ketone groups rendering this molecule electron deficiency. Although less investigated in the area of organic electronics than electron-rich triindole, owing to its poor solubility, truxenone has recently

attracted much interest in the development of electron-transport molecular semiconductors. In fact, electron mobility values above 1 $cm^2V^{-1}s^{-1}$ have been reported for truxenone-based semiconductors.[9-11]

On the other hand, to obtain organic materials able to transport holes and electrons charge carriers and thus, with ambipolar semiconducting properties, a widely employed strategy is the covalent linking of electron donor and electron acceptor moieties conformationally rigidified into fused π-conjugated molecular skeletons.[12-16] In this sense, it was recently theoretically demonstrated that the combination of the respective molecular characteristics of the electron rich triindole platform with those of the electron deficient truxenone one, in the diazatruxenone molecule (see Figure I.1c), would result in favorable ambipolar charge transport behavior.[17]

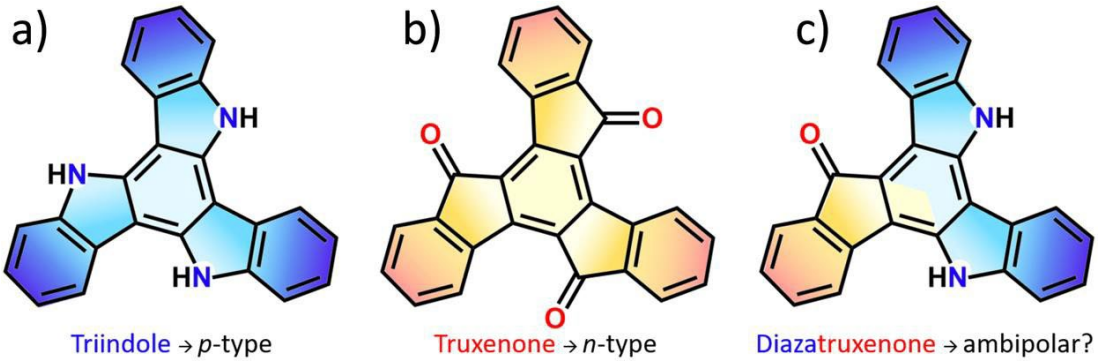

Figure I.1. Chemical structures of (a) triindole, (b) truxenone and (c) diazatruxenone molecules.

In this sense, we propose to study two families of triindole and diazatruxenone-based semiconductors functionalized at 3, 8 and 13 positions with different peripheral groups, such as methoxy electron donor groups or acetyl, nitrile and nitro electron-withdrawing groups (see Figure I.2). This work helps us to shed light on the influence that the electronic nature of the attached peripheral groups and the combination of electron rich and electron deficient segments in the same trigonal skeleton exert on the electronic, supramolecular and semiconducting properties of these disk-shaped materials.

To this purpose, we have performed a joint experimental and theoretical study that links UV-Vis spectroscopy, electrochemistry, Raman and OFETs characterization with DFT calculations performed at the B3LYP/6-31G** level of theory. M06-2X functional was also used and the results, which are comparable to those obtained at the B3LYP level, have been summarized in Appendix 6.2.1. This chapter is divided in two sections as a function of the nature of the platform (triindole or diazatruxenone).

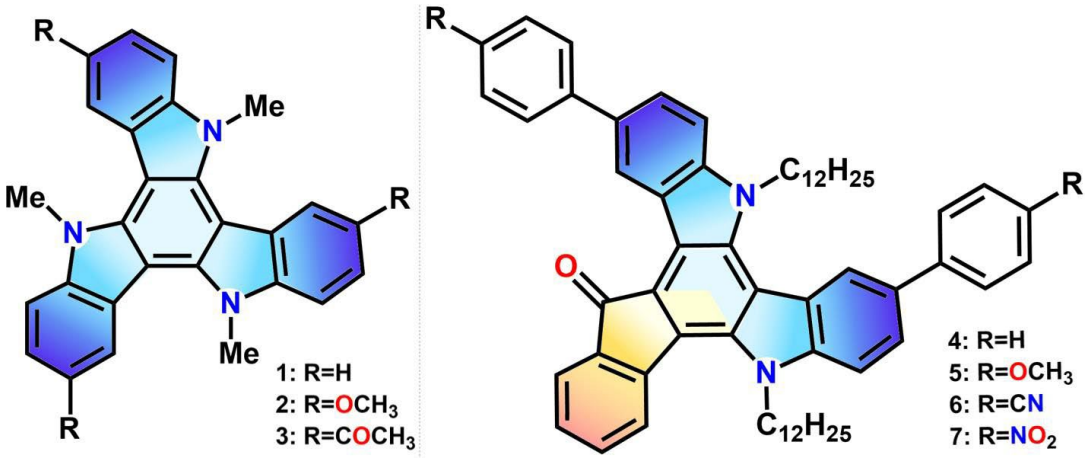

Figure I.2. Chemical structures of triindole **1**–**3** (left) and diazatruxenone-based systems **4**–**7** (right) studied in this chapter.

I.2. Triindole-based semiconductors

I.2.1. Structural features

Here we investigate how the electronic nature of the attached peripheral substituents influences the structural properties of the triindole platform, which can further determine their solid-state organization and semiconductor behavior. To this purpose, the optimized ground-state structure of the triindoles **1**-**3** were theoretically investigated. As seen in Figure I.3a, the DFT-calculated molecular geometries for the three systems result on similar twisted triindole platforms, with the three peripheral rings bending out of the plane of the central aromatic ring (with dihedral angles of 6°) and the methyl groups also slightly out of the molecular plane of the central ring. Interestingly, this fact indicates that functionalization on

the periphery exerts a slight impact on the structural conformation of the isolated triindole molecular structure. It is not surprising that the twisted triindole conformation is more energetically stable than the constrained planar conformation (around 6 Kcal/mol), since they contribute to relax the steric hindrance caused by the methyl groups and the outermost benzene rings.

a)

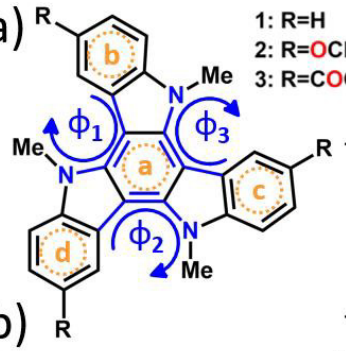

1: R=H
2: R=OCH_3
3: R=$COCH_3$

	Dihedral Angles / º			NICS(0) / ppm			
	ϕ_1	ϕ_2	ϕ_3	a	b	c	d
1	6	6	6	-9.2	-9.0	-8.9	-9.0
2	6	6	6	-8.8	-9.5	-9.6	-9.6
3	6	7	6	-9.4	-8.4	-8.4	-8.5

b)

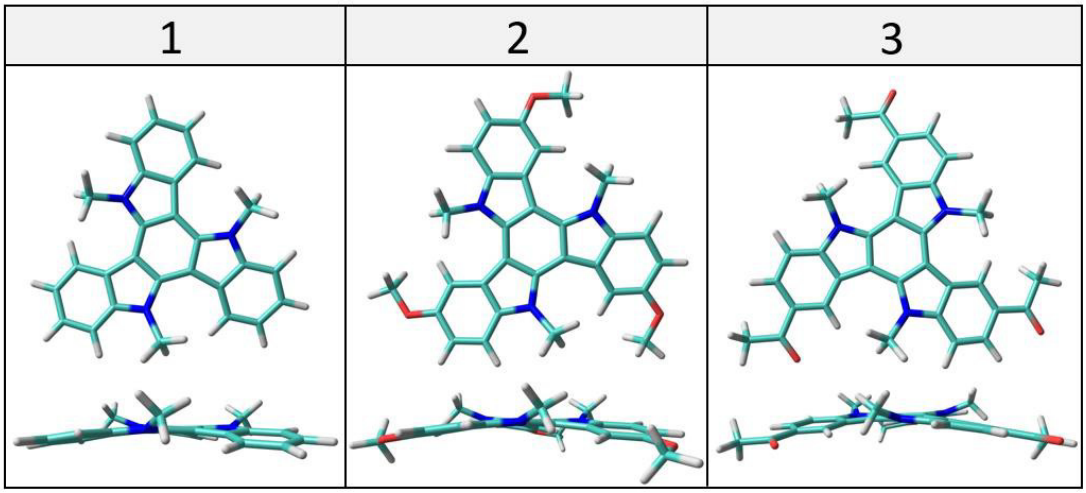

Figure I.3. (a) Chemical structures of compounds **1**-**3** together with the B3LYP/6-31G** calculated dihedral angles along the conjugated triindole platform and the NICS(0) values computed at B3LYP/6-311++G(2df,p)//B3LYP/6-31G** level. (b) Top and lateral views of the DFT-optimized structures for the triindoles **1**-**3** are also shown.

NICS parameter is a widely employed indicator of chemical aromaticity;[18, 19] being the more negative the NICS value, the more aromatic the system. In this sense, NICS values were calculated at the geometrical centers of all the phenyl rings (NICS(0)) by using the gauge-independent atomic orbital (GIAO) method.[18, 20] The calculations were performed at the

B3LYP/6-311++G(2df,p) level from the B3LYP/6-31G** optimized structures. On the basis of the calculated data, the aromaticity of these systems is affected by the electronic nature of the peripheral substituents. Compared to the reference **1** derivative, the insertion of electron-rich methoxy groups results in less (more) negative NICS(0) values of c.a. 0.5 ppm on the central (external) benzene ring, suggesting that the three-arm platform become more aromatic on the periphery and more quinoid on the innermost side at the same time. In contrast, the insertion of three electron-withdrawing acetyl groups in **3** results in less negative NICS(0) values (c.a. 0.5 ppm) on the external benzene rings. This can be explained in terms of the electron-withdrawing character of the acetyl groups, which decreases the aromaticity of the structure in consonance with better electronic delocalization.

I.2.2. Electronic properties

The electronic properties of these triindole-based semiconductors were investigated by using Ultraviolet-Visible (UV-Vis) absorption spectroscopy and cyclic voltammetry (CV) and rationalized with the help of DFT and time-dependent DFT (TD-DFT) calculations performed at B3LYP/6-31G** level of theory. Figure I.4a compares the absorption spectra of the three compounds in CH_2Cl_2 solution at a concentration of $5x10^{-6}$ M. Independently of the electronic nature of the substituents, a bathochromic shift on the maximum absorption band can be observed upon external functionalization of the triindole platform at 3, 8, and 13 positions when compared with the non-substituted derivative **1** (*i.e.* maximum absorption band appears at 317 nm in **1**, 332 nm in **2** and 339 nm in **3**).

Furthermore, the optical band gap estimated from the tangent to the low energy edge of the absorption band is also progressively redshifted going from the non-peripherally substituted triindole **1** (3.36 eV) to the derivatives substituted with electron donor methoxy groups (3.09 eV) and electron-withdrawing acetyl groups (2.66 eV), with the latter showing the lowest optical gap within the series.

TD-DFT vertical excitation energies calculated for triindoles **1**-**3** nicely reproduce the experimental data, predicting the red shifting of the lowest energy band upon

functionalization as well as the presence of several electronic transitions around 300 nm with a π-π* nature.[21] An inspection of the main vertical excited-state transitions reveals that in all the cases, the maximum absorption band results from the overlap of the $S_0 \rightarrow S_3$ and $S_0 \rightarrow S_4$ electronic transitions, which are assigned to different combinations of HOMO→LUMO, HOMO-1→LUMO, HOMO-1→LUMO+1 and HOMO→LUMO+1 one-electron excitations. Note that in these systems the $S_0 \rightarrow S_1$ electronic transition is forbidden by symmetry with respect to dipole−dipole selection rules, although distortions from the C_3 geometry in solution can contribute to the activation of these electronic transitions.[22]

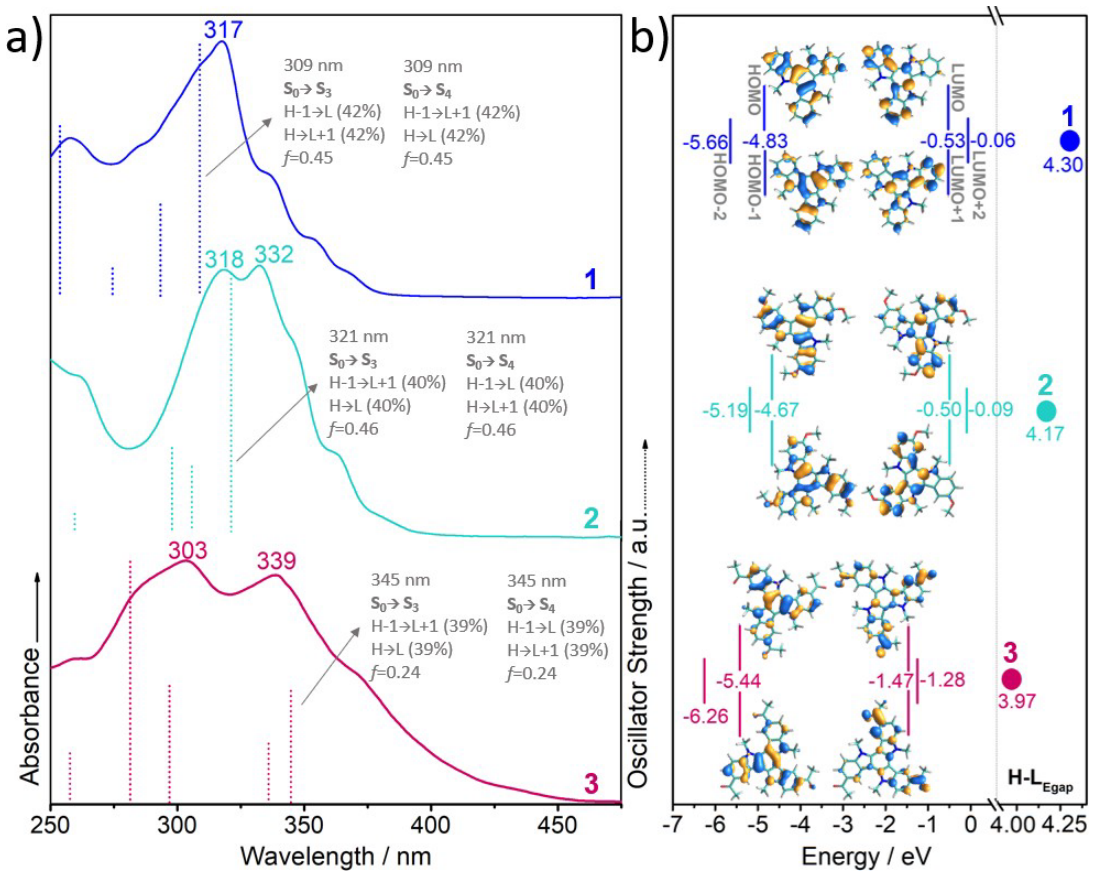

Figure I.4. (a) Normalized experimental UV-Vis absorption spectra of triindoles **1**-**3** in CH_2Cl_2 solution at c = $5x10^{-6}$ M. The main vertical excited-state transitions (shown as dotted bars) calculated at the TD-DFT//B3LYP/6-31G** level are also shown. (b) DFT-calculated (B3LYP/6-31G**) frontier molecular orbital energies for the triindoles under study. The topologies of HOMO, HOMO-1, LUMO and LUMO+1 are also shown.

On the basis of the calculated frontier molecular orbitals (FMO) diagram shown in Figure I.4b, the HOMO/HOMO-1 and LUMO/LUMO+1 energy levels are energetically degenerated as expected from the C_3-symmetry of these systems.[22] The inspection of the FMO topologies reveals that both HOMO and LUMO are delocalized over the entire π-molecular frameworks. Interestingly, the insertion of the methoxy groups in **2** causes the extension of the HOMO over these peripheral donor groups, producing a destabilization of the HOMO while the LUMO level is barely affected. Contrary, the attachment of acetyl groups in **3** produces the extension of LUMO over these electron-withdrawing groups, and results in a moderate HOMO and LUMO stabilization with this effect being more pronounced for the latter. Thus, the peripheral functionalization of the triindole scaffold leads to a more extended π-conjugation, decreasing the HOMO–LUMO gap in the following order: **1** (4.30 eV) > **2** (4.17 eV) > **3** (3.97 eV), in good agreement with the experimental reduction of the optical gaps. The observed difference in the FMO wavefunction upon peripheral substitution might influence the electronic coupling within the stacks as will be discussed below.

Since feasible hole/electron injection from electrodes is an indispensable prerequisite for the design of ambipolar semiconductors, charge injection was evaluated by analyzing the FMOs energy levels obtained from CV measurements. As shown in Figure I.5a, the three compounds under study can be easily and reversibly oxidized. As we expected, functionalization with methoxy electron-donor groups produces a shifting of the first oxidation potentials towards less positive values because of the increment in the electronic density of the π-system. On the contrary, functionalization with acetyl electron-withdrawing groups produces a shifting of the first oxidation potentials towards more positive values because of the vanishing in the electronic density. In this regard, we have estimated the HOMO level for **1**-**3** compounds through the first oxidation potentials referenced to the ferrocene/ferrocenium (Fc/Fc^+) redox couple, in comparison to the formal potential of Fc/Fc^+ with respect to zero vacuum level (4.8 eV) according to the equation:

$$E_{HOMO} = -[(E^{ox}_{onse} - E_{1/2}{}^{Fc/Fc+}) + 4.8\ eV].$$

The HOMO-LUMO gap were estimated by the absorption edge of the electronic spectra, allowing us to estimate the LUMO energy level as the difference between this value and the value previously determined for the HOMO level (see Figure I.5b).

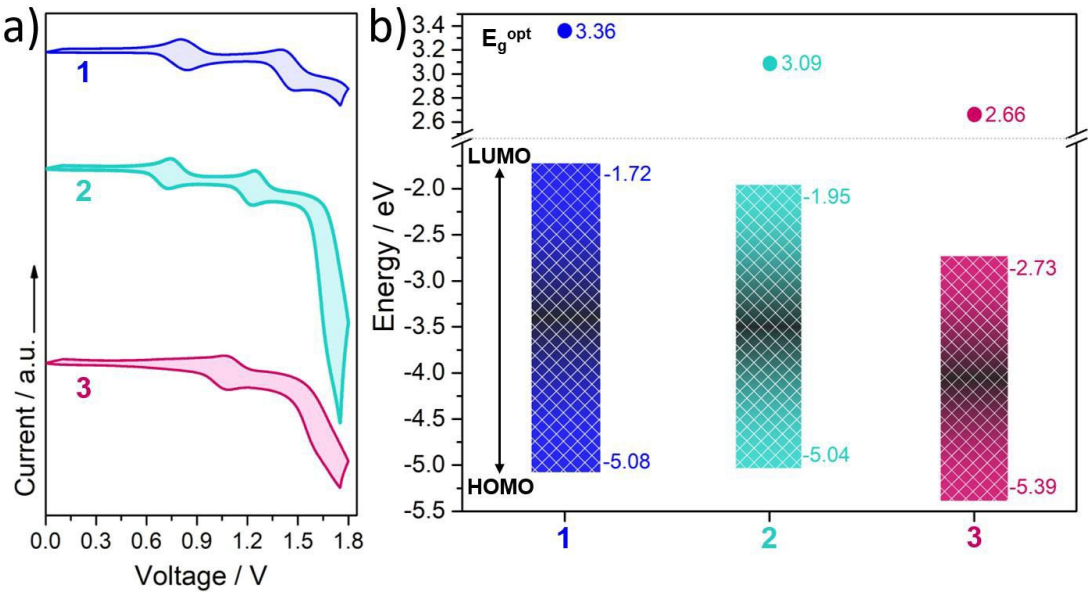

Figure I.5. (a) Cyclic voltammograms of triindoles **1**-**3** (c=1x10^{-5} M) recorded at a scan rate of 100 mV·s^{-1} in CH_2Cl_2/0.1 M Bu_4NPF_6 as electrolyte, using a Pt working electrode, an Ag/AgCl reference electrode and a Pt wire auxiliary electrode. (b) Experimentally determined HOMO-LUMO energy levels. The optical HOMO-LUMO$_{gap}$ values (E_g^{opt}) are also shown.

Compared to the unsubstituted triindole **1**, the insertion of methoxy groups in **2** barely affects the frontier energy levels, whereas the attachment of acetyl groups in **3** moderately stabilizes both HOMO and LUMO orbitals with the latter in a more pronounced extension (0.31 eV for HOMO vs 1.01 eV for LUMO). These results are in excellent agreement with the theoretically predicted FMO modulation upon peripheral functionalization. It is important to highlight that in all the cases, the HOMO energy matches very well with the work function of gold (ϕ_{Au}=5.1 eV),[23] which makes them potential candidates as p-type semiconductors.

I.2.3. Vibrational properties

We now make use of Raman spectroscopy to better understand the effect that the different electronic nature of the peripheral substituents plays on the effective π-conjugation of the triindole scaffold. It is well known that Raman spectroscopy renders valuable information about the electronic coupling between covalently connected conjugated moieties and about the effective π-conjugation length in semiconductors.[24-27] As seen in Figure I.6a, the Raman bands collected in the 1500-1600 cm^{-1} region, which are related with the C=C/C−C stretching modes, are selectively enhanced in the spectra as a consequence of the existence of an effective electron–phonon coupling.[28]

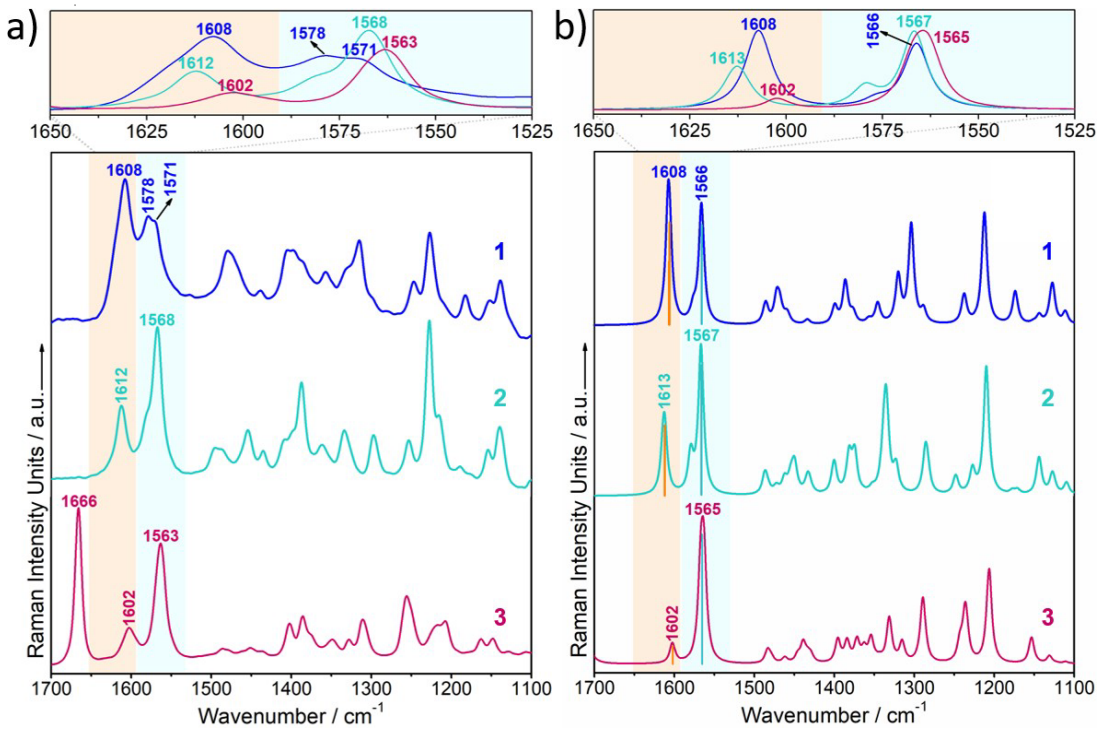

Figure I.6. (a) Solid state FT-Raman (λ_{exc}=1064 nm) and (b) simulated Raman spectra (B3LYP/6-31G** level) for triindoles **1**-**3**. The vibrational frequency values associated with the discussed C=C/C−C Raman features are also shown. An adjustment of the theoretical force fields where the frequencies were scaled down by a factor of 0.968 to disentangle experimental misassignments was used, as recommended by Scott and Random.[29]

Therefore, we pay attention to this spectral region and specifically, to the doublet localized at ~1605 cm^{-1} and ~1570 cm^{-1}. Importantly, the good agreement found between the experimental (Figure I.6a) and theoretical (Figure I.6b) Raman spectra gives support to the reliability of the structural information derived from this discussion as well as our Raman bands assignment (Figure I.7).

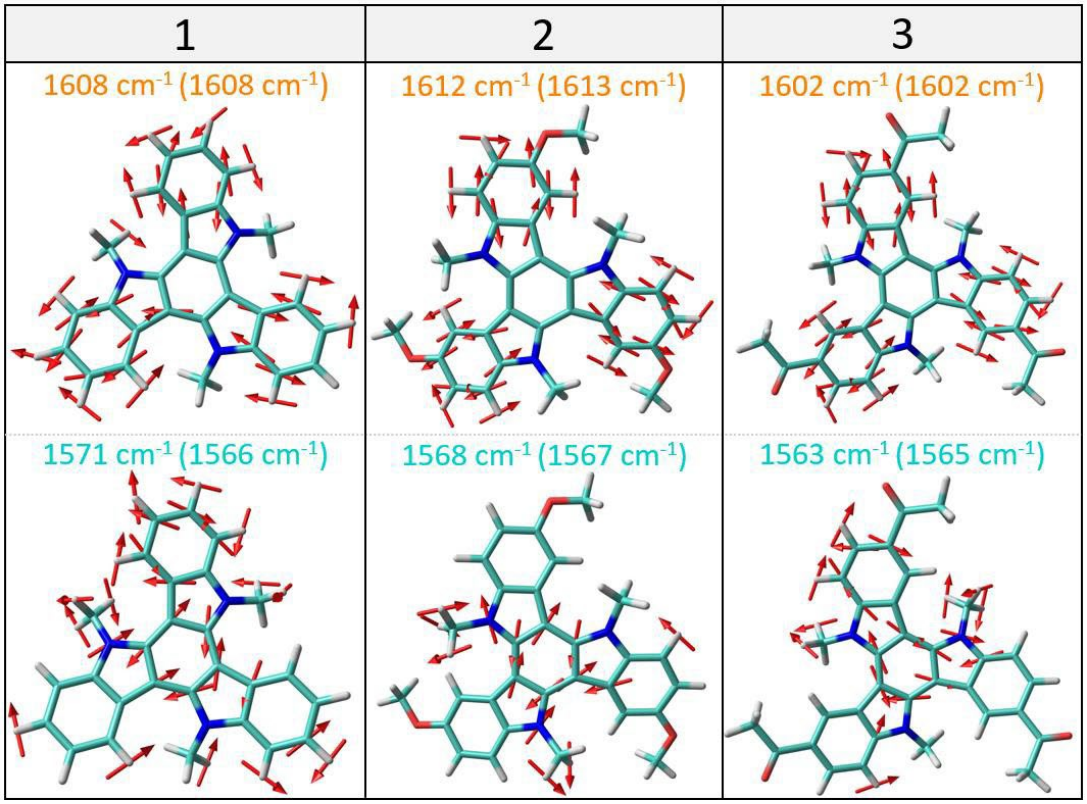

Figure I.7. B3LYP/6-31G** vibrational eigenvectors associated with the most outstanding C=C/C–C Raman features for the triindole-based compounds under study. The experimental and theoretical (in parentheses) wavenumbers are also shown.

In this sense, the Raman band localized at ~1605 cm^{-1} arises from a CC stretching mode (*i.e.* mode 8a of benzene)[30] mostly involving the external benzene rings, whereas the band localized at ~1570 cm^{-1} entailing the same CC vibration but localized on the innermost benzene rings (see Figure I.7). Please, note that in the case of triindole **3**, the Raman band recorded at 1666 cm^{-1} emerges from the stretching of the C=O groups.

The band at 1605 cm^{-1}, involving the external benzene rings, is very sensitive to the electronic nature of the peripheral substituent. This become evident by analyzing the shift towards higher or lower frequencies upon trimethoxy or triacetyl functionalization, which is ascribed to the electron-donor and electron-withdrawing character of these peripheral substituents, respectively. On the other hand, the Raman band corresponding to the CC stretching vibration of the innermost benzene rings, recorded at 1571 cm^{-1} in **1**, progressively downshifts to 1568 and 1563 cm^{-1} in **2** and **3** compounds, respectively. This trend reflects the better π-electronic delocalization upon functionalization, being more relevant in the case of the triacetyl functionalized triindole **3,** in agreement with its lowest HOMO-LUMO gap. The more efficient π-conjugation in **3** is also corroborated by an increase in the intensity of these CC stretching bands with respect to those appearing at ~1200–1300 cm^{-1} arising from non-conjugated CH_2 bending vibrations, due to the existence of an effective electron–phonon coupling in this semiconductor.[28, 31]

I.2.4. Electrical characterization

Considering the easy one-electron reversible oxidations, relative low-lying HOMO levels and good π-electron delocalization of these derivatives, OFETs were fabricated with the vacuum-deposited active layers in a standard bottom gate-top contact (BG-TC) architecture to gather information on how the electronic nature of the peripheral substituent influences the electrical performance of the final device.

As shown in Figure I.8, all devices exhibited typical unipolar p-channel characteristics with good output and transfer curves measured at ambient conditions. The main p-channel transport parameters, including hole charge carrier mobilities (μ_h), intensities ratios (I_{on}/I_{off}) and threshold voltages (V_T), were extracted from the saturated region of the transfer curves and summarized in Table I.1. It is important to highlight that although only the OFET electrical data for the best-performing devices are shown, in each case, the device performance was fully optimized by systematically investigating the effect of the annealing

conditions and substrate treatments on the charge transport characteristics of these semiconductors (see Appendix 6.3.1).

The optimization of the device fabrication steps suggests that both thermal annealing temperatures and substrate treatments play a relevant role in the resultant mobilities of the devices. It was found that the performance of OFETs fabricated on OTS-treated substrates of **1** and **2** is up to three orders of magnitude higher than those of HMDS or nontreated substrates. On the other hand, after thermal annealing at 60°C and 90°C, the mobilities for the OTS-treated substrates of **1** and **2** increased dramatically by three and two orders of magnitude, respectively. Curiously, the performance of OFETs based in triindole **3** is relatively insensitive to thermal annealing or substrate treatments.

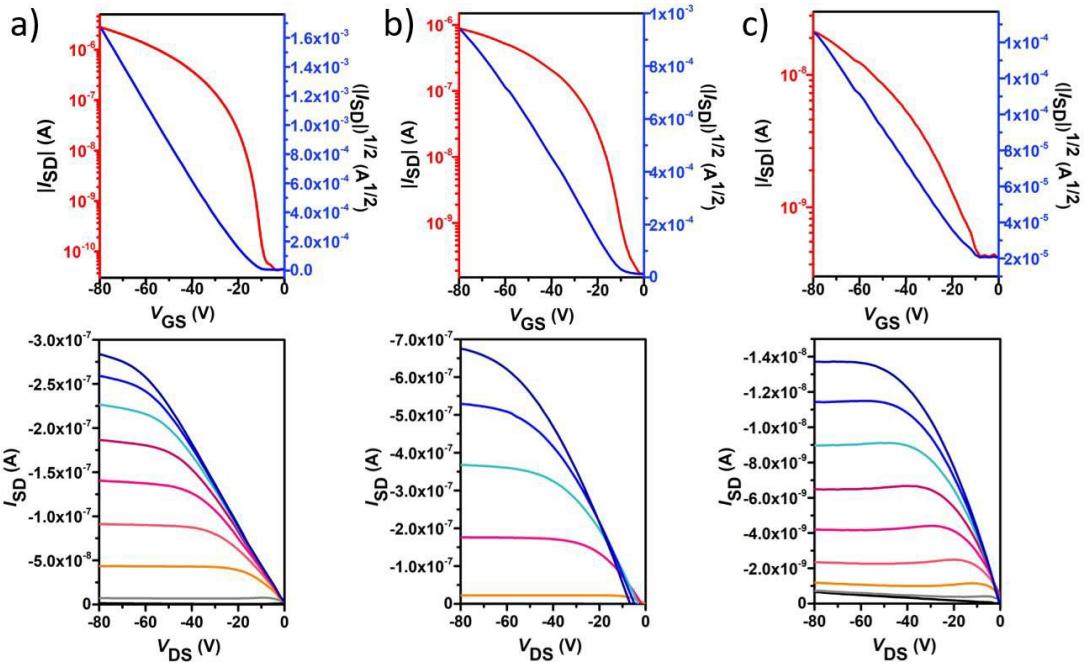

Figure I.8. OFET transfer (top) and output (bottom) curves of triindoles **1** (a), **2** (b) and **3** (c) prepared under the optimal device fabrication conditions and measured at ambient conditions. The transfer curves were measured at a constant source-drain voltage of -80 V, whereas the output curves were measured at gate voltages varying from 20 to -80 V at intervals of 10 V.

Table I.1. OFET electrical data for vapor deposited thin films of triindoles **1**–**3** prepared under the optimal device fabrication conditions and measured at ambient conditions. Average and the best (in parenthesis) values are shown. The average values were obtained from at least 6 representative devices for each material.

Compound	Deposition conditions	μ_h ($cm^2 V^{-1} s^{-1}$)	V_T(V)	I_{ON}/I_{OFF}
1	OTS, 60°C	2.2×10^{-2} (2.8×10^{-2})	-13 (-17)	1×10^7 (3×10^7)
2	OTS, 90°C	1.4×10^{-3} (1.6×10^{-3})	-4 (-8)	6×10^3 (1×10^4)
3	OTS, 120°C	3.1×10^{-5} (4.5×10^{-5})	-17 (-21)	2×10^2 (3×10^2)

In view of the results, the field effect mobilities of the studied semiconductors are modest, with the maximum p-type mobility of 2×10^{-2} $cm^2V^{-1}s^{-1}$ for the unsubstituted triindole **1** in accordance with previously reported data.[27] Quite high on/off ratios of $\sim10^7$ and low threshold voltages of −13 V were measured for this semiconductor, which is considered to be important for applications of ambipolar OFETs in complementary logic circuits.[32] Nevertheless, the introduction of peripheral methoxy donor groups in triindole **2** impairs the electrical properties, reducing by an order of magnitude the p-type mobility (1×10^{-3} $cm^2V^{-1}s^{-1}$) and by four orders of magnitude the on/off ratios ($\sim6\times10^3$) with respect to the parent triindole **1**. Comparable threshold voltages (−4 V) can be observed. Interestingly, the substitution with electron-withdrawing acetyl groups in triindole **3** maintain the p-type polarity, although the transistor parameters are strongly reduced in comparison with triindole **1** with three orders of magnitude lower field effect mobilities (3×10^{-5} $cm^2V^{-1}s^{-1}$) and five orders of magnitude lower on/off current ratios ($\sim2\times10^2$).

Curiously, opposite trends can be found comparing the electrical performance data of OFET devices and the π-electronic delocalization degree of **1**-**3** materials. In fact, the best OFET electrical data were measured for triindole **1**, despite its less conjugated skeleton as evidenced using UV-Vis absorption and Raman spectroscopies, CV and DFT calculations. This highlights the importance of a favorable supramolecular arrangement for achieving efficient

charge transport. Thus, the peripheral groups not only affect the electronic properties but also significantly influences crystal packing as we will demonstrate in the following section.

I.2.5. Self-assembly properties

As discussed in a previous section, the functionalization on the periphery exerts a slight impact on the energetics of the isolated molecular structures. However, since the influence that molecular neighbors play on each other can exert notable changes on the final packing, the analysis of their crystal structures is crucial. In this context, although X-ray data of compounds **1** and **2** reveals that both systems pack into the crystal forming very highly ordered columnar structures, in which the molecules pack face-to-face in an alternate arrangement (each molecular unit rotated by 60° with respect to its next neighbors in the stacks and with the central aromatic rings perfectly superimposed) forming columns that grow up along one-direction, remarkable differences can be found on their molecular structures. In particular, while compound **1** maintains the slightly twisted conformation of the triindole core on the crystal packing, functionalization with electron donor methoxy groups in **2** significantly planarize the molecule on the solid state (see Figure I.9).

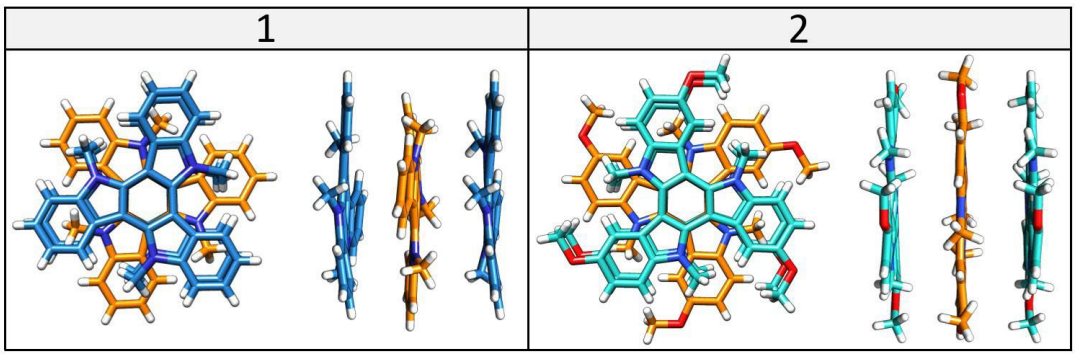

Figure I.9. Top and lateral views of the molecular packing for triindoles **1** and **2** as determined by X-ray diffraction analysis.

Unfortunately, it was not possible to obtain single crystals of the acetylated derivative **3**. Nevertheless, the position of the maxima peaks observed in its powder diffractogram

matches very well with the X-ray diffractogram obtained from single crystal data of triindole **2**, pointing to a similar structure and packing pattern.[21]

In order to find an explanation to the opposite trends observed on the previous section and rationalize the effect of the peripheral substitution on the charge transport properties of triindoles **1**-**3**, we have theoretically predicted the key molecular parameters impacting the charge mobility, such as intramolecular reorganization energies for holes (λ_h) and transfer integrals associated with hole transfer (t_h). In this context, the reorganization energy reflects the geometric changes needed to accommodate a positive charge (the smaller λ_h the larger the expected charge mobility) giving rise to the so-called local electron-phonon coupling.[33] It is important to highlight that here, we focus on the intramolecular contribution to λ_h as the polarization contribution is expected to be significantly smaller,[34] being directly calculated at the B3LYP/6-31G** level from the relevant points on the potential energy surfaces by using previously reported standard procedures.[35] On the other hand, t_h characterizes the electronic coupling for hole transfer between neighboring units, which, in turn, is determined by the supramolecular order.

A modest increase in the λ_h values is predicted upon peripheral substitution with λ_h values of 231 meV for **1**, 257 meV for **2** and 272 meV for **3**. Interestingly, DFT calculations predict a symmetric geometrical relaxation upon oxidation, where the accommodation of the positive charge take place along the three arms that the triindole platform has.

Prior to compute the transfer integrals for hole transport, we wanted to better understand the interplay between intramolecular and intermolecular interactions. With this goal in mind, we have performed DFT calculations including dispersion corrections [36] for a supramolecular complex formed by three molecules; in the case of triindole **1**, the supramolecular complex was extracted from its published crystalline structure,[6] where the molecules pack face-to-face in an alternate arrangement (each molecular unit rotated by 60° with respect to its next neighbors in the stacks and with the central aromatic rings perfectly superimposed) forming columns that grow up along one-direction. The same model was also used for **2** upon insertion of the peripheral methoxy groups. Triindole **3** has

been excluded of this study due to have a similar structure and packing pattern to that of triindole **2**.

As seen in Figure I.10, the resultant optimized geometries reveal that the non-peripherally substituted triindole **1** maintains the slightly twisted conformation of the triindole core, in line with the most favorable molecular structure predicted for the isolated molecules. Conversely, functionalization with three methoxy groups in **2** significantly planarize the molecule with the methyl and methoxy groups accommodated within the plane of the molecules and shorter π–π distances between them (see the molecules inside the box in Figure I.10); this points to the influence that molecular neighbors play in leading a planar conformation in the solid state overcoming the tendency to twist.[37]

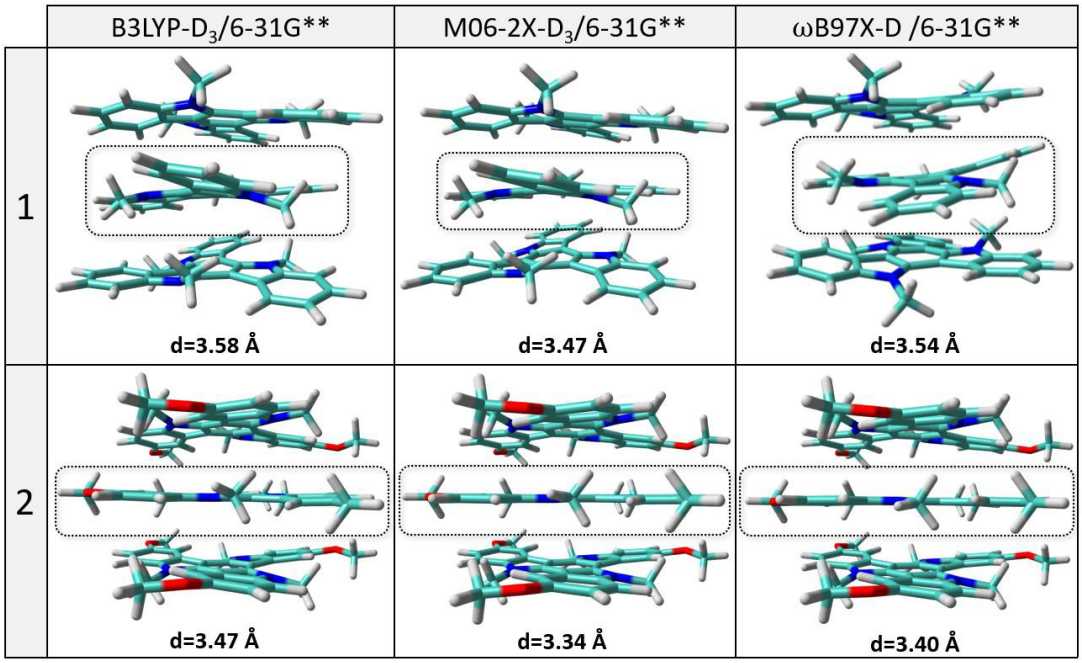

Figure I.10. DFT-optimized supramolecular complexes of **1** and **2** computed at different levels of theory. The average centroid–centroid distance of the central aromatic rings between adjacent molecules is also shown.

Interestingly, this effect was not observed for the same calculations performed without including an explicit correction for dispersion, highlighting the role played by weak,

noncovalent interactions in the stabilization of the planar structures upon methoxy substitution. In this sense, we can see that each methyl group is involved in CH···π interactions with the aromatic rings that lie above and below it, which has been found to stabilize similar alternated stacking in N-dodecyltriindole derivatives both in solution [5] and in the solid state.[4]

Based on the previous results, transfer integrals for cofacial dimers of **1** and **2** built from the X-ray determined structures at an intermolecular distance of 3.51 Å, were calculated at the B3LYP/6-31G** level by using the approach described by Valeev et al.[38] Since HOMO and HOMO-1 orbital on isolated molecules are degenerated in energy, the t_h values were calculated as: $[(t_{HOMO.HOMO}^2 + t_{HOMO-1.HOMO-1}^2 + t_{HOMO-1.HOMO}^2 + t_{HOMO.HOMO-1}^2)/4]^{1/2}$. Smaller t_h values were predicted for dimers of **2** (29 meV) when compared to those found for dimers of **1** (93 meV). This can be ascribed to less efficient HOMO and HOMO-1 wavefunctions overlap in **2**, despite their more planar backbones and smaller stacking distances (see Figure I.11).

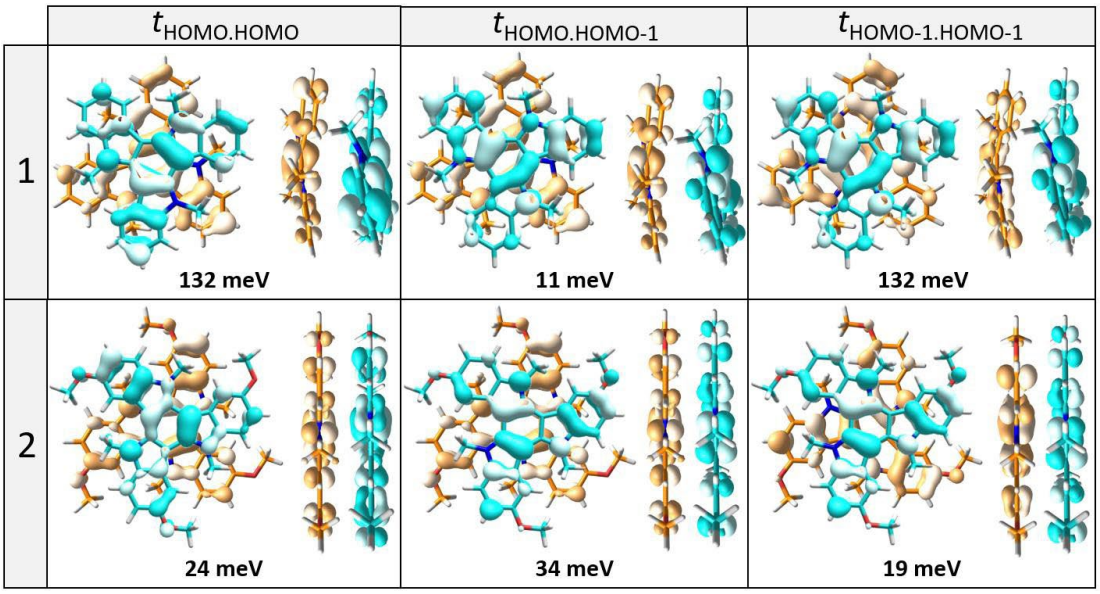

Figure I.11. Top and lateral views of the HOMO-HOMO, HOMO-HOMO-1 and HOMO-1-HOMO-1 orbital overlaps for cofacial dimers of **1** and **2**. The DFT-estimated hole transfer integrals (in meV) values are also shown.

Note that in an alternate arrangement where each molecular unit is rotated by 60°, only the central aromatic rings are perfectly superimposed, thus, the HOMO and HOMO-1 wavefunctions extension over the peripheral methoxy groups might result in less favorable wavefunctions overlap in the central core of the staggered triindole platforms, resulting in smaller t_h values.

Thus, our data reveal smaller t_h and higher λ_h values for **2** when compared to **1**, which might result in less efficient charge-transport properties in the former. This fact is in consonance with the better device performance exhibited in OFETs based on **1** than on **2** (hole mobilities of ca. 0.022 vs. 0.0014 $cm^2V^{-1}s^{-1}$ for **1** and **2** were measured, respectively). On the other hand, the lowest mobility obtained in compound **3** might be probably related to a combination of intrinsic molecular factors and less ordered columnar packing in agreement with the poor crystalline organization experimentally observed.

I.3. Diazatruxenone-based materials

I.3.1. Structural features

We now focus on the disk-shaped diazatruxenone-based molecules (named as **4**-**7** systems in Figure I.12a). First, we become interested in analysing the impact of the electronic nature of the attached peripheral substituents on the structural properties at the intramolecular level. Figure I.12 displays the top and lateral views of the DFT-optimized ground state structures (B3LYP/6-31G** level) in addition to the optimized dihedral angles values along the conjugated backbone for the whole series of systems under study.

As we can observe, the attached peripheral phenyl rings are largely distorted by ~38º from the rest of the π-conjugated backbone. On the other hand, a dual behaviour in the internal disorder of the diazatruxenone core is found. Considering the core as two carbazole and one fluorenone moieties that share a fused aromatic ring a dual effect can be observed: while the carbazole units result in a moderate distortion (ϕ_2 and ϕ_3 around 6-10º) of the platform due to the steric hindrance caused by the methyl groups and the outermost benzene rings, the fluorenone unit is totally coplanar (ϕ_1 ~1-0º). This is a consequence of the favourable intramolecular interaction between the ketone group and the adjacent hydrogen atom of the outermost benzene ring. In addition, as previously observed on the studied triindole semiconductors, similar geometrical distortions are predicted by attaching peripheral groups of different electronic nature on the diazatruxenone molecular structure, indicating that functionalization on the periphery exerts a slight impact at the molecular structural level.

Interestingly, the aromaticity of diazatruxenone **4** is barely influenced by attaching peripheral groups, but it is significantly affected when compared to that of the unsubstituted triindole homologous. In particular, the replacement of an electron donor carbazole unit by an electron acceptor fluorenone moiety on the diazatruxenone platform leads to less negative NICS(0) values, being this effect especially important in the outermost benzene ring of the fluorenone moiety (with NICS(0) values of around -3 ppm in compound **4** compared

to values of around -9 ppm for the unsubstituted triindole **1**, as previously discussed in Figure I.3). This can be explained in terms of the electron-withdrawing character of the ketone groups, which decreases the aromaticity of the structure in consonance with better electronic delocalization between the acceptor moiety and the two electron donor carbazole moieties.

a)

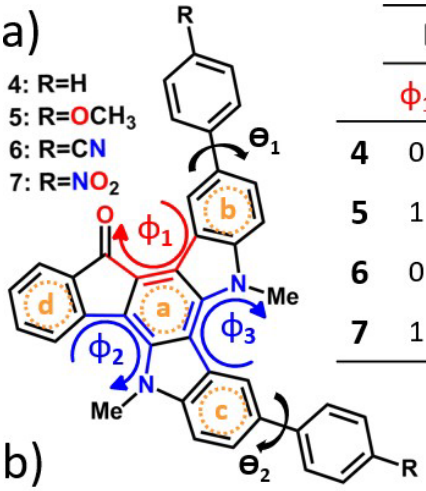

	Dihedral Angles / º					NICS(0) / ppm			
	ϕ_1	ϕ_2	ϕ_3	Θ_1	Θ_2	a	b	c	d
4	0	9	6	36	39	-7.5	-8.1	-7.9	-3.1
5	1	9	6	36	39	-7.5	-7.8	-8.1	-3.1
6	0	9	6	34	38	-7.6	-8.0	-7.9	-3.2
7	1	10	6	34	37	-7.6	-7.8	-8.0	-3.2

b)

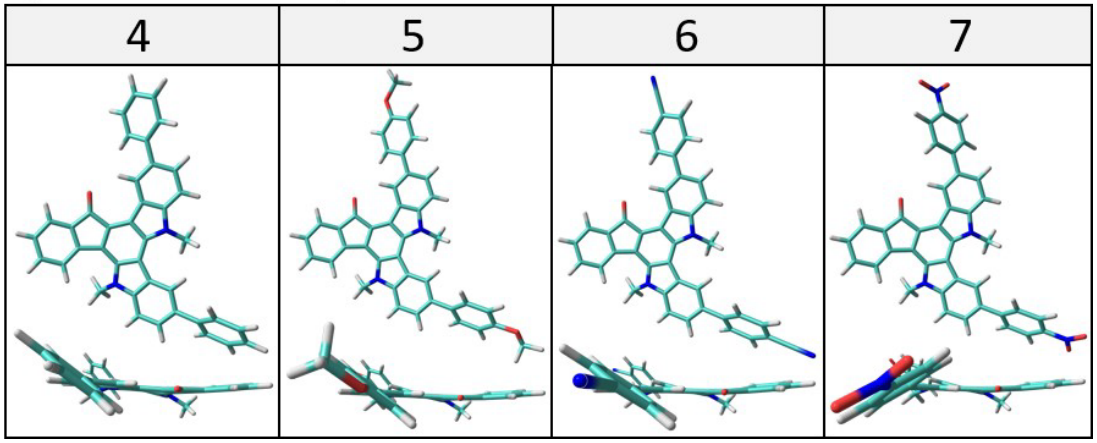

Figure I.12. (a) Chemical structures of compounds **4**-**7** together with the B3LYP/6-31G** calculated dihedral angles along the conjugated diazatruxenone platform and the NICS(0) values computed at B3LYP/6-311++G(2df,p)//B3LYP/6-31G** level. (b) Top and lateral views of the DFT-optimized structures for the diazatruxenones **4**-**7** are also shown.

I.3.2. Electronic properties

The UV–vis absorption spectra of all diazatruxenones in CH_2Cl_2 solution at a concentration of 10^{-5} M (Figure I.13a) exhibit two broad low energy bands localized around 470 and 560 nm which are barely influenced by the different electronic nature of the peripheral groups. In fact, similar optical gap values (1.91 eV) for all the compounds are obtained from the absorption edge of their electronic spectra.

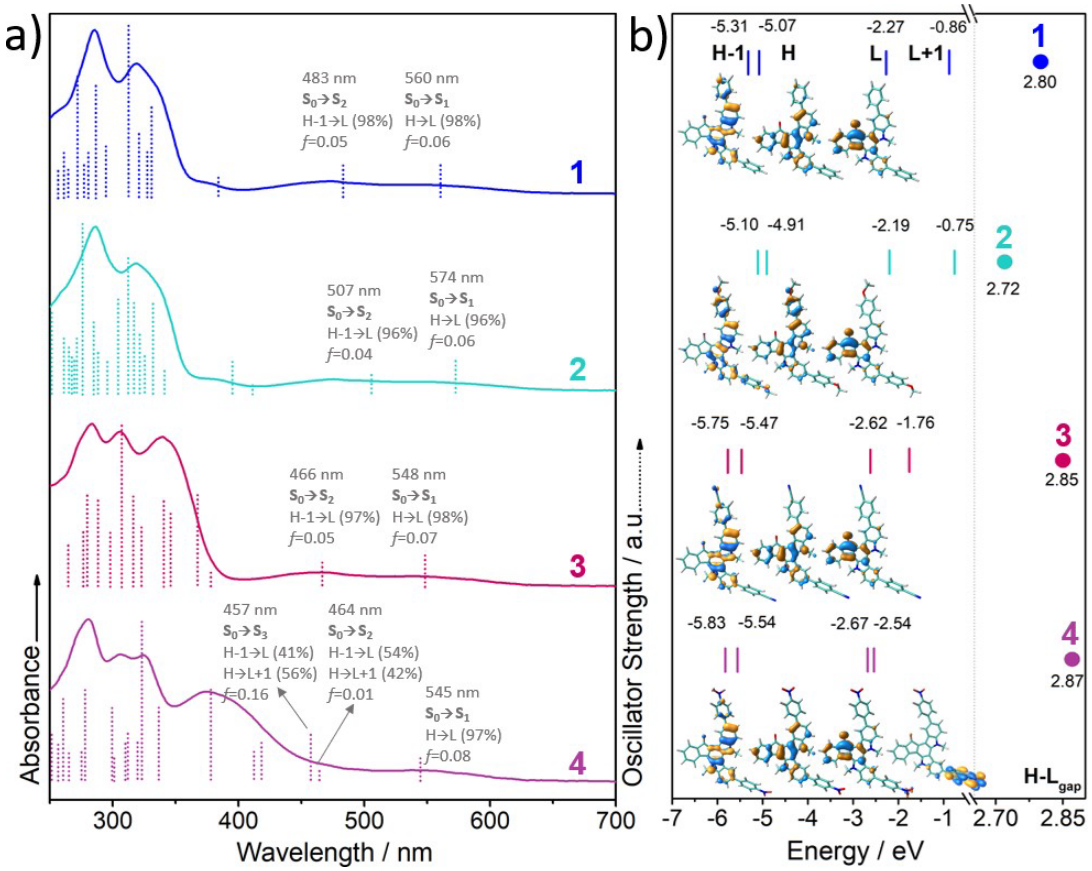

Figure I.13. (a) Normalized experimental UV-Vis absorption spectra of diazatruxenone-based semiconductors in CH_2Cl_2 solution at c = 10^{-5} M. The main vertical excited-state transitions (dot bars) calculated at the TD-DFT//B3LYP/6-31G** level are also shown. (b) DFT-calculated (B3LYP/6-31G**) molecular orbital energies for the diazatruxenones under study. The topologies for the molecular orbitals involved in the main electronic transitions are also shown.

In good agreement with the experimental data, TD-DFT calculations performed at B3LYP/6-31G** level of theory also predict the existence of two electronic transitions ($S_0 \rightarrow S_1$ and $S_0 \rightarrow S_2$) at low energies (c.a. 550 and 480 nm), which are assigned to HOMO→LUMO and HOMO-1→LUMO one electron excitations, respectively. Interestingly, due to the C_3 symmetry breaking caused by the replacement of a carbazole unit by a fluorenone moiety, an energy gap between HOMO/HOMO−1 and LUMO/LUMO+1 energy levels emerges (Figure I.13b), as previously pointed out in our first study based on asymmetric triindoles.[22] In this sense, HOMO and HOMO-1 are mainly located on the electron rich carbazole units (with HOMO orbital partially delocalized over the fluorenone unit), while the LUMO placed mainly in the electron deficient fluorenone moiety. Therefore, these low-energy electronic transitions display an intramolecular charge transfer (ICT) character.

It is important to mention that a negligible impact of the electronic nature of the different peripheral groups on the frontier orbital topologies was found, corroborating the insignificant participation of the peripheral groups on the electron density transfer and thus, explaining the similar wavelengths of the low energies absorption bands experimentally observed for all compounds. This effect could be a direct consequence of the presence of a twisted aromatic phenyl ring between the π-conjugated core and the peripheral substituents, which somewhat limits its participation in the intramolecular electron density transfer process.

On the other hand, these bands are accompanied by several high energy electronic transitions in the 250-350 nm spectral region which arise from electronic excitations between molecular orbitals either delocalized over the whole π-conjugated molecule or placed on specific segments, thus revealing a π to π* character.

As shown in Figure I.14a, CV measurements in CH_2Cl_2 solution were performed to further explore the electronic properties of the diazatruxenone-based systems. All the compounds under study show amphoteric redox character exhibiting perfectly reversible oxidation and reduction waves, which is an essential requirement to design ambipolar materials. This behavior is the result of the combination of two electron-rich carbazole and

one electron-deficient fluorenone units in the same π-conjugated platform making these systems efficient push-pull materials.

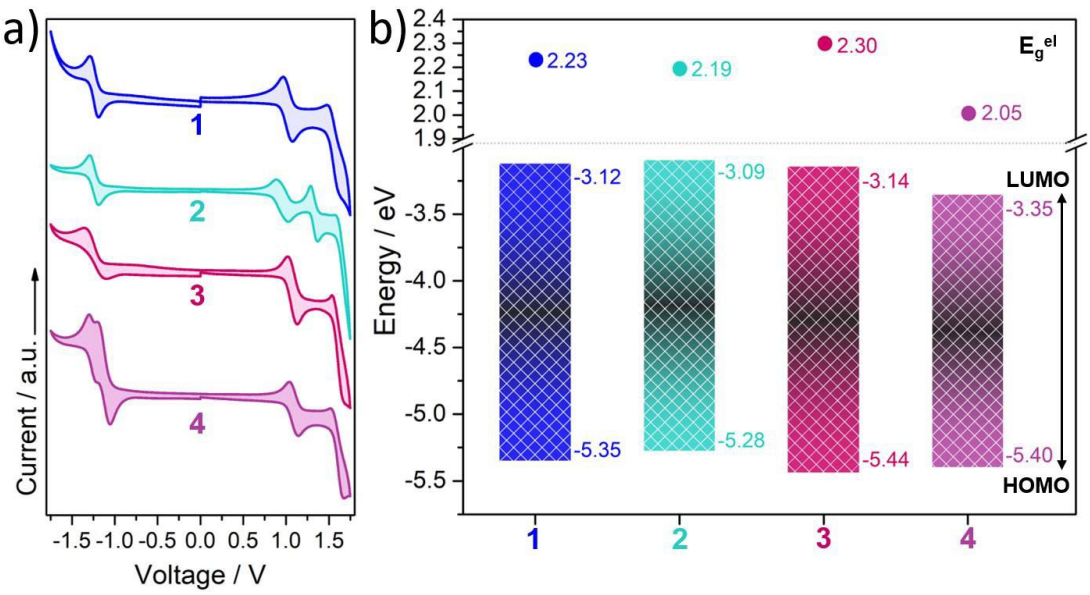

Figure I.14. (a) Cyclic voltammograms of diazatruxenone molecules (c=1×10^{-3} M) recorded at a scan rate of 100 mV·s^{-1} in CH_2Cl_2/0.1 M Bu_4NPF_6 as electrolyte, using a Pt working electrode, an Ag/AgCl reference electrode and a Pt wire auxiliary electrode. (b) Experimentally determined HOMO-LUMO energy levels of the diazatruxenones **4**-**7**.

Figure I.14b displays the HOMO and LUMO energy levels calculated from the onsets of oxidation and reduction potentials as previously described for the triindole systems. Compared to the unsubstituted diazatruxenone **4**, the attachment of two methoxy donor groups in **5** increases the oxidizability of the system, resulting in the most destabilized HOMO level across the series (-5.35 and -5.28 eV for **4** and **5**, respectively), while it barely affects the reduction process resulting in similar LUMO levels (-3.09 eV for **5** and -3.12 eV for **4**). This results in a slight HOMO-LUMO gap decrease when going from **4** (2.23 eV) to **5** (2.19 eV). The highest oxidizability of compound **5** is also manifested with the appearance of two subsequent reversible oxidation waves, with half-wave potentials at 0.92 and 1.38 V.

In contrast, the attachment of two CN (**6**) or NO_2 (**7**) electron withdrawing groups lowers the reduction potentials of the diazatruxenone platform, further stabilizing the

LUMO level (-3.14 and -3.35 eV for **6** and **7** respectively, vs. -3.12 eV for **4**). Note that this effect is more pronounced when the electron-withdrawing character of the peripheral group increase, as observed on the further LUMO stabilization of compound **7** (0.23 eV) with respect compound **6** (0.02 eV) when compared to the unsubstituted diazatruxenone **4**. Furthermore, the easier reduction of compound **7** is evidenced by the existence of two subsequent reversible reduction waves, with half-wave potentials at -1.01 and -1.27 V. On the other hand, in both **6** and **7** molecules, the HOMO level is slightly stabilized compared to the reference diazatruxenone **4** in 0.09 and 0.05 eV, respectively. These two aspects lead to a slightly wider HOMO-LUMO energy gap in **6** (2.30 eV) with respect **4** (2.23 eV), while the stronger electron-withdrawing character of nitro groups in **7** give rises to a notably HOMO-LUMO gap narrowing of 0.25 eV.

I.3.3. Self-assembly properties

Since disk-shaped molecules have a strong tendency to self-assemble by the action of intermolecular interactions, it would be very interesting to investigate the impact that the peripheral substituents exert on the self-assembly properties of these diazatruxenone-based compounds. With this purpose, the mesomorphic properties of compounds **4**-**7** were investigated. Nowadays, mesomorphic state definition given by the IUPAC Gold Book is "*a state of matter in which the degree of molecular order is intermediate between the perfect three-dimensional, long-range positional and orientational order found in solid crystals and the absence of long-range order found in isotropic liquids, gases, and amorphous solids*".[39]

In this context, compounds **4**-**7** were melted and then, progressively cooled from the isotropic phase. While compounds **4** and **5** slowly lose fluidity until crystallization, derivatives substituted with electron withdrawing groups **6** and **7** exhibit stable mesophases, which show birefringence together with fluidity when visualized by Polarized Optical Microscopy (POM), as displayed in Figure I.15. The X-ray diffraction patterns for supercooled mesophases of diazatruxenones **6** and **7** are indicative of hexagonal columnar organizations with lattice constants of 19.62 and 19.9 Å, respectively.

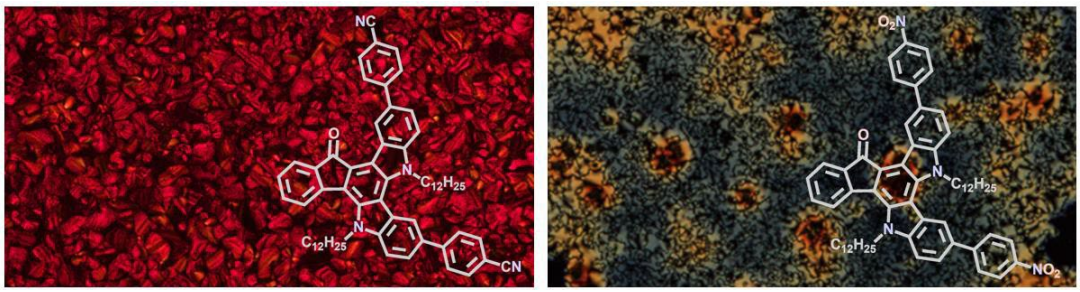

Figure I.15. Polarized optical photomicrographs of **6** and **7** upon cooling from the isotropic liquid.

In view of the results, it is conceivable that the intrinsic donor-acceptor character of diazatruxenone-based molecules not only confer them amphoteric characteristics, but might also renders them an important dipolar character which influence their supramolecular arrangement. In addition, the peripheral substitution with different functionals groups might also induce different molecular dipole moments that can influence the self-assembly properties through dipole-dipole interactions. To probe this hypothesis, the molecular dipole moments for all systems under study were calculated at B3LYP/6-31G** level of theory. As illustrated in Figure I.16, the molecular dipole moment significantly increases in derivatives with electron acceptor groups attached on the periphery, as a consequence of a higher polarization.

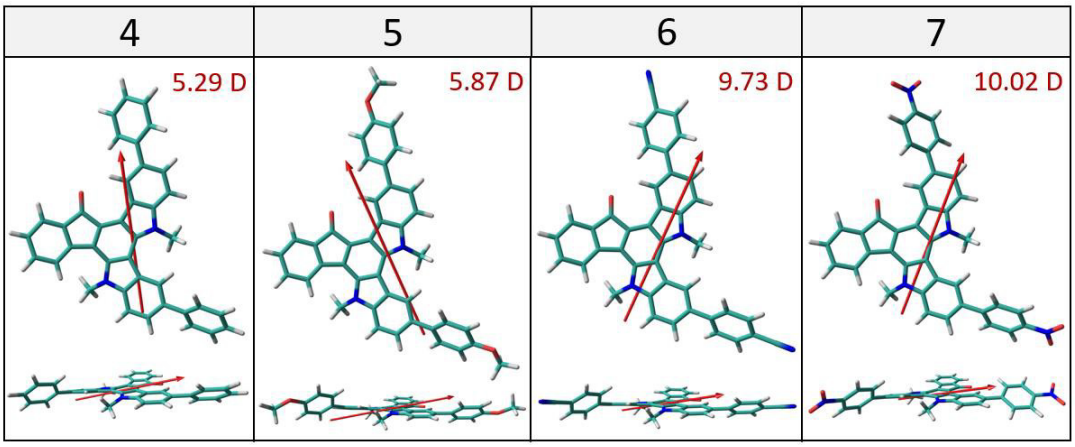

Figure I.16. DFT-calculated molecular dipole moments for the diazatruxenones **4**-**7** at the B3LYP/6-31G** level. The molecular dipole moment values are given in debye (red numbers).

In particular, molecular dipole moments of 9.73 and 10.02 D are predicted for compounds **6** and **7** respectively, which are almost twice larger than those of the rest of the studied compounds. Thus, the different mesomorphic properties observed across the series point to a more favorable dipole-driven arrangement of molecules **6** and **7**, as a consequence of the higher polarization of these systems, which leads to mesomorphism.

I.3.4. Vibrational properties

Focusing on the derivatives substituted with electron withdrawing groups **6** and **7**, due to its interesting mesomorphic properties, FT-Raman spectra were recorded to better understand the effective π-conjugation length of these diazatruxenone-base systems. In this sense, Raman spectroscopy has been proved as a useful technique to study the π-conjugational properties of disk-shaped semiconductors.[21, 25, 27]

Scrutiny of FT-Raman spectra displayed in Figure I.17a shows the presence of the same doublet previously observed on the C_3-symmetry based triindole semiconductors, localized in this case at ~1580 cm^{-1} (orange) and ~1558 cm^{-1} (blue). It should be remembered that this doublet arises from the same CC vibration (*i.e*. mode 8a of benzene) [30] but mostly localized on the external and innermost benzene rings, respectively. These two Raman bands are greatly downshifted for diazatruxenone-based compounds compared to those of the triindole analogous functionalized with electron-withdrawing triacetyl groups (**3**), as previously showed in Figure I.6. In fact, it appears at 1602/1563 cm^{-1} for triindole **3**, evidencing that the replacement of an electron donor carbazole unit by an electron acceptor fluorenone moiety on the diazatruxenone platform leads to a more π-conjugated system, in line with the results obtained by UV-vis absorption spectroscopy and DFT calculations.

Again, the nice agreement found between the experimental (Figure I.17a) and theoretical (Figure I.17b) Raman spectra gives support to the reliability of the structural information derived from this discussion as well as our Raman bands assignment (Figure I.18).

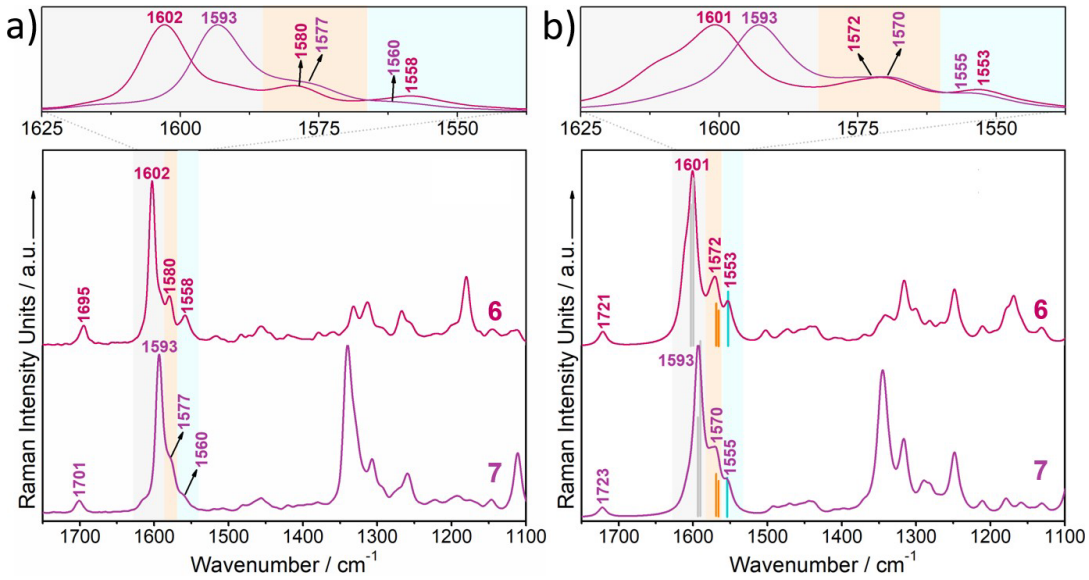

Figure I.17. (a) Solid state FT-Raman (λ_{exc}=1064 nm) and (b) simulated Raman spectra (B3LYP/6-31G** level) for the diazatruxenones **6** and **7**. The main vibrational frequencies associated with the discussed C=C/C−C Raman features are also shown. An adjustment of the theoretical force fields where the frequencies were scaled down by a factor of 0.967 to disentangle experimental misassignments was used, as recommended by Scott and Random.[29]

On the other hand, the most intense Raman band recorded at around 1600 cm^{-1}, which is ascribed to a C=C/C-C stretching normal mode mostly located on the external and peripherally functionalized benzene rings with a strong contribution of the C-C bonds linking them, as seen in the eigenvectors of Figure I.18, is found to be 9 cm^{-1} downshifted for the nitro-substituted compound **7** compared to the cyano-substituted homologous **6**. This fact suggests a better π-electronic delocalization produced by the insertion of a stronger nitro electron-withdrawing group, in agreement with its lower LUMO level. This effect becomes evident by analyzing the Raman band corresponding to the stretching of the C=O groups, recorded at 1695 and 1701 cm^{-1} in compound **6** and **7**, respectively. The moderated band upshifts observed in diazatruxenone **7** can be explain by an improved π-electronic delocalization upon functionalization with two nitro electron-withdrawing groups, which diminishes the cross-conjugation in the fluorenone moiety. Additionally, the strong activity exhibited by the band located at around 1340 cm^{-1}, which is easily recognized as the

symmetric stretching vibrations of the NO_2 groups, gives further support of the large involvement of the nitro groups in the π-conjugation.

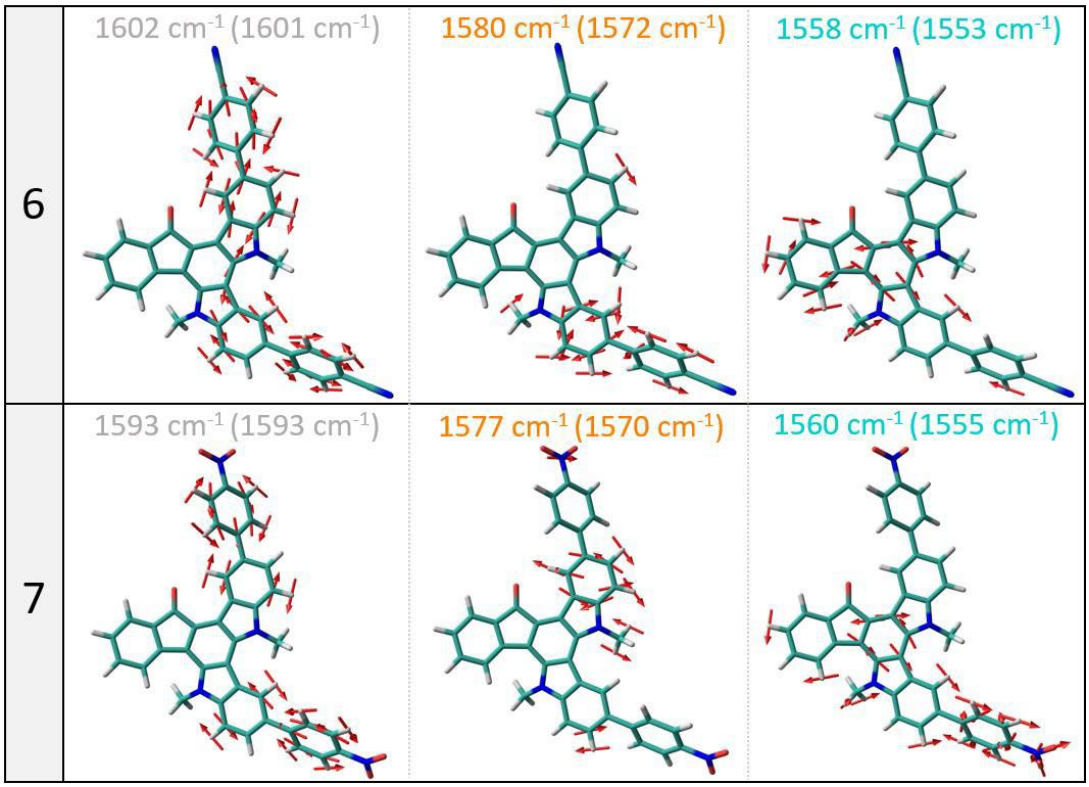

Figure I.18. B3LYP/6-31G** vibrational eigenvectors associated with the most outstanding C=C/C−C Raman features for the diazatruxenone-based semiconductors under study. The experimental and theoretical (in parentheses) wavenumbers are also shown.

I.3.5. Electrical characterization

On the basis of the evidence of the amphoteric redox character and good electronic delocalization observed on diazatruxenone-based semiconductors, and considering the acceptable mobility values observed for triindoles **1**-**3** as previously determined by OFET measurements, we have fabricated BG-TC thin-film transistors based on diazatruxenones **6**-**7** to gather information on how the donor-acceptor architecture and the different peripheral substitution influence the electrical performance. Although an exhaustive optimization process was carried out, where the effect of the substrate treatment, active layers

deposition method and annealing conditions on the charge transport characteristics of these semiconductors were systematically investigated, the devices prepared with these compounds were electrically inactive.

From a structural point of view, these disk-shaped systems are constituted by an aromatic core functionalized with two peripheral alkyl chains. It is known that diazatruxenone molecules self-assemble into columnar stacks with a parallel arrangement of the donor and acceptor moieties of the molecules, which might provide a favorable pathway for hole and electron transport respectively, while the peripheral alkyl chains provide an isolating cover.[17] Consequently, the charge transport properties of these materials are highly anisotropic, requiring an alignment step to show their optimal transport ability. For that, it is reasonable to think that the inefficient electrical conductivity observed on OFETs fabricated with these semiconductors can be ascribed to a partial or totally perpendicular molecular disposition with respect the substrate surface, which is detrimental for the charge transport in OFETs with a bottom-gate top-contact geometry.

With this in mind, the steady-state Space Charge-Limited Current (SCLC) technique has been widely used to obtain values of mobility in anisotropic liquid crystalline materials.[40-42] Considering that, SCLC measurements were carried out in collaboration with Prof. Atilio Golenme of Università della Calabria (Italy) to estimate charge mobilities in the columnar stacking direction of diazatruxenones **6** and **7**. With this purpose, a sample filling on ITO/Au cell was prepared by capillarity, heating the material up to around 180^{o}C and then cooling down until room temperature at 6^{o}C/hour. Finally, SCLC measurements were performed on 4 different points of the sample and average hole mobilities of $5x10^{-2}$ $cm^2V^{-1}s^{-1}$ were obtained for diazatruxenone **7**. For compound **6**, currents higher by two orders of magnitude were measured although the SCLC regime was never observed, which suggest that hole mobility in compound **6** could be similar or even higher than that of compound **7**.

In order to get more insight into this hypothesis, DFT calculations were performed to analyze the effect of the electron withdrawing moieties on the charge transport properties of the diazatruxenone platform. To this end, the main charge-transport parameters

impacting the charge mobility for holes at the molecular level (λ_h and t_h) were evaluated. Interestingly, functionalization with cyano groups results in slightly lower λ_h when compared to the nitro-substituted homologue, with values of 159 and 181 meV for compounds **6** and **7**, respectively. On the other hand, transfer integrals calculated for cofacial dimeric models in which molecules of the dimer are separated by 3.80 Å with an antiparallel dipole-dipole arrangement (see Figure I.19), remain almost unchanged by the nature of the electron-acceptor groups. For instance, t_h values of 155 and 153 meV are predicted for **6** and **7**, respectively.

Thus, the theoretical results are in good agreement with the experimental data as slightly lower λ_h and similar t_h values are predicted for the cyano-substituted compound **6** when compared to the nitro-substituted system **7**, which would result in similar or even slightly higher intrinsic hole mobilities. Thus, it has been demonstrated that the presence of electron-withdrawing groups, which dictate an enhanced molecular dipole moment, is an indispensable prerequisite in these systems to show good mesomorphic properties as well as moderate hole mobilities.

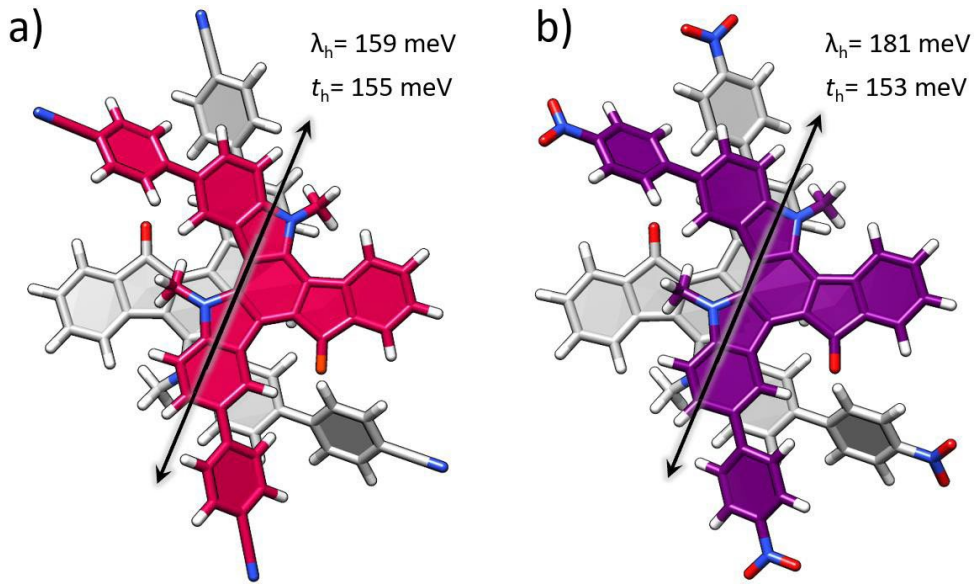

Figure I.19. Top views of the cofacial dimeric models used to compute the electron coupling parameter in diazatruxenones **6** and **7**. The λ_h and t_h values calculated at the B3LYP/6-31G** level are also shown.

I.4. Conclusions

In view of the results obtained in the study of the self-assembly properties of triindole and diazatruxenone series as models of disk-shaped systems, the following conclusions can be extracted:

- From a structural point of view, it has been theoretically demonstrated that peripheral functionalization of triindole and diazatruxenone scaffolds exerts a negligible impact at the molecular level. Nevertheless, the insertion of a ketone group on the diazatruxenone produces a dual effect, enhancing the planarity and electronic delocalization with respect its triindole homologous.

- CV, UV-Vis absorption and vibrational studies based on Raman spectroscopy confirm the modest improved π-electronic delocalization upon functionalization, being the platforms substituted with electron-withdrawing groups (**3** and **7**) the most affected cases, in agreement with its lowest HOMO-LUMO gap within their respective families. Moreover, the electronic delocalization enhancement of diazatruxenone-based materials compared to their triindole-based homologous has been corroborated.

- In contrast to triindole-based materials, the combination of two electron-rich carbazole and one electron-deficient fluorenone units in the same diazatruxenone π-conjugated platform confers to these systems an inherent push-pull nature. As a result, the presence of low energies intramolecular charge transfer transitions and amphoteric redox character have been observed in these systems, which are slightly affected by peripheral substitution except for the nitro substituted diazatruxenone **7**.

- Disk-shaped molecules under study were evaluated as semiconducting materials, Field-effect p-type mobilities of 2×10^{-2}, 1×10^{-3} and 3×10^{-5} $cm^2V^{-1}s^{-1}$ were measured for triindole **1**, **2** and **3**, respectively, despite the prediction of a π-conjugation enhancement on going from **1** to **3**. For diazatruxenone-based semiconductor, SCLC measurements were performed due to the intrinsic anisotropy of these systems, and

hole mobilities of $5x10^{-2}$ $cm^2V^{-1}s^{-1}$ were obtained for diazatruxenone **7**. These findings underline the strong impact of the intermolecular packing on the transport properties.

- It has been demonstrated with the help of DFT calculations that the peripheral groups slightly affect both molecular structure and electronic levels but significantly influences crystal packing. In the case of triindole-based molecules, it was found an inefficient wavefunction overlaps between molecules in **2** as a consequence of HOMO and HOMO-1 wavefunctions extension over the peripheral methoxy groups, resulting in less favorable wavefunctions overlap in the central core of the staggered triindole platforms. The poorly crystalline organization observed in triindole **3** is responsible of its lowest hole mobilities within the series. On the other hand, the intrinsic donor-acceptor character of diazatruxenone-based molecules not only make them ambipolar materials, but also confers an important dipole character which can be modulated by peripheral substitution influencing in this way its self-assembly properties through dipole-dipole interactions. In fact, derivatives substituted with electron withdrawing groups **6** and **7** exhibit stable mesophases in line with their high predicted molecular dipole moments.

To summarize, this combined experimental and theoretical study provides a clear picture of how the peripheral functionalization can impact the self-assembly and thus, the charge–transport properties of disk-shapes materials of importance to design new semiconductors with improved performance.

I.5. References

[1] Mas-Torrent, M.; Rovira, C., Role of Molecular Order and Solid-State Structure in Organic Field-Effect Transistors. *Chemical Reviews* **2011,** 111, (8), 4833-4856.

[2] Mei, J.; Diao, Y.; Appleton, A. L.; Fang, L.; Bao, Z., Integrated Materials Design of Organic Semiconductors for Field-Effect Transistors. *Journal of the American Chemical Society* **2013,** 135, (18), 6724-6746.

[3] Wang, C.; Dong, H.; Hu, W.; Liu, Y.; Zhu, D., Semiconducting π-Conjugated Systems in Field-Effect Transistors: A Material Odyssey of Organic Electronics. *Chemical Reviews* **2012,** 112, (4), 2208-2267.

[4] García-Frutos, E. M.; Omenat, A.; Barberá, J.; Serrano, J. L.; Gómez-Lor, B., Highly ordered π-extended discotic liquid-crystalline triindoles. *Journal of Materials Chemistry* **2011,** 21, (19), 6831-6836.

[5] García-Frutos, E. M.; Hennrich, G.; Gutierrez, E.; Monge, A.; Gómez-Lor, B., Self-Assembly of C3-Symmetrical Hexaaryltriindoles Driven by Solvophobic and CH−π Interactions. *The Journal of Organic Chemistry* **2010,** 75, (4), 1070-1076.

[6] García-Frutos, E. M.; Gutierrez-Puebla, E.; Monge, M. A.; Ramírez, R.; Andrés, P. d.; Andrés, A. d.; Gómez-Lor, B., Crystal structure and charge-transport properties of N-trimethyltriindole: Novel p-type organic semiconductor single crystals. *Organic Electronics* **2009,** 10, (4), 643-652.

[7] Benito-Hernández, A.; Pandey, U. K.; Cavero, E.; Termine, R.; García-Frutos, E. M.; Serrano, J. L.; Golemme, A.; Gómez-Lor, B., High Hole Mobility in Triindole-Based Columnar phases: Removing the Bottleneck of Homogeneous Macroscopic Orientation. *Chemistry of Materials* **2013,** 25, (2), 117-121.

[8] García-Frutos, E. M.; Pandey, U. K.; Termine, R.; Omenat, A.; Barberá, J.; Serrano, J. L.; Golemme, A.; Gómez-Lor, B., High Charge Mobility in Discotic Liquid-Crystalline Triindoles: Just a Core Business? *Angewandte Chemie International Edition* **2011,** 50, (32), 7399-7402.

[9] Isoda, K.; Yasuda, T.; Kato, T., Truxene-Based Columnar Liquid Crystals: Self-Assembled Structures and Electro-Active Properties. *Chemistry–An Asian Journal* **2009,** 4, (10), 1619-1625.

[10] Nielsen, C. B.; Voroshazi, E.; Holliday, S.; Cnops, K.; Cheyns, D.; McCulloch, I., Electron-deficient truxenone derivatives and their use in organic photovoltaics. *Journal of Materials Chemistry A* **2014,** 2, (31), 12348-12354.

[11] Gómez-Esteban, S.; Benito-Hernandez, A.; Termine, R.; Hennrich, G.; Navarrete, J. T. L.; Ruiz Delgado, M. C.; Golemme, A.; Gómez-Lor, B., High-Mobility Self-Assembling Truxenone-Based n-Type Organic Semiconductors. *Chemistry–A European Journal* **2018,** 24, (14), 3576-3583.

[12] Cheng, Y.-J.; Chen, C.-H.; Ho, Y.-J.; Chang, S.-W.; Witek, H. A.; Hsu, C.-S., Thieno[3,2-b]pyrrolo Donor Fused with Benzothiadiazolo, Benzoselenadiazolo and Quinoxalino Acceptors: Synthesis, Characterization, and Molecular Properties. *Organic Letters* **2011,** 13, (20), 5484-5487.

[13] Ye, Q.; Chang, J.; Huang, K.-W.; Chi, C., Thiophene-Fused Tetracene Diimide with Low Band Gap and Ambipolar Behavior. *Organic Letters* **2011,** 13, (22), 5960-5963.

[14] Tan, L.; Guo, Y.; Yang, Y.; Zhang, G.; Zhang, D.; Yu, G.; Xu, W.; Liu, Y., New tetrathiafulvalene fused-naphthalene diimides for solution-processible and air-stable p-type and ambipolar organic semiconductors. *Chemical Science* **2012,** 3, (8), 2530-2541.

[15] Geng, Y.; Pfattner, R.; Campos, A.; Wang, W.; Jeannin, O.; Hauser, J.; Puigdollers, J.; Bromley, S. T.; Decurtins, S.; Veciana, J.; Rovira, C.; Mas-Torrent, M.; Liu, S.-X., HOMO Stabilisation in π-Extended Dibenzotetrathiafulvalene Derivatives for Their Application in Organic Field-Effect Transistors. *Chemistry – A European Journal* **2014,** 20, (50), 16672-16679.

[16] Kato, S.-i.; Furuya, T.; Nitani, M.; Hasebe, N.; Ie, Y.; Aso, Y.; Yoshihara, T.; Tobita, S.; Nakamura, Y., A Series of π-Extended Thiadiazoles Fused with Electron-Donating Heteroaromatic Moieties: Synthesis, Properties, and Polymorphic Crystals. *Chemistry – A European Journal* **2015,** 21, (7), 3115-3128.

[17] Benito-Hernández, A.; El-Sayed, M. T.; López Navarrete, J. T.; Ruiz Delgado, M. C.; Gómez-Lor, B., Fused donor–acceptor π-conjugated diazatruxenones: synthesis and electronic properties. *Organic Chemistry Frontiers* **2018,** 5, (11), 1748-1755.

[18] Schleyer, P. v. R.; Maerker, C.; Dransfeld, A.; Jiao, H.; van Eikema Hommes, N. J. R., Nucleus-Independent Chemical Shifts: A Simple and Efficient Aromaticity Probe. *Journal of the American Chemical Society* **1996,** 118, (26), 6317-6318.

[19] Zywietz, T. K.; Jiao, H.; Schleyer, P. v. R.; de Meijere, A., Aromaticity and Antiaromaticity in Oligocyclic Annelated Five-Membered Ring Systems. *The Journal of Organic Chemistry* **1998,** 63, (10), 3417-3422.

[20] Wolinski, K.; Hinton, J. F.; Pulay, P., Efficient implementation of the gauge-independent atomic orbital method for NMR chemical shift calculations. *Journal of the American Chemical Society* **1990,** 112, (23), 8251-8260.

[21] Gámez-Valenzuela, S.; Benito-Hernández, A.; Echeverri, M.; Gutierrez-Puebla, E.; Ponce Ortiz, R.; Ruiz Delgado, M. C.; Gómez-Lor, B., Functionalized Crystalline N-Trimethyltriindoles: Counterintuitive Influence of Peripheral Substituents on Their Semiconducting Properties. *Molecules* **2022,** 27, (3), 1121.

[22] Ruiz, C.; García-Frutos, E. M.; da Silva Filho, D. A.; López Navarrete, J. T.; Ruiz Delgado, M. C.; Gómez-Lor, B., Symmetry Lowering in Triindoles: Impact on the Electronic and Photophysical Properties. *The Journal of Physical Chemistry C* **2014,** 118, (10), 5470-5477.

[23] Kahn, A., Fermi level, work function and vacuum level. *Materials Horizons* **2016,** 3, (1), 7-10.

[24] Echeverri, M.; Gámez-Valenzuela, S.; González-Cano, R. C.; Guadalupe, J.; Cortijo-Campos, S.; López Navarrete, J. T.; Iglesias, M.; Ruiz Delgado, M. C.; Gómez-Lor, B., Effect of the Linkage Position on the Conjugation Length of Truxene-Based Porous Polymers: Implications for Their Sensing Performance of Nitroaromatics. *Chemistry of Materials* **2019,** 31, (17), 6971-6978.

[25] Ruiz, C.; López Navarrete, J. T.; Ruiz Delgado, M. C.; Gómez-Lor, B., Triindole-Bridge-Triindole Dimers as Models for Two Dimensional Microporous Polymers. *Organic Letters* **2015,** 17, (9), 2258-2261.
[26] Liu, B.; Wang, Y.; Sun, H.; Gámez-Valenzuela, S.; Yan, Z.; Feng, K.; Uddin, M. A.; Koh, C.; Zhou, X.; López Navarrete, J. T.; Ruiz Delgado, M. C.; Meng, H.; Niu, L.; Woo, H. Y.; Ponce Ortiz, R.; Guo, X., Backbone Configuration and Electronic Property Tuning of Imide-Functionalized Ladder-Type Heteroarenes-Based Polymer Acceptors for Efficient All-Polymer Solar Cells. *Advanced Functional Materials* **2022,** 32, (21), 2200065.
[27] Ruiz, C.; Arrechea-Marcos, I.; Benito-Hernández, A.; Gutierrez-Puebla, E.; Monge, M. A.; López Navarrete, J. T.; Ruiz Delgado, M. C.; Ortiz, R. P.; Gómez-Lor, B., Solution-processed N-trialkylated triindoles for organic field effect transistors. *Journal of Materials Chemistry C* **2018,** 6, (1), 50-56.
[28] Hernandez, V.; Castiglioni, C.; Del Zoppo, M.; Zerbi, G., Confinement potential and ensuremath π-electron delocalization in polyconjugated organic materials. *Physical Review B* **1994,** 50, (14), 9815-9823.
[29] Scott, A. P.; Radom, L., Harmonic Vibrational Frequencies: An Evaluation of Hartree−Fock, Møller−Plesset, Quadratic Configuration Interaction, Density Functional Theory, and Semiempirical Scale Factors. *The Journal of Physical Chemistry* **1996,** 100, (41), 16502-16513.
[30] Wilson, E. B. D. J. C. C. P. C., *Molecular vibrations : the theory of infrared and Raman vibrational spectra*. McGraw-Hill: New York, 1955.
[31] Castiglioni, C.; Lopez Navarrete, J. T.; Zerbi, G.; Gussoni, M., A simple interpretation of the vibrational spectra of undoped, doped and photoexcited polyacetylene: Amplitude mode theory in the GF formalism. *Solid State Communications* **1988,** 65, (7), 625-630.
[32] Bisri, S. Z.; Piliego, C.; Gao, J.; Loi, M. A., Outlook and Emerging Semiconducting Materials for Ambipolar Transistors. *Advanced Materials* **2014,** 26, (8), 1176-1199.
[33] Coropceanu, V.; Cornil, J.; da Silva Filho, D. A.; Olivier, Y.; Silbey, R.; Brédas, J.-L., Charge Transport in Organic Semiconductors. *Chemical Reviews* **2007,** 107, (4), 926-952.
[34] Norton, J. E.; Brédas, J.-L., Polarization Energies in Oligoacene Semiconductor Crystals. *Journal of the American Chemical Society* **2008,** 130, (37), 12377-12384.
[35] Brédas, J.-L.; Beljonne, D.; Coropceanu, V.; Cornil, J., Charge-Transfer and Energy-Transfer Processes in π-Conjugated Oligomers and Polymers: A Molecular Picture. *Chemical Reviews* **2004,** 104, (11), 4971-5004.
[36] Grimme, S.; Antony, J.; Ehrlich, S.; Krieg, H., A consistent and accurate ab initio parametrization of density functional dispersion correction (DFT-D) for the 94 elements H-Pu. *The Journal of Chemical Physics* **2010,** 132, (15), 154104.
[37] Sutton, C.; Marshall, M. S.; Sherrill, C. D.; Risko, C.; Brédas, J.-L., Rubrene: The Interplay between Intramolecular and Intermolecular Interactions Determines the Planarization of Its Tetracene Core in the Solid State. *Journal of the American Chemical Society* **2015,** 137, (27), 8775-8782.
[38] Senthilkumar, K.; Grozema, F. C.; Bickelhaupt, F. M.; Siebbeles, L. D. A., Charge transport in columnar stacked triphenylenes: Effects of conformational fluctuations on

charge transfer integrals and site energies. *The Journal of Chemical Physics* **2003,** 119, (18), 9809-9817.

[39] Barón, M.; Stepto, R. F. T., Definitions of basic terms relating to polymer liquid crystals (IUPAC Recommendations 2001). *Pure and Applied Chemistry* **2002,** 74, (3), 493-509.

[40] Rose, A., Space-charge-limited currents in solids. *Physical Review* **1955,** 97, (6), 1538.

[41] Termine, R.; Golemme, A., Charge mobility in discotic liquid crystals. *International Journal of Molecular Sciences* **2021,** 22, (2), 877.

[42] De, J.; Bala, I.; Gupta, S. P.; Pandey, U. K.; Pal, S. K., High hole mobility and efficient Ambipolar charge transport in heterocoronene-based ordered columnar Discotics. *Journal of the American Chemical Society* **2019,** 141, (47), 18799-18805.

Chapter II:

Untangling the optoelectronic properties of 2D-organic polymers

Part of this work has been carried out at the *Instituto de Ciencia de Materiales de Madrid (ICMM)*, during a 3 month research stay in the group of *Estructura de Sistemas Nanométricos (ESISNA)* under the supervision of Prof. José Ignacio Martínez Ruíz.

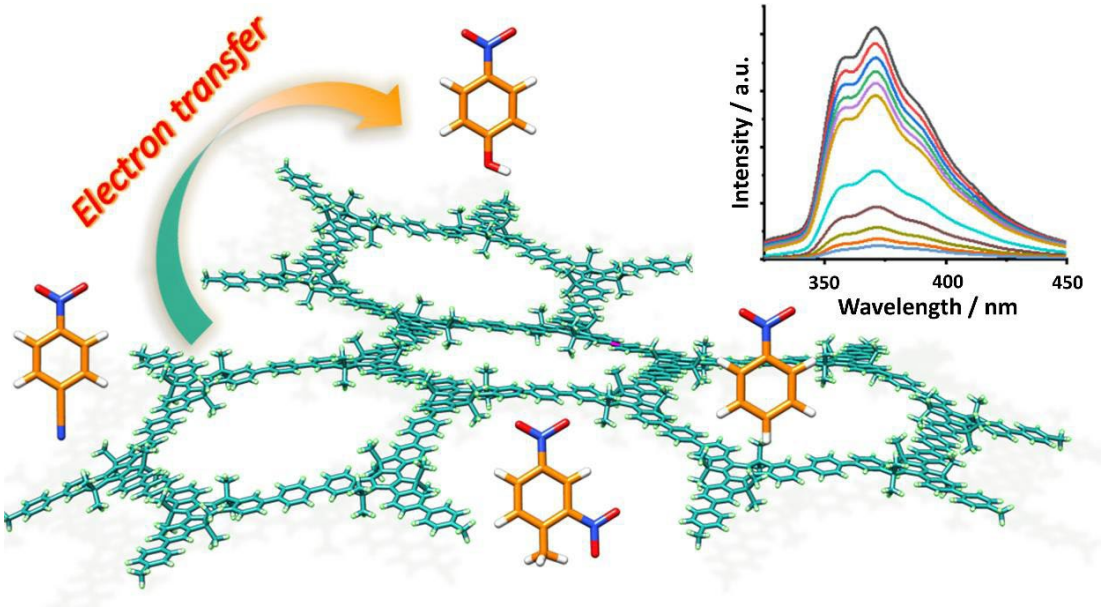

The most relevant results obtained in this study have given rise to publications 3, 4 and 5 listed in the Appendix 6.4:

3. Echeverri, M.; **Gámez-Valenzuela, S.**; González-Cano, R. C.; Guadalupe, J.; Cortijo-Campos, S.; López Navarrete, J. T.; Iglesias, M.; Ruiz Delgado, M. C.; Gómez-Lor, B., Effect of the Linkage Position on the Conjugation Length of Truxene-Based Porous Polymers: Implications for Their Sensing Performance of Nitroaromatics. Chemistry of Materials **2019**, 31, (17), 6971-6978.

4. **Gámez-Valenzuela, S.**; Echeverri, M.; Gómez-Lor, B.; Martínez, J. I.; Ruiz Delgado, M. C., In silico design of 2D polymers containing truxene-based platforms: insights into their structural and electronic properties. Journal of Materials Chemistry C **2020**, 8, (43), 15416-15425.

5. **Gámez-Valenzuela, S.**; Echeverri, M.; Ruiz Delgado, M. C.; Gómez-Lor, B., Donor-Acceptor Truxene-based Porous Polymers for Defense Applications. *In preparation*.

II.1. Introduction

Conjugated polymers constituted by one-dimensional chains have attracted great attention in the past decades because of their potential applications in modern optoelectronic devices.[1-4] However, numerous studies have shown that although charge transport along the direction of conjugated backbones can be very efficient, hopping of charge carriers between chains is significantly hindered, thus limiting the charge transport process.[5-7] To solve this drawback, an effective strategy involves extending π conjugation in polymers into the second dimension (2D), that is, synthesizing 2D-conjugated polymers that feature structural periodicity and inherent porosity.[8, 9] Thereby, bidimensional conjugated microporous polymers (CMPs) can be synthetized from the precise periodic integration of organic building blocks in-plane through covalent bonds. As a representative example, trigonal (C_3-based symmetry) π-conjugated monomers have emerged as excellent building blocks for the construction of functional CMPs with promising photocatalytic properties,[10, 11] sensing ability,[12, 13] energy storage,[14] thermoelectric[15] and field effect behavior.[16] Optimizing materials for these applications requires the correct structural design to fine-tuning key parameters such as molecular structure, energy levels or π-conjugation extension, which further determine the optoelectronic properties of final materials.

In this chapter, we firstly focus on C_3-based symmetry building blocks based on the truxene (**Tx**) π-conjugated platform (in line with the previously analyzed semiconductors of Chapter I), which can be connected by direct self-condensation of the **Tx** building blocks or by the connection through different linkers. As linkers, phenylene (**Ph**) and benzotiadiazole (**BTD**) rings are used, being connected at two different linkage positions (2,7,12-substitution in **T2** polymers and 3,8,13-substitution in **T3** polymers) as shown in Figure II.1. In particular, a combined experimental and theoretical approach was used to get a better understanding of the structure-properties relationship of the synthetized systems, by analyzing the effect that the different π-spacer groups and the linkage position plays on their optoelectronic properties. In addition, we also evaluate the potential use of these systems for the detection

of electron deficient nitroaromatics analytes of relevance for sectors that go from security to human health.

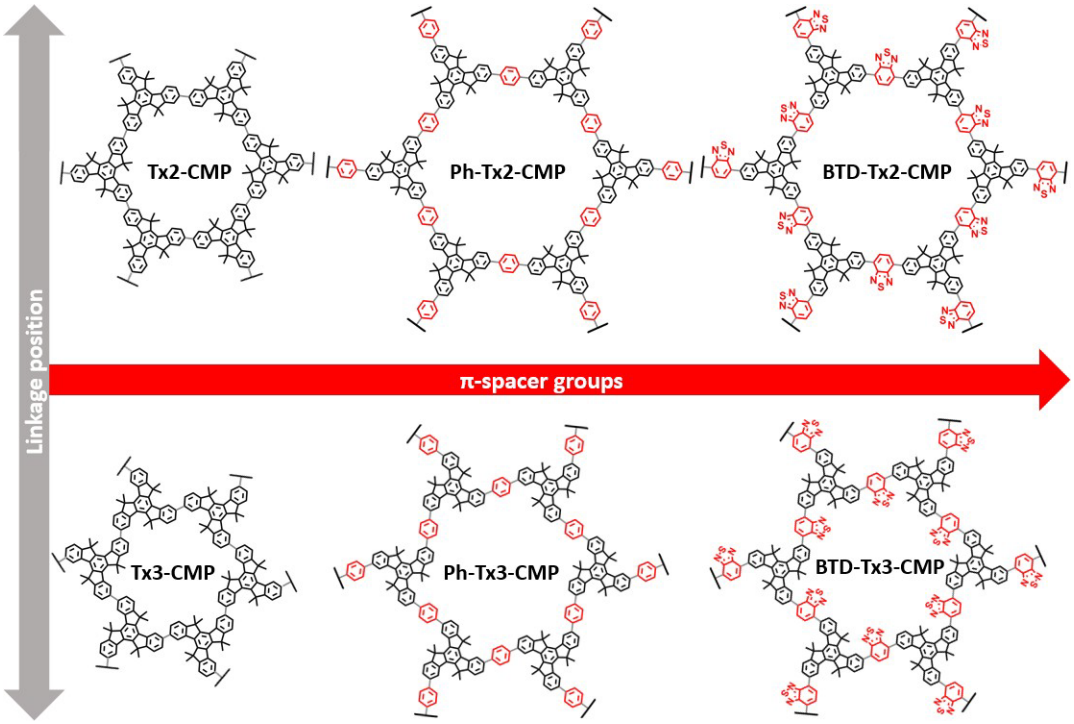

Figure II.1. Idealized chemical structures of the conjugated microporous polymers studied in the first section of Chapter II.

Secondly, inspired by the recent work of professor Huanli Dong in 2020,[16] where the analogous triindole-based system of **Ph-Tx2-CMP** was probed as active p-type semiconducting layer in OFETs, we have performed a purely theoretical investigation of the electronic and transport properties of truxene-based 2D-polymers (Figure II.2). The ultimate goal of this study is to explore how their structural, electronic and charge-transport properties can be modulated by molecular engineering. For this purpose, we have explored three different chemical structural changes: (i) the nature of the building blocks (from truxene to trindole or truxenone), (ii) insertion of different π-spacers (phenylene and alkyne) or (iii) the variation of the linkage position (from *para* in **T2** to *meta* in **T3** or by increasing the number of π-bridges from three units in **T2** and **T3** to six units in **T2,3**).

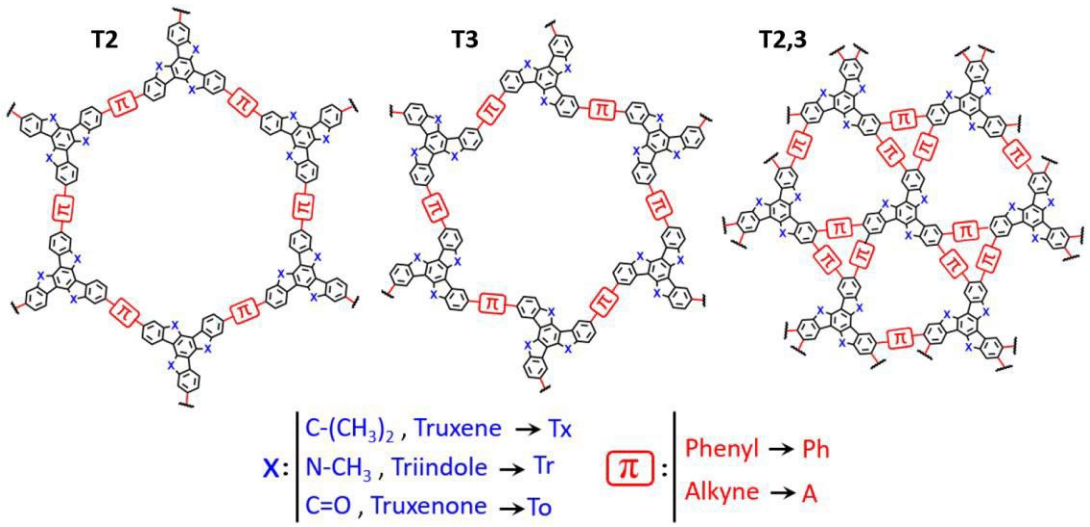

Figure II.2. Idealized chemical structures of the 2D-conjugated polymers studied in the second section of Chapter II.

This exhaustive and systematic study provides a powerful prefiltering protocol of these polymers towards different applications according to the targeted functionality.

II.2. Truxene-based polymers: a combined experimental and theoretical investigation

II.2.1. Structural features

The optimized ground-state structure of the porous polymers under study were theoretically investigated using a canonical bottom-up approach, with the main goal of exploring the structural differences exerted by the different π-spacers connecting the conjugated platforms and their respective linkage position.

First, we studied at PBE0/6-31G** level of theory the molecular structure of dimeric models in which two truxene units are directly linked (**Tx2** and **Tx3**) or through phenylene (**Ph-Tx2** and **Ph-Tx3**) or benzothiadiazole (**BTD-Tx2** and **BTD-Tx3**) spacers at the two different linkage positions under study. Note that it has been demonstrated that quantum chemical calculations of molecular fragments provide relevant information about the molecular and electronic structure of porous polymeric networks.[17-25] Figure II.3 displays selective optimized structures parameters for the dimeric models. The truxene cores show

a coplanar structure where each methyl group is oriented out of the plane defined by the conjugated platform and therefore does not sterically hinder the planarity of the overall fused system. However, the bridging connectors are moderately twisted due to steric repulsions caused by the hydrogen atoms of adjacent benzene rings. Importantly, slightly lower torsions are predicted for the *para*-connected dimers (~36º for **BTD-Tx2**, **Ph-Tx2** and **Tx2**) than for the *meta*-substituted isomers (~38-40º for **BTD-Tx3**, **Ph-Tx3** and **Tx3**).

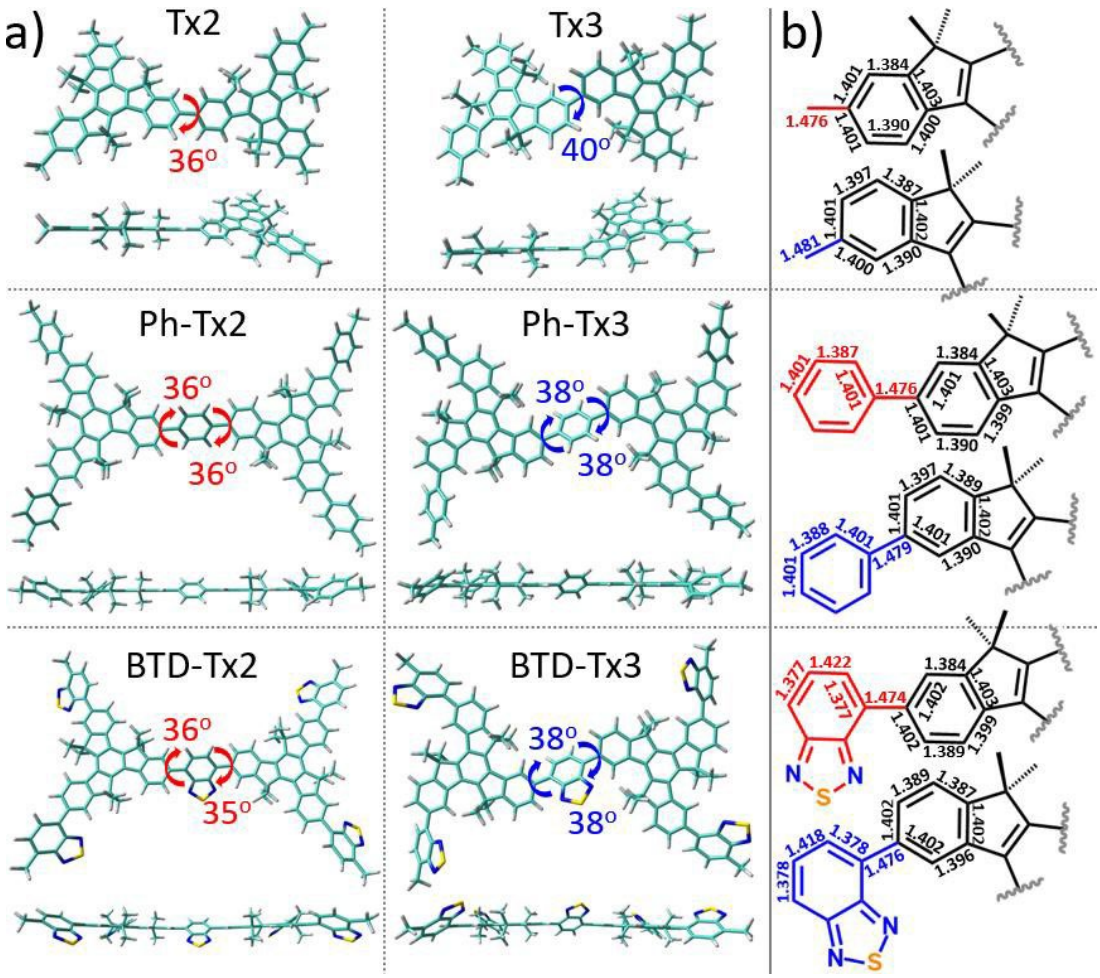

Figure II.3. (a) Top and lateral views of the DFT-optimized structures (PBE0/6-31G** level) for the dimeric models of the polymers under study. The dihedral angles between the conjugated cores and the π-bridges (in absolute values) are also shown. (b) Selected optimized bond distances (in Å) for the dimeric models under study. Top (bottom) structures refer to the **T2** (**T3**) polymers.

Furthermore, the variation of the linkage position from 3,8,13 (**T3**) to 2,7,12-positions (**T2**) induces a soft shortening of the single C-C bonds connecting the C_3 cores, suggesting a more extended and delocalized π-conjugated skeletons when the cores are connected in 2,7,12-positions. Interestingly, in contrast to the BTD-substituted polymers, the insertion of phenylene spacers between the truxene units does not significantly affects the bond distances when compared to those of the homocoupled dimeric systems, suggesting that the insertion of phenylene bridges barely affects the π-electron delocalization between the truxene units.

Second, these molecular fragments were then sequentially assembled using Periodic Boundary Conditions (PBC) to form larger subsystems, and the 2D lattices collected in Figure II.4 were generated. In accordance with the results obtained for dimeric models, the optimized periodic single layers predict a planar structure for the truxene core, with the π-spacers out-of-plane from the overall coplanarity of the system. This structural feature produces a homogeneous electronic charge distribution in the cutting-xy-plane (increasing charge density from the light green to the red/purple regions) for **Tx2** and **Tx3**. Similarly to dimeric models, an improvement of the planarity and thus of the electronic conjugation is found for the 2,7,12 covalently linked polymers in comparison with their 3,8,13-substituted isomers. Furthermore, the insertion of phenylene groups between the C_3 cores barely affects the electronic charge distribution in the cutting-xy-plane, suggesting similar π-electron delocalization with respect the homocoupled polymers. However, it is not the case of **BTD-Tx2** and **BTD-Tx3** polymers, which display higher electronic charge density on the proximities of the BTD bridging connectors, as a consequence of the incipient donor-acceptor character of BTD-spaced systems which lead to a strongly polarized molecular backbone. It is important to highlight that our calculations of dimeric models provide very accurate information about the molecular structures of the 2D conjugated polymers.

DFT-calculations reveal that pore surface engineering of these materials can be achieved by the correct structural design. As seen in Figure II.4, the size of the hexagonal mesopores can be modulated by the insertion of π-bridges between the cores (*i.e.*, an

increase of 7-8 Å is found when comparing the Ph- and BTD-based polymers with their directly linked homologues) or by changing the linkage position (*i.e.*, the pore size decreases by 4-6 Å when going from **T2** to **T3** polymers).

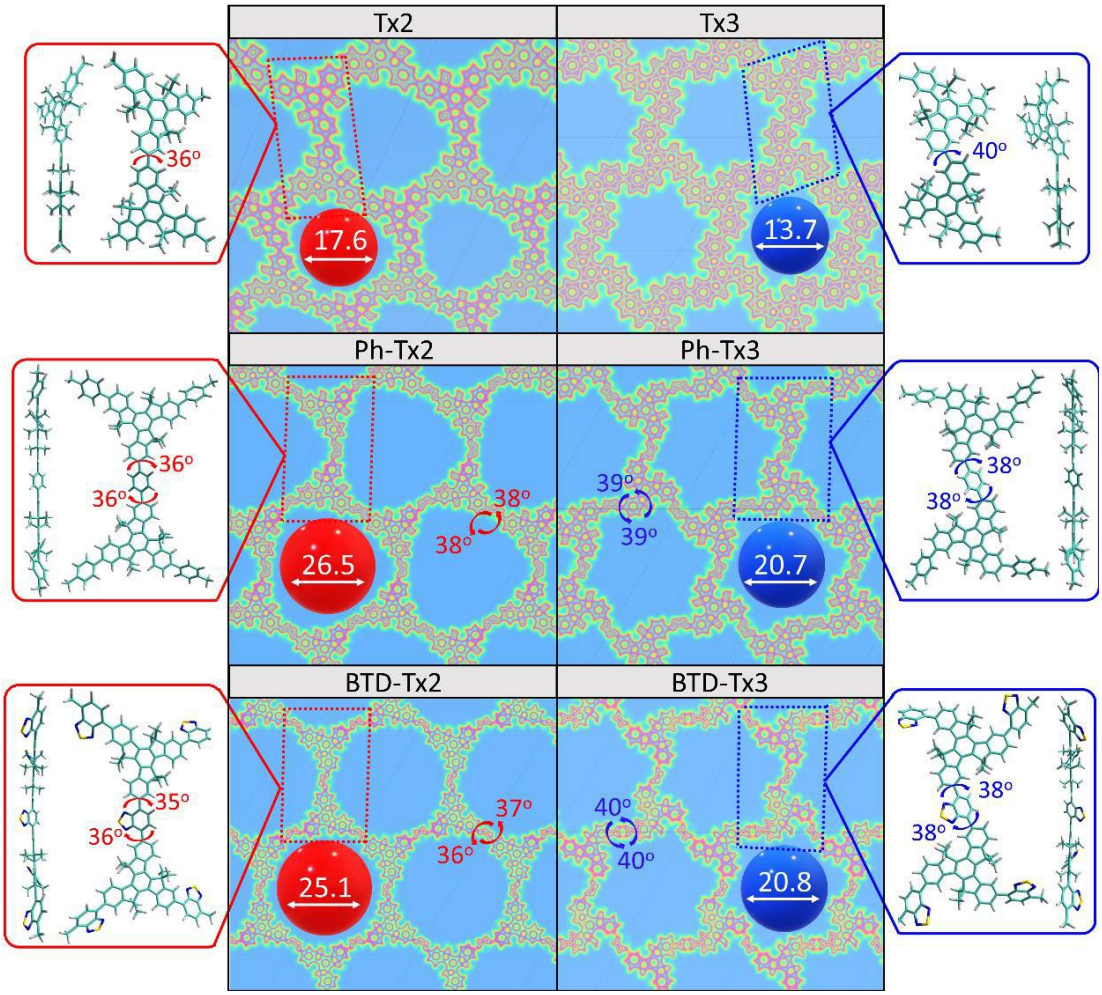

Figure II.4. Top and lateral views of the DFT-optimized structures (PBE0/6-31G** level) for the dimeric models of the truxene-based polymers in addition to the DFT-calculated (PBE0-D3) surface charge density colour maps in the xy-plane (at the z-position) for the polymeric layers. Accessible pore diameter (Å) for all the polymers and selected dihedral angles values (in absolute values) are also shown.

II.2.2. Optical Properties

The optical properties of these porous organic polymers were initially investigated via UV-Vis absorption and fluorescence spectroscopy and rationalized with the help of TD-DFT calculations. As we can observe in Figure II.5, the linkage position in these polymers has a strong influence on the absorption and light emitting properties of the final materials. In fact, both absorption and fluorescence spectra of polymers connected through the 2,7,12 positions are significantly red-shifted when compared with those of the polymers connected through the 3,8,13 positions, being this bathochromic shift especially important for directly and Ph-bridged polymers.

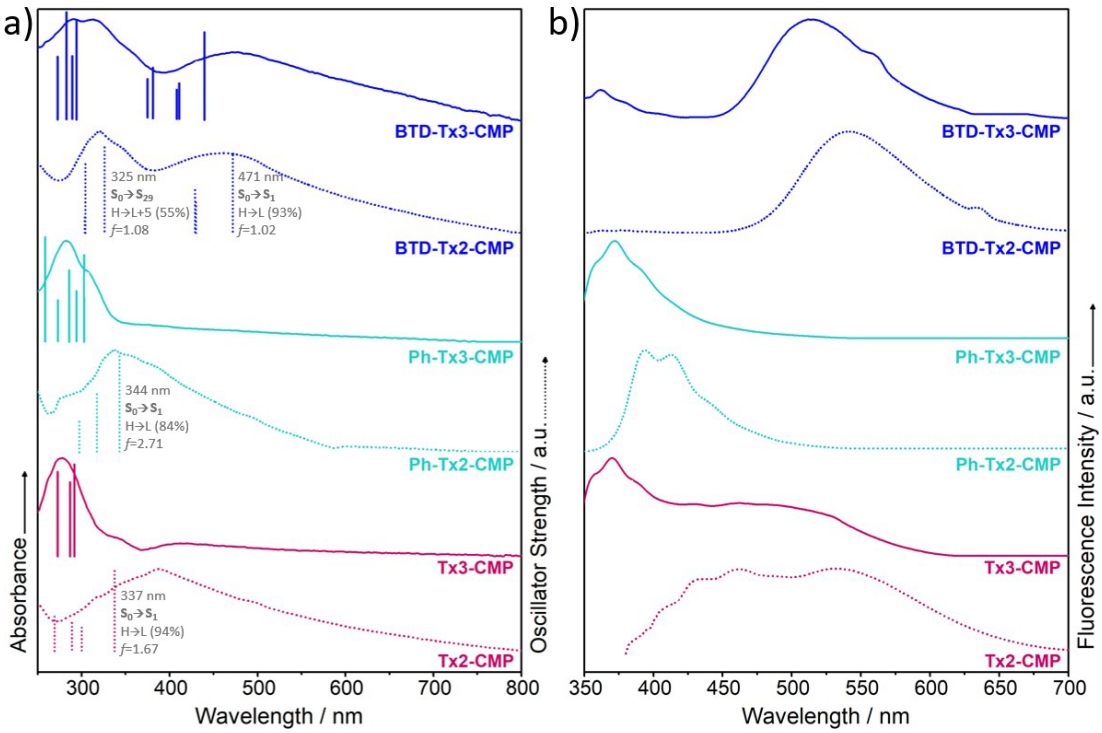

Figure II.5. (a) Normalized experimental UV-Vis absorption and (b) emission spectra of the porous polymers in CH_2Cl_2 suspensions. The main vertical excited-state transitions (vertical bars) calculated at the TD-DFT//PBE0/6-31G** level for their respective dimeric models and the compositions of the frontier molecular orbitals involved in the main transitions for the *para*-connected dimers, taken as representative examples, are also shown.

In order to shed light on the electronic nature of the lowest energy absorption bands of the polymers, TD-DFT calculations for the dimeric models were performed at PBE0/6-31G** level of theory. In this context, TD-DFT vertical excitation energies reproduce very well the experimentally observed red-shifting and reflect an increase in the conjugation length along the truxene backbones when varying the linkage position from *meta* (3,8,13) to *para* (2,7,12) connections. As showed in Figure II.6a, the observed phenomena can be associated to a significative reduction of the HOMO-LUMO gap on going from 3,8,13 to 2,7,12 systems, marked by a notable destabilization (stabilization) of HOMO (LUMO) energy levels. This HOMO-LUMO gap narrowing can be explain in terms of the π-conjugation extension degree, as shown in the topologies of HOMO and LUMO orbitals for the dimers (see Figure II.6a). Taking the directly connected models as example, HOMO and LUMO orbitals of **Tx2-CMP** spread over the six aligned central rings, while the connection of truxene units at the *meta* positions does not allow for direct conjugation and the pathway of alternating single and double bonds extends only through the two directly connected central phenyl rings. Note that our calculations for the 2D-polymeric layers (Figure II.6b) show the same behavior, where both valence and conduction bands (VB and CB, respectively) spread over selective directions in 2,7,12-connected polymers whereas these are located in specific regions of the polymeric backbone for the 3,8,13 isomers.

Upon the introduction of BTD π-bridges between the Tx cores, distinctive spectral changes are observed. While the UV−vis absorption spectra for the directly and phenylene-spaced porous polymers show only one band, their BTD-based homologous exhibit two predominant absorption bands localized around 300 and 470 nm. Focusing on *para*-connected systems, the lowest energy absorption band corresponds in all the cases to an $S_0 \rightarrow S_1$ transition that arises mainly from a HOMO➔LUMO one-electron promotion. In view of the results of Figure II.6a, we can confirm that this electronic transition is associated to a π-π* local excitation for **Tx2-CMP** and **Ph-Tx2-CMP**, whereas in the case of **BTD-Tx2-CMP** has a strong ICT character as the HOMO is delocalized over the six central rings, while the LUMO is strongly localized on the BTD acceptor moiety.

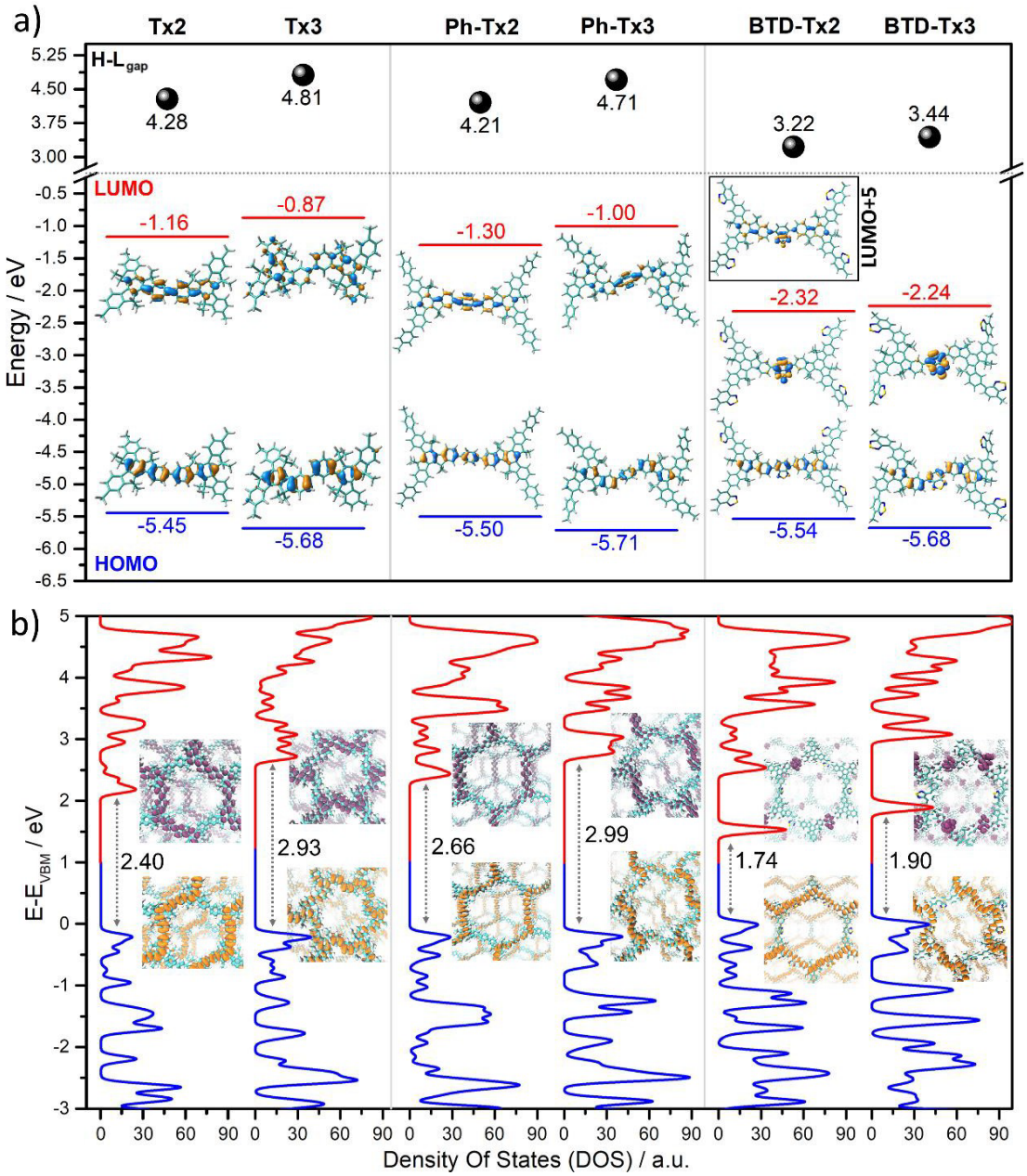

Figure II.6. (a) DFT-calculated (PBE0/6-31G** level) HOMO/LUMO energies and topologies for the dimeric models of the studied polymers. (b) DFT-PBE0-D3 computed total density of electronic states profiles (in arb. units) as a function of the energy (referred to the Fermi energy). The topologies of the valence (orange) and conduction (purple) bands are also shown.

Note that the donor-acceptor nature of the BTD-based porous polymers produces a dramatic bathochromic shift of the $S_0 \rightarrow S_1$ electronic transition compared to that of the directly or Ph-spaced ones. These results are in good accordance with the remarkable reduction of the band gap theoretically predicted for dimeric models and 2D-polymeric layers of **BTD-Tx2** and **BTD-Tx3** as a consequence of a notable stabilization of the LUMO level and the CB, respectively.

In contrast, the insertion of phenylene spacers between the truxene units has a weak influence on the optoelectronic properties of these truxene-based polymers, resulting in small blue-shifted absorption and emission maxima when compared to those found in the directly connected polymers. This fact suggests that the insertion of phenylene bridges barely affects the π-electron delocalization between the truxene units, as support their almost unchanged band gap when compared to those of the homocoupled polymeric systems (see Figure II.6b). It is important to highlight that the band gap obtained from PBC calculations of the 2D layers and the HOMO-LUMO gap calculated from the dimeric models give very similar trends.

The calculated data nicely reproduce the experimental trends obtained via Solid-state Ultraviolet−Visible Diffuse Reflectance (UV-DRS) experiments performed to estimate the bandgap of the four polymers, by using the Kubelka−Munk function. In fact, slightly lower energies are found for polymers **Tx2-CMP** and **Ph-Tx2-CMP** (3.10 and 3.33 eV, respectively) than for **Tx3-CMP** and **Ph-Tx3-CMP** (3.42 and 3.53 eV, respectively), corroborating that different linkage position produces a more notorious bandgap reduction than the insertion of phenylene spacers between the truxene units. On the other hand, the insertion of the electron-withdrawing BTD π-bridge produces a dramatic bandgap reduction respect to the homocoupled polymers (2.52 and 2.63 eV for **BTD-Tx2-CMP** and **BTD-Tx3-CMP**, respectively).

II.2.3. Vibrational properties

We now use Raman spectroscopy to further probe the impact produced by the nature and the linkage position of the bridging connectors on the electronic communication between the conjugated C_3-symmetric platforms. It is well known that Raman spectroscopy renders valuable information about the electronic coupling between covalently connected conjugated moieties and the effective π-conjugation length in polymers.[24, 26, 27] Figure II.7a compares the solid-state FT-Raman spectra of all the porous polymers under study.

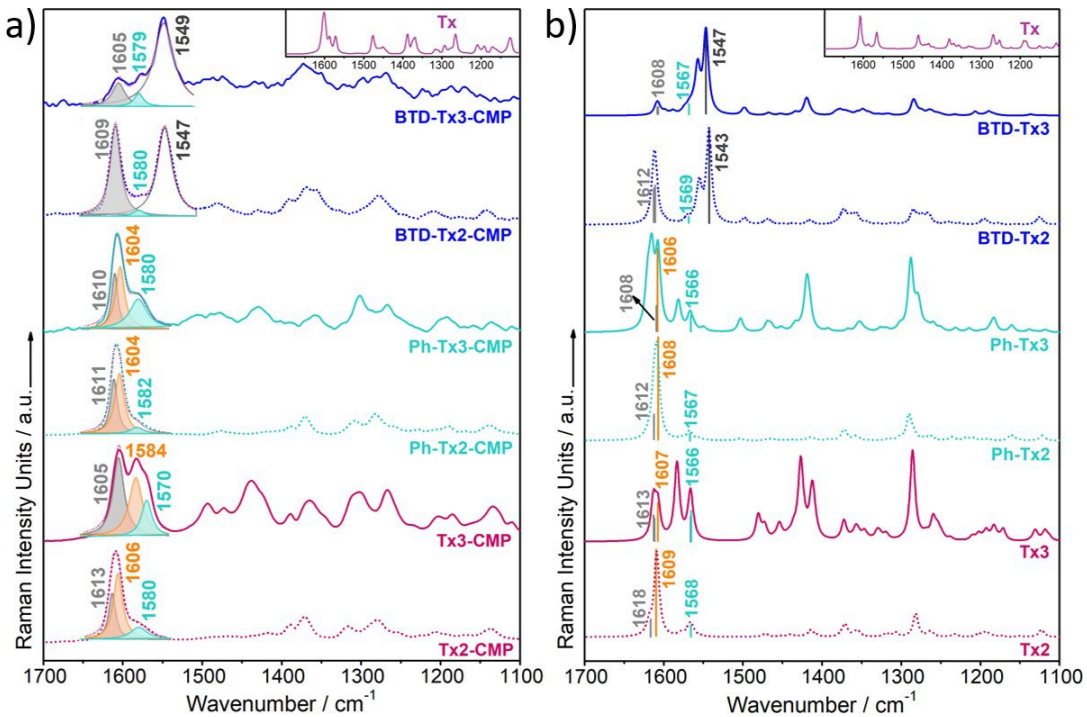

Figure II.7. (a) Solid state FT-Raman spectra for the truxene-based porous polymers and the hexamethyl truxene **Tx** monomer. (b) Theoretical Raman spectra (PBE0/6-31G**) calculated for the dimeric models of the truxene-based polymers and for the monomer **Tx**. The main vibrational frequencies associated with the discussed C=C/C−C Raman features are also shown. An adjustment of the theoretical force fields where the frequencies were scaled down by a factor of 0.954 to disentangle experimental misassignments was used, as recommended by Scott and Random.[28]

Compared to the **Tx** monomer (as an inset in Figure II.7), a band broadening of the strongest Raman band localized between 1500−1600 cm^{-1}, which is related with the C=C/C−C stretching modes, is observed in the polymers due to the higher conformational flexibility. In addition, an increase in the intensity of these bands with respect to the rest of the bands recorded below 1500 cm^{-1}, which arise from non-conjugated CH_2 bending vibrations, is found in the polymers. This effect reflects the better electronic communication in the polymers when compared to that of the monomer, being especially relevant in the case of **BTD-Tx2-CMP**, **Ph-Tx2-CMP** and **Tx2-CMP** as a result of the better electronic communication between the covalently linked moieties through the 2,7,12 connections than through the 3,8,13 connections, in good accordance with the conclusions previously obtained in the electronic properties analysis.

The most intense Raman bands (1550−1650 cm^{-1}) were deconvoluted into three distinct peaks by fitting with a Lorentzian function. Importantly, the experimental Raman spectra were well reproduced by DFT calculations for dimeric models of the polymers (Figure II.7b). The three experimentally observed peak contributions were assigned to the same C-C stretching mode (*i.e.*, mode 8a of benzene)[29] but located in different rings: (i) The grey bands localized at the highest frequencies (∼1610 cm^{-1}), related to the theoretical signal at ∼1612 cm^{-1}, involves the external benzene rings of the Tx cores. (ii) The orange bands at intermediate frequencies (∼1605 cm^{-1}), related to the theoretical signal at ∼1608 cm^{-1}, corresponds to the covalently linked external benzene rings. (iii) The light blue bands observed at lower frequencies (∼1580 cm^{-1}), related to the theoretical signal at ∼1568 cm^{-1}, is localized in the internal benzene ring of each truxene unit. In the case of the BTD-derivatives, a new Raman band can be observed at ∼1548 cm^{-1} (black band in Figure II.7b), corresponding to the C=C/C−C stretching mode of the BTD linking units, theoretically predicted at ∼1545 cm^{-1}. Figure II.8 shows the vibrational eigenvectors associated with the above-mentioned C=C/C−C Raman features, supporting our Raman bands assignment and confirming the good validity of our discussion.

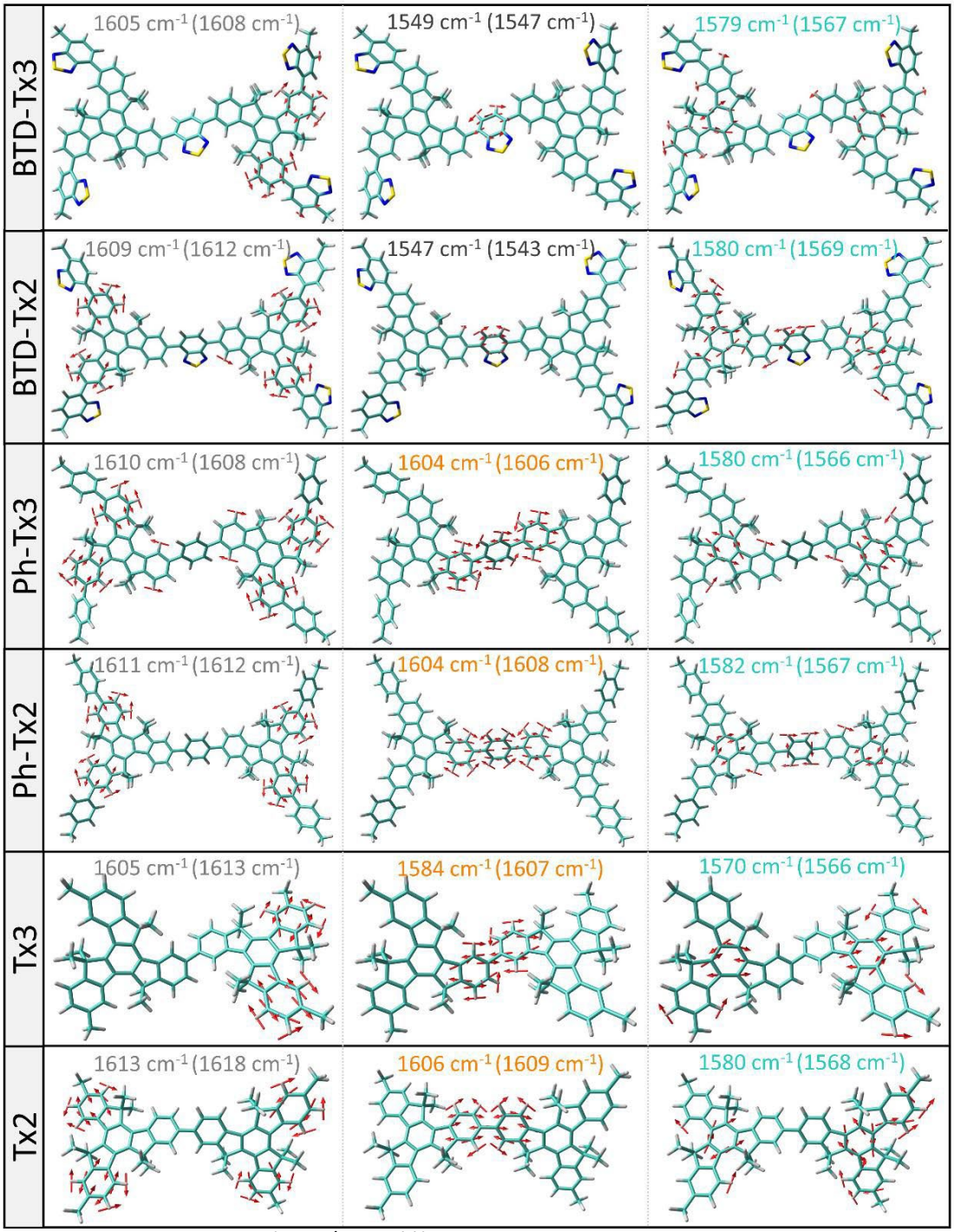

Figure II.8. DFT-calculated (PBE0/6-31G**) vibrational eigenvectors associated with the most outstanding C=C/C−C Raman features for the dimeric models of the polymers. The experimental and theoretical (in parentheses) wavenumbers are also shown.

With these considerations in mind, the experimental I_{1610}/I_{1580} intensity ratio can serve as a measure to estimate the effectiveness of the conjugation along the structures. As this ratio increases, the conjugation becomes more efficient.[26, 30, 31] If we compare all of the polymers, a clear trend on the electronic conjugation degree can be obtained as a function of the linkage position of the truxene moieties. We can observe that polymers connected through 2,7,12 positions give higher intensity ratio than their 3,8,13-connected homologous, further proving that polymers linked through the *para*- connections are much better conjugated than their *meta*-connected isomers.

Considering the effects of the π-bridge, the insertion of phenylene spacers in **Ph-Tx2-CMP** and **Ph-Tx3-CMP** polymers barely affects the I_{1610}/I_{1580} intensity ratio and therefore the π-electron delocalization between the truxene units when compared to the homocoupled homologous. On the contrary, introduction of BTD spacers between the truxene units produces an enhancement of the I_{1610}/I_{1580} intensity ratio with respect the homocoupled polymers, being this effect especially notorious in the case of **BTD-Tx2-CMP** polymer. This fact is in fully agreement with the slight impact caused by the insertion of phenylene spacers between the Tx cores on the HOMO/LUMO energy levels when compared to the BTD-derivative systems, suggesting a greater influence on the π-electron delocalization the introduction of the latter.

II.2.4. Sensing of nitroaromatic analytes

Inspired by the pioneering work of Swager in 1998,[32] one of the most appealing applications of light-emitting porous conjugated polymers is the detection of analytes of interest. Taking advantage of the persistent porosity that characterizes these polymers, the confinement and close contact of the analyte with the photo-active organic moiety is facilitated, resulting in an enhanced optical response.[13, 33-37] Accordingly, we have evaluated the potential use of these systems for the detection of electron deficient nitroaromatics analytes of relevance for sectors that go from security to human health, such as, dinitrotoluene (DNT), *p*-nitrobencene (NB) and *p*-nitrobenzonitrile (NBN).[38]

With the main goal of determining the implication of the different linkage position on the sensing performance, the variation of the fluorescence spectra of truxene-based polymers **Ph-Tx2-CMP** and **Ph-Tx3-CMP** suspended in CH_2Cl_2 (c=50μg/ml) was recorded in the presence of increasing amounts (0−350 μM) of the different nitroaromatics (Figure II.9).

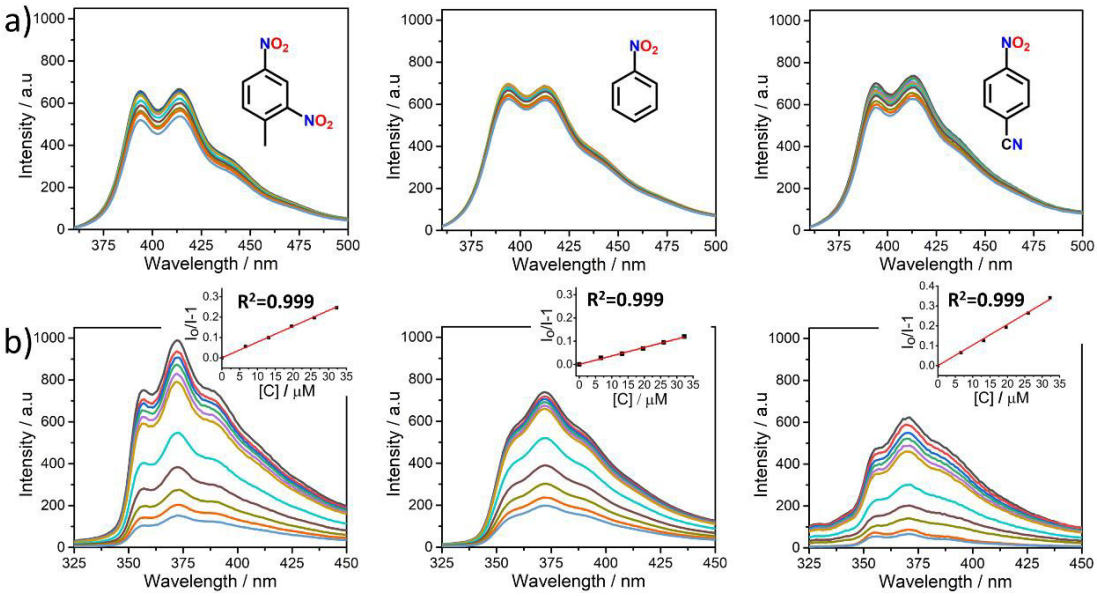

Figure II.9. Fluorescence spectral changes of (a) **Ph-Tx2-CMP** and (b) **Ph-Tx3-CMP** upon addition of increasing amounts (0−350 μM) of DNT (left), NB (center) and NBN (right). The insets show the corresponding Stern−Volmer plots for **Ph-Tx3-CMP** polymer.

As one can observe, changes in the spectra of 3,8,13 connected polymer are much more important than those observed for its 2,7,12 homologous, testifying more efficient sensing properties for the former (Figure II.10a). An explanation to this effect can be found on the basis of the Photoinduced Electron Transfer (PET) mechanism, in which the electron deficient nitroaromatic compounds act as electron acceptors for photoexcited electrons of the porous polymers (see Figure II.10b). Therefore, the larger the difference between the polymer and the guest LUMO levels, the most favorable the electron transfer process will be.[39] On the basis of these considerations, the superior quenching response to the nitroaromatic analytes exhibited by **Ph-Tx3-CMP** polymer can be understood in terms of LUMO energy levels, where the higher LUMO of the polymer **Ph-Tx3-CMP** in comparison to

that of **Ph-Tx2-CMP** would result in a more exergonic electron transfer to the LUMO of the analytes. In addition, the trend observed when going from NBN to NB can also be rationalized on the basis of a PET mechanism, since the lower the LUMO level of the analyte, the more favored the electron transfer process.

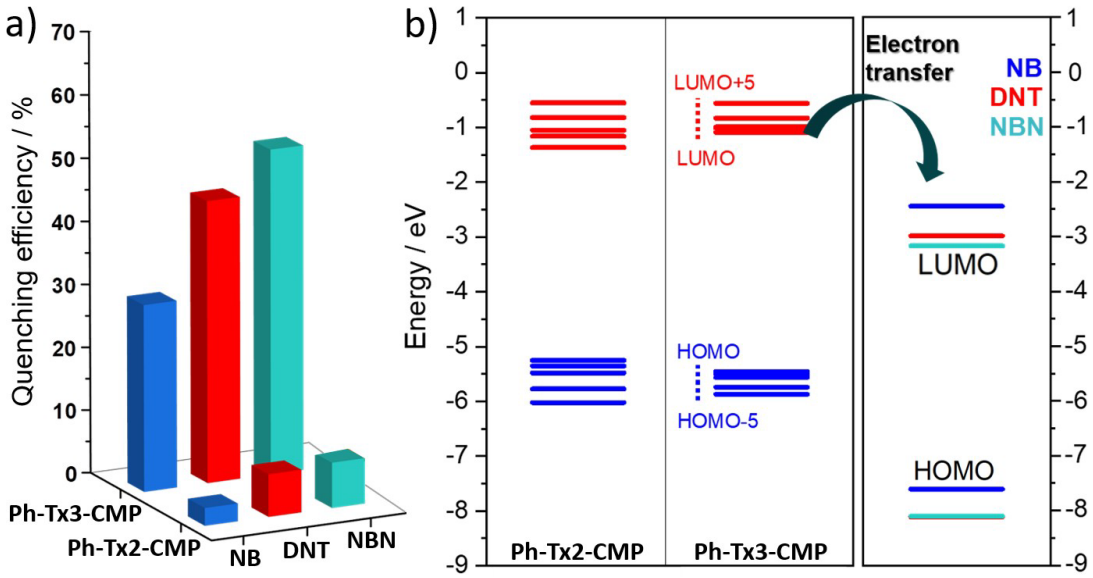

Figure II.10. (a) Quenching efficiencies of **Ph-Tx2-CMP** and **Ph-Tx3-CMP** polymers with NB, DNT and NDN at 100 µM. (b) DFT-Calculated molecular orbital energies (PBE0/6-31G** level) for the dimeric models of the truxene-based polymers **Ph-Tx2-CMP** and **Ph-Tx3-CMP**, in comparison with the orbital energies of the analytes.

We have also analyzed the quenching data using the Stern−Volmer equation $I_o/I=1+K_{SV}[Q]$, which provides a quantitative relationship between the changes in fluorescence intensity (I_o/I) related to the initial signal (I_o) and the concentration of added nitroaromatic compounds ([Q]). Graphic representations of Stern−Volmer equation for **Ph-Tx3-CMP** polymer are shown as insets in Figure II.9. In this context, high Stern−Volmer constants of 7.8×10^3, 3.6×10^3 and 10.4×10^3 M^{-1} were obtained for DNT, NB, and NBN analytes, respectively.

II.3. 2D-polymers containing truxene-based platforms: an in-silico study

In this section, we explore the design principles to build functional 2D-polymers, which involve control of π-conjugation and electronic structure of the building blocks. The former is achieved by correct selection of the π-bridge groups and the linkage position of them, while the latter is controlled by the electronic nature of the C_3 symmetry platform. Inspired by the recent work of professor Huanli Dong, where **Ph-Tr2** conjugated polymer was probed as active layer in OFETs,[16] we have performed a purely theoretical investigation of a total of 27 different porous conjugated polymers (Figure II.11) with the main goal of exploring how their the electronic and charge-transport properties can be modulated by the following effects: (i) the nature of the conjugated platform, going from electron-rich truxene (**Tx**) and triindole (**Tr**) cores to the electron-deficient truxenone (**To**) unit, (ii) the spacing of these conjugated platforms with different π-spacers (*i.e.*, phenylene (**Ph**) or ethynylene (**A**) groups), (iii) the linker position (2,7,12-substitution in **T2** polymers and 3,8,13-substitution in **T3** polymers), and (iv) the increased number of π-spacers connecting the cores, from three units in **T2** and **T3** to six units in **T2,3**. To this purpose, a large battery of DFT calculations was performed for the corresponding porous polymers (infinite monolayers and self-assembled monolayers) using periodic boundary conditions.

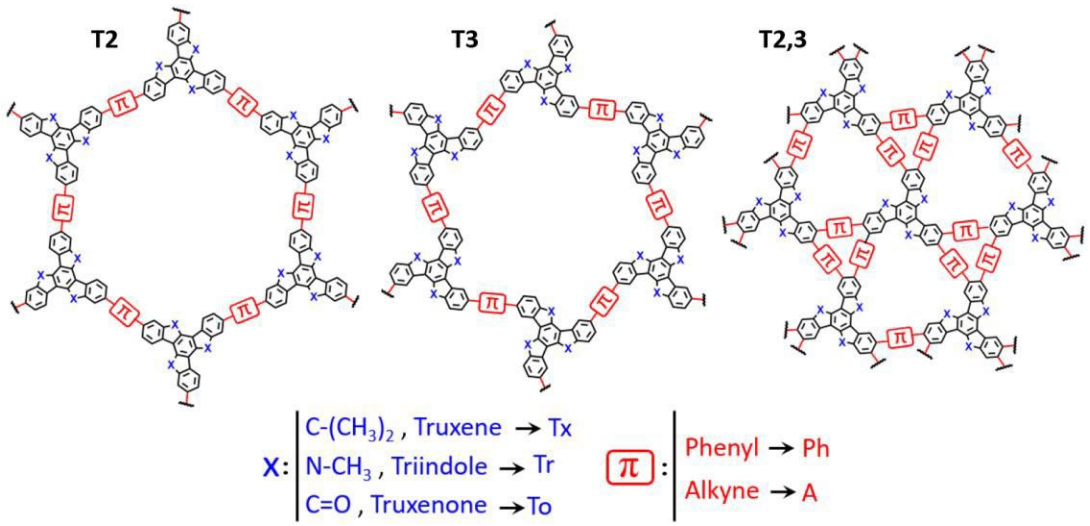

Figure II.11. Idealized chemical structures of the 2D-polymers studied in this section.

II.3.1. Molecular structure

We first focused on analysing the optimized ground-state structures of single-layer truxene-based 2D polymers. As we can observe in Figure II.12, pore surface engineering of these materials can be achieved by a correct structural design. Whereas hexagonal mesopores defined by an accessible pore diameter up to 26 Å are predicted for **T2** and **T3** polymers, **T2,3** polymers display both hexagonal and triangular micropores defined by accessible pore diameters of ~6-11 Å and ~4-6 Å, respectively (see Figure II.13). Interestingly, the pore size can be modulated by the insertion of π-bridges between the cores (*i.e.*, increases of 8 and 4 Å were predicted for **T2** and **T3** polymers by introduction of phenylene and alkyne linking groups, respectively) or by changing the linkage position (*i.e.*, the pore size decreases by ~5 Å when going from *para*-connected **T2** to *meta*-connected **T3** polymers). It is interesting to remark that the wide range of pore sizes and geometries could bring novel functionalities to these polymers, such as multi-selectivity, which can be exploited in versatile applications in the field of adsorption and separation science.[40-42]

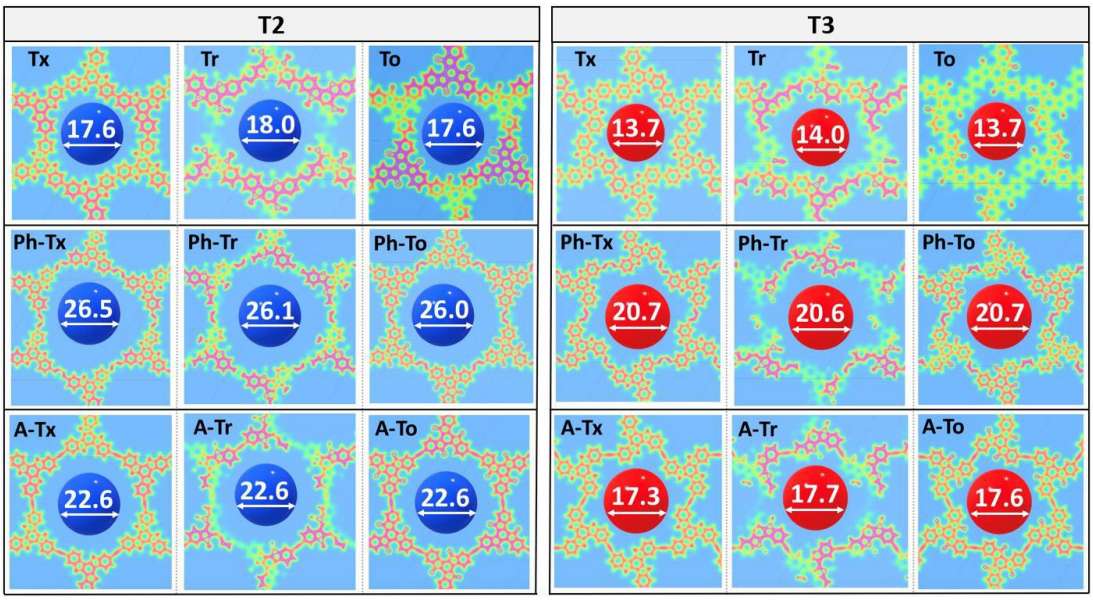

Figure II.12. DFT-calculated (PBE0-D3) surface charge density colour maps in the xy-plane (at the z-position) for **T2** and **T3**-based polymeric layers. Accessible pore diameter (Å) values are also shown.

Optimized periodic single layers predict that **Tx**- and **To**-based polymers show almost planar chemical structures, especially for the latter where favourable intramolecular interactions between the ketone groups and the hydrogen atoms of adjacent benzene rings (with C=O•••H distances of 2.12 Å) take place. This is not the case of **Tr**-homologues, which have a moderately distorted configuration as a consequence of the steric hindrance between the only existing methyl group and the hydrogen atoms of the outermost benzene rings. This structural feature plays a key role in the electronic total charge distribution of these 2D materials. In fact, the analysis of the colour total electronic charge distribution maps at the cutting-xy-plane (increasing charge density from the light green to the red/purple regions) reveals slightly inhomogeneous electronic charge distribution in specific regions for **Tr**-polymers due to out-of-plane distortions of the structures. It is worth to mention that the distorted configuration of the **Tr**-based monolayers will influence the preferential interlayered bulk stacking, as discussed below.

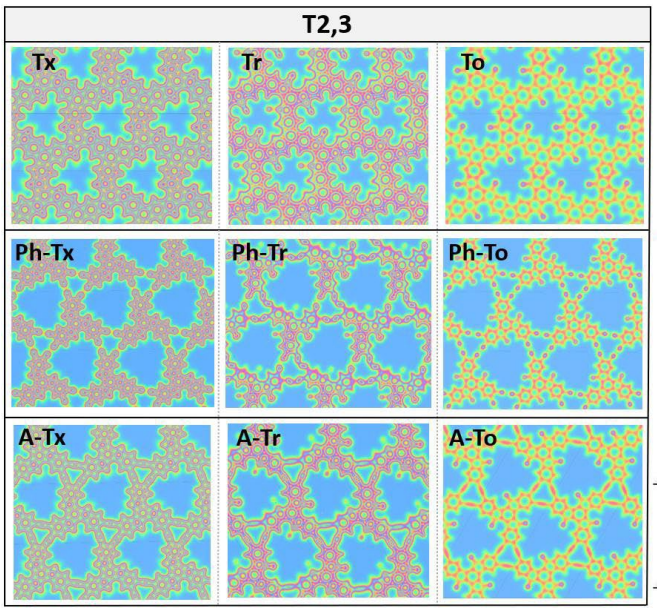

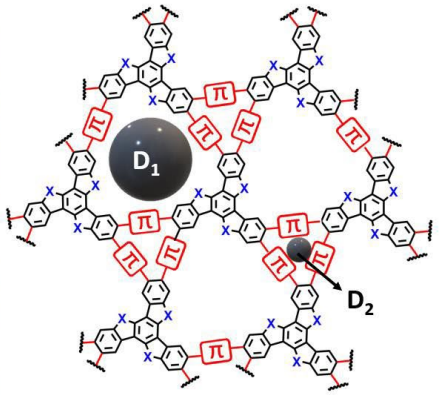

	D_1	D_2		D_1	D_2		D_1	D_2
Tx	**6.3**		Ph-Tx	**11.2**	**5.1**	A-Tx	**9.5**	**4.1**
Tr	**6.0**		Ph-Tr	**11.4**	**5.3**	A-Tr	**9.0**	**4.1**
To	**5.9**		Ph-To	**11.3**	**5.1**	A-To	**9.2**	**4.1**

Figure II.13. DFT-calculated (PBE0-D3) surface charge density colour maps in the xy-plane (at the z-position) for **T2,3**-based polymeric layers. Accessible pore diameter (Å) values are also shown.

Importantly, a more homogeneous electronic charge distribution can be observed for **Tr**-polymers when the number of linking units increase from three to six units in **T2,3**, suggesting more extended and coplanar skeletons specially in the cases where the cores are directly linked (due to the formation of fully fused benzene rings) or when alkyne groups are connecting the cores (see Figure II.13). In order to further understand the influence of these structural modifications on the π-electron delocalization along the polymeric backbone, we have examined the electronic band structures of the 2D-polymers under study.

II.3.2. Electronic band structures of the single-layer 2D-polymers

A first interesting finding that can be extracted from the band structures is that these polymers can be classified as semiconducting 2D-materials with energy bandgap values in the range of 1.1-3.1 eV, as shown in Figure II.14.

In view of the calculated data, the following observations can be pointed out: (i) a bandgap decrease is predicted when going from **Tx-** and **Tr-** to **To**-based polymers, with values of 2.37, 2.22 and 1.77 eV for **Tx2**, **Tr2** and **To2**, respectively. (ii) On the other hand, a notable bandgap increase can be observed when changing the linkage position from *para* to *meta* connections, suggesting more effective conjugation pathways in the **T2** polymers compared to its **T3** isomers. (iii) The insertion of phenylene π-spacer groups slightly increases the bandgaps in the trisubstituted **T2** and **T3**, being this effect even more remarkable in the case of the hexasubstituted **T2,3** polymers. This effect can be ascribed to the more twisted structures of **Ph-T2,3** polymers where three-dimensional cyclic cavities are created between the three phenylene units connecting the cores, thus decreasing the electronic conjugation between the cores. (iv) Finally, a significant decrease of the bandgap was observed in the alkyne-connected 2D polymers, with the lowest value of 1.17 eV found for **A-To2,3**, indicating that the flat truxenone platforms hexasubstituted with alkyne linking groups facilitate the extension of the electronic conjugation and enable better electronic communication between the C_3 symmetry cores.

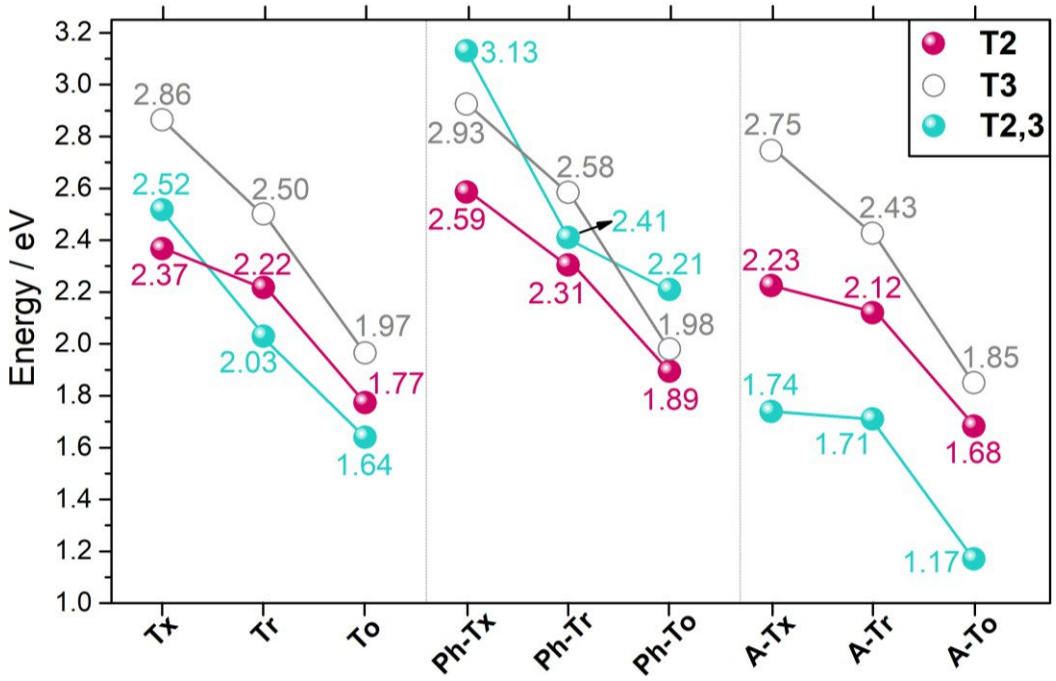

Figure II.14. Comparison of the DFT-calculated bandgap values (PBE0-D3) for all the 2D-polymers under study.

Then, we focus on the DFT-calculated (at PBE0-D3 level) electronic band structures of these 2D-polymers. Only a few cases will be discussed as representative examples. Starting from the trisubstituted **T2** and **T3**-based polymers, all of them belong to the class of honeycomb-Kagome hexagonal lattices with the honeycomb lattice sites occupied by the three-armed platforms (grey dots in Figure II.15a) and the Kagome lattice sites occupied by the connecting points between them (red dots in Figure II.15a). In this way, each node of the honeycomb lattice has three nearest neighbors on the Kagome lattice while each node on the Kagome has two nearest neighbors on the honeycomb lattice.[43, 44]

The DFT-PBE-D3 band structure of the directly connected 2D-polymeric lattices are displayed in Figure II.15b. The most striking feature is that the bottom conduction band and the top valence band are both totally flat in all the cases. In this context, a flat band means an infinite effective mass for charge carriers injected into these bands, which translates into fully localized charge carriers and thus, low charge carrier mobilities.

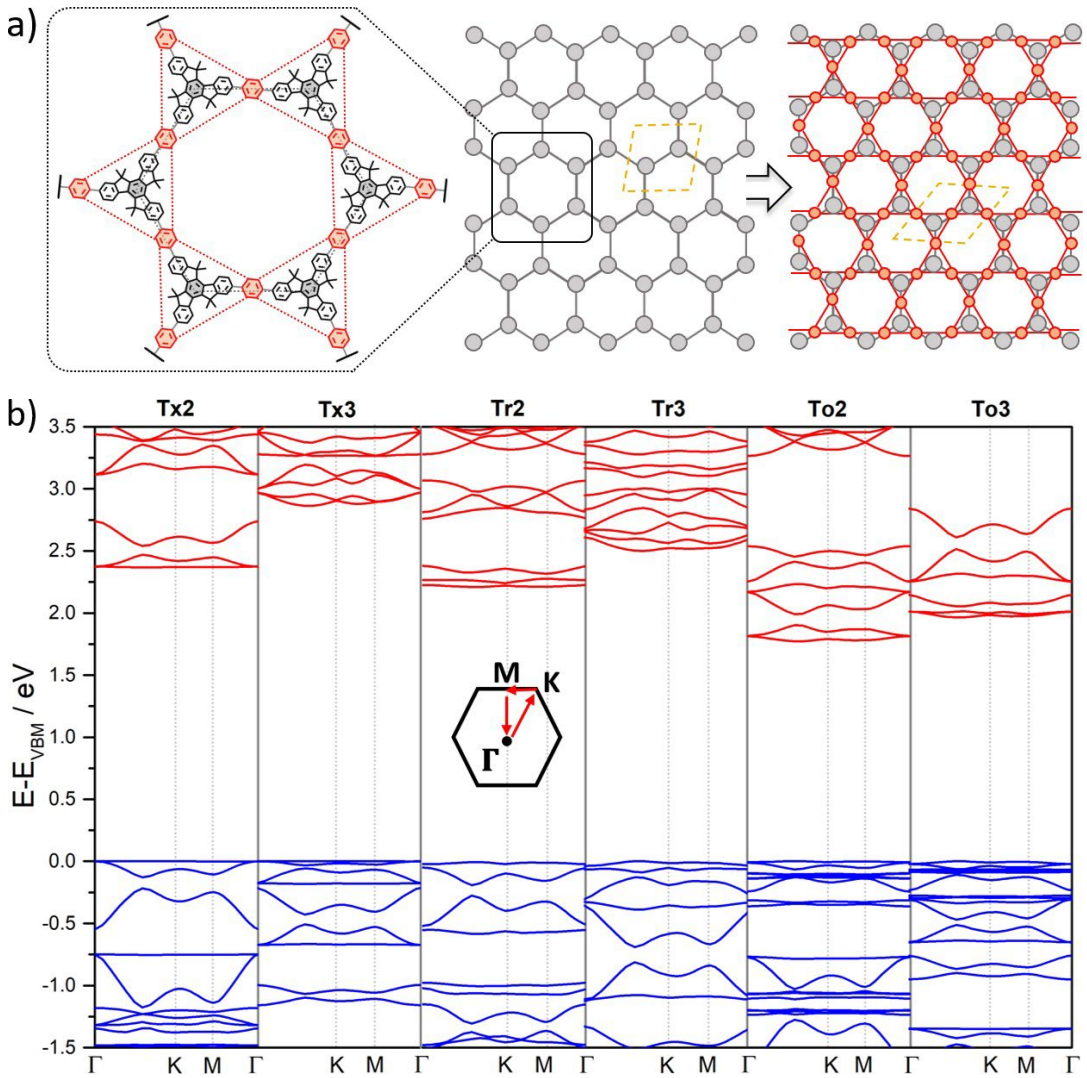

Figure II.15. (a) illustration of how the 2D honeycomb lattice (grey balls) transform into a Kagome lattice (red balls). The primitive unit cells, highlighted in orange are also shown. (b) DFT-calculated (at PBE0-D3 level) electronic band structures for the directly connected 2D-polymers. The valence and conduction bands are marked in blue and red, respectively. The zero energy is taken to correspond to the valence band maximum (E_{VBM}) while the x-axis labels denote a path through the 2D-space of k-vectors. Points of high symmetry in the Brillouin zone are labeled as Γ (0,0,0), M (0,1/2,0) and K (1/3,2/3,0), all in reciprocal space crystal coordinates.

Only a very slight gain of bands dispersion is observed when the cores are directly connected through *meta* connections (**T3**).

Interestingly, each flat band is degenerate at the Γ point with a dispersive sub-band, suggesting that both light and heavy mass carriers could therefore coexist at high temperatures.[45]

Since the totally flat character of the bands around the Fermi level is retained by the insertion of phenylene or alkyne π-bridges between the cores and changing the linkage position between them (whose electronic band structures have been omitted), it is conceivable that the origin of the flat bands is in fact topological, meaning that it is a direct consequence of its kagome symmetry and more precisely, due to destructive interference in the wavefunctions of adjacent sites on the lattices.[46-48]

When the interest lies in 2D conjugated polymers with high charge-carrier mobilities, it is essential to seek chemical structures and lattice topologies that favor highly dispersive bands around the Fermi energy. However, in other contexts flat bands can be appealing, for instance, in terms of properties related to superconductivity[49] or magnetism.[50] Since honeycomb-Kagome hexagonal lattices built from this kind of C_3 symmetry platforms essentially lead to flat bands that are undesirable from a carrier mobility point of view, it is useful at this stage to evaluate the replacing of the lattice topology. For that, we have computed the electronic band structures of **T2,3** polymers, in which the combination of both 2,7,12 and 3,8,13 connecting positions leads to polymer lattices with a triangular structure, in which each C_3 symmetry platform coordinates with six neighbours (Figure II.16a-b).

By looking the DFT-PBE0-D3 band structures for the directly connected hexasustituted **T2,3** porous polymers (Figure II.16c), we can see that in marked contrast to the honeycomb-Kagome lattices calculated for the trisustituted systems, the electronic structures of porous polymers based on six-armed cores result in more dispersive bands. In this context, it is worth noting that the more dispersive the valence band (conduction band) at the VB maximum (CB minimum), the smaller the hole (electron) effective mass and thus the larger the expected charge-carrier mobility.

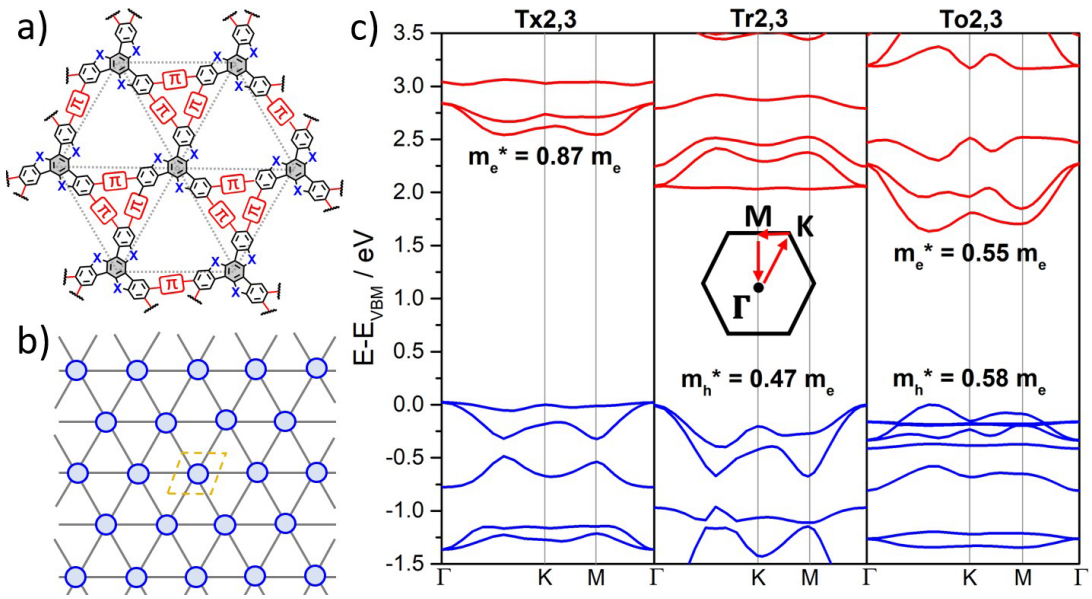

Figure II.16. (a) Atomistic structure of a 2D polymer with triangular lattice and (b) scheme of this kind of lattice (with the unit cell marked in light blue). (C) DFT-calculated (at PBE0-D3 level) electronic band structures for the directly connected **T2,3** polymers. The valence and conduction bands are marked in blue and red, respectively. The zero energy is taken to correspond to the valence band maximum (E_{VBM}) while the x-axis labels denote a path through the 2D-space of the k-vectors. Points of high symmetry in the Brillouin zone are labeled as Γ (0,0,0), M (0,1/2,0) and K (1/3,2/3,0), all in reciprocal space crystal coordinates.

Particularly large variation of the bandwidths was found for the **T2,3** polymers, with values in the range of 26-400 meV for the CB and 6-633 meV for the VB (see Figure II.17). In fact, large CB bandwidths and low effective masses for electron were found for **Tx2,3** (m_e*=0.87 m_e) and **A-To2,3** (m_e*=1.26 m_e) polymers, making them promising electron charge-transport 2D materials. On the other hand, large VB bandwidths and low effective masses for holes were found for **Tr2,3** (m_h*=0.47 m_h) and **A- Tr2,3** (m_h*=1.21 m_h) polymers, making them promising hole charge-transport 2D materials. Curiously, large bandwidths for both CB and VB (and thus, low hole and electron effective masses) were predicted for **To2,3** (m_h*=0.58 m_h and m_e*=0.55 m_e), suggesting that polymers as attractive ambipolar charge carrier material. It should be noted that phenylene-spaced polymers (**Ph-T2,3**) retain the low CB and VB bandwidths (see Figure II.17). This fact suggests that these linkers effectively

reduce the electronic couplings among the C_3 symmetry cores, vanishing the next-nearest-neighbor interactions. This effect is in line with the more twisted structure predicted for Ph-based polymers which vanishes the electronic delocalization along the polymeric backbone. From the differences between the triangular and the honeycomb-Kagome nets, we see that the network connectivities are determinant for forming the electronic band structures. In this sense, the directly connected hexasustituted **T2,3** porous polymers and their alkyne-spaced analogous can be considered promising candidates for optoelectronic applications as evidenced by their large bandwidths and low effective masses.

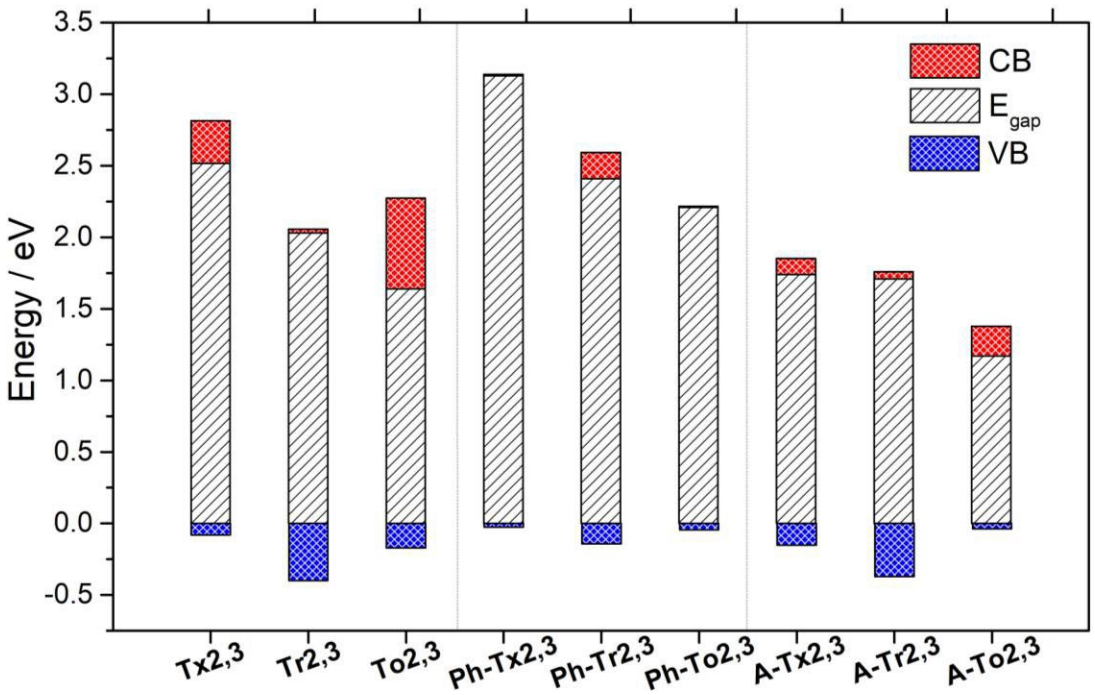

Figure II.17. DFT-calculated bandgap and bandwidth values (PBE0-D3) for the conduction and valence bands of **T2,3** polymers. The zero energy is taken to correspond to the VB maximum.

Interestingly, it should be mentioned that a favorable electronic coupling between the cores of the adjacent layers may clearly increase the bandwidths along the vertical direction. In order to reinforce this hypothesis, we have analyzed the preferential interlayer stacking of selected 2D polymers.

II.3.3. Preferential interlayer stacking of 2D-polymers

As shown in Figure II.18, the infinite crystal-bulk in both AA and AB stacking configurations were computed for the alkyne-based trisubstituted polymers (which showed more pronounced band dispersion at the intralayer level), in order to check the preferential interlayered bulk-stacking fashion adopted by the layers. Other intermediate configurations between AA and AB stacking were analyzed, rendering unfavorable cohesive energies E_c compared with the canonical AA and AB stacking modes. Since the inter-layer cohesive energies were computed as the difference between the total energies of the crystal bulks and the optimized corresponding single-layers, a more negative E_c value renders a more favorable interlayered bulk-stacking.

	Stacking	L (Å)	E_c (Kcal/mol)
A-Tx2	AA	3.86	+87.75
	AB	3.22	-34.20
A-Tr2	AA	3.79	-35.67
	AB	2.21	-58.80
A-To2	AA	4.12	-46.42
	AB	4.25	-24.12
A-Tx3	AA	3.94	+341.08
	AB	3.23	-36.83
A-Tr3	AA	3.79	-36.00
	AB	2.49	-67.01
A-To3	AA	4.20	-33.24
	AB	4.38	-28.07

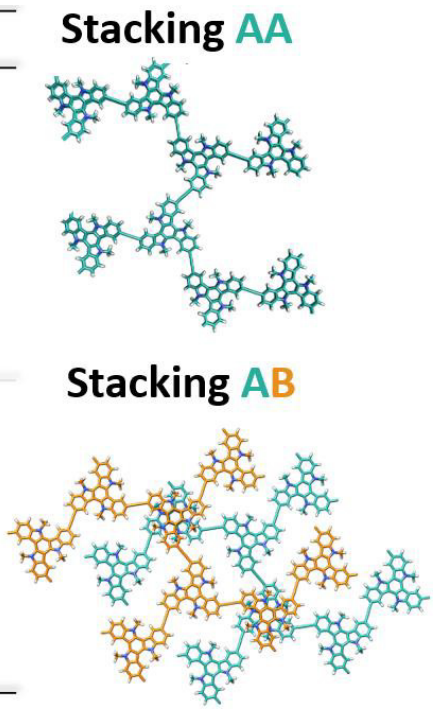

Figure II.18. Computed data (PBE0-D3) of the optimized inter-layer stacking distance (in Å) and inter-layer cohesive energy (in kcal/mol), defined as the difference between the total energy crystal-bulk and the isolated single-layer, for **A-T2** and **A-T3** polymers. Pictorial top views of the two different stacking AA and AB configurations are also shown.

As we expected, a wide range of cohesive energies were obtained for the different systems, with E_c values decreasing when inter-layer distances decrease (L values ranging between 2.21 and 4.38 Å are predicted). It is important to note that AB stacking is the preferential configuration for **A-Tr** and **A-Tx** polymers, especially for the latter where the AA stacking leads to unstable configurations (which is reflected in their high positive E_c values) due to physical steric hindrance towards stacking. In contrast, **A-To** polymers prefer to stack in AA fashion. Interestingly, these results are in excellent accordance with prevously reported X-ray data for triindole [30, 51, 52] (truxenone) [53] cores in self-assembling systems, where a preferential staggered (eclipsed) stacking configuration of the cores is adopted and for which large electronic couplings are obtained. This large electronic coupling between the cores of adjacent layers may increase the bandwidth along the vertical direction and probably give rise to the high carrier mobility experimentally measured in **Ph-Tr2** polymer [16] despite of the flat bands predicted for **T2** and **T3**-based single-layer polymers.

II.4. Conclusions

Considering the results obtained from the Section II.2 of this chapter, regarding the role that the different π-bridges and linkage position of the conjugated building blocks exhibits on the opto-electronic properties of the microporous polymers, the following conclusions can be established:

- Both experimental (UV–vis absorption, emission, and Raman spectroscopies) and computational results point to the fact that connecting the truxene building blocks through the 2,7,12 positions results in better electronic communication between the covalently linked monomers, thus strongly influencing the extension on the conjugation and reducing the band gap of the final materials.

- The insertion of a phenylene group between the C_3 symmetry cores barely affect the optoelectronic properties of these polymers, suggesting a weak influence on the π-electron delocalization between the conjugated scaffolds. Nevertheless, the insertion of BTD π-bridges not only entail an increase on the inherent porosity, but also involve

a more efficient π-electron delocalization across de structure dramatically narrowing the band gap due to a notable stabilization of the CB. This effect is attributed to the inherent donor-acceptor nature of BTD-based porous polymers, which is corroborated by the appearance of low energy absorption bands ascribed to an ICT process on their absorption spectra.

- From a theoretical point of view, it has been probed that quantum chemical calculations of molecular fragments provide relevant information about the molecular and electronic structure of porous polymeric networks, providing a very good agreement between the results obtained from the dimeric models and those obtained at the PBC level for 2D layers.

- The potential use of these porous organic polymers for the detection of DNT, NB and NBN electron deficient nitroaromatics analytes has been demonstrated. Sensing efficiency has been proved to be remarkably influenced by the different linkage position of the C_3-simmetry scaffolds, with the **Ph-Tx3-CMP** polymer showing the most efficient sensing properties.

On the other hand, the results shown in Section II.3 from the exhaustive theoretical study of 27 different 2D-polymers based on C_3-symmetric platforms have helped us to draw key structure–property relationships for understanding the charge transport behavior of these systems. In this sense, the following conclusions can be pointed out:

- On the basis of the theoretical data, wide tuning of the structural (*i.e.*, geometry and pore size) and electronic properties (*i.e.* band-gap and band dispersion) can be achieved in these 2D-polymers by suitable selection of the C_3-based symmetry building blocks and the nature and position of the connecting π-spacers. In fact, optimized periodic single layers predict a notable bandgap decrease when going from **Tx-** and **Tr-** to **To**-based polymers, by changing the linkage position from **T3** and **T2** to **T2,3** connections or by insertion of alkyne π-spacer groups. The insertion of phenylene

π-spacer groups slightly increases the bandgaps of the trisubstituted **T2** and **T3** polymers, with this effect being more noticeable in hexasubstituted polymers.

- The incipient C_3-based symmetry platforms together with the properties conferred by the presence of honeycomb-Kagome lattices, directly lead to flat bands in **T2** and **T3** polymers that are undesirable from a carrier mobility point of view. To solve this obstacle, we build triangular nets combining both 2,7,12 and 3,8,13 connecting positions in **T2,3** polymers. From the differences between the hexagonal and the triangular nets, we see that the network connectivities are determinant for forming dispersive electronic band structures since large bandwidths and low effective masses (and thus, high charge carrier mobilities) are predicted for 2D-polymers with six-armed cores. Particularly, the directly connected (**Tx2,3**, **Tr2,3** and **To2,3**) or alkyne-spaced (**A-Tr2,3** and **A-To2,3**) polymers are found to be potential charge carrier transport materials.

- Preferential interlayered stacking is also expected to positively affects electronic couplings between the cores, which may increase the bandwidths along the vertical direction, and thus the charge-carrier mobilities. This fact explains the high mobility experimentally measured for **Ph-Tr2** in spite of the DFT-calculated flat bands for **T2** and **T3** polymers.

In summary, the results of this chapter highlight the importance of understanding the structure-property relationships to stablish new design tools for tuning the electronic properties of these electroactive porous polymers with emerging real-life applications.

II.5. References

[1] Fratini, S.; Nikolka, M.; Salleo, A.; Schweicher, G.; Sirringhaus, H., Charge transport in high-mobility conjugated polymers and molecular semiconductors. *Nature materials* **2020,** 19, (5), 491-502.

[2] Yang, J.; Zhao, Z.; Wang, S.; Guo, Y.; Liu, Y., Insight into high-performance conjugated polymers for organic field-effect transistors. *Chem* **2018,** 4, (12), 2748-2785.

[3] Huang, F.; Bo, Z.-s.; Geng, Y.-h.; Wang, X.-h.; Wang, L.-x.; Ma, Y.-g.; Hou, J.-h.; Hu, W.-p.; Pei, J.; Dong, H.-l., Study on optoelectronic polymers: an overview and outlook. *Acta Polym. Sin* **2019,** 50, 988-1046.

[4] Wang, B.; Facchetti, A., Mechanically flexible conductors for stretchable and wearable e-skin and e-textile devices. *Advanced Materials* **2019,** 31, (28), 1901408.

[5] Sirringhaus, H., 25th Anniversary Article: Organic Field-Effect Transistors: The Path Beyond Amorphous Silicon. *Advanced Materials* **2014,** 26, (9), 1319-1335.

[6] Dong, H.; Hu, W., Multilevel investigation of charge transport in conjugated polymers. *Accounts of Chemical Research* **2016,** 49, (11), 2435-2443.

[7] Yao, Y.; Dong, H.; Liu, F.; Russell, T. P.; Hu, W., Approaching intra-and interchain charge transport of conjugated polymers facilely by topochemical polymerized single crystals. *Advanced Materials* **2017,** 29, (29), 1701251.

[8] Waller, P. J.; Gándara, F.; Yaghi, O. M., Chemistry of Covalent Organic Frameworks. *Accounts of Chemical Research* **2015,** 48, (12), 3053-3063.

[9] Liu, W.; Loh, K. P., Two-dimensional conjugated polymers based on C–C coupling. *Accounts of Chemical Research* **2017,** 50, (3), 522-526.

[10] Guadalupe, J.; Ray, A. M.; Maya, E. M.; Gómez-Lor, B.; Iglesias, M., Truxene-based porous polymers: from synthesis to catalytic activity. *Polymer Chemistry* **2018,** 9, (36), 4585-4595.

[11] Valverde-González, A.; Lopez Calixto, C. G.; Barawi, M.; Gomez-Mendoza, M.; de la Peña O'Shea, V. c. A.; Liras, M.; Gómez-Lor, B.; Iglesias, M., Understanding charge transfer mechanism on effective truxene-based porous polymers–TiO2 hybrid photocatalysts for hydrogen evolution. *ACS Applied Energy Materials* **2020,** 3, (5), 4411-4420.

[12] Echeverri, M.; Gámez-Valenzuela, S.; González-Cano, R. C.; Guadalupe, J.; Cortijo-Campos, S.; López Navarrete, J. T.; Iglesias, M.; Ruiz Delgado, M. C.; Gómez-Lor, B., Effect of the Linkage Position on the Conjugation Length of Truxene-Based Porous Polymers: Implications for Their Sensing Performance of Nitroaromatics. *Chemistry of Materials* **2019**.

[13] Liu, X.; Xu, Y.; Jiang, D., Conjugated Microporous Polymers as Molecular Sensing Devices: Microporous Architecture Enables Rapid Response and Enhances Sensitivity in Fluorescence-On and Fluorescence-Off Sensing. *Journal of the American Chemical Society* **2012,** 134, (21), 8738-8741.

[14] Li, X.-C.; Zhang, Y.; Wang, C.-Y.; Wan, Y.; Lai, W.-Y.; Pang, H.; Huang, W., Redox-active triazatruxene-based conjugated microporous polymers for high-performance supercapacitors. *Chemical Science* **2017,** 8, (4), 2959-2965.

[15] Sadak, A. E.; Karakus, E.; Chumakov, Y. M.; Dogan, N. A.; Yavuz, C. T., Triazatruxene-based ordered porous polymer: high capacity CO2, CH4, and H2 capture, heterogeneous

Suzuki–Miyaura catalytic coupling, and thermoelectric properties. *ACS Applied Energy Materials* **2020,** 3, (5), 4983-4994.

[16] Li, C.; Wang, Y.; Zou, Y.; Zhang, X.; Dong, H.; Hu, W., Two-dimensional conjugated polymer synthesized by interfacial Suzuki reaction: towards electronic device applications. *Angewandte Chemie* **2020,** 132, (24), 9489-9493.

[17] Gutzler, R.; Perepichka, D. F., π-Electron Conjugation in Two Dimensions. *Journal of the American Chemical Society* **2013,** 135, (44), 16585-16594.

[18] Baryshnikov, G. V.; Minaev, B. F.; Karaush, N. N.; Minaeva, V. A., The art of the possible: computational design of the 1D and 2D materials based on the tetraoxa[8]circulene monomer. *RSC Advances* **2014,** 4, (49), 25843-25851.

[19] Li, L.; Cai, Z.; Wu, Q.; Lo, W.-Y.; Zhang, N.; Chen, L. X.; Yu, L., Rational Design of Porous Conjugated Polymers and Roles of Residual Palladium for Photocatalytic Hydrogen Production. *Journal of the American Chemical Society* **2016,** 138, (24), 7681-7686.

[20] Li, L.; Lo, W.-y.; Cai, Z.; Zhang, N.; Yu, L., Donor–Acceptor Porous Conjugated Polymers for Photocatalytic Hydrogen Production: The Importance of Acceptor Comonomer. *Macromolecules* **2016,** 49, (18), 6903-6909.

[21] Wen, J.; Luo, D.; Cheng, L.; Zhao, K.; Ma, H., Electronic Structure Properties of Two-Dimensional π-Conjugated Polymers. *Macromolecules* **2016,** 49, (4), 1305-1312.

[22] Thomas, S.; Li, H.; Dasari, R. R.; Evans, A. M.; Castano, I.; Allen, T. G.; Reid, O. G.; Rumbles, G.; Dichtel, W. R.; Gianneschi, N. C.; Marder, S. R.; Coropceanu, V.; Brédas, J.-L., Design and synthesis of two-dimensional covalent organic frameworks with four-arm cores: prediction of remarkable ambipolar charge-transport properties. *Materials Horizons* **2019,** 6, (9), 1868-1876.

[23] Jhulki, S.; Evans, A. M.; Hao, X.-L.; Cooper, M. W.; Feriante, C. H.; Leisen, J.; Li, H.; Lam, D.; Hersam, M. C.; Barlow, S.; Brédas, J.-L.; Dichtel, W. R.; Marder, S. R., Humidity Sensing through Reversible Isomerization of a Covalent Organic Framework. *Journal of the American Chemical Society* **2020,** 142, (2), 783-791.

[24] Echeverri, M.; Gámez-Valenzuela, S.; González-Cano, R. C.; Guadalupe, J.; Cortijo-Campos, S.; López Navarrete, J. T.; Iglesias, M.; Ruiz Delgado, M. C.; Gómez-Lor, B., Effect of the Linkage Position on the Conjugation Length of Truxene-Based Porous Polymers: Implications for Their Sensing Performance of Nitroaromatics. *Chemistry of Materials* **2019,** 31, (17), 6971-6978.

[25] Gámez-Valenzuela, S.; Echeverri, M.; Gómez-Lor, B.; Martínez, J. I.; Ruiz Delgado, M. C., In silico design of 2D polymers containing truxene-based platforms: insights into their structural and electronic properties. *Journal of Materials Chemistry C* **2020,** 8, (43), 15416-15425.

[26] Ruiz, C.; López Navarrete, J. T.; Ruiz Delgado, M. C.; Gómez-Lor, B., Triindole-Bridge-Triindole Dimers as Models for Two Dimensional Microporous Polymers. *Organic Letters* **2015,** 17, (9), 2258-2261.

[27] Liu, B.; Wang, Y.; Sun, H.; Gámez-Valenzuela, S.; Yan, Z.; Feng, K.; Uddin, M. A.; Koh, C.; Zhou, X.; López Navarrete, J. T.; Ruiz Delgado, M. C.; Meng, H.; Niu, L.; Woo, H. Y.; Ponce Ortiz, R.; Guo, X., Backbone Configuration and Electronic Property Tuning of Imide-

Functionalized Ladder-Type Heteroarenes-Based Polymer Acceptors for Efficient All-Polymer Solar Cells. *Advanced Functional Materials* **2022,** 32, (21), 2200065.

[28] Scott, A. P.; Radom, L., Harmonic Vibrational Frequencies: An Evaluation of Hartree−Fock, Møller−Plesset, Quadratic Configuration Interaction, Density Functional Theory, and Semiempirical Scale Factors. *The Journal of Physical Chemistry* **1996,** 100, (41), 16502-16513.

[29] Wilson, E. B. D. J. C. C. P. C., *Molecular vibrations : the theory of infrared and Raman vibrational spectra*. McGraw-Hill: New York, 1955.

[30] Ruiz, C.; Pandey, U. K.; Termine, R.; García-Frutos, E. M.; López-Espejo, G.; Ortiz, R. P.; Huang, W.; Marks, T. J.; Facchetti, A.; Ruiz Delgado, M. C.; Golemme, A.; Gómez-Lor, B., Mobility versus Alignment of a Semiconducting π-Extended Discotic Liquid-Crystalline Triindole. *ACS Applied Materials & Interfaces* **2016,** 8, (40), 26964-26971.

[31] Gámez-Valenzuela, S.; Benito-Hernández, A.; Echeverri, M.; Gutierrez-Puebla, E.; Ponce Ortiz, R.; Ruiz Delgado, M. C.; Gómez-Lor, B., Functionalized Crystalline N-Trimethyltriindoles: Counterintuitive Influence of Peripheral Substituents on Their Semiconducting Properties. *Molecules* **2022,** 27, (3), 1121.

[32] Yang, J.-S.; Swager, T. M., Fluorescent Porous Polymer Films as TNT Chemosensors: Electronic and Structural Effects. *Journal of the American Chemical Society* **1998,** 120, (46), 11864-11873.

[33] Namgung, H.; Lee, J. J.; Gwon, Y. J.; Lee, T. S., Synthesis of tetraphenylethylene-based conjugated microporous polymers for detection of nitroaromatic explosive compounds. *RSC Advances* **2018,** 8, (60), 34291-34296.

[34] Mothika, V. S.; Räupke, A.; Brinkmann, K. O.; Riedl, T.; Brunklaus, G.; Scherf, U., Nanometer-Thick Conjugated Microporous Polymer Films for Selective and Sensitive Vapor-Phase TNT Detection. *ACS Applied Nano Materials* **2018,** 1, (11), 6483-6492.

[35] Geng, T.-M.; Li, D.-K.; Zhu, Z.-M.; Zhang, W.-Y.; Ye, S.-N.; Zhu, H.; Wang, Z.-Q., Fluorescent conjugated microporous polymer based on perylene tetraanhydride bisimide for sensing o-nitrophenol. *Analytica Chimica Acta* **2018,** 1011, 77-85.

[36] Zhang, Q.; Yu, S.; Wang, Q.; Xiao, Q.; Yue, Y.; Ren, S., Fluorene-Based Conjugated Microporous Polymers: Preparation and Chemical Sensing Application. *Macromolecular Rapid Communications* **2017,** 38, (23), 1700445.

[37] Novotney, J. L.; Dichtel, W. R., Conjugated Porous Polymers For TNT Vapor Detection. *ACS Macro Letters* **2013,** 2, (5), 423-426.

[38] Toal, S. J.; Trogler, W. C., Polymer sensors for nitroaromatic explosives detection. *Journal of Materials Chemistry* **2006,** 16, (28), 2871-2883.

[39] Sun, X.; Wang, Y.; Lei, Y., Fluorescence based explosive detection: from mechanisms to sensory materials. *Chemical Society Reviews* **2015,** 44, (22), 8019-8061.

[40] Liang, R.-R.; Xu, S.-Q.; Zhang, L.; A, R.-H.; Chen, P.; Cui, F.-Z.; Qi, Q.-Y.; Sun, J.; Zhao, X., Rational design of crystalline two-dimensional frameworks with highly complicated topological structures. *Nature Communications* **2019,** 10, (1), 4609.

[41] Zhou, T.-Y.; Xu, S.-Q.; Wen, Q.; Pang, Z.-F.; Zhao, X., One-Step Construction of Two Different Kinds of Pores in a 2D Covalent Organic Framework. *Journal of the American Chemical Society* **2014,** 136, (45), 15885-15888.

[42] Nagai, A.; Guo, Z.; Feng, X.; Jin, S.; Chen, X.; Ding, X.; Jiang, D., Pore surface engineering in covalent organic frameworks. *Nature Communications* **2011,** 2, (1), 1-8.
[43] Syôzi, I., Statistics of Kagomé Lattice. *Progress of Theoretical Physics* **1951,** 6, (3), 306-308.
[44] Barreteau, C.; Ducastelle, F.; Mallah, T., A bird's eye view on the flat and conic band world of the honeycomb and Kagome lattices: towards an understanding of 2D metal-organic frameworks electronic structure. *Journal of Physics: Condensed Matter* **2017,** 29, (46), 465302.
[45] ANDREVV, A., A., THE BAND EDGE STRUCTURE OF THE IV-VI SEMICONDUCTORS. *J. Phys. Colloques* **1968,** 29, (C4), C4-50-C4-61.
[46] Asano, K.; Hotta, C., Designing Dirac points in two-dimensional lattices. *Physical Review B* **2011,** 83, (24), 245125.
[47] Wang, J.; Deng, S.; Liu, Z.; Liu, Z., The rare two-dimensional materials with Dirac cones. *National Science Review* **2014,** 2, 22-39.
[48] Thomas, S.; Li, H.; Zhong, C.; Matsumoto, M.; Dichtel, W. R.; Bredas, J.-L., Electronic Structure of Two-Dimensional π-Conjugated Covalent Organic Frameworks. *Chemistry of Materials* **2019,** 31, (9), 3051-3065.
[49] Volovik, G. E., Graphite, Graphene, and the Flat Band Superconductivity. *JETP Letters* **2018,** 107, (8), 516-517.
[50] Tasaki, H., From Nagaoka's Ferromagnetism to Flat-Band Ferromagnetism and Beyond: An Introduction to Ferromagnetism in the Hubbard Model. *Progress of Theoretical Physics* **1998,** 99, (4), 489-548.
[51] García-Frutos, E. M.; Gutierrez-Puebla, E.; Monge, M. A.; Ramírez, R.; Andrés, P. d.; Andrés, A. d.; Gómez-Lor, B., Crystal structure and charge-transport properties of N-trimethyltriindole: Novel p-type organic semiconductor single crystals. *Organic Electronics* **2009,** 10, (4), 643-652.
[52] García-Frutos, E. M.; Hennrich, G.; Gutierrez, E.; Monge, A.; Gómez-Lor, B., Self-Assembly of C3-Symmetrical Hexaaryltriindoles Driven by Solvophobic and CH–π Interactions. *The Journal of Organic Chemistry* **2010,** 75, (4), 1070-1076.
[53] Gómez-Esteban, S.; Benito-Hernandez, A.; Termine, R.; Hennrich, G.; Navarrete, J. T. L.; Ruiz Delgado, M. C.; Golemme, A.; Gómez-Lor, B., High-Mobility Self-Assembling Truxenone-Based n-Type Organic Semiconductors. *Chemistry – A European Journal* **2018,** 24, (14), 3576-3583.

Chapter III:

Extended π-conjugation effect of NDI and PDI-based semiconductors on n-type electrical properties

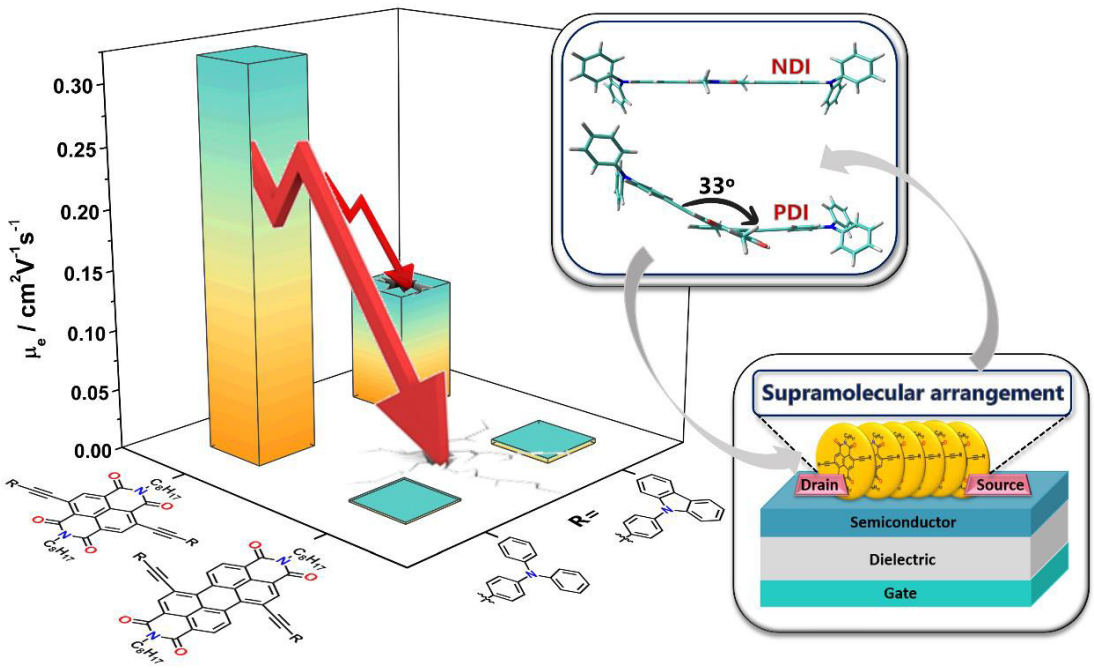

The most relevant results obtained in this study have given rise to publication 6 listed in Appendix 6.4:

6. **Gámez-Valenzuela, S**.; Torres-Moya, I.; Sánchez, A.; Donoso, B.; López Navarrete, J. T.; Ruiz Delgado, M. C.; Prieto, P.; Ponce Ortiz, R., Extended π-conjugation and structural planarity effects of novel symmetrical D-π-A-π-D naphthalene and perylene diimide semiconductors on n-type electrical properties. *In preparation*.

III.1. Introduction

Since the initial report of electrochemically grown polythiophene as semiconducting layer in an Organic Thin Films Transistor (OTFT), with a p-type (hole-transporting) mobility of $\sim 10^{-5}$ $cm^2V^{-1}s^{-1}$,[1] considerable efforts have been carried out to the design and synthesis of new materials with the high mobilities needed to realize devices capable of sustaining the switching frequencies, driving currents and device footprint required in modern electronics.[2, 3] Although mostly in a trial and error way, remarkable progress has been achieved for p-type semiconductors with hole mobilities surpassing 35 $cm^2V^{-1}s^{-1}$,[4] whereas high-performance n-type semiconductors lags behind their p-type counterparts.[5] Therefore, given that electron-transporting semiconductors are essentially required for the development of ambipolar transistors (electron and hole transporting materials) and complementary metal oxide (CMOS)-like logic circuits,[6, 7] one of the major challenges in the field of organic semiconductors is the development of n-type materials with good transport properties as well as good air and thermal stability. Fortunately, incorporation of molecular electron donor (D) and acceptor (A) units in an alternating manner has been proven one of the most promising strategies to stabilize n-type charge formation and thus, to obtain unipolar and ambipolar electron transport semiconductors with narrow bandgap associated with fine-tuned energy levels by choosing different D or A units.[8-10] Among the different A units, imide-functionalized arenes such as diketopyrrolopyrrole (DPP),[11] benzothiadiazole (BTD),[12] perylenediimide (PDI),[13] naphthalenediimide (NDI),[14] and isoindigo (IIG),[15] have demonstrated to be excellent building blocks for n-type semiconductors due to their highly electron-deficient character, chemical accessibility, good stability and the solubilizing ability provided by N-alkylation.[16] On the other hand, arylamine donor moieties such as triphenylamine (TPA) and its derivatives constitute outstanding building blocks for the design of electroactive materials for opto-electronic applications.[17-19]

In this context, we have investigated a series of four D-π-A-π-D small molecules having NDI and PDI as central acceptor cores in addition to triphenylamine and phenylcarbazole donor groups laterally linked through ethynyl bonds (Figure III.1). This study was motivated

by interest in exploring the effects of the π-conjugation extension either via (i) the enlargement of the acceptor central core going from NDI to PDI-based semiconductors or (ii) the lateral substitution with different electron rich conjugated groups on the molecular structure, energy levels and supramolecular order of the resulting n-type materials, factors which will determine the charge transport properties of the final materials.

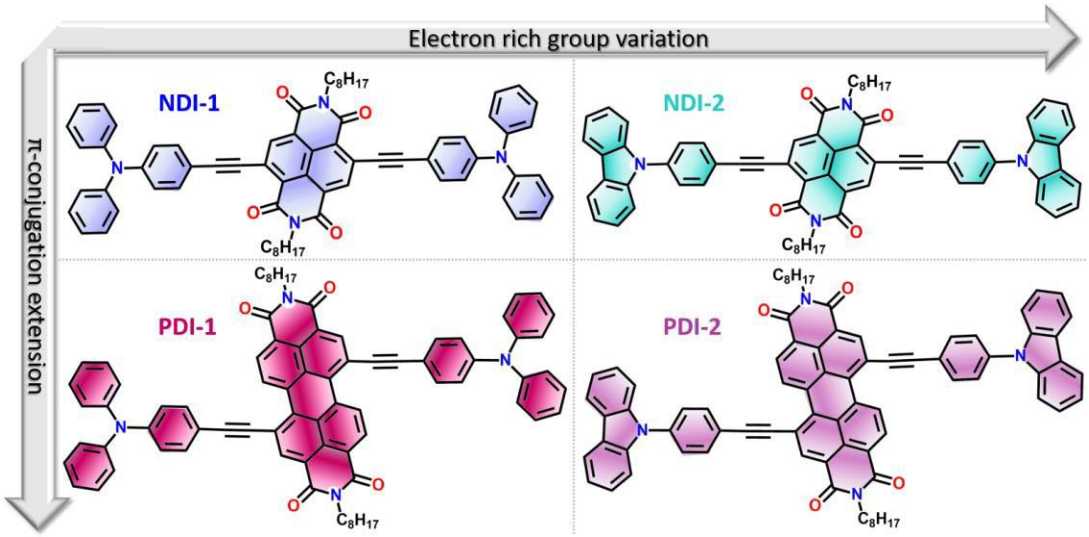

Figure III.1. Chemical structures of semiconducting **NDI** and **PDI**-based materials studied on this chapter.

To this end, a wide range of techniques such as UV-Vis absorption and emission spectroscopies, electrochemistry and OFET characterization were used, in addition to DFT calculations, performed at the B3LYP/6-31G** level of theory. M06-2X functional were also used and the results, which are comparable to those obtained at the B3LYP level, have been summarized in Appendix 6.2.2. The contributions of this study to the overall understanding of the structure-electronic properties of NDI and PDI-based semiconducting materials provide interesting guidelines to design novel n-type semiconductors.

III.2. Structural features

It is widely recognized that the molecular structure of semiconductors exerts important influences on their intermolecular interactions, which in turn, play a key role in their stacking motifs and opto-electronic performances in solid state.[20, 21] Indeed, the molecular ground-state geometries were optimized by performing density functional theory calculations at the B3LYP/6-31G** level of theory.

The results plotted in Figure III.2 indicate a totally coplanar π-conjugated backbone for NDI derivatives, while the extension of the arylene π-conjugated core on PDI-based semiconductors lead to the twisting of the two naphthalene halves of the central unit (with torsion angles about 17°) due to steric effects between the lateral substituents and the hydrogen atoms of adjacent benzene rings. Similar distortion effects on the PDI skeleton have been previously reported.[21] On the other hand, the attached lateral donor groups at 1,7 bay positions are largely distorted by ~46-50° respect to the π-conjugated backbone, independently of the π-conjugated central platform.

This data highlights the impact of the enlargement of the acceptor central core and the lateral substitution with different electron rich conjugated groups on the molecular structure, but what about the chemical aromaticity and electronic delocalization of these materials? To which extent it is affected by these structural modifications? According to that, Nucleus-Independent Chemical Shifts values at the geometrical centers of selected rings (NICS(0)), as aromaticity criterion,[22, 23] were calculated (values inside the rings in Figure III.2). As explained in Chapter I, the more negative the NICS(0) value, the more aromatic the system. On the basis of the calculated data, the aromaticity of these systems is moderately affected by the extension of the π-conjugated arylene platform. In fact, less negative NICS(0) values can be found on the naphthalene central unit for PDI-based semiconductors (with values between -4.5 and -5.1 ppm) when compared with that of their NDI counterpart (-5.7 ppm), which translates in a more delocalized quinoide-like structure.

Note that the most pronounced difference is found on the rings that bring the 1,7 bay positions, suggesting an effective electronic communication between donor and acceptor moieties in PDI-based molecules which can be justified by the more twisted central PDI platform. Considering the lateral substitution effect, a negligible influence on the chemical aromaticity can be observed. In fact, differences of NICS(0) values of -0.2 and -0.1 ppm are predicted on going from **NDI-1** to **NDI-2** and from **PDI-1** to **PDI-2**, respectively.

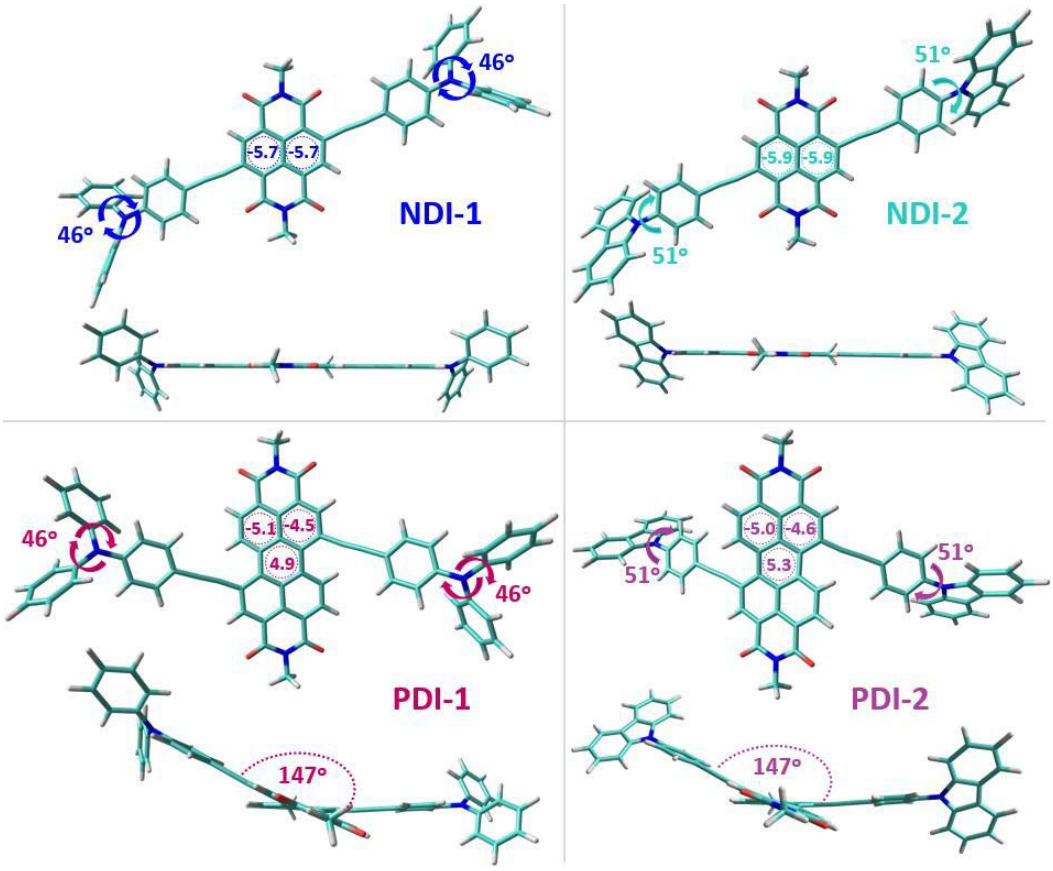

Figure III.2. Top and lateral views of the optimized geometries of NDI and PDI-based semiconductors calculated at the B3LYP/6-31G** level of theory. Dihedral angles and DFT-calculated NICS(0) values (B3LYP/6-311^{++}G(2df,p)//B3LYP/6-31G** level) for selected rings are also shown.

III.3. Optical properties

The optical properties of all compounds under study were initially studied by UV-Vis absorption and fluorescence spectroscopies. As we can observe in Figure III.3, via comparison of the absorption and emission spectra of NDI- and PDI-based semiconductors in CH_2Cl_2 solutions, the elongation of the π-conjugated arylene unit has a strong influence on the optoelectronic properties of these materials. In fact, practically superimposable absorption and emission spectra for the PDI-based semiconductors are registered, which are significantly different when compared to those of their NDI-based analogous.

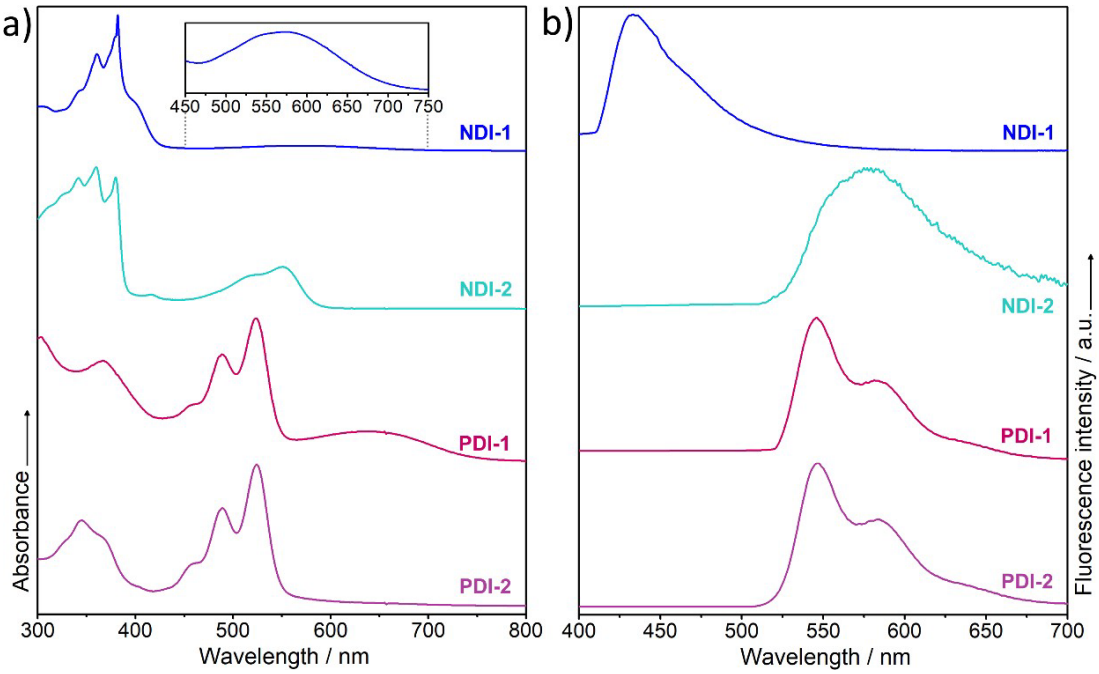

Figure III.3. (a) Normalized experimental UV absorption and (b) emission spectra of the semiconductors under study in CH_2Cl_2 suspensions at a concentration of 10^{-5} M.

Concerning the absorption spectra, spectral profiles determined by a vast number of high energy electronic transitions (with π-π* nature) and the presence of one low intense and broad band localized at lower energies can be observed. Regarding the latter absorption band, it should be noted that it is basically absent for **NDI-2** and **PDI-2** in accordance with

previously reported naphthalene and perylenediimide systems laterally substituted with phenylcarbazole groups.[24] To further understand the origin of the differences exerted by the structural modifications across the series, TD-DFT calculations have been performed to analyze the electronic nature of the main absorption bands. Focusing on the lowest energy band, TD-DFT calculations predict that this band is defined as a $S_0 \rightarrow S_1$ transition ascribed to a HOMO→LUMO one electron promotion. As we can see on the frontier molecular orbital (FMOs) topologies of Figure III.4, this $S_0 \rightarrow S_1$ electronic transition entails an electron density redistribution from the lateral electron-rich units (HOMO) to the electron deficient NDI or PDI central cores (LUMO).

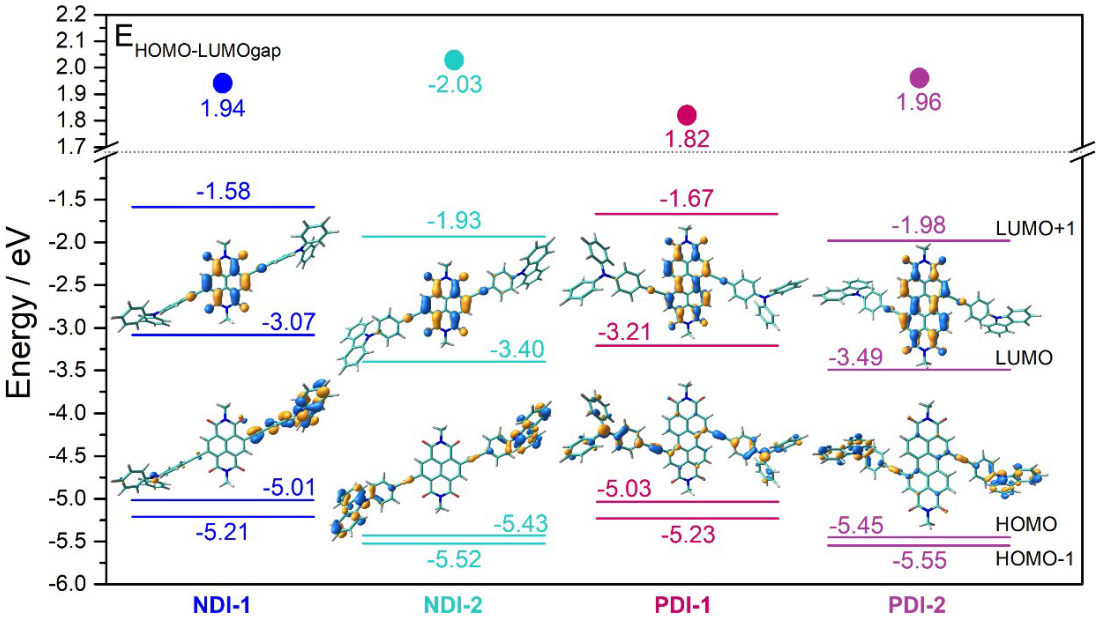

Figure III.4. DFT-calculated FMOs energies and topologies for all the compounds under study at the B3LYP/6-31G** level of theory.

However, only in triarylamine-substituted derivatives **NDI-1** and **PDI-1** this low energy band has the structureless and broad profile typical of intramolecular charge transfer (ICT) absorption bands, while it is much less intense in phenyl-carbazole derivatives **NDI-2** and **PDI-2**. This fact is intimately connected to the observed solvatochromic behavior, in which solvent polarity has a negligible influence in the photophysical properties of phenyl-

carbazole derivatives **NDI-2** and **PDI-2**, whereas both absorption and emission spectra for the triarylamine-substituted derivatives **NDI-1** and **PDI-1** display a moderate solvatochromic behavior (Figure III.5). Based on these considerations, we can confirm the ICT character of this absorption band for the compounds substituted with the strong triphenylamine donor groups.

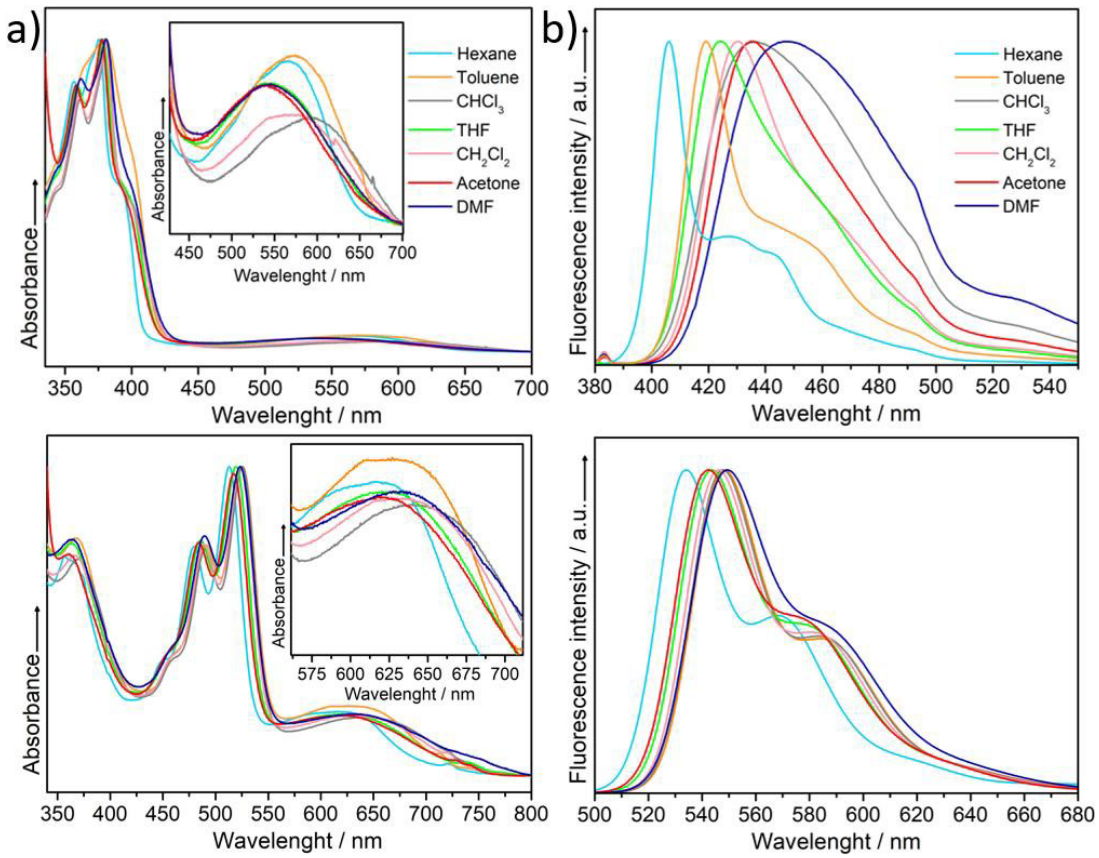

Figure III.5. (a) UV-vis absorption and (b) fluorescence spectrum variation for compounds **NDI-1** (top) and **PDI-1** (bottom), registered in different solvents at a concentration of 10^{-5} M.

Curiously, the observed solvent-dependent behavior is more accentuated for the fluorescence spectra, with emission bands shifting bathochromically as the solvent polarity increases from hexane to dimethylformamide (from 406 to 448 nm for **NDI-1** and from 534 to 549 nm for **PDI-1**). This behavior suggests a more polarized first excited S_1 state when

compared to the S_0 ground state, in line with the higher B3LYP/6-31G** predicted molecular dipole moment in the first excited state (0.58 and 7.16 D for **NDI-1** and **PDI-1**, respectively) when compared to the ground state (0.07 and 2.56 D for **NDI-1** and **PDI-1**, respectively).

Comparison of the ICT band for NDI and PDI derivatives reveals a bathochromic shift going from 572 nm in **NDI-1** to 640 nm in **PDI-1**, in line with the HOMO-LUMO gap narrowing theoretically predicted when comparing **NDI-1** vs. **PDI-1**, and **NDI-2** vs. **PDI-2**. An explanation to this effect can be found on the more extended π-conjugated central core of PDI-based compounds with respect their NDI-based homologous, resulting in a stabilization of the LUMO orbital after the elongation of the arylene unit, with minimal change of the HOMO energy level (see Figure III.4). Likewise, lateral substitution at 1,7 bay positions with electron-rich groups has a significant impact on the FMOs. In particular, the change of the lateral substituents from triphenylamine to phenylcarbazole groups induces a noticeable stabilization of both LUMO and HOMO energy levels, being slightly more pronounced in the latter and thus, provoking an increase of the HOMO-LUMO gap. This result corroborates the more electron-donating character of the triphenylamine group.

On the other hand, concerning the photoluminescence properties (Figure III.3b), the practically superimposed emission spectra of the PDI-based semiconductors upon excitation at 500 nm, suggests that the emission comes primarily from the perylenediimide core with a negligible contribution of the lateral electron-rich groups. This behavior is in line with the highly emissive nature of extended arylene diimides cores in solution.[25] Differently from PDI-based semiconductors, remarkable changes on the emission spectra of NDI-based compounds were observed (with emission maxima going from 433 to 578 nm for **NDI-1** and **NDI-2**, respectively), supporting the key role that the lateral donor groups play on the photoluminescence properties of these systems. This is related to the more limited aromatic core of NDI derivatives, which results in a less emissive response either in solution or in the solid state.[26] Furthermore, intermolecular interactions in less emissive NDI derivatives have been demonstrated to be able to enhance their emissions through the formation of excimers.[27-29] These observations anticipate that aggregation effects due to efficient

intermolecular interactions could play a key role on the photophysical properties of these NDI-based materials.

III.4. Spectroelectrochemical analysis

In order to get further insight on the ability of NDI and PDI platforms to accommodate negative charges, as a crucial aspect for electron injection and stabilization in OFETs, the evolution of the UV-Vis absorption spectra upon progressive spectroelectrochemical reduction of all the semiconductors ($c=1\times10^{-5}$ M) was recorded using an optically transparent thin layer electrochemical (OTTLE) cell in CH_2Cl_2/0.1 M $(n\text{-}Bu)_4NPF_6$ as electrolyte (Figure III.6). Focusing on the case of **NDI-1** (Figure III.6a), when the potential negatively increases the initial UV-Vis absorption spectrum of the neutral state (black curve) progressively evolves to four new absorption peaks centered at 478, 612, 674 and 747 nm (red curve), which are ascribed to the formation of radical anion species as a consequence of one electron injection on the naphthalenediimide fragment. Further electrochemical reduction provokes the vanishing of this spectral profile together with the appearance of a new one characterized by the presence of absorption bands at 395, 419, 548 and 595 nm (blue curve). This fact suggests the second electron injection on the naphthalenediimide fragment and the formation of dianion species. Clear isosbestic points can be observed in both electrochemical processes.

As can be expected considering the LUMO topology shown in Figure III.4, the injected negative charges are mainly delocalized over the naphthalenediimide fragment. To corroborate this, DFT calculations of charges species were performed, and an accommodation of around 80% of each injected charge (-0.82 and -1.50 *e* for the radical anion and dianion states, respectively) by the NDI platform was predicted, in line with previously reported data.[30, 31] A strong supportive evidence for this statement has been obtained from the practically superimposed spectral profile evolution of **NDI-2** with respect its homologous **NDI-1**, evidencing the stabilization of the negative charges by the central NDI core independently of the side groups attached to it.

On the other hand, the extension of the π-conjugated central core in **PDI-1** allows to accommodate a third negative charge on the perylendiimide moiety. In this way, the absorption spectrum of dianion species (blue curve) progressively evolves until the appearance of a new one characterized by the presence of three absorption bands between 550-650 nm (orange curves in Figures III.6c and III.6d), which are ascribed to the stabilization of radical trianion species.

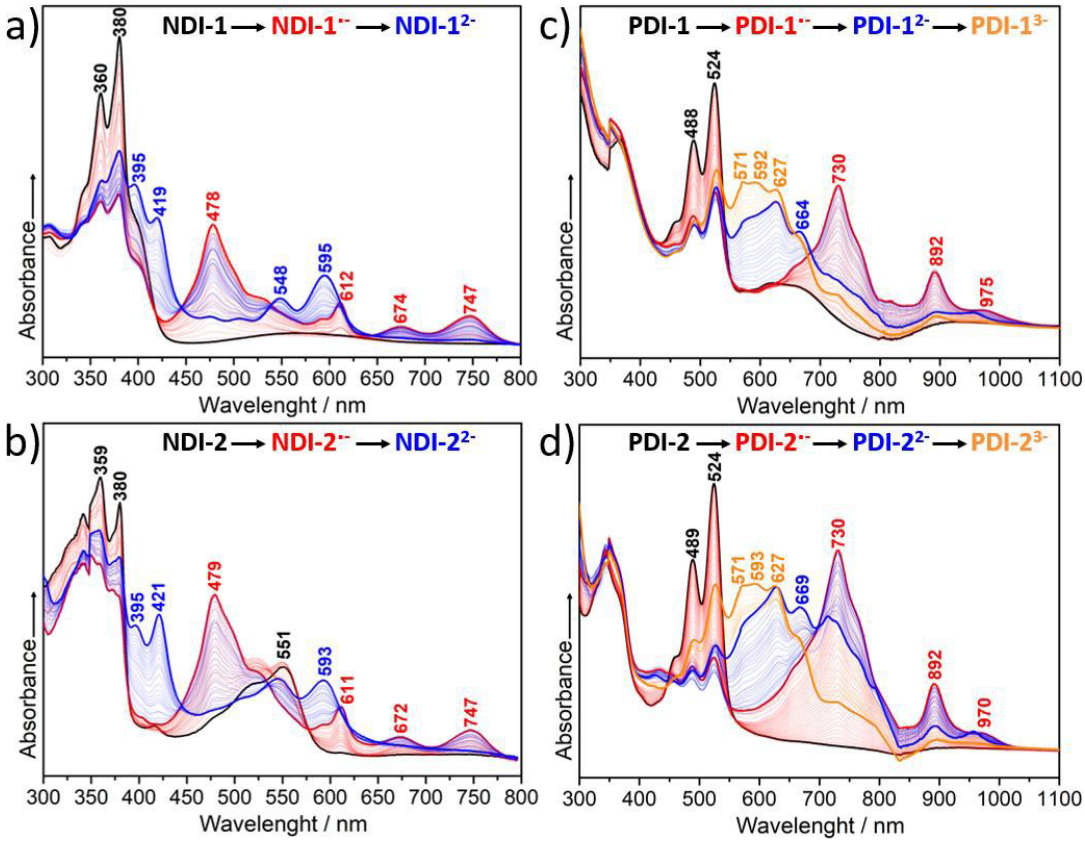

Figure III.6. In situ UV-Vis spectral changes upon electrochemical reduction of **NDI-1** (a), **NDI-2** (b), **PDI-1** (c) and **PDI-2** (d) semiconductors. The black, red, blue and orange curves represent the absorption bands for the neutral, anion, dianion and trianion states, respectively.

In this case, DFT calculations of charged species for **PDI-1** predict the accommodation of around 65% of each injected charge by the PDI platform (-0.63, -1.40 and -1.85 *e* for the radical anion, dianion and radical trianion states, respectively). Note that this percentage is

slightly lower than that predicted for the NDI molecules. Furthermore, an increment of negative charge density on the ethynyl group of **PDI-1** compared to that of **NDI-1** in their radical anion (from -0.048 *e* for **NDI-1** to -0.106 *e* for **PDI-1**) and dianion (from -0.061 *e* for **NDI-1** to -0.098 *e* for **PDI-1**) states, is predicted. These facts suggest a higher electronic communication between the electron-deficient PDI core and the lateral electron donor groups with respect NDI compounds, probably due to the more twisted central framework of PDI-based derivatives, explaining the differences recorded in the spectroelectrochemical behavior of **PDI-1** and **PDI-2** samples when compared with their NDI-based homologous.

On the other hand, the evolution of the UV-Vis absorption spectra upon progressive electrochemical oxidation of **NDI-1** and **PDI-1** samples was also registered and is shown in Figure III.7. In this case, only the formation of radical cation species is observed for both molecules, whereas **NDI-2** and **PDI-2** systems, with less electron-donating phenyl carbazole lateral groups, do not stabilize any oxidized species. This observation further probes the greater electron-donor ability of triarylamine-substituted systems with respect their phenyl-carbazole derivatives, which can explain the more efficient ICT character observed in the former.

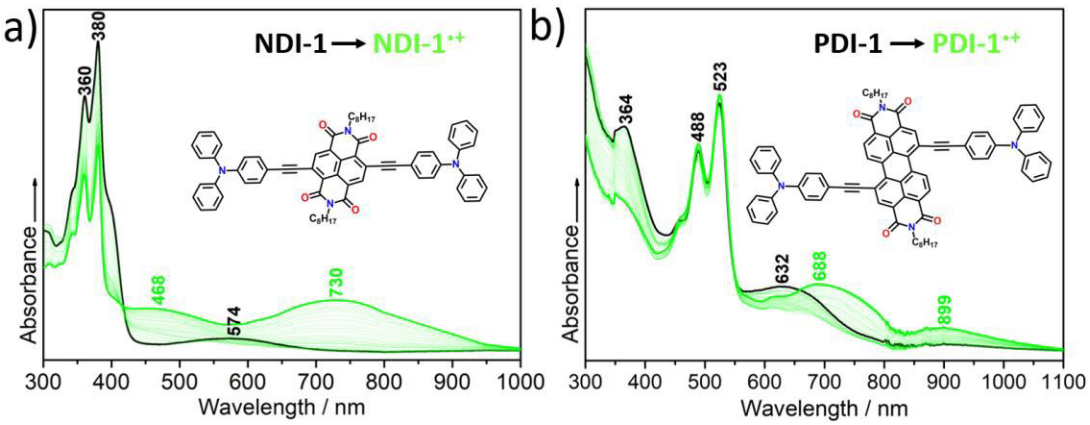

Figure III.7. In situ UV-Vis spectral changes upon electrochemical oxidation of **NDI-1** (a) and **PDI-1** (b) semiconductors. The black and green curves represent the absorption bands for the neutral and cation states, respectively.

III.5. Electrical characterization and charge transport parameters

Organic field effect transistors were fabricated using a bottom-gate top-contact device structure to characterize the charge transport properties of these semiconductors, emphasizing on the influence produced by the π-conjugated core elongation as well as by the different lateral groups. Although only the devices prepared under the optimal device fabrication conditions are shown in this section, the transistors performance was fully optimized by systematically analyzing the effect of the substrate treatment and annealing conditions on the charge transport properties of these semiconductors. The OFET performance optimization process includes different surface treatments with OTS and HMDS self-assembled monolayer as well as annealing treatments at 120-150°C for 2 hours (see detailed data in Appendix 6.3.2).

As illustrated in Figure III.8, all devices exhibit typical unipolar n-channel characteristics with excellent transfer and output curves measured under vacuum.

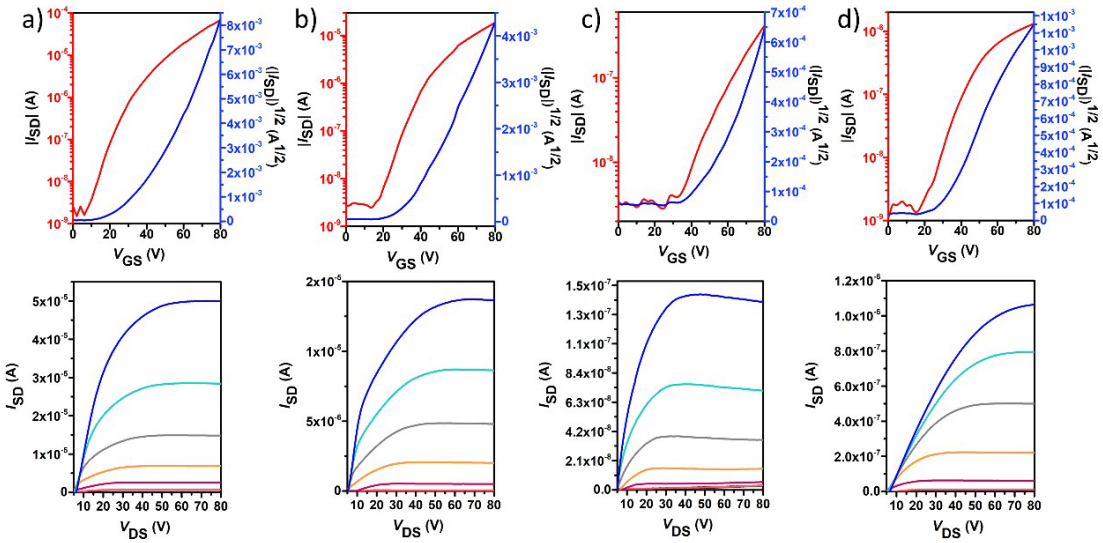

Figure III.8. Typical OFET transfer (top) and output (bottom) characteristics of **NDI-1** (a), **NDI-2** (b), **PDI-1** (c) and **PDI-2** (d) compounds. Transfer curves were measured at a source–drain voltage (V_{DS}) of 80 V, whereas the output curves were measured at gate voltages (V_G) varying from 0 to 80 V at intervals of 10 V and over a V_{DS} range from 0 to 80 V.

The main device performance parameters extracted from the saturated region in transfer curves, including electron charge carrier mobilities (μ_e), intensities ratios (I_{on}/I_{off}) and threshold voltages (V_T) are summarized in Table III.1. The highest electron mobility was registered for **NDI-1** semiconductor, with a value of 0.3 $cm^2V^{-1}s^{-1}$, which is 3-fold higher than those of devices based on **NDI-2** (0.1 $cm^2V^{-1}s^{-1}$). However, the electrical performances of the PDI-based semiconductors are substantially lower than those of the NDI-based materials ($1.5x10^{-3}$ and $4.0x10^{-3}$ $cm^2V^{-1}s^{-1}$ for **PDI-1** and **PDI-2**, respectively). This can be explained considering the theoretically predicted structural twisting of perylenediimide scaffold, which could induce an inefficient overlap of LUMO orbitals and thus lower electronic coupling in the thin films.

Table III.1. OFET electrical data for thin films of all the semiconductors under study prepared under the optimal device fabrication conditions and measured under vacuum. Average and maximum (in parenthesis) values are shown. The average values were obtained from at least 6 devices for each material.

Sample	μ_e (cm^2 V^{-1} s^{-1})	I_{ON}/I_{OFF}	V_T (V)	Method
NDI-1	3.1×10^{-1} (3.2×10^{-1})	1×10^5 (2×10^5)	40 (36)	OTS, RT
NDI-2	7.3×10^{-2} (1.0×10^{-1})	2×10^4 (4×10^4)	44 (38)	HMDS, RT
PDI-1	1.3×10^{-3} (1.5×10^{-3})	2×10^4 (1×10^5)	49 (42)	HMDS, RT
PDI-2	3.0×10^{-3} (4.0×10^{-3})	3×10^3 (5×10^3)	17 (3)	OTS, RT

As observed for NDI-based semiconductors, comparison of the electrical performances of PDI-based derivatives with varying lateral electron-rich groups shows that the substitution with phenylcarbazole groups renders devices with mobilities around 3-fold lower than those substituted with triphenylamine groups. This result is surprising considering that the more electron-rich triphenylamine group destabilizes the LUMO energy level, increasing the energetic barrier with gold electrodes Fermi level. Additionally, triphenylamine group is bulkier than phenylcarbazole, which could be detrimental for

molecular packing. Regarding these results, the role of the different planarity and lateral substitution of the π-conjugated core in the electrical properties of these systems seem to be relevant points that need to be further addressed.

The optimization of the device fabrication steps suggests that both substrate treatments and thermal annealing play a relevant role in the resultant mobilities of the devices: (i) it was found that OFET performance is moderately enhanced for treated-substrates (in a similar way for HMDS- and OTS-treated substrates), increasing the charge carrier mobilities up to three (one) order of magnitude in **NDI-1** (**NDI-2**, **PDI-1** and **PDI-2**); (ii) on the other hand, thermal annealing of the thin films at 120ºC for 2 hours results in a notable decrease of the OFET performances. Of special relevance is the case of **NDI-2**, which completely lost the electrical mobility after the thermal treatment.

III.6. Thin-film characterization

To clarify the impact that different π-conjugated platforms and their lateral substitutions exert on device performance, the microstructures of the semiconducting films prepared under the optimal device fabrication conditions were first characterized via Grazing Incidence X-Ray Diffraction (GIXRD), as depicted in Figure III.9a. Inspection of the GIXRD patters reveals that all the semiconductors films show moderate crystallinity, with the triphenylamine-substituted semiconductors **NDI-1** and **PDI-1** showing slightly sharper diffraction peaks in accordance with a more ordered solid-state packing. In fact, a predominant characteristic (100) reflection at 2Θ=4.04° in **NDI-1**, **NDI-2** and **PDI-1**, and at 2Θ=3.78° in **PDI-2**, which correspond to an interlayer spacing of d_{100}=21.85 Å and d_{100}=23.36 Å respectively, was observed. Accordingly, we assume that all the semiconductors under study self-organize into a lamellar crystalline structure with a practically total interdigitation of alkyl chains. This assumption is supported by the fact that the lamellar packing distance d_{100} is almost identical than expected from the C_8 alkyl chain length, as previously observed for similar derivatives.[32, 33]

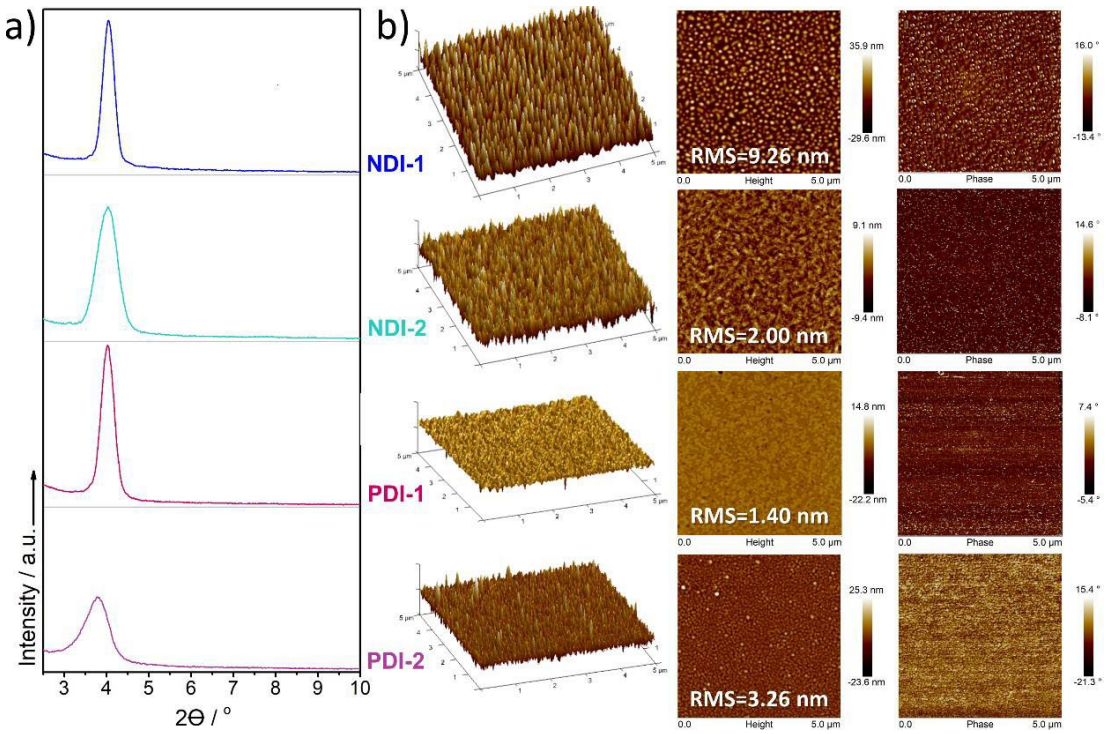

Figure III.9. (a) GIXRD patterns and (b) 5x5 μm^2 tapping-mode AFM images of 3D-topography (left), height (middle) and phase (right) for **NDI-1**, **NDI-2**, **PDI-1** and **PDI-2** thin films fabricated under the optimal device performance conditions. An Intensity spectral range from 0 to 2100 a.u. was used for the GIXRD spectra of all semiconductors. The corresponding root-mean-square (RMS) roughness are also shown.

Interestingly, discernible differences can be observed on their AFM images (Figure III.9b). Larger crystalline domains on the submicron scale can be identified on the height images of NDI-based thin films, contributing significantly to the higher OFET performance measured in these systems with respect their PDI-based analogous, whose thin films show smoother texture defined by small grain sizes. It is well known that a better interconnection of the crystalline domains induces soft grain boundaries on AFM images, leading to higher OFET mobilities.[34, 35] In this sense, although more pronounced contrast can be observed in the contours of the crystalline grains in phase images of NDI-based semiconductors (even more notorious in the case of **NDI-1**), the absence of considerable crystalline domains in PDI-based thin films leads to lower OFET performance of **PDI-1** and **PDI-2** devices. Accordingly, a much higher rougher surface value of root-mean-square (RMS) roughness was found for

NDI-1 (RMS=9.3 nm) in comparison with the rest of semiconductors (RMS values of 1.4-3.3 nm), which is in good agreement with its largest crystalline domains. Taken all these facts into account, it seems reasonable to conclude that **NDI-1** and **NDI-2** samples exhibit easier aggregation and nucleation compared to their PDI-based counterparts, which can be ascribed to the more coplanar central arylene unit. Therefore, the observed differences in crystallinity between these compounds may also support the differences found in device performances.

III.7. Conclusions

In view of the results obtained on this systematic physical chemistry study, some remarkable structure–property guidelines have been obtained for these semiconductors. Thereby, the following conclusions can be stablished:

- Extension of the arylene fragment in PDI derivatives produces two apparently opposite effects: an energy gap narrowing can be observed at the same time that the planarity of the π-conjugated skeleton is somewhat broken. As a result, a bathochromic shift and a more twisted molecular structure has been observed going from **NDI-1**/**NDI-2** to **PDI-1**/**PDI-2**.

- According to the results gathered by electronic spectroscopies and theoretical calculations, the different lateral substitution at 1,7 bay positions with electron-rich groups has a negligible impact on the molecular structure of the resulting materials. On the contrary, the photophysical properties of these molecules are greatly affected by the lateral substitution, with the change of the lateral substituents from triphenylamine to phenylcarbazole groups inducing a blue-shifting of the absorption maxima as well as a less efficient intramolecular charge transfer process.

- Remarkable differences have been observed on the emission spectra of **NDI-1** and **NDI-2**, further probing the key role that the lateral substituents play on the optoelectronic properties of these materials.

- The ability of NDI and PDI scaffolds to accommodate negative charges have been studied by spectroelectrochemical measurements and rationalized with the help of theoretical calculations. While NDI-based semiconductors undergo only two reduction processes, the more extended PDI scaffold can accommodate up to 3 negative charges. Furthermore, spectroelectrochemical analysis of charged species indicate that the inclusion of different electron-rich groups has a minimal impact on electron injection and stabilization. Interestingly, the formation of radical cation species is only observed on **NDI-1** and **PDI-1** systems.

- Regarding the semiconducting properties of these systems, the electrical performance measured in OFETs highly depends on the nature of the central unit. In this sense, the lower n-type electrical performance found in PDI-derivatives (with values around 10^{-3} $cm^2V^{-1}s^{-1}$) compared to their NDI-based homologous (with mobilities up to 0.3 $cm^2V^{-1}s^{-1}$ for **NDI-1**) can be related to the more twisted molecular structure of perylenediimide scaffold, which could induce a poor molecular packing and thus, a low electronic coupling between LUMO orbitals.

- Further characterization of semiconducting thin films, including AFM and GIXRD measurements, revealed that larger crystalline domains with an adequate interconnection between them are an indispensable requirement to achieve highly-performance OFETs. Thus, the presence of significantly higher crystalline domains in NDI versus PDI semiconducting films explains the enhanced electrical properties in the former. In addition, the presence of sharper diffraction peaks on the laterally triphenylamine substituted samples compared to those of their phenyl-carbazole analogous support the higher electron mobilities observed in **NDI-1** and **PDI-1** with respect **NDI-2** and **PDI-2**.

III.8. References

[1] Tsumura, A.; Koezuka, H.; Ando, T., Macromolecular electronic device: Field-effect transistor with a polythiophene thin film. *Applied Physics Letters* **1986,** 49, (18), 1210-1212.

[2] Yoo, B.; Jung, T.; Basu, D.; Dodabalapur, A.; Jones, B. A.; Facchetti, A.; Wasielewski, M. R.; Marks, T. J., High-mobility bottom-contact n-channel organic transistors and their use in complementary ring oscillators. *Applied Physics Letters* **2006,** 88, (8), 082104.

[3] Sirringhaus, H., 25th Anniversary Article: Organic Field-Effect Transistors: The Path Beyond Amorphous Silicon. *Advanced Materials* **2014,** 26, (9), 1319-1335.

[4] Luo, C.; Kyaw, A. K. K.; Perez, L. A.; Patel, S.; Wang, M.; Grimm, B.; Bazan, G. C.; Kramer, E. J.; Heeger, A. J., General Strategy for Self-Assembly of Highly Oriented Nanocrystalline Semiconducting Polymers with High Mobility. *Nano Letters* **2014,** 14, (5), 2764-2771.

[5] Zheng, Y.-Q.; Lei, T.; Dou, J.-H.; Xia, X.; Wang, J.-Y.; Liu, C.-J.; Pei, J., Strong Electron-Deficient Polymers Lead to High Electron Mobility in Air and Their Morphology-Dependent Transport Behaviors. *Advanced Materials* **2016,** 28, (33), 7213-7219.

[6] Quinn, J. T. E.; Zhu, J.; Li, X.; Wang, J.; Li, Y., Recent progress in the development of n-type organic semiconductors for organic field effect transistors. *Journal of Materials Chemistry C* **2017,** 5, (34), 8654-8681.

[7] Liu, J.; Liu, J.; Zhang, J.; Li, C.; Cui, Q.; Teng, F.; Li, H.; Jiang, L., High-performance n- and p-type organic single-crystal field-effect transistors with an air-gap dielectric towards anti-ambipolar transport. *Journal of Materials Chemistry C* **2020,** 8, (13), 4303-4308.

[8] Zhu, C.; Zhao, Z.; Chen, H.; Zheng, L.; Li, X.; Chen, J.; Sun, Y.; Liu, F.; Guo, Y.; Liu, Y., Regioregular Bis-Pyridal[2,1,3]thiadiazole-Based Semiconducting Polymer for High-Performance Ambipolar Transistors. *Journal of the American Chemical Society* **2017,** 139, (49), 17735-17738.

[9] Osaka, I.; Takimiya, K., Naphthobischalcogenadiazole Conjugated Polymers: Emerging Materials for Organic Electronics. *Advanced Materials* **2017,** 29, (25), 1605218.

[10] Wang, Y.; Guo, H.; Harbuzaru, A.; Uddin, M. A.; Arrechea-Marcos, I.; Ling, S.; Yu, J.; Tang, Y.; Sun, H.; López Navarrete, J. T.; Ortiz, R. P.; Woo, H. Y.; Guo, X., (Semi)ladder-Type Bithiophene Imide-Based All-Acceptor Semiconductors: Synthesis, Structure–Property Correlations, and Unipolar n-Type Transistor Performance. *Journal of the American Chemical Society* **2018,** 140, (19), 6095-6108.

[11] Liu, Q.; Bottle, S. E.; Sonar, P., Developments of Diketopyrrolopyrrole-Dye-Based Organic Semiconductors for a Wide Range of Applications in Electronics. *Advanced Materials* **2020,** 32, (4), 1903882.

[12] Wang, Y.; Michinobu, T., Benzothiadiazole and its π-extended, heteroannulated derivatives: useful acceptor building blocks for high-performance donor–acceptor polymers in organic electronics. *Journal of Materials Chemistry C* **2016,** 4, (26), 6200-6214.

[13] Yuen, J. D.; Pozdin, V. A.; Young, A. T.; Turner, B. L.; Giles, I. D.; Naciri, J.; Trammell, S. A.; Charles, P. T.; Stenger, D. A.; Daniele, M. A., Perylene-diimide-based n-type semiconductors with enhanced air and temperature stable photoconductor and transistor properties. *Dyes and Pigments* **2020,** 174, 108014.

[14] Guo, X.; Facchetti, A.; Marks, T. J., Imide- and Amide-Functionalized Polymer Semiconductors. *Chemical Reviews* **2014,** 114, (18), 8943-9021.
[15] Wei, X.; Zhang, W.; Yu, G., Semiconducting Polymers Based on Isoindigo and Its Derivatives: Synthetic Tactics, Structural Modifications, and Applications. *Advanced Functional Materials* **2021,** 31, (21), 2010979.
[16] Zhan, X.; Facchetti, A.; Barlow, S.; Marks, T. J.; Ratner, M. A.; Wasielewski, M. R.; Marder, S. R., Rylene and Related Diimides for Organic Electronics. *Advanced Materials* **2011,** 23, (2), 268-284.
[17] Blanchard, P.; Malacrida, C.; Cabanetos, C.; Roncali, J.; Ludwigs, S., Triphenylamine and some of its derivatives as versatile building blocks for organic electronic applications. *Polymer International* **2019,** 68, (4), 589-606.
[18] Malacrida, C.; Habibi, A. H.; Gámez-Valenzuela, S.; Lenko, I.; Marqués, P. S.; Labrunie, A.; Grolleau, J.; López Navarrete, J. T.; Ruiz Delgado, M. C.; Cabanetos, C.; Blanchard, P.; Ludwigs, S., Impact of the Replacement of a Triphenylamine by a Diphenylmethylamine Unit on the Electrochemical Behavior of Pentaerythritol-Based Push-Pull Tetramers. *ChemElectroChem* **2019,** 6, (16), 4215-4228.
[19] Shirota, Y.; Kageyama, H., Charge carrier transporting molecular materials and their applications in devices. *Chemical Reviews* **2007,** 107, (4), 953-1010.
[20] Geng, Y.; Wu, S.-X.; Li, H.-B.; Tang, X.-D.; Wu, Y.; Su, Z.-M.; Liao, Y., A theoretical discussion on the relationships among molecular packings, intermolecular interactions, and electron transport properties for naphthalene tetracarboxylic diimide derivatives. *Journal of Materials Chemistry* **2011,** 21, (39), 15558-15566.
[21] Geng, Y.; Li, H.-B.; Wu, S.-X.; Su, Z.-M., The interplay of intermolecular interactions, packing motifs and electron transport properties in perylene diimide related materials: a theoretical perspective. *Journal of Materials Chemistry* **2012,** 22, (39), 20840-20851.
[22] Schleyer, P. v. R.; Maerker, C.; Dransfeld, A.; Jiao, H.; van Eikema Hommes, N. J. R., Nucleus-Independent Chemical Shifts: A Simple and Efficient Aromaticity Probe. *Journal of the American Chemical Society* **1996,** 118, (26), 6317-6318.
[23] Zywietz, T. K.; Jiao, H.; Schleyer, P. v. R.; de Meijere, A., Aromaticity and Antiaromaticity in Oligocyclic Annelated Five-Membered Ring Systems. *The Journal of Organic Chemistry* **1998,** 63, (10), 3417-3422.
[24] Keerthi, A.; Valiyaveettil, S., Regioisomers of Perylenediimide: Synthesis, Photophysical, and Electrochemical Properties. *The Journal of Physical Chemistry B* **2012,** 116, (15), 4603-4614.
[25] Sivamurugan, V.; Kazlauskas, K.; Jursenas, S.; Gruodis, A.; Simokaitiene, J.; Grazulevicius, J. V.; Valiyaveettil, S., Synthesis and Photophysical Properties of Glass-Forming Bay-Substituted Perylenediimide Derivatives. *The Journal of Physical Chemistry B* **2010,** 114, (5), 1782-1789.
[26] Sakai, N.; Mareda, J.; Vauthey, E.; Matile, S., Core-substituted naphthalenediimides. *Chemical Communications* **2010,** 46, (24), 4225-4237.
[27] Basak, S.; Nanda, J.; Banerjee, A., Assembly of naphthalenediimide conjugated peptides: aggregation induced changes in fluorescence. *Chemical Communications* **2013,** 49, (61), 6891-6893.

[28] Choudhury, P.; Das, K.; Das, P. K., l-Phenylalanine-Tethered, Naphthalene Diimide-Based, Aggregation-Induced, Green-Emitting Organic Nanoparticles. *Langmuir* **2017,** 33, (18), 4500-4510.

[29] Fang, X.; Ke, H.; Li, L.; Lin, M.-J., Structural insights into the aggregation-induced emission mechanism of naphthalene diimide solids. *Dyes and Pigments* **2017,** 145, 469-475.

[30] Alonso-Navarro, M. J.; Harbuzaru, A.; de Echegaray, P.; Arrechea-Marcos, I.; Harillo-Baños, A.; de la Peña, A.; Ramos, M. M.; López Navarrete, J. T.; Campoy-Quiles, M.; Ponce Ortiz, R.; Segura, J. L., Effective interplay of donor and acceptor groups for tuning optoelectronic properties in oligothiophene–naphthalimide assemblies. *Journal of Materials Chemistry C* **2020,** 8, (43), 15277-15289.

[31] Guha, S.; Goodson, F. S.; Corson, L. J.; Saha, S., Boundaries of Anion/Naphthalenediimide Interactions: From Anion−π Interactions to Anion-Induced Charge-Transfer and Electron-Transfer Phenomena. *Journal of the American Chemical Society* **2012,** 134, (33), 13679-13691.

[32] Guo, X.; Kim, F. S.; Seger, M. J.; Jenekhe, S. A.; Watson, M. D., Naphthalene Diimide-Based Polymer Semiconductors: Synthesis, Structure–Property Correlations, and n-Channel and Ambipolar Field-Effect Transistors. *Chemistry of Materials* **2012,** 24, (8), 1434-1442.

[33] Hwang, Y.-J.; Murari, N. M.; Jenekhe, S. A., New n-type polymer semiconductors based on naphthalene diimide and selenophene derivatives for organic field-effect transistors. *Polymer Chemistry* **2013,** 4, (11), 3187-3195.

[34] Tsao, H. N.; Müllen, K., Improving polymer transistor performance via morphology control. *Chemical Society Reviews* **2010,** 39, (7), 2372-2386.

[35] Eckstein, B. J.; Melkonyan, F. S.; Wang, G.; Wang, B.; Manley, E. F.; Fabiano, S.; Harbuzaru, A.; Ponce Ortiz, R.; Chen, L. X.; Facchetti, A.; Marks, T. J., Processable High Electron Mobility π-Copolymers via Mesoscale Backbone Conformational Ordering. *Advanced Functional Materials* **2021,** 31, (15), 2009359.

Chapter IV:

Towards high performance ambipolar field effect transistors: the fluorination effect

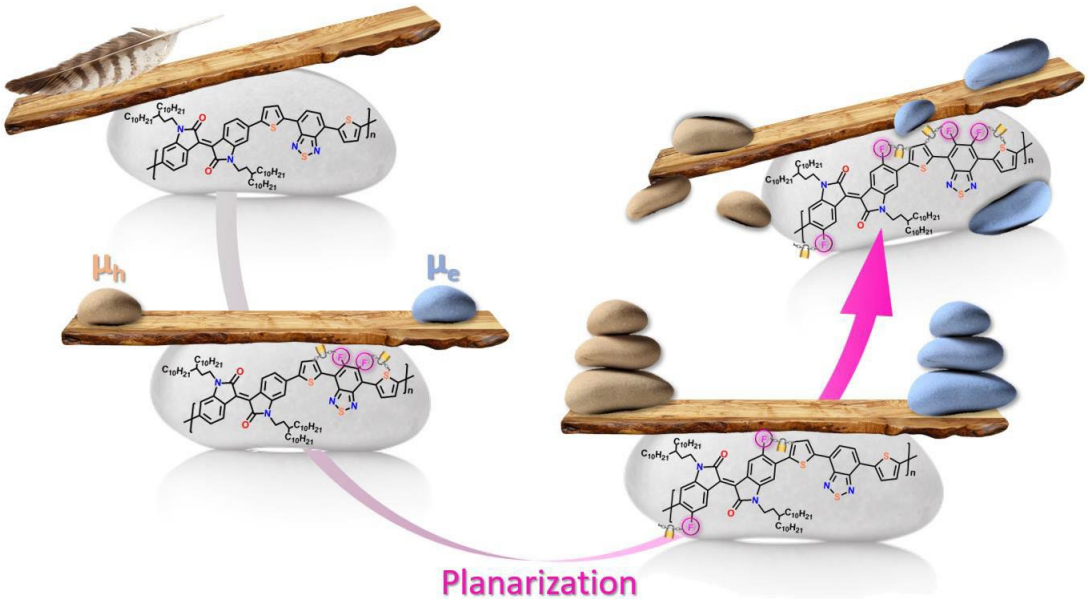

The most relevant results obtained in this study have given rise to publication 7 listed in Appendix 6.4:

7. **Gámez-Valenzuela, S.**; Comí, M.; Rodríguez González, S.; Ruiz Delgado, M. C.; Al-Hashimi, M.; Ponce Ortiz, R., The Fluorination Effect: Importance of Backbone Planarity in Achieving High Performance Ambipolar Field Effect Transistors. Journal of Materials Chemistry C, **2023**, Accepted. (DOI: https://doi.org/10.1039/D2TC05073K).

IV.1. Introduction

In the state-of-the-art design of new semiconducting π-conjugated polymers, controlling the polymer conformation to ensure an optimal backbone planarity constitutes one of the key aspects to achieve high-performing conjugated materials, since the planarity of the π-conjugated backbone can facilitate intramolecular delocalization of π-electrons.[1-5] This prerequisite is achieved to a maximum effect when the system adopts a totally coplanar conformation, also allowing for the most efficient π-orbital overlap. Furthermore, changes on the backbone planarity can determine critical aspects as molecular ordering and thin-film morphology, which ultimately determine device performances.[6]

In this sense, an efficient strategy to restrict the rotation of the single bonds connecting neighboring units is the creation of additional covalent bonds to form ladder-type structures. However, this methodology usually requires complex multiple-step syntheses, which may limit their technologic applications.[7-9] To address this issue, materials with noncovalent conformational locks have emerged as a useful alternative to control the rotation and enforce the planarity of the conjugated backbones. Among them, isoindigo derivatives-based polymers have been widely studied since it was firstly used in organic electronics in 2010,[10] reaching hole and electron mobilities of 14.4 and 14.9 $cm^2V^{-1}s^{-1}$ in p- and n-type OFETs as well as hole/electron mobilities up to 6/7 $cm^2V^{-1}s^{-1}$ in ambipolar transistors.[11-13] In addition, current approaches involving conformational locks in organic semiconductors also utilize S•••X (X = halide) noncovalent interactions to this respect, taking advantage of the attractive interaction between the lone pair electrons of X atoms and the antibonding orbitals of the sulphur atom.[14, 15] Thereby, the most widely used approach is the introduction of fluorine atoms, which not only allows stronger intra-chain interactions and more ordered thin-film morphologies due to the locked conformation of the polymer backbones, but also effectively lowers the LUMO energy level for efficient and air stable n-type mobilities.[16, 17]

Within the framework of this ongoing research, we have investigated a series of A-D-A´ copolymers composed of isoindigo (IIG) and benzothiadiazole (BTD) units with a flanking

thiophene monomeric building block, which have been subjected to a progressive fluorination process giving rise to four different copolymers with different degrees of fluorination (Figure IV.1).

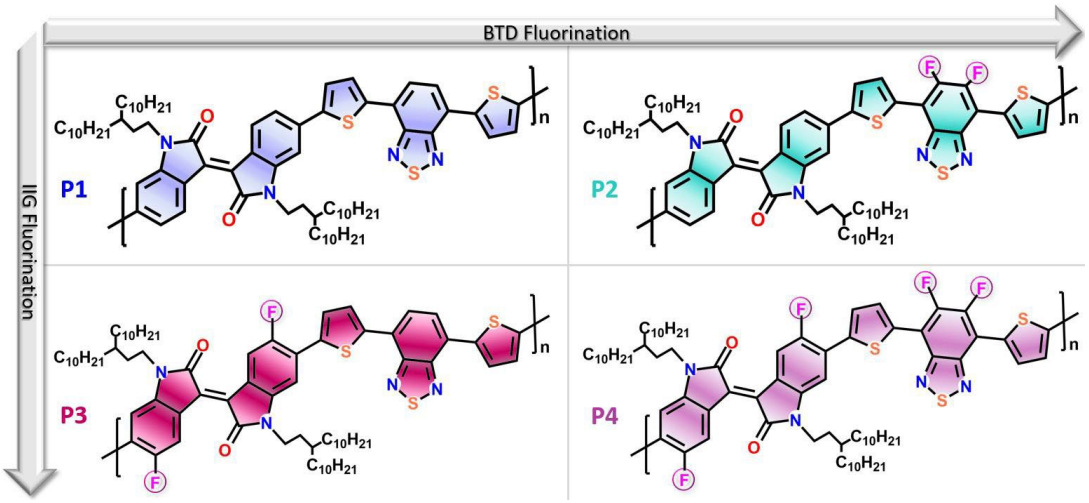

Figure IV.1. Chemical structures of the four copolymers studied on this chapter.

The main goal of this study focuses on exploring the effects of the progressive fluorination on the polymer structure, energy levels and intermolecular stacking of the analyzed systems, factors which will determine the charge transport properties of the final materials. To this end, a wide range of techniques such as UV-Vis absorption and Raman spectroscopies, electrochemistry and OFET characterization were used, in addition to DFT and TD-DFT calculations performed at the B3LYP/6-31G** level of theory. The ωB97X-D functional was also used and the results, which are comparable to those obtained at the B3LYP level, are presented in Appendix 6.2.3. The outcome of this study will help drawing the key structure–property–function relationships for understanding the electron transport behavior in these systems, and more generally, it will provide insights in the design of new polymer-based semiconductors for electronic applications.

IV.2. Structural features

To gain perception into the complicated interplay of intra- and intermolecular interactions, packing motifs and electron transport properties, the effect of the progressive fluorination on the molecular ground-state geometry was analyzed by performing density functional theory calculations at the B3LYP/6-31G** level of theory. In view of the results of Figure IV.2a, a lack of severe distortions in the conjugated backbone of the non-fluorinated **P1** copolymer is predicted, with dihedral angles that fluctuate between 6 and 21°.

a)

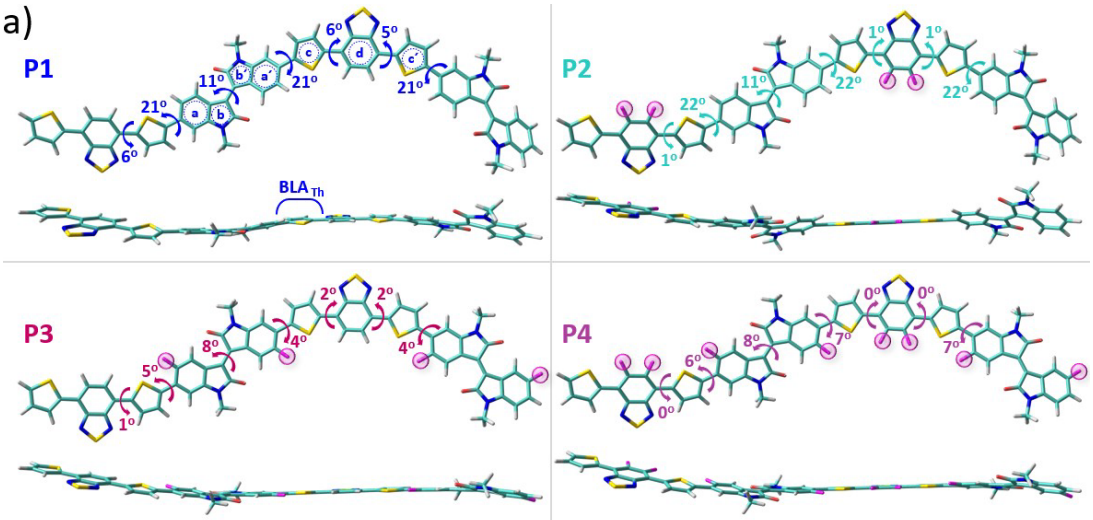

b)

Sample	BLA_{Th}	$NICS(0)_a$	$NICS(0)_b$	$NICS(0)_{b'}$	$NICS(0)_{a'}$	$NICS(0)_c$	$NICS(0)_d$	$NICS(0)_{c'}$
P1	0.030	-4.5	2.6	2.5	-4.5	-7.1	-3.0	-7.1
P2	0.025	-4.5	2.5	2.6	-4.5	-8.4	-6.2	-8.5
P3	0.022	-6.4	2.4	2.3	-6.4	-7.6	-2.9	-7.7
P4	0.018	-6.3	2.4	2.4	-6.4	-8.8	-6.1	-8.9

Figure IV.2. (a) Top and lateral views of the DFT-optimized structures (B3LYP/6-31G** level) for dimeric models of **P1**-**P4** copolymers. The dihedral angles between selected rings are also shown. (b) DFT-calculated BLA (B3LYP/6-31G**) and NICS(0) (B3LYP/6-311++G(2df,p)//B3LYP/6-31G** level) values given in Angstroms and ppm, respectively, for selected parts of the systems under study. See Figure IV.2a for the zones/rings labelling.

Fluorination of the BTD unit in copolymer **P2** induces a slight planarization of the dihedral angle between this acceptor moiety and the adjacent thiophene rings with respect

the non-fluorinated counterpart (from 6° for **P1** to 1° for **P2**). This effect can be attributed to the attractive interaction between the lone pair electrons of fluorine atoms and the antibonding orbitals of the sulphur atom of the thiophene rings.[18]

Note that, the most notable distortions in **P1** and **P2** copolymers were observed where no S•••F interactions were observed, that is, between the IIG acceptor unit and the adjacent thiophene rings. After fluorination at the α-position of IIG acceptor unit, this dihedral angle value significantly decreases from 21° in **P1** to 4° in **P3**, manifesting the presence of additional non-covalent sulphur-fluorine intramolecular interactions that further planarize the conjugated skeleton in copolymer **P3**. Interestingly, the fluorination in **P3** not only has a notable effect on the above mentioned interring torsional angle, but it also affects to the internal planarization of the IIG acceptor unit, with a slight planarization of 3° in copolymer **P3** with respect the parent **P1**.

Combining the fluorination of both BTD and IIG acceptor moieties in **P4** results on the best planarity among the series due to the cooperative effects observed for both partially difluorinated **P2** and **P3** systems. Note however than planarization in **P3** is already quite efficient and similar to that of **P4**, with dihedral angles between 1 and 8°. Therefore, the polymer planarity is not only directly related to the amount of fluorine atoms incorporated to the polymeric backbone, but also to the acceptor unit where F atoms are added. The polymer coplanarity can modulate intra- and intermolecular aspects, directly affecting the molecular and electronic properties, molecular packing and active layer morphology, which we will discuss in detail in next sections.

In order to get further insight on the possible modulation of the electronic delocalization along the polymeric backbone by progressive fluorination the successive single-double CC Bond Length Alternation (BLA) and NICS(0), as aromaticity criterions,[19, 20] were calculated for the dimeric models (Figure IV.2b). In this sense, BLA values closer to zero indicate an increased quinoidization, whereas the more negative the NICS value, the more aromatic the system.

On the basis of the calculated data, the aromaticity of these systems is affected by the fluorination degree which translates into a modulation of the π-conjugation efficiency. In fact, when compared to the reference **P1** copolymer, the DFT-calculated BLA values show a gradual increment of the quinoidal character for the thiophene ring localized between both IIG and BTD acceptor moieties upon progressive fluorination (with BLA_{Th} values going from 0.030 Å for **P1** to 0.018 Å for **P4**). This can be explained in terms of the coplanarity enhancement going from **P1** to **P4**, as previously pointed out, which improve the electronic delocalization in consonance with the more quinoide-like structure of the polymeric backbone upon fluorination.

The inspection of the DFT-calculated NICS(0) values reveals that the insertion of electron-withdrawing fluorine atoms lead to more negative NICS(0) values on the six membered rings of IIG and BTD acceptor moieties, suggesting that they become more aromatic. This effect is more important in the case of the BTD acceptor group than in the IIG one, with a vanishing of the NICS(0) values in *c.a*. 3.2 and 2 ppm, respectively. Interestingly, fluorination on the IIG and BTD acceptor groups produce a secondary effect on the neighbouring thiophene rings, reducing around 0.5 and 1.3 ppm their NICS(0) values, respectively.

IV.3. Optical properties

A comparison of the UV-Vis-NIR absorption spectra for the four copolymers in chlorobenzene solutions are depicted in Figure IV.3. Across the series, all the polymers exhibit similar spectral profiles with typically dual-absorption bands (Bands I and II).

TD-DFT calculations indicate that the broad and intense absorption band extending from 400 to 800 nm (Band I), is due to a $S_0 \rightarrow S_1$ electronic transition theoretically ascribed to one electron promotion from HOMO to LUMO. As illustrated by the frontier molecular orbital topologies shown in Figure IV.4, this electronic transition entails an electronic density redistribution from the whole π-conjugated backbone (HOMO) to both the IIG and BTD acceptor moieties (LUMO).

a)

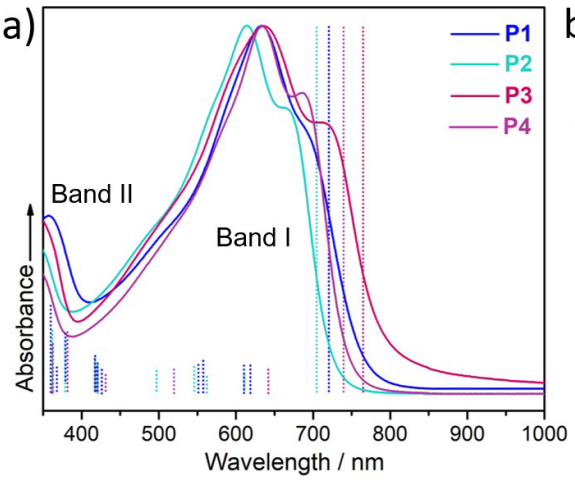

b)

	Experimental		B3LYP/6-31G**			
	λ_{max} (nm)	E_g^{opt} (eV)	E_{HOMO} (eV)	E_{LUMO} (eV)	E_g (eV)	λ_{max} (nm)
P1	633	1.55	-5.05	-3.05	2.00	721
P2	614	1.63	-5.14	-3.08	2.06	705
P3	636	1.50	-5.13	-3.21	1.92	765
P4	634	1.61	-5.22	-3.25	1.97	739

Figure IV.3. (a) Normalized UV-Vis absorption spectra of 10^{-4} M chlorobenzene solutions of copolymers **P1**-**P4**. The main vertical excited-state transitions (dot bars) calculated at the TD-DFT//B3LYP/6-31G** level are also shown. (b) Summary of optical parameters of copolymers **P1**-**P4**. The optical band gaps (E_g^{opt}) were estimated from the tangent to the low energy edge of the absorption band.

For the sake of comparison, the influence of the different fluorine atoms number and substitution position were analyzed separately. The introduction of fluorine atoms on the BTD acceptor unit in **P2** produces a blue shifting of 19 nm in the maximum absorption wavelength (λ_{max}) with respect the parent copolymer **P1**. In order to shed light on this effect, the frontier energy levels evolution upon progressive fluorination was theoretically investigated for dimeric models of copolymers **P1**-**P4** and the results are shown in Figure IV.3b. In this sense, the introduction of the fluorine atoms on the BTD unit has a greater stabilization effect on the HOMO (0.09 eV) than on the LUMO (0.03eV) energy level, giving rise to an slight increase of the HOMO-LUMO gap in line with the wider optical HOMO-LUMO gap (E_g^{opt}) experimentally observed in **P2** (1.63 eV) with respect the non-fluorinated counterpart **P1** (1.55 eV).

On the other hand, the introduction of fluorine atoms on the IIG acceptor moiety in copolymer **P3** has the opposite effect, further stabilizing the LUMO (0.16 eV) than the HOMO (0.08 eV). This indicates the increase of the electron withdrawing ability of the IIG acceptor, which results in a slight bathochromic shift (of around 3 nm) compared with the non-

fluorinated copolymer **P1** as a consequence of the optical HOMO-LUMO gap narrowing going from **P1** (1.55 eV) to **P3** (1.50 eV) copolymers.[4, 21] It is important to note that fluorination of IIG unit provokes a much more pronounced deepening on HOMO and LUMO energy levels than fluorination on BTD acceptor moiety.

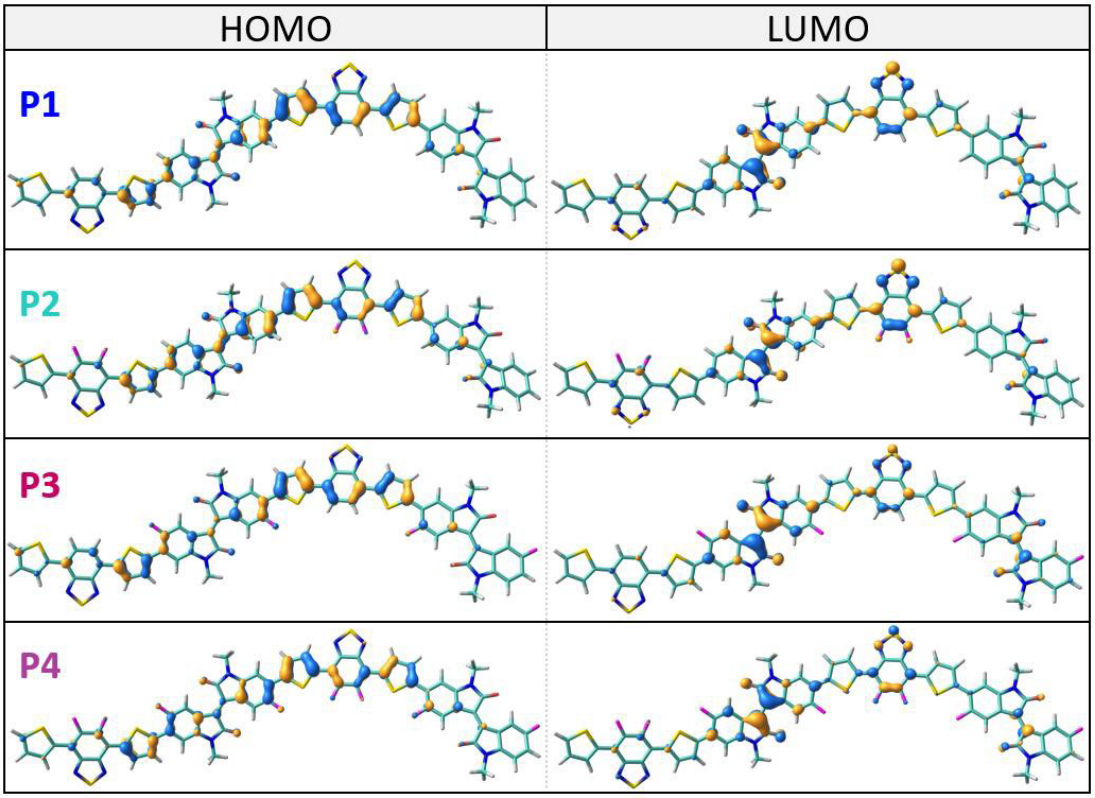

Figure IV.4. DFT-calculated HOMO and LUMO topologies for dimeric models of the polymers under study at the B3LYP/6-31G** level of theory.

The two independent effects caused by difluorination at different positions are cooperative in **P4**, which is supported by the null spectral shift observed in this copolymer with respect the unsubstituted system **P1**. This is due to a similar stabilization of both HOMO and LUMO energy levels (0.17/0.20 eV). It is worth noting that our DFT calculated data nicely reproduce the experimental absorption spectra trend and the HOMO-LUMO energy gaps variation upon fluorination.

In addition, the FMO topologies plotted in Figure IV.4 show that both HOMO and LUMO have remarkable contributions on the IIG and BTD acceptor units, thus explaining the deepening of both orbitals upon fluorination.

With the above considerations in mind, the adjusting the fluorination degree would be advantageous for tuning the electronic energy levels and band gaps of the resulting polymers. Nevertheless, polymers with excess substituted fluorine atoms are generally less soluble and easily pre-aggregative which is unfavorable for device performance. In fact, it is known that intermolecular stacking and conformational changes may significantly shift the absorption spectra and change vibrational peak intensities.[22] In this sense, as depicted in Figure IV.5, all the copolymers under study show three different vibrational peaks (*0-0*, *0-1* and *0-2*) in the Band I region in both solution and spin-coated thin films. Scrutiny of the spectra reveals that although absorption spectra in both solution and solid state follow the same trend, some remarkable aspects can be pointed out:

(i) the main absorption peaks of all the copolymers under study are red shifted on going from solution to film state, indicating a further planarization of the polymer backbone in solid state as a consequence of considerable inter-chain interactions. This effect is maximized in the difluorinated **P2** copolymer (with a bathochromic shift of 16 nm going from solution to film), suggesting **P2** as the copolymer that might take a more different molecular conformation and supramolecular organization in solid state.

(ii) It is worth noting that the gradual increase of fluorine atoms decreases *0-1* and increases *0-0* peak intensity in both states, indicating that fluorination promotes the planarization of the polymer backbone in line with the molecular modelling results.

(iii) Curiously, the relative intensity of the *0-2* vibrational peak of IIG-fluorinated copolymers **P3** and **P4** increases in films when compared to solution, being this effect practically negligible in the case of copolymers **P1** and **P2**. This phenomenon can be explained in terms of the more coplanar backbone of **P3** and **P4** copolymers, resulting in stronger inter-chain interactions, which usually echoes with a highly ordered crystallinity in

the solid state. This fact highlights the importance of the fluorination on the IIG acceptor unit on the molecular packing.

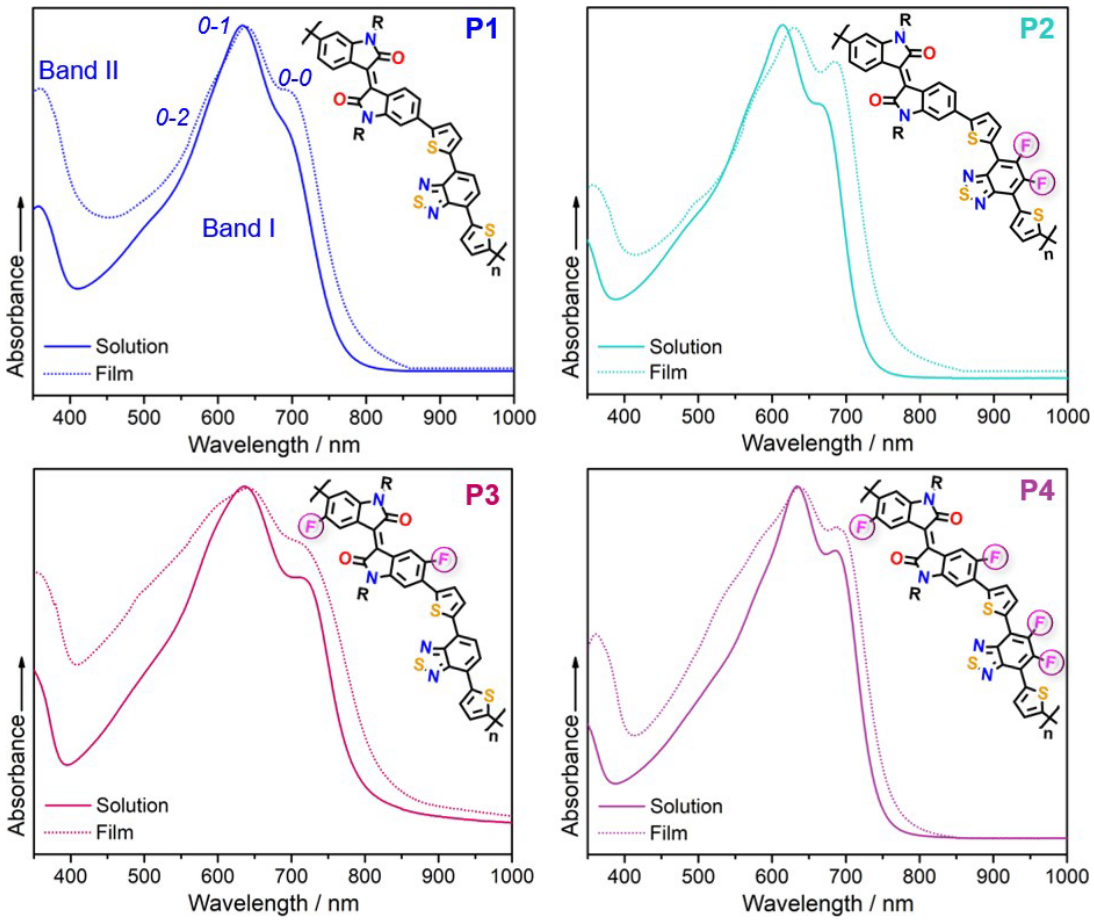

Figure IV.5. (a) Normalized UV-Vis absorption spectra of 10^{-4} M chlorobenzene solution vs thin film for copolymers **P1**-**P4**.

IV.4. Electrochemical analysis

As widely recognized, feasible charge injection of both holes and electrons from source and drain electrodes is key for the design of high-mobility balanced ambipolar polymers. In this regard, charge injection was evaluated by analyzing the FMOs energy levels obtained from cyclic voltammetry measurements of copolymers **P1**-**P4** as thin films (Figure IV.6a).

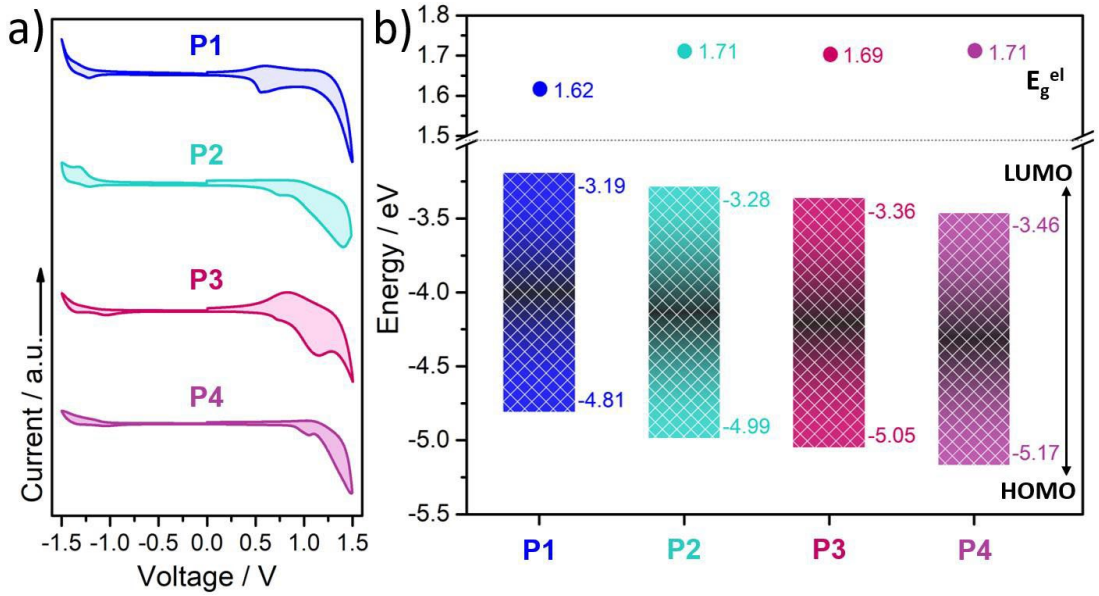

Figure IV.6. (a) Thin film cyclic voltammograms of copolymers **P1**-**P4** recorded at a scan rate of 100 mV·s^{-1} in acetonitrile/0.1 M Bu_4NPF_6 as electrolyte, using a platinum disk working electrode, an Ag/AgCl reference electrode and a platinum wire auxiliary electrode. (b) Experimental HOMO-LUMO energy levels and electrochemical energy gap (E_g^{el})of copolymers **P1**-**P4**.

Notably, all the copolymers are amphoteric redox materials since they exhibit both oxidation and reduction peaks, which is an essential requirement to design ambipolar materials. HOMO and LUMO energy levels were calculated from the onsets of oxidation and reduction potentials referenced to the ferrocene/ferrocenium (Fc/Fc^+) redox couple, in comparison to the formal potential of Fc/Fc^+ with respect to zero vacuum level (-4.8 eV), as determined by the equation $E = - [(E_{onset} - E_{1/2}^{Fc/Fc+}) + 4.80 \text{ eV}]$. In view of the results of Figure IV.6b, it is corroborated than difluorination of the IIG unit provokes a much more pronounced deepening on HOMO and LUMO energy levels than fluorination on BTD acceptor unit. Concretely, difluorination of the BTD acceptor unit in **P2** further stabilizes the HOMO (0.18 eV) than the LUMO (0.09 eV), leading to a wider HOMO-LUMO energy gap (H-L_{Egap}) with respect the non-fluorinated **P1** counterpart (1.62 eV for **P1** vs 1.71 eV for **P2**), as found in the absorption spectra and in the theoretical calculations. In marked contrast, the introduction of fluorine atoms on the IIG acceptor moiety in copolymer **P3**, stabilizes both HOMO and LUMO energy levels in a similar extent (c.a. 0.20 eV) with respect those of **P1**.

Further extended fluorination degree in copolymer **P4** lead to the lowest HOMO and LUMO energy levels (-5.17 and -3.46 eV, respectively), although the similar stabilization of both HOMO and LUMO energy levels results in equivalent E_g^{el} value (1.71 eV) when compared to **P2** and **P3**.

At this point, it is important to highlight that the stronger and reversible oxidation peaks of these copolymers, in addition to their high-lying HOMO levels (lower than -4.80 eV) suggest that they may be useful for developing p-channel OFETs. Moreover, the fluorinated polymers may be excellent candidates as semiconductors for ambipolar OFETs due to their low-lying LUMO levels (<-3.30 eV) and their quasi-reversible reduction peaks.

IV.5. Electrical characterization and charge transport parameters

The effect that fluorination plays on the charge transport properties of these copolymers was investigated by the fabrication of bottom-gate top-contact OFETs. Although only the devices prepared under the optimal device fabrication conditions for each polymer are shown, the device performance was systematically optimized by modifying substrate treatment and annealing conditions (see Appendix 6.3.3). In particular, different surface treatments with OTS and HMDS self-assembled monolayer were tested. Furthermore, annealing treatments at 100, 150 and 200°C for 2 hours were performed on the deposited copolymers.

The optimization of the device fabrication steps suggests that both substrate treatments and thermal annealing temperatures play a relevant role in the resultant mobilities of the devices. It was found that OFET performance is dramatically enhanced for treated-substrates (specially for OTS-treated substrates), going from non-active to active devices in the cases of polymers **P1**, **P2** and **P3** or increasing the charge carrier mobilities up to one order of magnitude in **P4**. On the other hand, thermal annealing of the thin films at 150°C (200°C) for 2 hours increases hole and electron mobilities by one order of magnitude for the OTS-treated substrated of **P2** (**P3**), whereas the OFET performance for polymer **P1** is relatively insensitive to thermal treatments in consonance with the amorphous nature of

the films. In the case of **P4**, only the enhancement of hole mobility was observed after a thermal treatment at 150°C for 2 hours.

The representative OFET transfer and output curves, measured under vacuum, are illustrated in Figure IV.7, and the optimized main device performance parameters, extracted from transfer curves in the saturated regime, are summarized in Table IV.1.

Table IV.1. OFET electrical data for thin films of copolymers **P1**-**P4** prepared under the optimal device fabrication conditions and measured under vacuum. Average and the best (in parenthesis) values are shown. The average values data were obtained from at least 6 devices for each polymer.

		P-channel				N-channel			
Sample	Mn* (KDa)	μ_h ($cm^2 V^{-1} s^{-1}$)	I_{ON}/I_{OFF}	V_T (V)	Method	μ_e ($cm^2 V^{-1} s^{-1}$)	I_{ON}/I_{OFF}	V_T (V)	Method
P1	21	1.1×10^{-5} (1.4×10^{-5})	8×10^{1} (1×10^{2})	4 (-3)	OTS, 150°C, 2h	—	—	—	—
P2	24	2.9×10^{-3} (3.3×10^{-3})	1×10^{3} (2×10^{3})	-1 (-17)	OTS, 150°C, 2h	3.8×10^{-3} (4.0×10^{-3})	4×10^{3} (9×10^{3})	58 (52)	OTS, 150°C, 2h
P3	32	1.2×10^{-1} (1.5×10^{-1})	2×10^{2} (4×10^{2})	-26 (-31)	OTS, 200°C, 2h	9.8×10^{-2} (1.1×10^{-1})	8×10^{1} (1×10^{2})	57 (53)	OTS, 200°C, 2h
P4	29	3.3×10^{-2} (7.4×10^{-2})	1×10^{5} (4×10^{5})	-11 (-29)	OTS, 150°C, 2h	1.1×10^{-2} (1.3×10^{-2})	2×10^{3} (7×10^{3})	17 (8)	OTS

*Determined by gel permeation chromatography (against polystyrene standards) in chlorobenzene at 80°C.

In view of the results, **P1** shows typical p-channel behavior with a low hole mobility (~1×10^{-5} $cm^2V^{-1}s^{-1}$). The low mobility can be attributed to the slightly lower molecular weight, higher energy band gap and somewhat twisted molecular backbone that may produce inefficient orbital overlapping and thus low electronic coupling, which is generally detrimental for efficient charge transport in OFETs devices.[23, 24] The incorporation of fluorine atoms on the backbone enhances the polymer coplanarity and electron affinity, progressively decreasing the electron-injection barrier from the gold electrode to the polymeric semiconducting layers. Consequently, the electronic properties of these polymers change from low hole-dominated to balanced ambipolar charge transport on going from **P1** to **P4**. As a result, typical V-shaped transfer curves and characteristic output curves of ambipolar OFETs were recorded, with the latter characterized by the superposition of the

standard saturation behavior for one type of carriers at high V_G and a superlinear current increase at low V_G and high V_{DS}, due to the injection of the opposite carriers.

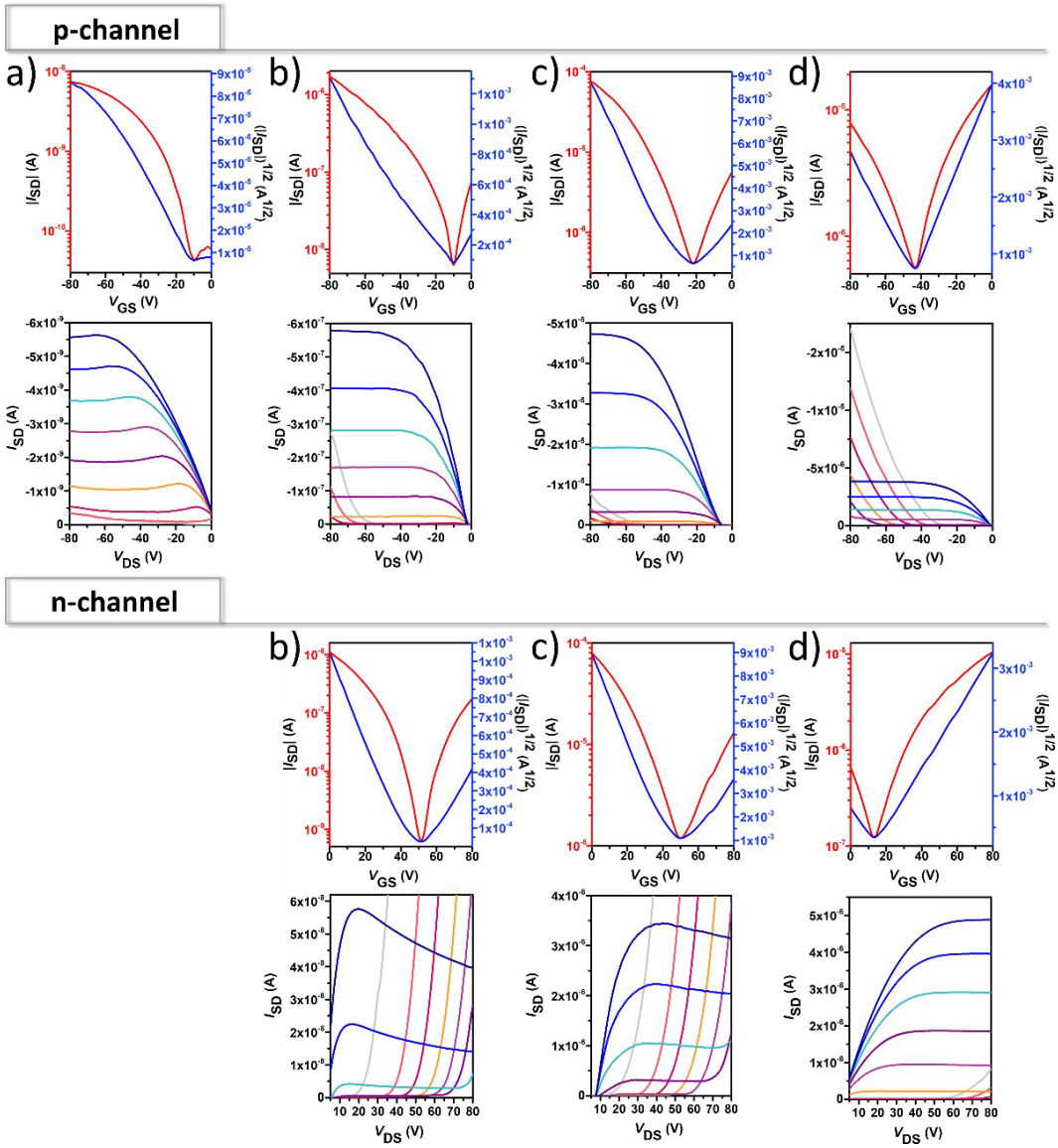

Figure IV.7. p and n-channel OFET transfer (top) and output (bottom) characteristics of **P1** (a), **P2** (b), **P3** (c) and **P4** (d) polymers. For p/n-type charge carrier mobilities, transfer curves were measured at a source–drain voltage (V_{DS}) of -80/80 V, whereas the output curves were measured at gate voltages (V_G) varying from 0 to -80/80 V at intervals of 10 V and over a V_{DS} range of 0 to -80/80 V.

In marked contrast to the reference copolymer **P1**, the partially fluorinated copolymer **P2** exhibits well-balanced ambipolar transport characteristic (μ_h/μ_e= 0.82), with hole and electron mobilities of 3.3x10^{-3} and 4.0x10^{-3} cm^{2}V^{-1}s^{-1} respectively, and I_{on}/I_{off} ratio of 10^3 in both p- and n-channel operations. Among the series, copolymer **P3** exhibits the highest and most-balanced ambipolar charge-transport characteristic (μ_h/μ_e=1.36), with hole and electron mobilities of 0.15 and 0.11 cm^{2}V^{-1}s^{-1}, respectively (around 2 orders of magnitude higher than those of the **P2**-based copolymer). This fact can be explained in terms of its high molecular weight (see Table IV.1), low energy band gap and high backbone planarity. An I_{on}/I_{off} ratio of 10^2 in both p- and n-channel operations was measured for **P3**. It is important to highlight that this performance is similar to the best IIG-based polymers measured in a BG-TC device structure.[25-27]

However, contrary to what we expected, further extended fluorination degree in copolymer **P4** reduces the OFET performance, with hole mobilities nearly 5-fold higher than electron mobilities (0.074 vs 0.013 cm^{2}V^{-1}s^{-1}, respectively). This fact seems to be inconsistent with the lower energy levels and higher coplanarity observed for copolymer **P4** compared to that of **P3**, suggesting that other factors such as solid-state morphology is also influencing the charge transport properties. Indeed, polymers with excess substituted F atoms may cause too low-lying HOMO/LUMO energy levels or repulsive F···F interactions, which will fairly decrease the mobilities or lead to more twisted intermolecular packing. Therefore, the number of F atoms should be carefully designed in order to obtain high-performance balanced ambipolar systems. Moderately high I_{on}/I_{off} of 10^5 and 10^3 were found in **P4** for p- and n-channel operations, respectively, which is considered to be key for applications of ambipolar OFETs in complementary logic circuits.[28]

IV.6. Polymeric thin-film characterization

In order to better understand the remarkable differences measured on device performance as a function of the fluorination degree, the molecular crystallinity and morphology for **P1**-**P4** thin films, fabricated under the optimal device performance

conditions, were characterized via GIXRD and AFM. As depicted in Figure IV.8a, even when all the films are moderately amorphous, the crystallinity is directly related to the percentage of backbone fluorination: while the non-fluorinated copolymer **P1** shows an amorphous nature in the film state, certain degree of crystallinity appears for the fluorinated systems, being this effect more evidenced in the case of the fully fluorinated copolymer **P4**. This higher crystalline tendency, upon the progressive fluorination, can be attributed to the increment of torsional barriers between the subunits, limiting rotation and enforcing coplanarity, effects that *a priori* lead to a better molecular packing in the solid state. At this point, it is important to highlight that these factors were previously predicted in the theoretical molecular structure analysis, showing almost flat (partially twisted) polymer backbone for **P4** (**P1**) in line with its higher (lower) crystallinity.

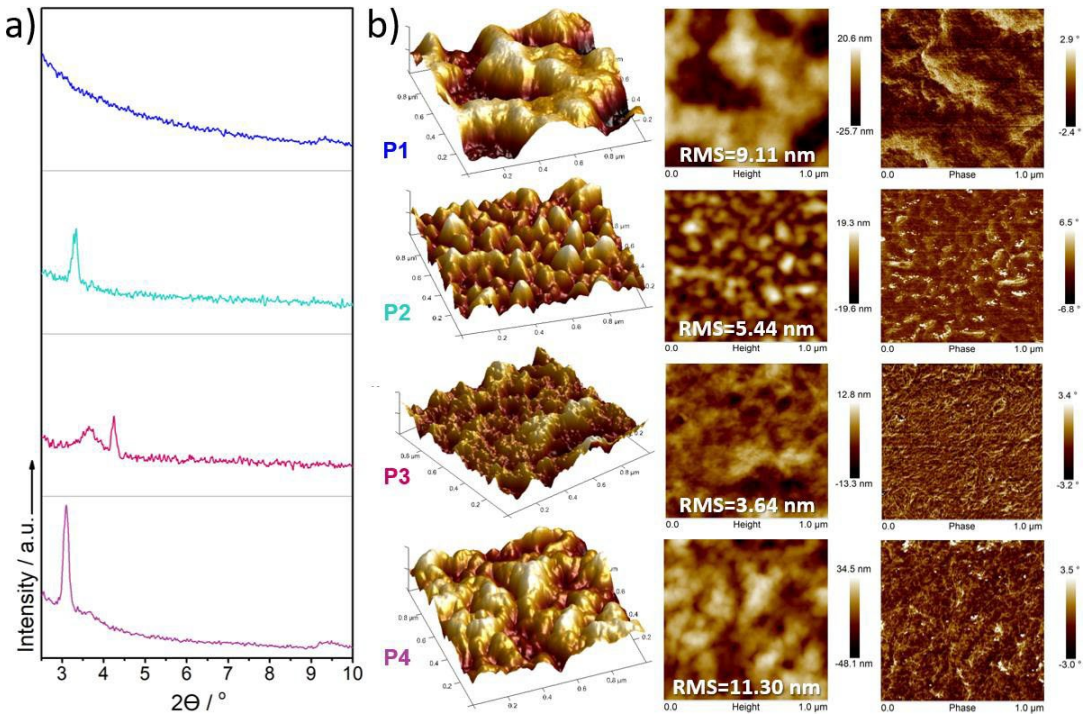

Figure IV.8. (a) GIXRD patterns and (b) 1x1 μm^2 tapping-mode AFM images of 3D-topography (left), height (middle) and phase (right) for **P1**-**P4** thin films fabricated under the deposition conditions that render the best device performances. An Intensity spectral range from 0 to 350 a.u. was used for the GIXRD spectra of all copolymers.

Hence, the presence of a main lamellar (100) reflection at lower 2Θ values in addition to the absence of diffraction peaks corresponding to π-π stacking for the fluorinated copolymers suggest that these systems self-organize into lamellar planes consisting of edge-on orientations relative to the substrate, which is beneficial for charge transport along the horizontal transport channel in BG-TC OFETs. In particular, the fluorinated copolymers **P2**, **P3** and **P4** present a 100 reflection at 2Θ=3.28, 3.64 and at 3.10°, which corresponds with interchain distances (d_{100}) of 26.92, 24.25 and 28.48 Å, respectively. We note that copolymer **P3** has the smallest d_{100} values, resulting in an enhanced inter-chain charge transport in consonance with its higher mobilities measured in OFETs.[29] Furthermore, a second diffraction peak at 2Θ= 4.24° (d_{100}=20.82 Å) can be observed for **P3** films.

These results can be corroborated by analyzing the AFM images of **P1**-**P4** thin films (Figure IV.8b). In this sense, fluorinated polymers display more homogeneous texture than the non-fluorinated counterpart **P1**, which presents a poor uniformity with larger deformations on the surface. Interestingly, discernible differences in domain shape and size can be observed for each of the fluorinated polymers. Note that, although bigger size polymer grains can be observed for thin films of **P2** and **P4** compared to that of **P3**, their surface phase images vary by a higher extent outlining the contours of the crystalline grains. This effect can be clearly observed in the 3D-topography and height images of **P4** thin films, which shows larger surface roughness (RMS=11.30 nm) and domain sizes compared to the **P3** analogous (RMS=3.64 nm), presumably due to its high degree of self-assembly and its higher crystallinity. It is generally recognized that the well interconnected domains can minimize the crystalline grain boundaries, leading to higher OFET mobilities.[30, 31] Thus, the higher OFET performance of **P3** devices can be explain by their higher homogeneity, as a result of a better interconnection of the crystalline domains and thus softer grain boundaries. These considerations indicate that the introduction of fluorine atoms dramatically influences the interactions between neighboring polymeric chains, giving rise to changes on the solid-state packing. Therefore, the numbers and position of introduced F atoms should be carefully designed to obtain high-performance OFET devices.

IV.7. Raman spectroscopy study

As indicated in the previous section, control of the film nanostructure is essential because it influences the charge transport process in OFETs. However, while GIXRD can only analyze crystalline domains, Raman spectroscopy is able to explore ordered and disordered phases, which are both crucial in the final device performance. Therefore, we recorded the FT-Raman spectra of the **P1**-**P4** copolymers as solid powders, and the results are shown in Figure IV.9a. As can be observed in Figure IV.9b, simulated Raman spectra nicely reproduce the experimental ones, further probing the reliability of the structural information derived from this discussion as well as our Raman bands assignment.

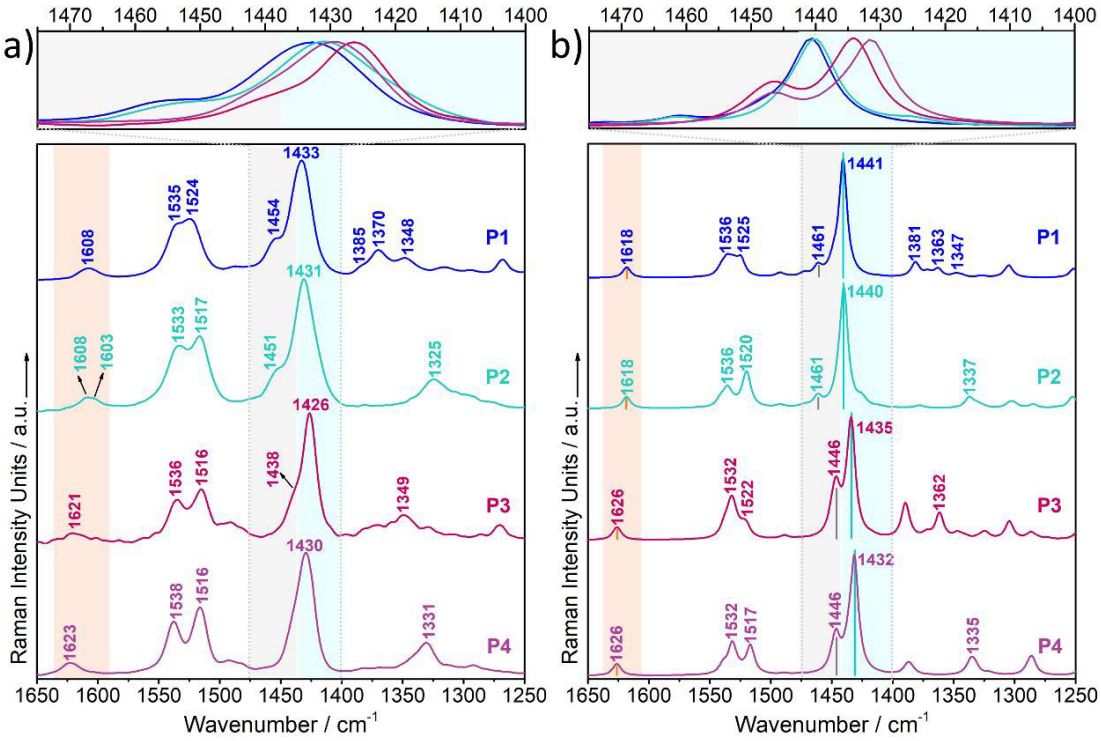

Figure IV.9. (a) Solid state FT-Raman spectra (λ_{exc}=1064nm) for the copolymers **P1**-**P4**. (b) Theoretical Raman spectra (B3LYP/6-31G** level) calculated for the dimeric models of the copolymers **P1**-**P4**. The main vibrational frequencies associated with the discussed C=C/C−C Raman features are highlighted and zoom out. An adjustment of the theoretical force fields where the frequencies were scaled down by a factor of 0.971 to disentangle experimental misassignments was used, as recommended by Scott and Random.[32]

Firstly, we focus our attention on two representative Raman bands: (i) The most intense Raman band is recorded around 1430 cm^{-1} (highlighted in light blue in Figure IV.9) and, as seen in the eigenvectors in Figure IV.10, it is ascribed to a symmetric normal mode mostly located on the thiophene rings with certain contribution on the BTD acceptor moiety and (ii) the Raman band recorded at 1455-1435 cm^{-1} (highlighted in grey in Figure IV.9), which is ascribed to a normal mode located on the IIG acceptor unit.

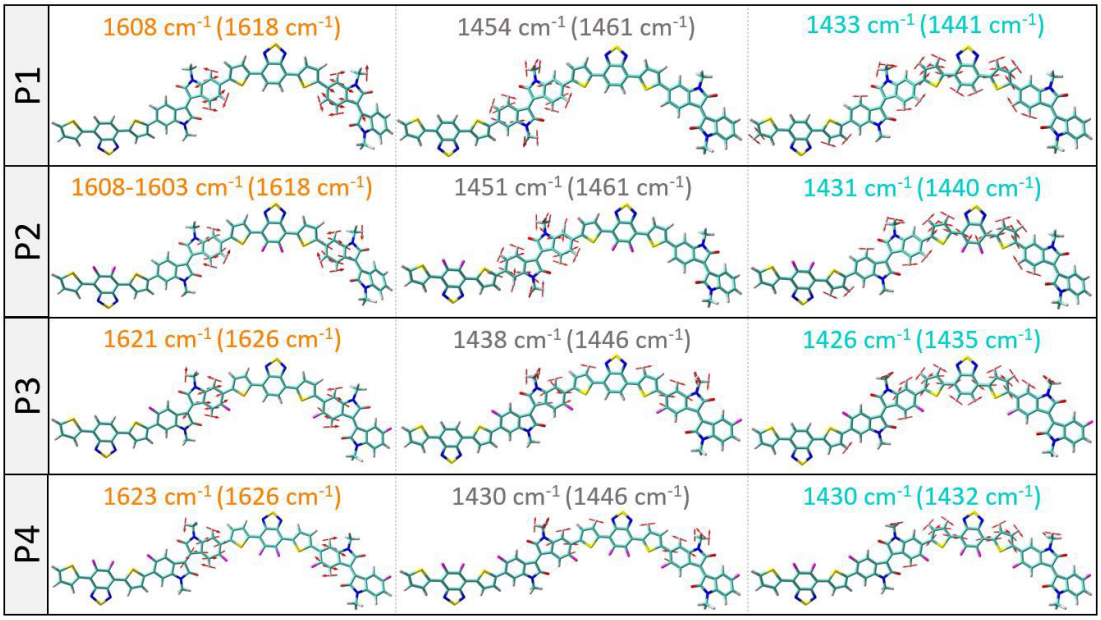

Figure IV.10. B3LYP/6-31G** vibrational eigenvectors associated with the above discussed C=C/C−C Raman features for the copolymers under study. The experimental and theoretical (in parentheses) wavenumbers are also shown.

Interestingly, this second band is theoretically predicted to gain intensity and gradually merge with the most intense Raman band on going from **P1**-**P2** to **P3**-**P4**. That is in perfectly agreement with the Lorentzian deconvolution of the 1400−1475 cm^{-1} Raman bands showed in Figure IV.11a, where this Raman band is recorded as a high energy shoulder for **P3** and **P4** copolymers. Note also that the most intense Raman band is found to be wider for **P1** and **P2** polymers, suggesting the presence of different disordered and ordered phases in the sample. In order to prove this, deconvolution of the most intense Raman band into distinct

peaks based on Lorentzian fitting was performed as showed in Figure IV.11b. It was found that the Lorentzian fitting is optimal when two different contributions are assumed for copolymers **P1** and **P2**, corroborating the presence of both disordered and ordered phases on these materials. On the other hand, as fluorine atoms are included in the IIG unit for **P3** and **P4**, this Raman band sharpens and thus, only a single component is needed to achieve an optimal fitting, indicating the presence of only an ordered phase as a consequence of the effective planarization of the polymeric backbone. Therefore, Raman spectra confirm that selective fluorination of the BTD moiety (in **P2**) is not enough to significantly increase the supramolecular order within the material, being necessary the fluorination on the IIG unit (in **P3**) to achieve an effective skeleton planarity.

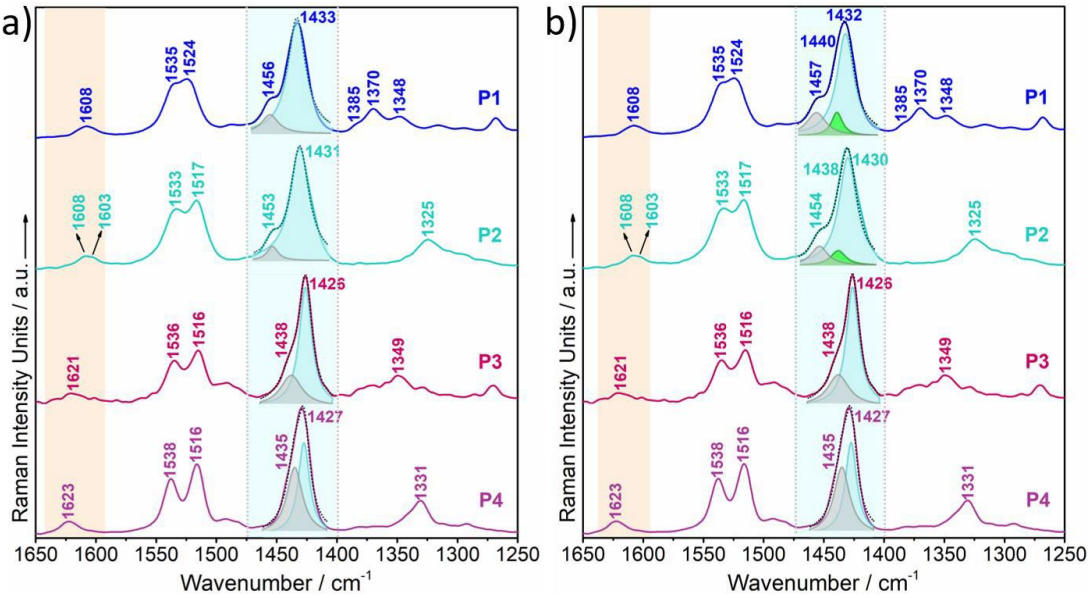

Figure IV.11. (a) Solid state FT-Raman spectra (λ_{exc}=1064nm) of polymers **P1**-**P4** with a (a) two-component deconvolution of representative Raman bands and (b) the optimal deconvolution which best fit the experimental data.

This is further corroborated by comparison of the recorded Raman spectra of copolymers **P1**-**P4** under different laser excitations (Figure IV.12). Note that when using 473, 532 or 633 nm laser wavelengths, resonance conditions occur with more disordered phases, and thus, their Raman signal should be enhanced. In this sense, the contribution

corresponding to the more disordered phase for **P1** and **P2** polymers, recorded at around 1440 cm^{-1}, notably increase its intensity when using high energy lasers. It is important to note that this intensity enhancement is less remarkable in the case of **P2**, suggesting some skeletal planarization as a consequence of the insertion of fluorine atoms on the BTD unit. Interestingly, no disordered phases are observed for polymers **P3** and **P4** independently of the laser wavelength used, indicating efficient skeleton planarity.

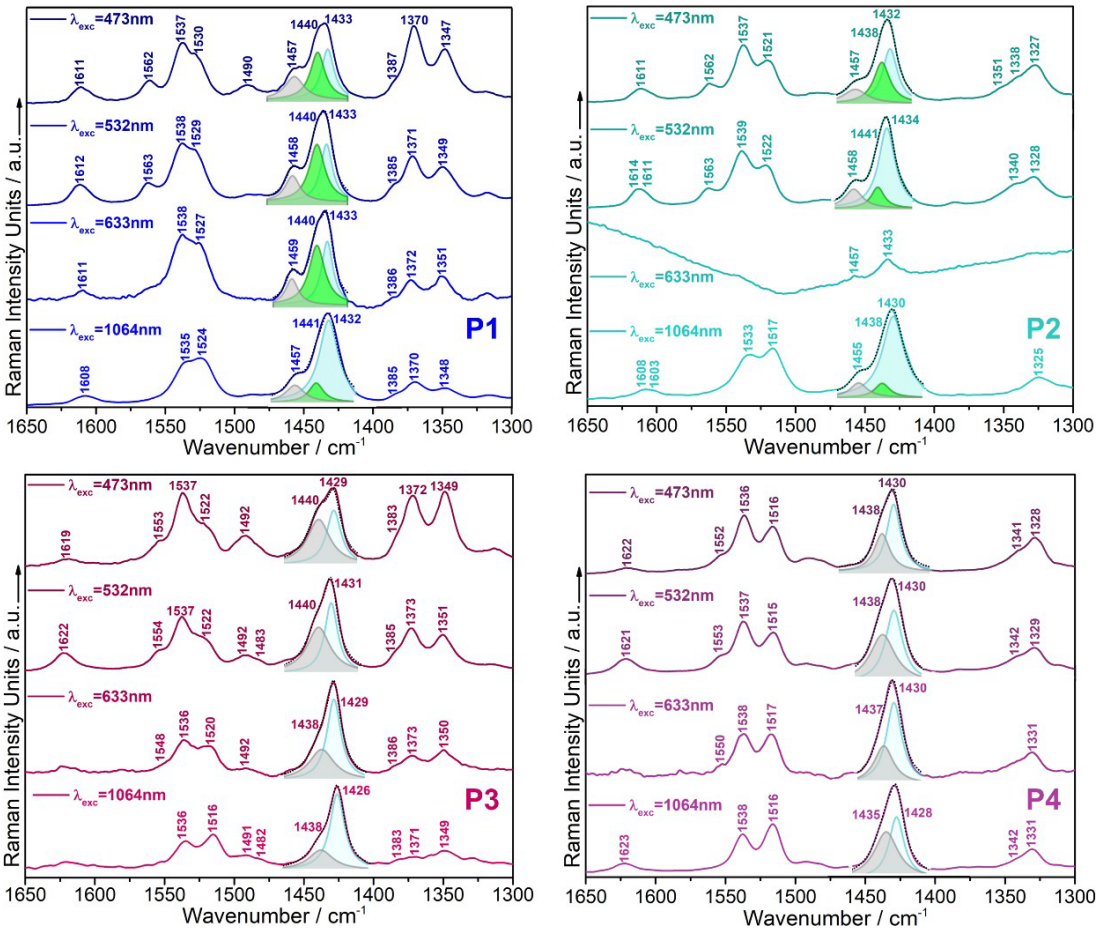

Figure IV.12. Resonance Raman spectra of copolymers **P1**-**P4** under different laser excitations.

In addition, the enhancement of the backbone planarity by fluorine addition is also corroborated by others changes in Raman spectra (see Figure IV.9), as explained as follows. (i) As fluorine atoms are progressively introduced in the conjugated backbone, the most

intense Raman band recorded at 1433 cm^{-1} for **P1** copolymer not only sharpens but also gradually downshifts, indicating a higher π-conjugation degree as a consequence of the planarization produced by the presence of S•••F interactions. In fact, it can be found at 1431, 1426 and 1430 cm^{-1} for **P2**, **P3** and **P4** copolymers, respectively. Note that, the most remarkable downshift of 7 cm^{-1} is found for **P3**, where the fluorine atoms are introduced on the IIG acceptor moiety. It is in line with its lower BLA values theoretically predicted (see Figure IV.2b), corroborating that fluorination on IIG monomeric unit is the most effective strategy to induce planarity and increase π-conjugation. (ii) The Raman band recorded at 1454 cm^{-1} for **P1** (ascribed to a normal mode located on the IIG acceptor unit) greatly downshifts for copolymers **P3** and **P4** (by approx. 17-20 cm^{-1}) where the fluorine atoms planarize the IIG unit and the adjacent thiophene rings. On the contrary, a slight downshift of only 3 cm^{-1} is recorded for copolymer **P2** respect to **P1**, which is in consonance with the slight backbone planarization when the fluorine atoms are included on the BTD acceptor moiety. (iii) The Raman band corresponding to the indolinone subunit of the IIG acceptor moiety, recorded at ca. 1608 cm^{-1} in **P1**, significantly upshifts in **P3** and **P4** copolymers (by 13-15 cm^{-1}). This is due to an improved intra-chain π-electronic delocalization due to planarization, which diminishes the cross-conjugation in IIG moiety.

IV.8. Conclusions

The results of this study have helped us to draw key structure–property–function relationships for understanding the charge transport behavior of these semiconductors, and the following conclusions can be pointed out:

- We have demonstrated that "multifluorination", *i.e.*, introducing F atoms into both IIG and BTD units, not only lowers the frontier orbital energy levels of the polymers, but also induces planarity of their conjugated backbones via S•••F non-covalent interactions.
- The impact that the gradual fluorination of the polymer backbone produces on the electronic properties clearly depends on the molecular section where the fluorine

atoms are introduced. In fact, the introduction of fluorine atoms on the BTD acceptor unit in **P2** produces a λ_{max} blue shifting with respect the parent copolymer **P1**, while fluorination of IIG acceptor moiety in copolymer **P3** shows a slight bathochromic shift. Difluorination at different positions are cooperative in **P4**, which is supported by the null spectral shift observed in this copolymer with respect the unsubstituted system **P1**.

- Comparison of UV-Vis-NIR absorption spectra of all copolymers in both solution and film state points out a further planarization of the polymer backbone in solid state due to considerable inter-chain interactions, with **P3** and **P4** copolymers showing the strongest inter-chain interactions.

- **P1**-**P4** copolymers have been also evaluated as efficient semiconducting materials. The enhanced polymer planarity and electron affinity, upon fluorination, progressively decreases the electron-injection barrier from gold electrodes to the polymeric semiconducting layers, changing their electrical properties from low hole-dominated ($\sim$1x10^{-5} cm^{2}V^{-1}s^{-1}) to balanced ambipolar charge transport (with mobilities up to 0.1 cm^{2}V^{-1}s^{-1} for **P3**) on going from **P1** to **P4**.

- Characterization of the thin films by using AFM and GIXRD revealed that fluorination remarkably affects the inter-chain interactions of polymer backbones. In this context, the crystallinity is directly related to the percentage of backbone fluorination, which is attributed to the increment of torsional barriers between the subunits, limiting rotation and enforcing coplanarity, effects that *a priori* lead to a better molecular packing on the solid state and thus explain the higher device performance observed upon fluorination. Nevertheless, poor film uniformity with inefficient interconnection of crystalline domains has been observed for **P4**, which can be the reason of its lower mobilities when compared to **P3**.

- It has been demonstrated that the impact of gradual fluorination on the supramolecular order is highly dependent on the building blocks in which the fluorine

atoms are introduced. In this sense, Raman spectroscopy helps us to analyze both ordered and disordered phases of the polymeric samples, demonstrating that fluorination of the BTD moiety is not enough to significantly increase the supramolecular order within the sample, while fluorination on the IIG acceptor unit is a much more effective way to promote skeleton planarity and enhance π-conjugation.

IV.9. References

[1] Liu, B.; Wang, Y.; Sun, H.; Gámez-Valenzuela, S.; Yan, Z.; Feng, K.; Uddin, M. A.; Koh, C.; Zhou, X.; López Navarrete, J. T.; Ruiz Delgado, M. C.; Meng, H.; Niu, L.; Woo, H. Y.; Ponce Ortiz, R.; Guo, X., Backbone Configuration and Electronic Property Tuning of Imide-Functionalized Ladder-Type Heteroarenes-Based Polymer Acceptors for Efficient All-Polymer Solar Cells. *Advanced Functional Materials* n/a, (n/a), 2200065.

[2] Dong, T.; Lv, L.; Feng, L.; Xia, Y.; Deng, W.; Ye, P.; Yang, B.; Ding, S.; Facchetti, A.; Dong, H., Noncovalent Se··· O conformational locks for constructing high-performing optoelectronic conjugated polymers. *Advanced Materials* **2017,** 29, (34), 1606025.

[3] Yuan, J.; Ford, M. J.; Zhang, Y.; Dong, H.; Li, Z.; Li, Y.; Nguyen, T.-Q.; Bazan, G. C.; Ma, W., Toward Thermal Stable and High Photovoltaic Efficiency Ternary Conjugated Copolymers: Influence of Backbone Fluorination and Regioselectivity. *Chemistry of Materials* **2017,** 29, (4), 1758-1768.

[4] Yang, J.; Zhao, Z.; Geng, H.; Cheng, C.; Chen, J.; Sun, Y.; Shi, L.; Yi, Y.; Shuai, Z.; Guo, Y.; Wang, S.; Liu, Y., Isoindigo-Based Polymers with Small Effective Masses for High-Mobility Ambipolar Field-Effect Transistors. *Advanced Materials* **2017,** 29, (36), 1702115.

[5] Roncali, J., Molecular engineering of the band gap of π-conjugated systems: Facing technological applications. *Macromolecular Rapid Communications* **2007,** 28, (17), 1761-1775.

[6] Zheng, Y.-Q.; Lei, T.; Dou, J.-H.; Xia, X.; Wang, J.-Y.; Liu, C.-J.; Pei, J., Strong Electron-Deficient Polymers Lead to High Electron Mobility in Air and Their Morphology-Dependent Transport Behaviors. *Advanced Materials* **2016,** 28, (33), 7213-7219.

[7] Wu, W.; Liu, Y.; Zhu, D., π-Conjugated molecules with fused rings for organic field-effect transistors: design, synthesis and applications. *Chemical Society Reviews* **2010,** 39, (5), 1489-1502.

[8] Youn, J.; Kewalramani, S.; Emery, J. D.; Shi, Y.; Zhang, S.; Chang, H. C.; Liang, Y. j.; Yeh, C. M.; Feng, C. Y.; Huang, H., Fused Thiophene Semiconductors: Crystal Structure–Film Microstructure Transistor Performance Correlations. *Advanced Functional Materials* **2013,** 23, (31), 3850-3865.

[9] Liu, B.; Wang, Y.; Sun, H.; Gámez-Valenzuela, S.; Yan, Z.; Feng, K.; Uddin, M. A.; Koh, C.; Zhou, X.; López Navarrete, J. T.; Ruiz Delgado, M. C.; Meng, H.; Niu, L.; Woo, H. Y.; Ponce Ortiz, R.; Guo, X., Backbone Configuration and Electronic Property Tuning of Imide-Functionalized Ladder-Type Heteroarenes-Based Polymer Acceptors for Efficient All-Polymer Solar Cells. *Advanced Functional Materials* **2022,** 32, (21), 2200065.

[10] Mei, J.; Graham, K. R.; Stalder, R.; Reynolds, J. R., Synthesis of isoindigo-based oligothiophenes for molecular bulk heterojunction solar cells. *Organic Letters* **2010,** 12, (4), 660-663.

[11] Kim, G.; Kang, S.-J.; Dutta, G. K.; Han, Y.-K.; Shin, T. J.; Noh, Y.-Y.; Yang, C., A Thienoisoindigo-Naphthalene Polymer with Ultrahigh Mobility of 14.4 cm2/V·s That Substantially Exceeds Benchmark Values for Amorphous Silicon Semiconductors. *Journal of the American Chemical Society* **2014,** 136, (26), 9477-9483.

[12] Gao, Y.; Deng, Y.; Tian, H.; Zhang, J.; Yan, D.; Geng, Y.; Wang, F., Multifluorination toward high-mobility ambipolar and unipolar n-type donor–acceptor conjugated polymers based on isoindigo. *Advanced Materials* **2017,** 29, (13), 1606217.

[13] Shi, K.; Zhang, W.; Gao, D.; Zhang, S.; Lin, Z.; Zou, Y.; Wang, L.; Yu, G., Well-balanced ambipolar conjugated polymers featuring mild glass transition temperatures toward high-performance flexible field-effect transistors. *Advanced Materials* **2018,** 30, (9), 1705286.

[14] Huang, H.; Chen, Z.; Ortiz, R. P.; Newman, C.; Usta, H.; Lou, S.; Youn, J.; Noh, Y.-Y.; Baeg, K.-J.; Chen, L. X., Combining electron-neutral building blocks with intramolecular "conformational locks" affords stable, high-mobility p-and n-channel polymer semiconductors. *Journal of the American Chemical Society* **2012,** 134, (26), 10966-10973.

[15] Takacs, C. J.; Sun, Y.; Welch, G. C.; Perez, L. A.; Liu, X.; Wen, W.; Bazan, G. C.; Heeger, A. J., Solar cell efficiency, self-assembly, and dipole–dipole interactions of isomorphic narrow-band-gap molecules. *Journal of the American Chemical Society* **2012,** 134, (40), 16597-16606.

[16] Gao, Y.; Deng, Y.; Tian, H.; Zhang, J.; Yan, D.; Geng, Y.; Wang, F., Multifluorination toward High-Mobility Ambipolar and Unipolar n-Type Donor–Acceptor Conjugated Polymers Based on Isoindigo. *Advanced Materials* **2017,** 29, (13), 1606217.

[17] Lei, T.; Xia, X.; Wang, J.-Y.; Liu, C.-J.; Pei, J., "Conformation Locked" Strong Electron-Deficient Poly(p-Phenylene Vinylene) Derivatives for Ambient-Stable n-Type Field-Effect Transistors: Synthesis, Properties, and Effects of Fluorine Substitution Position. *Journal of the American Chemical Society* **2014,** 136, (5), 2135-2141.

[18] Huang, H.; Chen, Z.; Ortiz, R. P.; Newman, C.; Usta, H.; Lou, S.; Youn, J.; Noh, Y.-Y.; Baeg, K.-J.; Chen, L. X.; Facchetti, A.; Marks, T., Combining Electron-Neutral Building Blocks with Intramolecular "Conformational Locks" Affords Stable, High-Mobility P- and N-Channel Polymer Semiconductors. *Journal of the American Chemical Society* **2012,** 134, (26), 10966-10973.

[19] Schleyer, P. v. R.; Maerker, C.; Dransfeld, A.; Jiao, H.; van Eikema Hommes, N. J. R., Nucleus-Independent Chemical Shifts: A Simple and Efficient Aromaticity Probe. *Journal of the American Chemical Society* **1996,** 118, (26), 6317-6318.

[20] Zywietz, T. K.; Jiao, H.; Schleyer, P. v. R.; de Meijere, A., Aromaticity and Antiaromaticity in Oligocyclic Annelated Five-Membered Ring Systems. *The Journal of Organic Chemistry* **1998,** 63, (10), 3417-3422.

[21] Lei, T.; Dou, J.-H.; Ma, Z.-J.; Yao, C.-H.; Liu, C.-J.; Wang, J.-Y.; Pei, J., Ambipolar Polymer Field-Effect Transistors Based on Fluorinated Isoindigo: High Performance and Improved Ambient Stability. *Journal of the American Chemical Society* **2012,** 134, (49), 20025-20028.

[22] Kim, J.; Swager, T. M., Control of conformational and interpolymer effects in conjugated polymers. *Nature* **2001,** 411, (6841), 1030-1034.

[23] Osaka, I.; Akita, M.; Koganezawa, T.; Takimiya, K., Quinacridone-Based Semiconducting Polymers: Implication of Electronic Structure and Orientational Order for Charge Transport Property. *Chemistry of Materials* **2012,** 24, (6), 1235-1243.

[24] Sirringhaus, H.; Brown, P. J.; Friend, R. H.; Nielsen, M. M.; Bechgaard, K.; Langeveld-Voss, B. M. W.; Spiering, A. J. H.; Janssen, R. A. J.; Meijer, E. W.; Herwig, P.; de Leeuw, D. M.,

Two-dimensional charge transport in self-organized, high-mobility conjugated polymers. *Nature* **1999,** 401, 685-688.

[25] Dutta, G. K.; Han, A.-R.; Lee, J.; Kim, Y.; Oh, J. H.; Yang, C., Visible-Near Infrared Absorbing Polymers Containing Thienoisoindigo and Electron-Rich Units for Organic Transistors with Tunable Polarity. *Advanced Functional Materials* **2013,** 23, (42), 5317-5325.

[26] Zhang, G.; Ye, Z.; Li, P.; Guo, J.; Wang, Q.; Tang, L.; Lu, H.; Qiu, L., A new thieno-isoindigo derivative-based D–A polymer with very low bandgap for high-performance ambipolar organic thin-film transistors. *Polymer Chemistry* **2015,** 6, (21), 3970-3978.

[27] Huang, K.; Zhao, X.; Du, Y.; Kim, S.; Wang, X.; Lu, H.; Cho, K.; Zhang, G.; Qiu, L., Modulating charge transport characteristics of bis-azaisoindigo-based D–A conjugated polymers through energy level regulation and side chain optimization. *Journal of Materials Chemistry C* **2019,** 7, (25), 7618-7626.

[28] Bisri, S. Z.; Piliego, C.; Gao, J.; Loi, M. A., Outlook and Emerging Semiconducting Materials for Ambipolar Transistors. *Advanced Materials* **2014,** 26, (8), 1176-1199.

[29] Eom, S. H.; Nam, S. Y.; Do, H. J.; Lee, J.; Jeon, S.; Shin, T. J.; Jung, I. H.; Yoon, S. C.; Lee, C., Dark current reduction strategies using edge-on aligned donor polymers for high detectivity and responsivity organic photodetectors. *Polymer Chemistry* **2017,** 8, (23), 3612-3621.

[30] Tsao, H. N.; Müllen, K., Improving polymer transistor performance via morphology control. *Chemical Society Reviews* **2010,** 39, (7), 2372-2386.

[31] Eckstein, B. J.; Melkonyan, F. S.; Wang, G.; Wang, B.; Manley, E. F.; Fabiano, S.; Harbuzaru, A.; Ponce Ortiz, R.; Chen, L. X.; Facchetti, A.; Marks, T. J., Processable High Electron Mobility π-Copolymers via Mesoscale Backbone Conformational Ordering. *Advanced Functional Materials* **2021,** 31, (15), 2009359.

[32] Scott, A. P.; Radom, L., Harmonic Vibrational Frequencies: An Evaluation of Hartree−Fock, Møller−Plesset, Quadratic Configuration Interaction, Density Functional Theory, and Semiempirical Scale Factors. *The Journal of Physical Chemistry* **1996,** 100, (41), 16502-16513.

5 Resumen y Conclusiones

Tabla de contenidos

5.1. Introducción

Mirando a nuestro alrededor, vivimos en un mundo en el que la mayoría de nuestras actividades diarias implican el uso de dispositivos electrónicos. De hecho, aspectos fundamentales como la economía, ocio o salud, están íntimamente relacionados con el progreso tecnológico. Esta relación, cada vez más dependiente entre sí, abre el escenario al diseño y síntesis de nuevos materiales que mejoren las propiedades y aplicaciones de los tradicionales basados en silicio, cuyo alto costo de fabricación, compleja procesabilidad, y escasa modulación de sus propiedades electrónicas los alejan de las nuevas demandas tecnológicas.[1, 2] En este sentido, la Electrónica Orgánica ha emergido como una solución efectiva para saciar dicha demanda social, dando lugar a una nueva generación de dispositivos electrónicos basados en semiconductores orgánicos, entre los cuales cabe destacar los transistores orgánicos de efecto campo (OFETs, del inglés "Organic Field-Effect Transistors"), [3] células solares orgánicas (OSCs, del inglés "Organic Solar Cells") [4] y diodos orgánicos emisores de luz (OLEDs, del inglés "Organic Light Emitting Diodes") mostrados en la Figura 5.1.[5] El gran interés generado por estos materiales radica en las excelentes propiedades que pueden conferir a los dispositivos electrónicos, tales como gran ligereza y flexibilidad, biocompatibilidad, coste reducido de fabricación a larga escala y una amplia capacidad de modulación de sus propiedades gracias a su versatilidad sintética.

No obstante, a pesar del gran progreso que la Electrónica Orgánica ha experimentado en las últimas tres décadas, como demuestra la tecnología OLED empleada en la fabricación y comercialización de pantallas flexibles extraplanas, los dispositivos optoelectrónicos basados en semiconductores orgánicos suelen mostrar menor rendimiento y estabilidad en comparación con sus homólogos basados en materiales inorgánicos. Este hándicap es en gran medida debido a la naturaleza estructural propia de sólidos moleculares que presentan este tipo de materiales.[6] A diferencia de semiconductores inorgánicos, donde todos los átomos se mantienen unidos mediante enlaces covalentes formando así una estructura altamente ordenada en su estado sólido, el orden de los sólidos moleculares está determinado por interacciones no covalentes débiles, principalmente interacciones π-π, que

posibilitan la aparición de cambios estadísticos en el entorno molecular de cada molécula que constituye el material, dificultando así la formación de dominios ordenados.[7]

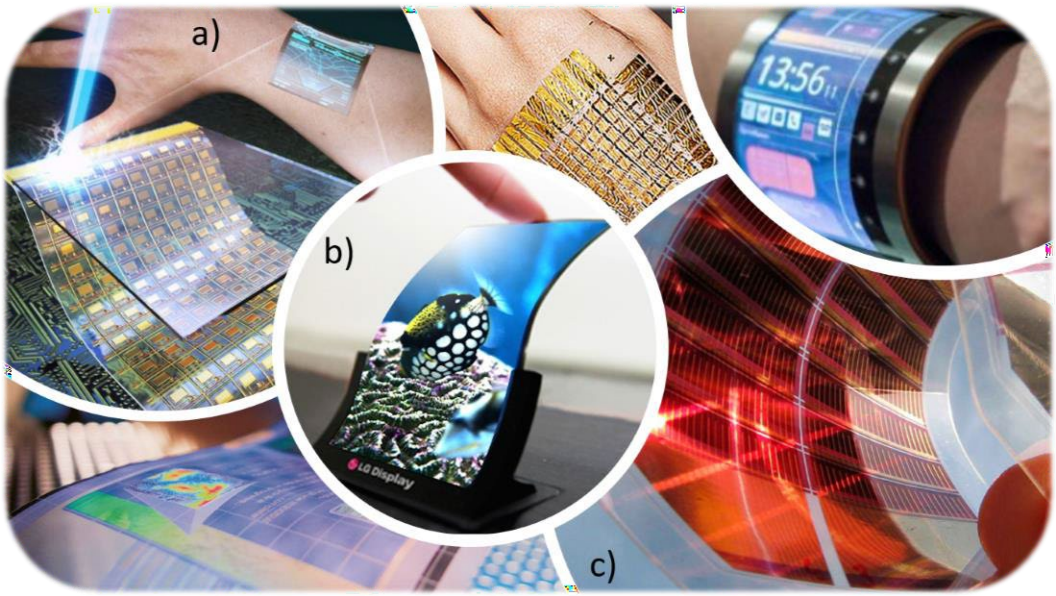

Figura 5.1. Ejemplos de dispositivos electrónicos basados en materiales orgánicos. Entre ellos, caben destacar los (a) transistores de efecto campo ultrafinos, flexibles y transparentes, (b) pantallas OLEDs de alta resolución comercializadas por la empresa LG y (c) células solares flexibles y ligeras.

Este aspecto afecta en gran medida al mecanismo de transporte de carga. De hecho, los semiconductores inorgánicos con estructuras altamente ordenadas forman un continuo de niveles de energía que dan como resultado una estructura de bandas a través de las cuales las cargas (electrones y huecos) pueden moverse casi libremente, mientras que el desorden inherente de semiconductores orgánicos implica que las cargas generalmente salten de un nivel energético asociado a una molécula a otro correspondiente a una molécula adyacente a través de un entorno denominado Densidad de Estados (Density Of States, DOS), el cual complica el movimiento de cargas a través del seno del material. Esta transferencia de carga mediante saltos le confiere la denominación de mecanismo "hopping".[8, 9]

En consecuencia, dada la dificultad que conlleva el transporte de carga en materiales orgánicos, varios modelos teóricos han sido propuestos con el objetivo de comprender la manera en la que este mecanismo opera y los fundamentos que lo rigen. Entre todos los propuestos hasta la fecha, destaca el modelo semiclásico de la teoría de transferencia electrónica de Marcus,[10] la cual define la constante de transferencia electrónica intermolecular (K_{ET}) como:

$$K_{ET} = \frac{4\pi^2}{h}\frac{1}{\sqrt{4\pi K_B T}}t^2 exp\left(-\frac{(\lambda)}{4k_B T}\right) \qquad [5.1]$$

Donde h y K_B son las constantes de Planck y Boltzmann respectivamente, T es la temperatura absoluta, λ es la energía de reorganización y t es la integral de transferencia. En vista de dicha expresión, este modelo predice que el transporte electrónico está controlado esencialmente por estos dos últimos parámetros: (i) t, que refleja la eficiencia del solapamiento entre los niveles energéticos involucrados en la transferencia de carga y (ii) el término λ, que describe el costo energético asociado a los cambios estructurales de una molécula para que esta pueda acomodar y/o liberar carga durante el proceso de hopping. En vista de la Ecuación 5.1, para que el transporte de carga sea efectivo requiere de altas integrales de transferencia y bajas energías de reorganización, es decir, sistemas capaces de aceptar y ceder cargas a moléculas cercanas de forma efectiva y al mínimo coste energético posible.[11] Llegados a este punto, es importante destacar que estos dos parámetros están estrechamente asociados a la estructura molecular y el empaquetamiento en estado sólido.[12]

Desde el punto de vista molecular, un sistema π-conjugado está formado por cuatro componentes estructurales básicos: esqueleto π-conjugado, cadenas laterales, heteroátomos y sustituyentes dadores o aceptores de electrones. Entre estos componentes, el esqueleto π-conjugado es inequívocamente el que dicta la mayoría de las propiedades optoelectrónicas de los sistemas orgánicos, el cual es deseable que tenga una alta planaridad como prerrequisito para lograr un solapamiento óptimo entre los orbitales π adyacentes. Con el objetivo de reducir el desorden torsional del esqueleto molecular, tanto la fusión de

unidades aromáticas mediante la formación de enlaces covalentes adicionales como el bloqueo conformacional causado por interacciones no covalentes resultan en estrategias de diseño molecular altamente efectivas (Figura 5.2).[13] Además de la planaridad, es importante que el esqueleto π-conjugado tenga una extensión óptima que asegure una buena deslocalización electrónica a nivel intramolecular sin llegar a repercutir negativamente sobre la procesabilidad final.[14] En este sentido, para garantizar una solubilidad suficiente en sistemas π-conjugados rígidos y, por lo tanto, mejorar la procesabilidad de los semiconductores orgánicos en solución, generalmente se introducen cadenas laterales en el esqueleto π-conjugado.

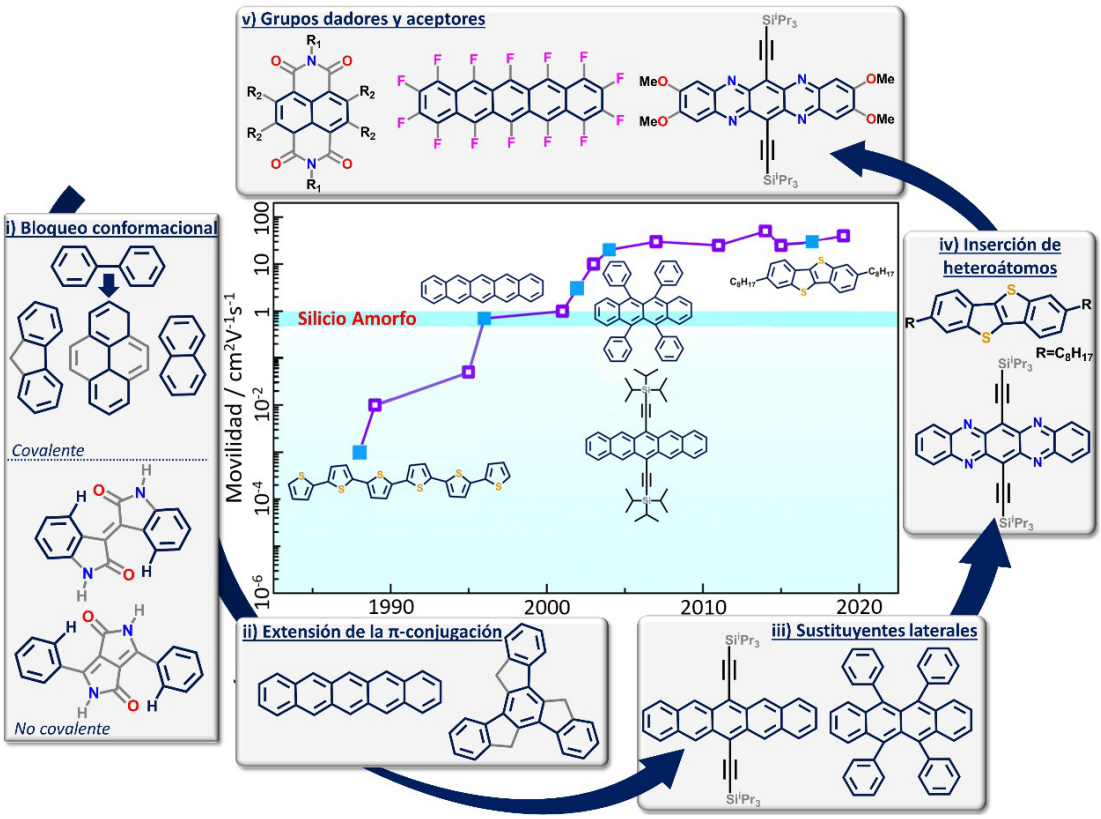

Figura 5.2. Evolución del rendimiento de OFET basados en moléculas pequeñas en función del año. Las principales estrategias de diseño molecular que han dado lugar a sistemas de especial relevancia en el campo están destacadas.

Es importante que la incorporación de grupos laterales ayude a solubilizar el material sin alterar la planaridad molecular del mismo.[15, 16] Además de una buena procesabilidad, un requisito indispensable para la aplicabilidad de estos materiales en dispositivos orgánicos es que tengan una buena estabilidad ambiental, es decir, que sean poco vulnerables a la oxidación por exposición al oxígeno. Una estrategia comúnmente empleada para mejorar este punto es la introducción de heteroátomos como el azufre, el cual no sólo dota a los sistemas π-conjugados de una gran robustez ambiental sino que además, ofrece una gran capacidad para mejorar el empaquetamiento molecular en estado sólido como resultado de múltiples interacciones intermoleculares S···S.[17] Por último, la introducción de grupos sustituyentes con naturaleza electro-dadora o electro-aceptora posibilita la modulación de los niveles energéticos HOMO y LUMO de un sistema determinado. Esta estrategia ha sido ampliamente usada en el diseño de semiconductores transportadores de electrones, en donde la introducción de grupos aceptores de electrones (derivados de imida, ciano, nitro, halógenos, etc.) produce un déficit de densidad electrónica en la plataforma π-conjugada, reduciendo esencialmente la energía del LUMO y por lo tanto, facilitando la inyección de electrones.[18]

No obstante, cabe destacar que además de la naturaleza de la molécula en sí (como se ha descrito previamente), la presencia de un empaquetamiento molecular ordenado con un solapamiento π-π óptimo en el estado sólido se considera de crucial importancia para el diseño de materiales con buenas propiedades de transporte de carga.[19] El punto clave detrás de esta filosofía es que si las moléculas adoptan una disposición π-π, el acoplamiento electrónico entre las funciones de onda de moléculas vecinas debería de ser *a priori* ventajoso para obtener una migración eficiente de carga eléctrica dentro de un semiconductor.[20]

Así pues, tal y como ha quedado expuesto en el trascurso de esta sección, el transporte de carga en materiales orgánicos es un proceso complejo que depende de muchos factores. Esto hace que, aún hoy en día, los mecanismos de transporte de carga en semiconductores orgánicos no se entiendan completamente, debido principalmente al limitado conocimiento

de la relación estructura-propiedad. Por lo tanto, la principal motivación para el diseño y síntesis de nuevos materiales en las últimas décadas no solo ha sido la mejora de sus propiedades optoelectrónicas o el descubrimiento de aplicaciones novedosas, sino también comprender en mayor medida la compleja relación estructura-propiedad de los mismos.

5.2. Objetivos

A pesar de la dificultad que entraña el estudio de la relación estructura-propiedad cuando se trata del transporte de carga en semiconductores orgánicos, esta Tesis Doctoral se centra por un lado en estudiar el efecto que las distintas modificaciones estructurales, en una serie de semiconductores orgánicos, juegan en las propiedades ópticas y electrónicas de los mismos, así como analizar el impacto de dichas modificaciones estructurales a nivel supramolecular como factor clave en la determinación de las propiedades de transporte de carga del material final. Con este objetivo en mente, esta memoria se ha dividido en cuatro capítulos según la estructura π-conjugada de los sistemas a estudio, los cuales van desde pequeñas moléculas hasta polímeros unidimensionales o incluso bidimensionales, tal y como muestra la Figura 5.3.

En el primer capítulo, trataremos de analizar el impacto producido por la sustitución periférica con grupos dadores (metoxilo) o aceptores de electrones (acetilo, nitrilo y nitro) sobre las propiedades electrónicas, supramoleculares y de transporte de carga de dos familias de semiconductores basados en triindol y diazatruxenona. Además, el efecto de la combinación de segmentos ricos y deficientes en electrones en la misma unidad π-conjugada de diazatruxenona será también analizado. La síntesis de estos semiconductores fue llevada a cabo por el grupo de la profesora Berta Gómez-Lor del Instituto de Ciencia de Materiales de Madrid (ICMM).

Con respecto al segundo capítulo, una serie de polímeros microporosos derivados de plataformas π-conjugadas con simetría C_3 fueron estudiados. En primer lugar, el efecto producido por la inserción de distintos espaciadores π-conjugados (fenilo o benzotiadiazol) así como la distinta posición de unión entre las plataformas con simetría C_3 (*para* en **T2** o

meta en **T3**) sobre el grado de deslocalización electrónica del sistema fue investigado mediante un procedimiento experimental-teórico. La habilidad de estos polímeros para la detección de analitos nitroaromáticos fue también estudiada. La síntesis de estos polímeros fue llevada a cabo por el grupo de la profesora Berta Gómez-Lor del Instituto de Ciencia de Materiales de Madrid (ICMM). En segundo lugar, realizamos una investigación puramente teórica de un total de 27 polímeros porosos diferentes con el objetivo de explorar la capacidad de modulación de las propiedades estructurales, electrónicas y de transporte de carga de estos sistemas mediante tres tipos de modificaciones estructurales: (i) la naturaleza de las plataformas con simetría C_3 (truxeno, triindol y truxenona), (ii) la inserción de diferentes espaciadores π-conjugados (fenilo y alquino) o (iii) la distinta posición de unión (*para* en **T2**, *meta* en **T3** o combinando ambas en **T2,3**).

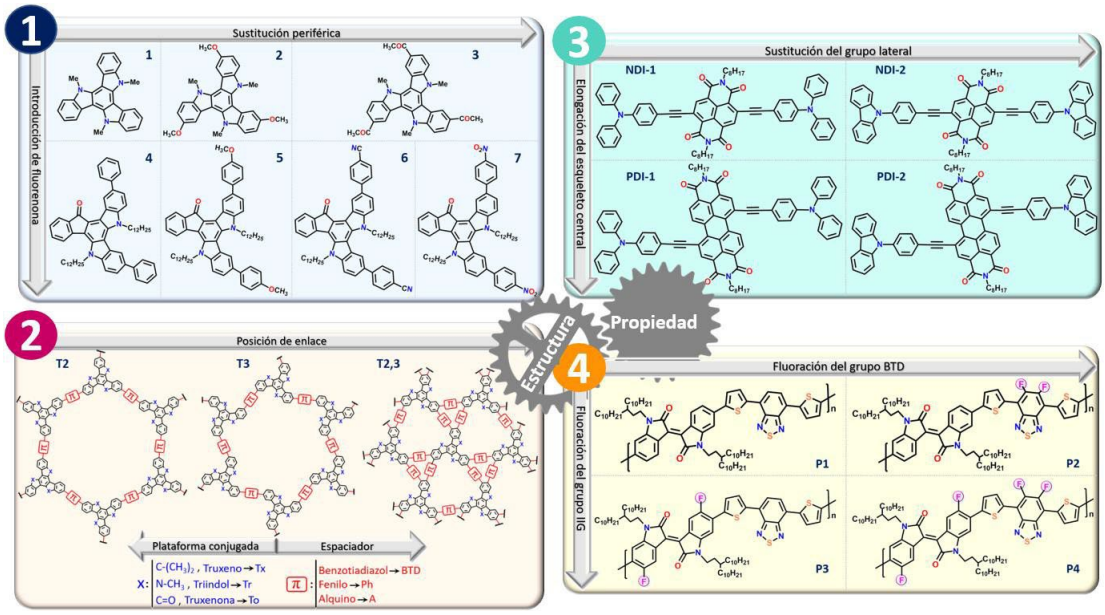

Figura 5.3. Estructuras químicas de los sistemas π-conjugados estudiados en la presente tesis doctoral, enmarcadas según el capítulo en el cual se investiga la relación estructura-propiedad de las mismas.

El tercer capítulo tiene como principal objetivo analizar los efectos producidos en la estructura molecular, propiedades electrónicas y el grado de ordenamiento en estado sólido

de cuatro nuevos semiconductores orgánicos basados en naftalenodiimida (NDI) y perilenodiimida (PDI), ya sea por la extensión del esqueleto central o por la sustitución lateral con diferentes grupos ricos en electrones. La síntesis de estos semiconductores ha sido realizada por el grupo de la profesora María Pilar Prieto de la Universidad de Castilla-La Mancha.

En el último capítulo se comparan los efectos producidos por la fluoración de las unidades isoindigo (IIG) y benzotiadiazol (BTD) en la estructura, niveles de energía e interacciones intramoleculares de cuatro polímeros A-D-A´ sintetizados por el grupo del profesor Mohammed Al-Hashimi de la Universidad Texas A&M de Qatar.

El resultado de esta Tesis doctoral ayudará a elucidar relaciones estructura-propiedad claves para la comprensión del proceso de transporte de carga en estos sistemas y, de manera más general, proporcionará información útil para el diseño de nuevos semiconductores con aplicaciones en el campo de la electrónica.

5.3. Metodología

Con el objetivo de abordar la problemática planteada en el apartado anterior, hemos llevado a cabo un estudio sistemático de cuatro etapas que combina una parte experimental con cálculos de modelización molecular (Figura 5.4):

En primer lugar, los sistemas a estudio han sido sometidos a un proceso de caracterización tanto en disolución como en estado sólido mediante el uso de técnicas espectroscópicas de absorción electrónica UV-Vis, emisión y Raman (resonante y no resonante), así como de técnicas electroquímicas de voltamperometría cíclica y espectroelectroquímica. Este análisis nos permitirá evaluar la implicación que ejerce la modificación química sobre la estructura molecular y grado de π-conjugación de estos sistemas.

Posteriormente, los resultados obtenidos han sido interpretados con la ayuda de cálculos químico-cuánticos a nivel DFT (del inglés “Density Functional Theory”), los cuales

nos han permitido interpretar los espectros en detalle y por lo tanto recabar una mayor información sobre el papel que juegan las sustituciones estructurales en las propiedades optoelectrónicas de nuestros sistemas.

Figura 5.4. Esquema de las distintas etapas metodológicas abordadas en la presente tesis.

Una vez caracterizados los sistemas a estudio, trataremos de implementarlos en dispositivos electrónicos, tales como OFETs o sensores. El objetivo de este punto es la evaluación de la capacidad de transporte de carga que presenta el material semiconductor, como etapa crucial en cualquier dispositivo electrónico, y relacionarla con las propiedades conjugacionales observadas previamente. En este apartado, el desarrollo de cálculos químico-cuánticos será de crucial importancia para entender el papel que juegan las interacciones intermoleculares en el empaquetamiento molecular de estos materiales en el estado sólido y, por lo tanto, en sus propiedades de transporte de carga.

Por último, la morfología de las láminas delgadas será analizada mediante el uso de técnicas como microscopia de fuerza atómica (AFM, Atomic Force Microscopy), difracción de rayos X con incidencia rasante (GIXRD, Grazing Incidence X-Ray Diffraction) o espectroscopía Raman, con el objetivo de recabar una mayor información sobre el efecto que la estructura morfológica juega en las eficiencias eléctricas de los dispositivos.

5.4. Resultados y discusión

A continuación, detallaremos los resultados más relevantes obtenidos de los sistemas estudiados en la presente tesis doctoral.

5.4.1. Capítulo I: Papel de la sustitución periférica en el ordenamiento molecular de semiconductores con forma de disco: el caso de triindol y diazatruxenona.

En este capítulo se ha estudiado el efecto que produce la distinta sustitución periférica con grupos dadores (metoxilo) y aceptores de electrones (acetilo, nitrilo y nitro) en las propiedades electrónicas y supramoleculares de semiconductores con forma de disco basados en triindol y diazatruxenona. Con el objetivo de mostrar los resultados obtenidos de la forma más clara posible, este capítulo se ha dividido en dos secciones de acuerdo a la naturaleza de la plataforma π-conjugada, diferenciando así entre sistemas basados en triindol y sistemas basados en diazatruxenona.

En relación con los primeros, la Figura 5.5 resume el estudio tanto experimental como teórico realizado sobre los triindoles **1** (sin funcionalizar), **2** (funcionalizado con grupos metoxilo) y **3** (funcionalizado con grupos acetilo). Cálculos químico-cuánticos realizados a nivel DFT (B3LYP/6-31G**) predicen que la distinta naturaleza electrónica de los sustituyentes periféricos no tiene repercusión alguna sobre la estructura molecular de la plataforma de triindol, la cual presenta los tres anillos periféricos distorsionados con respecto al anillo aromático central como resultado del impedimento estérico entre los grupos *N*-alquilo y los fenilos externos. Sin embargo, la funcionalización periférica de la plataforma de triindol afecta en gran medida las propiedades electrónicas de la misma. En este sentido, los espectros de absorción de estos sistemas medidos en CH_2Cl_2 ($c=5x10^{-6}$ M) muestran como la banda de máxima absorción se desplaza batocrómicamente tras la funcionalización de la plataforma de triindol, dando lugar a una disminución del gap óptico a medida que vamos del triindol **1** no sustituido (3.36 eV) a los derivados sustituidos con grupos metoxilo dadores de electrones (3.09 eV) y grupos acetilo aceptores de electrones (2.66 eV). Gracias al desarrollo de cálculos químico cuánticos a nivel TD-DFT demostramos

que en estos sistemas la transición electrónica $S_0 \rightarrow S_1$ está prohibida por simetría con respecto a las reglas de selección dipolo−dipolo. Del mismo modo, los niveles de energía HOMO/HOMO-1 y LUMO/LUMO+1 están degenerados energéticamente como resultado de la simetría C_3 que presentan estos sistemas.

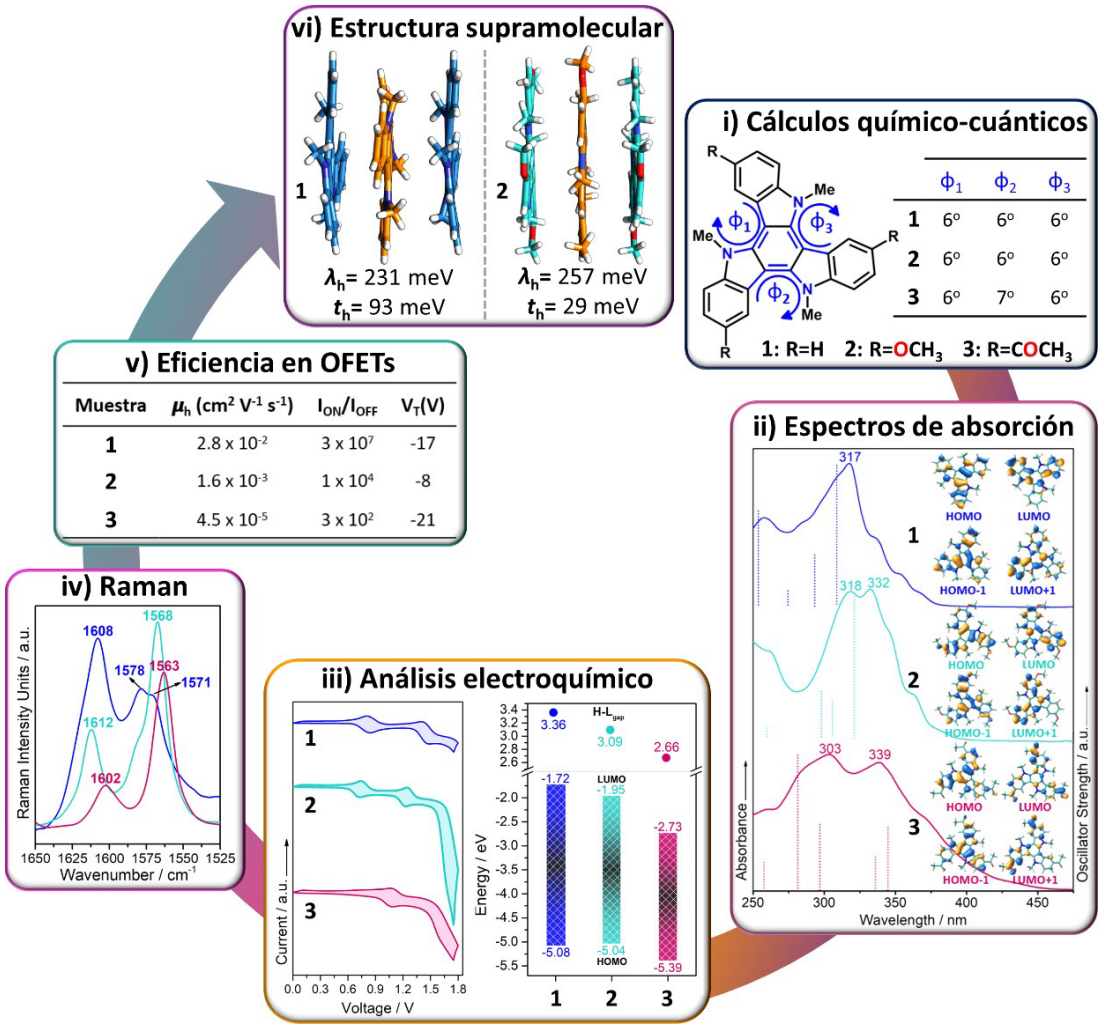

Figura 5.5. Resumen del estudio experimental y teórico llevado a cabo para los sistemas basados en triindol **1**, **2** y **3**.

Con el objetivo de poder explicar la disminución del gap óptico previamente observada cuando la plataforma de triindol es sustituida con grupos dadores y aceptores de electrones,

medidas de voltamperometría cíclica (CV) de los tres triindoles bajo estudio fueron llevadas a cabo. Interesantemente, todos los triindoles mostraron ser fácilmente oxidados de forma reversible. El análisis de las topologías de los orbitales frontera revela que tanto el HOMO como el LUMO están deslocalizados sobre la plataforma de triindol. Curiosamente, la inserción de grupos dadores o aceptores de electrones en **2** y **3** produce la extensión de dichos orbitales frontera sobre estos sustituyentes periféricos, resultando de este modo en una extensión de la π-conjugación y por tanto en una disminución del HOMO-LUMO gap en el siguiente orden: **1** > **2** > **3**, en línea con la tendencia observada para los gaps ópticos. La mejora en la deslocalización electrónica tras la funcionalización también se pone de manifiesto mediante el análisis de los espectros Raman de los triindoles **1**, **2** y **3**, en donde el progresivo desplazamiento de la banda Raman correspondiente a la vibración CC del anillo aromático central junto con el aumento de intensidad de esta banda con respecto a las vibraciones de flexión de los grupos CH_2 no conjugados al pasar del triindol **1** al **2** y al **3**, reflejan una mayor eficiencia en la π-conjugación en este mismo sentido.

Teniendo en cuenta la facilidad y reversibilidad de las oxidaciones, la cercanía de los niveles HOMO con respecto a la función de trabajo del oro (ϕ_{Au}=5.1 eV) y la eficiencia en la π-conjugación observada en estos sistemas, podemos pensar que son buenos candidatos para el estudio de sus propiedades semiconductoras en OFETs. Por ello, los triindoles bajo estudio se implementaron en tales dispositivos siguiendo una configuración de contacto-superior, puerta-inferior (bottom-gate top-contact, BG-TC). Como se puede ver en la Figura 5.5, la sustitución periférica de la plataforma de triindol repercute negativamente en la eficiencia del transistor, reduciendo en uno y tres ordenes de magnitud la movilidad de huecos medida para la plataforma de triindol (~$2x10^{-2}$ $cm^2V^{-1}s^{-1}$) al introducir grupos metoxilo o acetilo en **2** y **3**, respectivamente. En vista de estos resultados, tendencias opuestas del rendimiento de los dispositivos y el grado de conjugación intramolecular en los triindoles **1**-**3** fueron encontradas. De hecho, la mejor (peor) eficiencia en OFETs se midió para el triindol **1** (**3**), a pesar de mostrar una estructura menos (más) conjugada tal y como

se determinó mediante el uso de espectroscopía de absorción UV-Vis, Raman, cálculos químico cuánticos y medidas electroquímicas.

Por lo tanto, cabe pensar que aunque los grupos periféricos no afectan la estructura molecular del triindol, pueden influir significativamente en la disposición supramolecular en estado sólido. En este sentido, las estructuras determinadas a través de difracción de rayos X para los compuestos **1**-**3** muestran que estos sistemas empaquetan formando columnas en las que cada unidad molecular se encuentra rotada 60° con respecto a sus vecinas dentro de la columna, de modo que los anillos aromáticos centrales quedan perfectamente solapados. Sin embargo, notables diferencias en la estructura molecular de estos sistemas fueron encontradas, ya que mientras el sistema **1** mantiene la conformación distorsionada de la plataforma de triindol en estado sólido, la funcionalización con grupos periféricos en **2** y **3** planariza significativamente el esqueleto π-conjugado. Este efecto resulta en valores de t_h más pequeños para dímeros de **2** (29 meV) con respecto a dímeros de **1** (93 meV), debido a que en una disposición columnar alternada en la que solo los anillos aromáticos centrales están perfectamente solapados, la extensión de las funciones de onda HOMO y HOMO-1 sobre los grupos periféricos resulta en un solapamiento menos eficiente en la parte central de las plataformas de triindol. Esto sumado a los mayores valores de λ_h calculados para **2** (257 meV) en comparación con **1** (231 meV) podría explicar las movilidades más bajas observadas en **2** con respecto a **1**. Por otro lado, la menor movilidad obtenida para **3** es atribuida a la combinación de factores moleculares intrínsecos y el pobre ordenamiento supramolecular observado experimentalmente.

Con relación a sistemas basados en diazatruxenona, la Figura 5.6 muestra a modo de resumen el estudio tanto experimental como teórico realizado sobre las diazatruxenonas **4** (sin funcionalizar), **5** (funcionalizada con grupos metoxilo), **6** (funcionalizada con grupos nitrilo) y **7** (funcionalizada con grupos nitro).

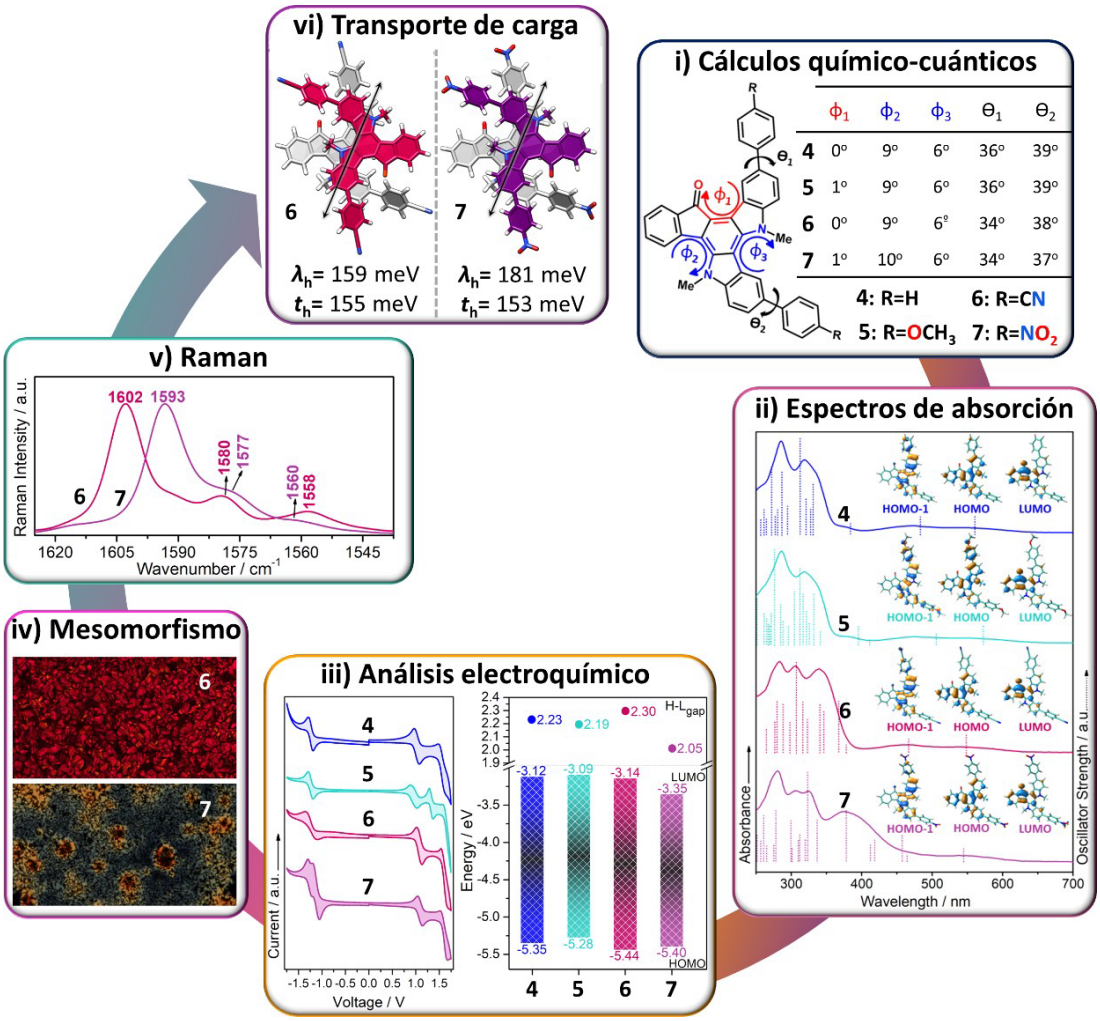

Figura 5.6. Resumen del estudio experimental y teórico llevado a cabo para los sistemas basados en diazatruxenona **4**, **5**, **6** y **7**.

Cálculos químico-cuánticos realizados a nivel DFT (B3LYP/6-31G**) predicen una dualidad en el desorden interno de la plataforma de diazatruxenona, ya que mientras las unidades de carbazol mantienen una moderada distorsión en torno a 6-10º, la unidad de fluorenona queda totalmente plana fruto de la interacción intramolecular entre el oxígeno del grupo cetónico y el átomo de hidrógeno del anillo de benceno adyacente. Tal y como se observó previamente para los sistemas basados en triindol, la distinta naturaleza electrónica de los sustituyentes periféricos no tiene repercusión alguna sobre la estructura molecular

de la diazatruxenona ni sobre los fenilos periféricos en los que se introducen, los cuales se encuentran distorsionados en gran medida (en torno a 38º) con respecto a la unidad de diazatruxenona.

Del mismo modo, los espectros de absorción medidos en CH_2Cl_2 ($c=1x10^{-5}$ M) muestran que la distinta naturaleza electrónica de los grupos periféricos apenas afecta sus propiedades ópticas. De hecho, valores similares de gap óptico (1.91 eV) fueron observados para todas las diazatruxenonas. No obstante, diferencias significativas pueden observarse en los espectros de absorción de las diazatruxenonas cuando las comparamos con los de sus análogos triindoles, como por ejemplo la aparición de dos bandas anchas situadas en la zona de baja energía. Tales bandas surgen de la ruptura de la simetría C_3 causada por el reemplazamiento de una unidad de carbazol por una unidad de fluorenona, permitiendo los tránsitos electrónicos $S_0 \rightarrow S_1$ y $S_0 \rightarrow S_2$ asociados a excitaciones de transferencia de carga intramolecular HOMO→LUMO y HOMO-1→LUMO, respectivamente. En vista de las topologías de los orbitales de frontera, es importante destacar que no se aprecian variaciones significativas en función de la naturaleza electrónica de los distintos grupos periféricos, lo que sugiere una insignificante transferencia de densidad electrónica de los mismos y, por lo tanto, explica los similares gaps ópticos observados experimentalmente para todos los compuestos.

Esta hipótesis fue corroborada mediante medidas CV en CH_2Cl_2 ($c=1x10^{-3}$ M), gracias a la cual las propiedades electrónicas de estos sistemas fueron analizadas en detalle. Tal y como muestra la Figura 5.6, todas las diazatruxenonas bajo estudio muestran un carácter redox anfotérico definido por procesos de oxidación y reducción perfectamente reversibles. El análisis de los niveles energéticos HOMO y LUMO extraídos a partir de los potenciales de oxidación y reducción respectivamente, muestran que la inserción de dos grupos metoxilo, dadores de electrones, en **5** produce una ligera desestabilización del HOMO (0.07 eV) y del LUMO (0.03) con respecto a la diazatruxenona sin sustituir, resultando en valores de HOMO-LUMO gap similares al pasar de **4** (2.23 eV) a **5** (2.19 eV). Por otro lado, la unión de grupos aceptores de electrones produce una estabilización de los orbitales HOMO y LUMO, siendo

este efecto más pronunciado para el LUMO de la diazatruxenona **7** sustituida con grupos nitro de mayor carácter electrón atrayente (con estabilizaciones del LUMO de 0.02 y 0.23 eV para las diazatruxenonas **6** y **7** respectivamente, cuando las comparamos con la diazatruxenona sin sustituir). Como resultado, valores de HOMO-LUMO gap ligeramente mayores en **6** y menores en **7** fueron observados con respecto a la diazatruxenona sin sustituir (con valores de HOMO-LUMO gap de 2.23, 2.30 y 2.05 eV para los sistemas **4**, **6** y **7**, respectivamente). En vista de las sutiles diferencias observadas en los valores de HOMO-LUMO gap para estos sistemas, podemos corroborar que hay una insignificante transferencia de densidad electrónica de los sustituyentes periféricos y la plataforma π-conjugada basada en diazatruxenona.

No obstante, los sustituyentes periféricos influyen enormemente en las propiedades de autoensamblaje de estos compuestos. De hecho, las diazatruxenonas sustituidas con grupos electrón atrayentes **6** y **7** mostraron excelentes propiedades mesomórficas, dando lugar a mesofases estables caracterizadas por una buena birrefringencia junto con fluidez cuando se visualizaron por microscopía óptica polarizada. Estas diferencias observadas en las propiedades mesomórficas a lo largo de la serie pueden ser explicadas en términos de una efectiva modulación del momento dipolar intrínseco de la unidad de diazatruxenona en función del sustituyente insertado a la misma, lo cual afecta en gran medida a las interacciones dipolo-dipolo que determinan la estructura supramolecular. En este sentido, cálculos teóricos a nivel DFT predicen un aumento de casi el doble en el valor del momento dipolar de los derivados **6** (9.73 D) y **7** (10.02 D) con respecto a los demás, apuntando así a una disposición dipolo-dipolo más favorable en estos sistemas como consecuencia de una mayor polarización.

Con el objetivo de analizar la polarización molecular de los derivados **6** y **7**, se llevaron a cabo medidas de sus espectros Raman. En línea con los resultados obtenidos mediante medidas electroquímicas y cálculos DFT, el desplazamiento hacia menores (mayores) frecuencias de la banda Raman asociada a la vibración de los anillos de benceno funcionalizados periféricamente (vibración del grupo C=O) para la diazatruxenona **7** en

comparación con su homólogo **6**, sugiere una mejor deslocalización electrónica en el primero como consecuencia de la inserción de un grupo NO_2 aceptor de electrones más fuerte. Además, los espectros Raman corroboran que el reemplazo de una unidad de carbazol por una unidad de fluorenona en la plataforma de diazatruxenona aumenta significativamente la conjugación.

Considerando las interesantes propiedades mesomórficas, carácter anfotérico y efectiva deslocalización electrónica de las diazatruxenonas sustituidas con grupos aceptores de electrones **6** y **7**, estos sistemas se implementaron en OFETs siguiendo una configuración BG-TC. Desafortunadamente, los dispositivos preparados con estos sistemas fueron eléctricamente inactivos. Dicha ineficiencia en la conductividad eléctrica de los OFETs fabricados con estos semiconductores fue adscrita a un empaquetamiento molecular perpendicular con respecto a la superficie del sustrato, lo cual es perjudicial para el transporte de carga de OFETs fabricados en una configuración BG-TC.

Con esto en mente, se hizo uso de la técnica SCLC (del inglés, Space Charge-Limited Current) para estimar las movilidades de carga en la dirección columnar de apilamiento de las diazatruxenonas **6** y **7**. Como resultado, se obtuvieron movilidades de huecos de $5x10^{-2}$ $cm^2V^{-1}s^{-1}$ para diazatruxenona **7**, mientras que para la diazatruxenona **6** no se pudo observar el régimen SCLC. Curiosamente, cálculos teóricos a nivel DFT para modelos diméricos de **6** y **7** en los que las moléculas del dímero se encuentran con los dipolos enfrentados predicen valores muy similares tanto de λ_h como de t_h, sugiriendo valores de movilidades similares o incluso ligeramente superiores para el caso de la diazatruxenona **6**, aunque no se haya podido observar el régimen SCLC.

5.4.2. Capítulo II: Análisis de las propiedades optoelectrónicas de polímeros orgánicos porosos.

En analogía al estudio realizado en el capítulo anterior, en esta sección llevamos cabo el análisis de una serie de polímeros microporosos derivados de plataformas π-conjugadas con simetría C_3. En primer lugar, se ha estudiado el efecto producido por la inserción de distintos espaciadores π-conjugados (fenilo o benzotiadiazol) o la distinta posición de unión entre las unidades de truxeno (*para* en **T2** o *meta* en **T3**) en las propiedades optoelectrónicas del polímero final. En vista de la Figura 5.7, en la que se resume el estudio tanto experimental como teórico realizado sobre estos sistemas, ambos factores estructurales repercuten notablemente en las propiedades optoelectrónicas del material.

En este sentido, cálculos teóricos llevados a cabo tanto para láminas periódicas (PBE0-D3) como para modelos diméricos (PBE0/6-31G*) de estos polímeros predicen una mayor planaridad junto con un acortamiento (alargamiento) de los enlaces simples C-C (dobles C=C) para los sistemas unidos covalentemente en posición -*para* con respecto a sus isómeros sustituidos en -*meta*, sugiriendo así una mejor comunicación electrónica entre las unidades de truxeno para los polímeros **T2**. Curiosamente, la inserción de grupos fenilo (**Ph**) entre las unidades con simetría C_3 apenas afecta la distribución de carga electrónica ni las distancias de enlace en comparación con las de los polímeros unidos directamente, lo que sugiere que la inserción de grupos fenilo afecta mínimamente la deslocalización de los electrones π entre las unidades de truxeno. Este no es el caso de los grupos benzotiadiazol (**BTD**), los cuales producen una estructura molecular fuertemente polarizada en la que la densidad de carga electrónica en las proximidades de los espaciadores π-conjugados aumenta notablemente como consecuencia del carácter dador-aceptor de los polímeros conectados a través de grupos **BTD**. Es importante resaltar que nuestros cálculos basados en modelos diméricos dan información muy precisa sobre las estructuras moleculares de los polímeros conjugados bidimensionales.

Del mismo modo, la distinta posición de unión entre las unidades de truxeno tiene un fuerte impacto en las propiedades ópticas y fotofísicas de estos polímeros porosos. De

hecho, los espectros de absorción y emisión de los polímeros conectados en posición -*para* están significativamente desplazados hacia el rojo en comparación con los de los análogos conectados en -*meta*. Este efecto puede ser explicado en términos de una disminución significativa en el valor del HOMO-LUMO gap al pasar de uniones **T3** a uniones **T2**.

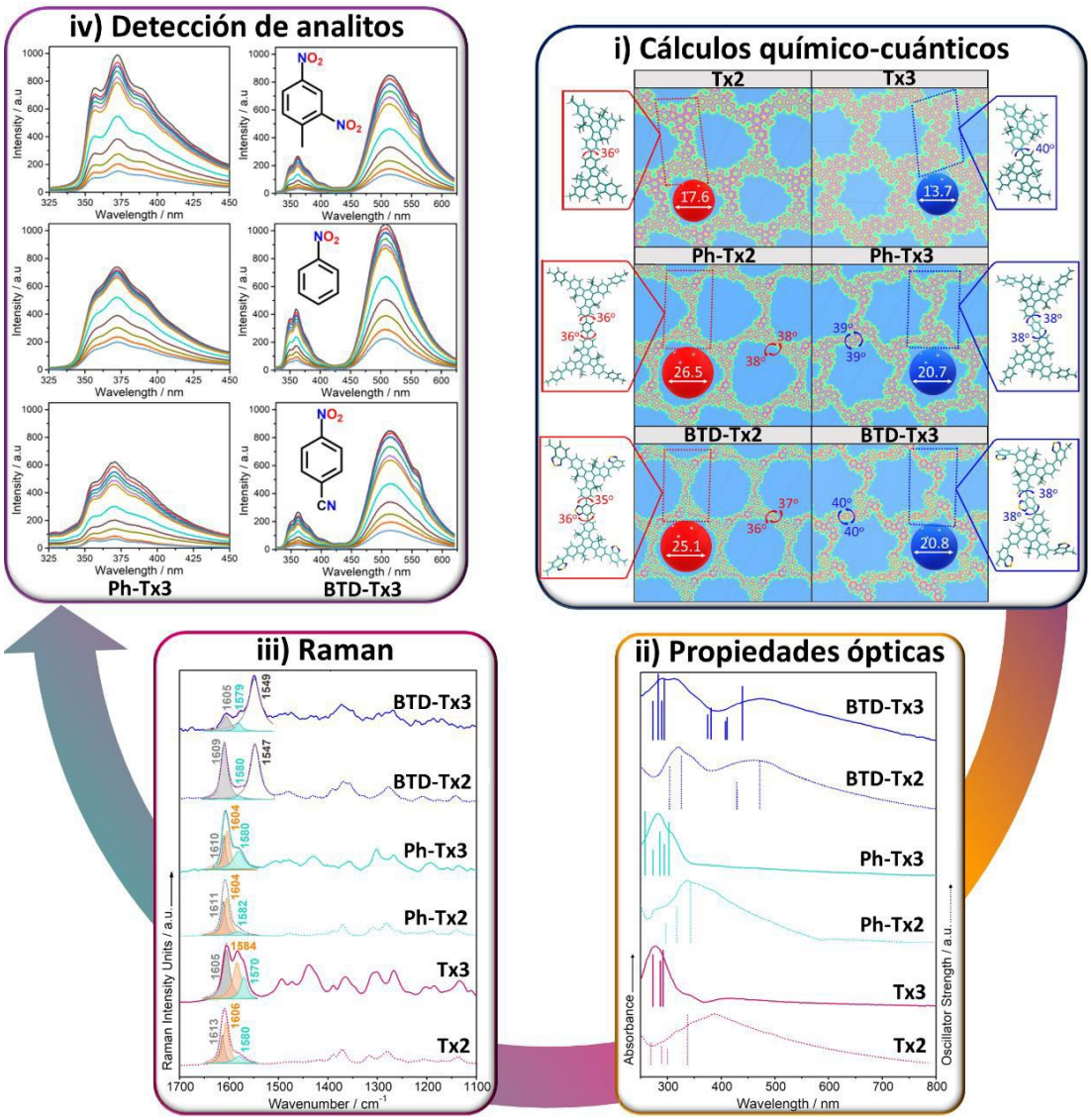

Figura 5.7. Resumen del estudio experimental y teórico llevado a cabo para los polímeros porosos basados en la unidad de truxeno.

Aún más importante es el impacto producido por la introducción de espaciadores **BTD** entre las unidades de truxeno, los cuales producen que el tránsito $S_0 \rightarrow S_1$, asociado en este caso a una excitación con fuerte carácter de transferencia de carga intramolecular, esté notablemente desplazado hacia el rojo con respecto a los sistemas unidos directamente o a través de grupos fenilo. Este resultado refleja una notable reducción del HOMO-LUMO gap para los polímeros **BTD-Tx2** y **BTD-Tx3** debido a la fuerte estabilización de su nivel LUMO. Por el contrario, la inserción de espaciadores fenilo entre las unidades de truxeno tiene una influencia débil en las propiedades optoelectrónicas de estos polímeros, lo que da como resultado, máximos de absorción y emisión muy similares en comparación a los observados para los polímeros conectados directamente. Este hecho corrobora que la inserción de grupos fenilo apenas afecta la deslocalización de los electrones π entre las unidades de truxeno.

La mejor comunicación electrónica de los polímeros cuyas unidades de truxeno están unidas covalentemente en posición *-para* o mediante espaciadores **BTD** queda de nuevo evidenciada mediante el análisis de los espectros Raman de estos polímeros. En este sentido, el aumento de las bandas Raman localizadas entre 1500-1600 cm^{-1} (asociadas a vibraciones C=C/C-C del esqueleto π-conjugado) con respecto al resto de bandas registradas por debajo de 1500 cm^{-1} adscritas a vibraciones de flexión de los grupos CH_2 no conjugados, así como la mayor relación de intensidades I_{1610}/I_{1580} observadas en los polímeros **T2** con respecto a sus homólogos **T3**, reafirman la mayor efectividad en la conjugación electrónica para los primeros. Por otro lado, el mayor (similar) valor I_{1610}/I_{1580} obtenido para los polímeros basados en **BTD** (**Ph**) con respecto a los polímeros en los cuales las unidades de truxeno están directamente unidas corroboran la notable (imperceptible) mejora en la deslocalización de electrones π entre las unidades de truxeno.

Interesantemente, la habilidad de estos polímeros para la detección de analitos nitroaromáticos (como dinitrotolueno, *p*-nitrobenceno o *p*-nitrobenzonitrilo) está enormemente influenciada por la distinta posición de unión entre las unidades de truxeno. En este sentido, las variaciones en los espectros de emisión del polímero **Ph-Tx3-CMP**

suspendido en CH_2Cl_2 (c=50 µg/ml) en presencia de cantidades crecientes (0−350 µM) de los diferentes analitos fueron mucho mayores que las del polímero **Ph-Tx2-CMP**. Valores en las constantes de Stern-Volmer para **Ph-Tx3-CMP** de 7.8×10^3, 3.6×10^3 y 10.4×10^3 M^{-1} fueron determinadas para dinitrotolueno, *p*-nitrobenceno y *p*-nitrobenzonitrilo, respectivamente.

En segundo lugar, teniendo en cuenta las interesantes propiedades de los polímeros microporosos previamente estudiados, realizamos una investigación puramente teórica de un total de 27 polímeros porosos diferentes con el objetivo de explorar la capacidad de modulación de sus propiedades estructurales, electrónicas y de transporte de carga mediante tres tipos de modificaciones estructurales: (i) la naturaleza de las plataformas con simetría C_3 (truxeno en **Tx**, triindol en **Tr** y truxenona en **To**), (ii) la inserción de diferentes espaciadores π-conjugados (fenilo en **Ph-** y alquino en **A-**) o (iii) la distinta posición de unión (*para* en **T2**, *meta* en **T3** o combinando ambas en **T2,3**). Como podemos observar en la Figura 5.8, el tamaño de poro de estos polímeros bidimensionales se puede modular mediante la correcta selección de tales factores estructurales. En este sentido, la inserción de espaciadores π-conjugados como fenilo (alquino) entre las plataformas con simetría C_3 producen un aumento en el tamaño de poro de 8 Å (4 Å) para los polímeros **T2** y **T3**, mostrando estos últimos un menor tamaño de poro (en torno a 5 Å) con respecto a sus homólogos conectados en posición -*para*. Curiosamente, los polímeros **T2,3** muestran microporos triangulares además de los microporos hexagonales vistos en **T2** y **T3**. Esta amplia gama de tamaños y geometrías de poro abre la aplicabilidad de estos polímeros en el campo de la adsorción/separación multiselectiva de analitos.

Tal y como muestran los mapas de densidad electrónica sobre el plano que contiene la lámina polimérica, mientras que los sistemas basados en **Tx** y **To** muestran una estructura molecular plana definida por una distribución de densidad electrónica bastante homogénea, sus homólogos **Tr** tienen una configuración moderadamente distorsionada (tal y como comentamos en el Capítulo I) y por lo tanto una distribución de carga electrónica ligeramente heterogénea. Es importante destacar que este efecto se suaviza cuando el

número de uniones covalentes aumenta de tres a seis unidades en **T2,3**, lo que sugiere una mayor deslocalización electrónica de los electrones π a lo largo de la estructura polimérica.

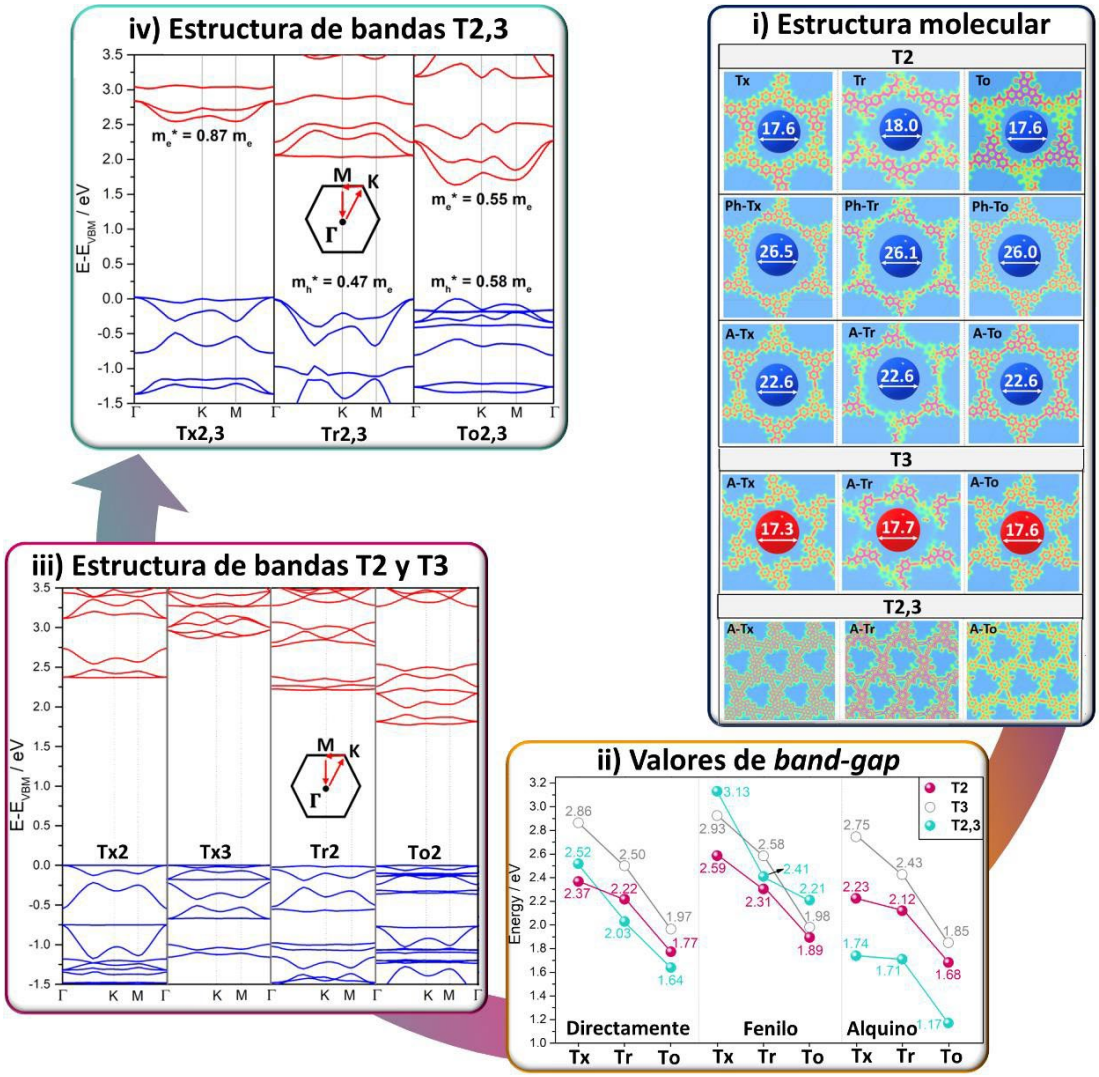

Figura 5.8. Resumen del estudio teórico llevado a cabo para polímeros porosos basados en plataformas π-conjugadas con simetría C_3.

Esta hipótesis fue corroborada gracias al estudio de las estructuras de bandas electrónicas de los polímeros bidimensionales bajo estudio. En este contexto, se observó una disminución significativa en el valor de *band-gap* para los polímeros **T2,3** con respecto

a sus análogos **T2** y **T3**, especialmente para aquellos en los que las unidades con simetría C_3 están conectados a través de grupos alquino. Del mismo modo, se prevé una disminución del *band-gap* a medida que la naturaleza de la plataforma π-conjugada va de **Tx-** a **Tr**- y **To**, con valores de 2.37, 2.22 y 1.77 eV para los polímeros **Tx2**, **Tr2** y **To2**, respectivamente. En vista de las dos observaciones anteriores, podemos decir que el valor más bajo de *band-gap* (1.17 eV) ha sido observado para **A-To2,3**.

Por otro lado, en línea con las conclusiones obtenidas para los sistemas estudiados experimentalmente durante la primera parte de este capítulo, se ha observado un aumento notable del *band-gap* al cambiar la posición de conexión de las plataformas C_3 de -*para* a -*meta*, lo que sugiere una conjugación π-electrónica más efectiva en los polímeros **T2** con respecto a sus isómeros **T3**. Además, la inserción de grupos espaciadores fenilo no altera de forma significativa el *band-gap* en los polímeros trisustituidos **T2** y **T3**, aunque si produce mayores valores de *band-gap* en los polímeros hexasustituidos **T2,3** como consecuencia de una mayor distorsión estructural que posibilita la creación de cavidades cíclicas tridimensionales entre las tres unidades de fenilo que conectan las plataformas C_3.

Curiosamente, la estructura de bandas de los polímeros trisustituidos **T2** y **T3** muestran un carácter prácticamente plano en la banda de conducción inferior (BC), así como en la banda de valencia superior (BV). Dado que este comportamiento se mantiene tras la inserción de puentes π-conjugados o cambiando la posición de enlace entre los mismos, es evidente pensar que el origen de la planaridad de estas bandas sea una consecuencia directa de la simetría “kagome” presente en las distintas redes poliméricas. Es importante destacar que cuando el interés radica en el diseño de polímeros conjugados bidimensionales con alta movilidad de portadores de carga, es esencial buscar redes que favorezcan la dispersión de las bandas situadas alrededor del nivel de energía de Fermi. En este contexto, hemos demostrado que el aumento del número de puentes π-conjugados entre las plataformas conjugadas con simetría C_3 en los polímeros **T2,3** da lugar a redes poliméricas con simetría triangular caracterizadas por estructuras electrónicas definidas por bandas notablemente dispersas. De hecho, altos valores de dispersión para la BC (BV) junto con pequeñas masas

efectivas para electrones (huecos) fueron observados para los polímeros **Tx2,3** y **A-To2,3** (**Tr2,3** y **A-Tr2,3**), lo que los hace posibles candidatos para su uso como materiales bidimensionales transportadores de electrones y huecos, respectivamente. Además, altos valores de dispersión tanto para BC como para BV (y por lo tanto pequeños valores de masa efectiva para electrones y huecos) fueron observados para **To2,3** y **A-Tx2,3**, lo que los convierte en prometedores transportadores de carga ambipolares.

Curiosamente, los polímeros que contienen fenilo como espaciador π-conjugado conservan la planaridad de las bandas situadas alrededor del nivel de energía de Fermi, lo cual puede estar adscrito a la mayor distorsión estructural de estos sistemas que actúa en detrimento del acoplamiento electrónico entre las plataformas con simetría C_3. Este hecho contrasta con los altos valores de movilidad obtenidos experimentalmente para el polímero **Ph-Tr2**,[21] donde los valores de movilidad probablemente se atribuyan a un acoplamiento electrónico favorable entre láminas adyacentes y por lo tanto, a un aumento de la dispersión a lo largo de la dirección vertical. Esta hipótesis fue reforzada mediante el análisis del apilamiento interlaminar preferencial de polímeros basados en triindol, en donde se predijeron altos valores de energía de cohesión para una configuración AB (en la que las unidades de triindol están rotadas 60º con respecto a sus vecinas dentro de la columna) para la cual han sido publicados acoplamientos electrónicos eficientes.[22, 23]

5.4.3. Capítulo III: Efectos producidos por la extensión del esqueleto π-conjugado en las propiedades eléctricas de semiconductores basados en NDI y PDI.

En este capítulo se ha investigado el papel que juega la elongación del esqueleto π-conjugado, así como la distinta sustitución lateral del mismo en las propiedades optoelectrónicas de una serie de cuatro semiconductores basados en **NDI** y **PDI**. Tal y como muestra la Figura 5.9, en la que se resume parte del estudio tanto experimental como teórico realizado sobre estos sistemas, ambos factores estructurales repercuten notablemente en las propiedades finales del material. De hecho, cálculos químico-cuánticos realizados a nivel DFT (B3LYP/6-31G**) predicen un esqueleto π-conjugado totalmente

plano para los derivados de **NDI**, mientras que la extensión del mismo en semiconductores basados en **PDI** resulta en la distorsión de las dos mitades de naftaleno de la unidad central. Por otro lado, los grupos lateralmente insertados en las posiciones bahía están distorsionados en gran medida con respecto a la unidad central, independientemente de la naturaleza de esta.

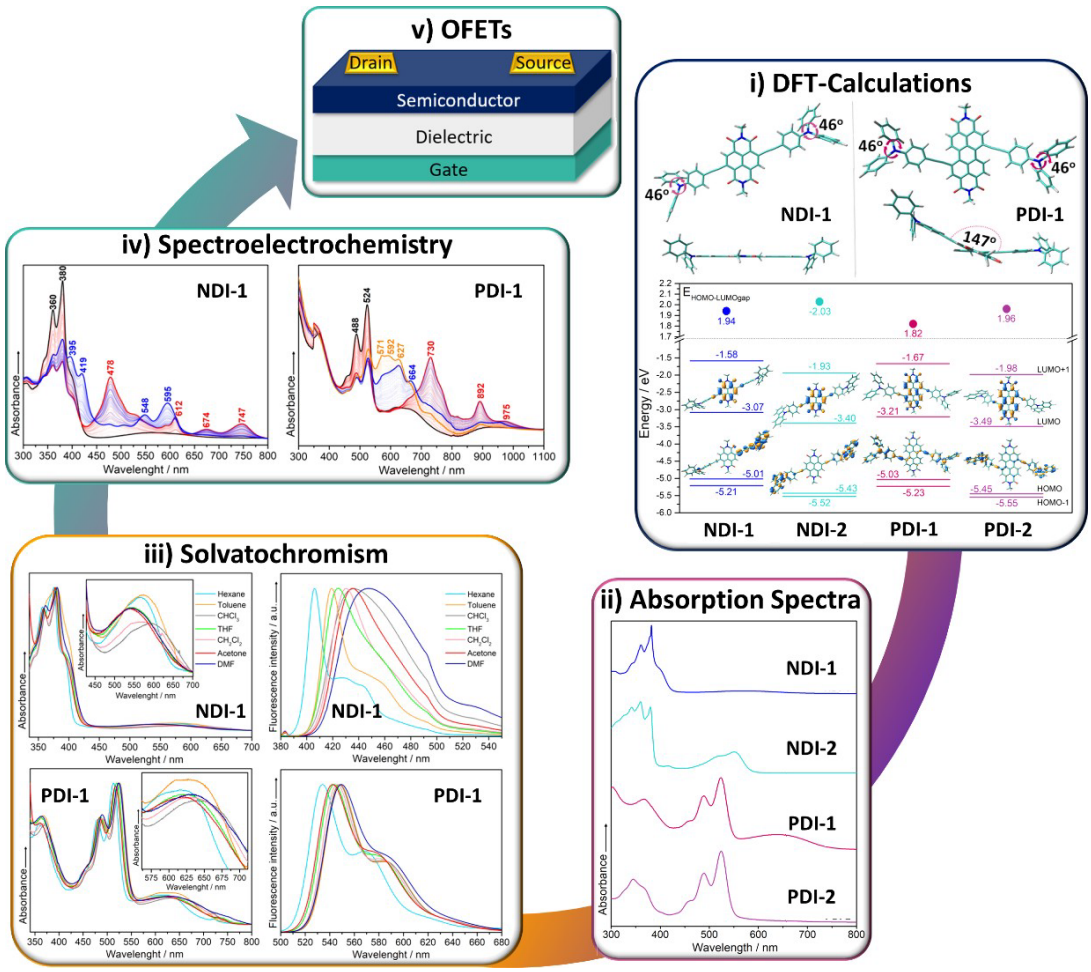

Figura 5.9. Resumen del estudio llevado a cabo para los sistemas basados en **NDI** y **PDI**.

Sin embargo, la naturaleza de los grupos laterales repercute enormemente en las propiedades electrónicas del material. Tal y como muestran los espectros de absorción medidos en CH_2Cl_2 ($c=10^{-5}$ M), exclusivamente los derivados sustituidos con la unidad de triarilamina **NDI-1** y **PDI-1** muestran una banda ancha y desestructurada en la zona de baja

energía típica de procesos de transferencia de carga intramolecular (ICT). Curiosamente, mientras que las propiedades fotofísicas de los derivados **NDI-2** y **PDI-2** se mostraron indiferentes a cambios en la polaridad del disolvente, un moderado comportamiento solvatocrómico fue observado en los espectros de absorción y emisión de los derivados **NDI-1** y **PDI-1**, confirmando así el carácter ICT de esta banda de absorción para los compuestos sustituidos con trifenilamina. En este sentido, el análisis de dicha banda ICT revela que la extensión de la π-conjugación en la unidad de arileno afecta enormemente las propiedades electrónicas de estos materiales. De hecho, un desplazamiento batocrómico de 68 nm puede ser observado al pasar de **NDI-1** a **PDI-1**, en línea con el menor HOMO-LUMO gap calculado teóricamente, ocurriendo lo mismo al pasar de **NDI-2** a **PDI-2**. Este efecto se explica en términos de la estabilización del LUMO para los sistemas **PDI** con respecto a sus homólogos basados en **NDI**, como consecuencia de la elongación de la unidad central electrón-deficiente.

Como último paso previo a la implementación de estos semiconductores en OFETs, se analizó la capacidad de los mismos para albergar carga, lo cual supone un aspecto clave en la inyección y estabilización de carga en el dispositivo. Para ello, se llevó a cabo la progresiva reducción espectroelectroquímica de todos los semiconductores usando CH_2Cl_2/0,1 M $(n\text{-}Bu)_4NPF_6$ como electrolito ($c=1 \times 10^{-5}$ M), gracias a lo cual se observó que mientras los derivados **NDI** albergan hasta dos cargas negativas en el fragmento de naftalenodiimida, la extensión del esqueleto central en los derivados **PDI** permite acomodar una tercera carga en la plataforma central. Interesantemente, perfiles espectrales prácticamente superpuestos fueron obtenidos independientemente del grupo lateral unido a la plataforma central, evidenciando que la inyección y estabilización de carga se produce mayormente sobre las plataformas **NDI** y **PDI**. No obstante, cálculos DFT sobre especies cargadas sugieren que mientras la plataforma de **NDI** acomoda alrededor del 80% de cada carga inyectada, su homóloga extendida **PDI** acomoda un porcentaje de carga ligeramente inferior (entorno al 65%). Esto, junto al hecho de que el grupo acetileno albergue una mayor densidad de carga negativa en derivados de **PDI**, sugiere una mayor comunicación electrónica entre la

plataforma central y los grupos laterales en estos sistemas con respecto a los compuestos basados en **NDI**, probablemente debido a la mayor distorsión del esqueleto π-conjugado basado en **PDI**.

Finalmente, dado los bajos valores de energía del LUMO (alrededor de -3 eV), efectiva π-conjugación y alta capacidad de estos materiales para acomodar electrones en su estructura molecular, los cuatro semiconductores bajo estudio fueron implementados en OFETS siguiendo una configuración de contacto-superior y puerta-inferior (bottom-gate top-contact, BG-TC). Como se puede ver en la Figura 5.10, todos ellos exhiben comportamientos unipolares de tipo-n en condiciones de vacío. Sin embargo, las movilidades electrónicas (μ_e) medidas para los semiconductores basados en **PDI** son sustancialmente inferiores a las de sus análogos **NDI** ($1.5x10^{-3}$ y $3.2x10^{-1}$ $cm^2V^{-1}s^{-1}$ para **PDI-1** y **NDI- 1**, respectivamente). Esto puede deberse a la distorsión estructural de la plataforma de perilenodiimida causando un solapamiento ineficiente entre orbitales LUMO de moléculas adyacentes y consecuentemente, un acoplamiento electrónico más bajo. Por otro lado, cabe destacar que sistemas sustituidos lateralmente con grupos trifenilamino (**NDI-1** y **PDI-1**) exhiben movilidades en torno a 3 veces mayores que los sustituidos con grupos fenil-carbazol (**NDI-2** y **PDI-2**).

En vista de estos resultados, el efecto que tanto la planaridad del esqueleto π-conjugado como el carácter electro-dador de los sustituyentes laterales ejercen sobre el rendimiento del dispositivo son puntos relevantes que han de ser abordados. Para ello, las microestructuras de las láminas semiconductoras se caracterizaron mediante GIXRD y AFM, evidenciando que aunque todos los semiconductores muestran una cristalinidad moderada, los semiconductores sustituidos con grupos trifenilamina **NDI-1** y **PDI-1** muestran picos de difracción ligeramente más estrechos de acuerdo con un empaquetamiento en estado sólido más ordenado. Además, dicho ordenamiento se ha relacionado con una estructura cristalina lamelar con una interdigitación casi completa de las cadenas alquílicas. Curiosamente, también se observaron diferencias perceptibles en las imágenes de AFM, en donde se identificaron dominios cristalinos moderadamente más grandes en los dispositivos

basados en **NDI**, lo que contribuye significativamente al mayor rendimiento de los OFETs fabricados con estos sistemas con respecto a sus análogos basados en **PDI**, cuyos dispositivos muestran una textura más suave definida por granos pequeños.

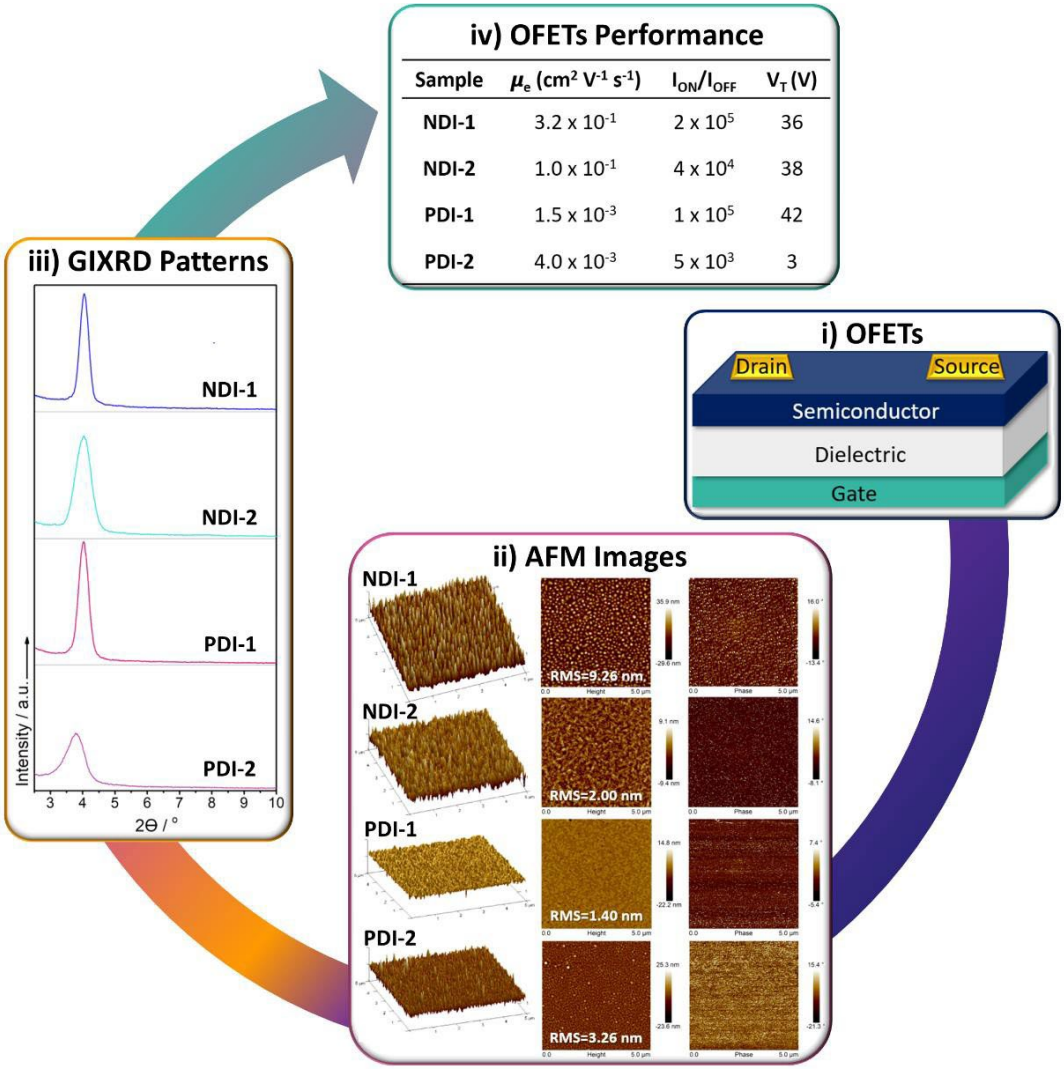

Figura 5.10. Resumen de los principales parámetros eléctricos obtenidos en OFETs fabricados con los semiconductores bajo estudio, así como la caracterización de la lámina semiconductora.

Teniendo en consideración todos estos efectos, parece razonable concluir que las muestras de **NDI-1** y **NDI-2** exhiben una agregación y nucleación más efectiva en comparación con sus análogos basados en **PDI**.

5.4.4. Capítulo IV: Importancia de la planaridad del esqueleto π-conjugado en la obtención de transistores de efecto campo eficientes.

Por último, en este capítulo se ha estudiado una serie de copolímeros A-D-A´ basados en las unidades de IIG y BTD conectadas a través de un anillo de tiofeno, con distinto grado de fluoración. En vista de la Figura 5.11, tanto la posición como el grado de fluoración afectan en gran medida a las propiedades intramoleculares del sistema, lo cual determina a su vez las interacciones intermoleculares, ordenamiento en estado sólido y propiedades de transporte de carga.

En este sentido, cálculos químico-cuánticos a nivel DFT (B3LYP/6-31G**) realizados para modelos diméricos de los polímeros **P1**-**P4** predicen que la planaridad de la estructura polimérica de estos sistemas está directamente relacionada con la cantidad de átomos de flúor incorporados a la misma, debido a la presencia de interacciones intramoleculares entre el par de electrones solitario de los átomos de flúor y los orbitales antienlazantes de los átomos de azufre de los tiofenos adyacentes. Como resultado, cuanto mayor es el grado de fluoración, la estructura polimérica es más plana (**P4** > **P3** > **P2** > **P1**). En este punto es importante resaltar que a pesar de que el mismo número de átomos de flúor son introducidos en los polímeros **P3** y **P2**, la fluoración selectiva de la unidad IIG en **P3** induce una mayor planarización del esqueleto conjugado con respecto a la fluoración de la unidad BTD en **P2**.

A su vez, la inserción de flúor modula la energía de los niveles electrónicos HOMO/LUMO, y por tanto el valor de HOMO-LUMO gap de los polímeros. Así, los espectros de absorción UV-Vis-NIR de estos sistemas fueron medidos en disoluciones de clorobenceno ($c=10^{-4}$ M). De forma contraria a lo esperado, dado el significativo carácter electro-atrayente del átomo de flúor, la introducción de dichos átomos en la unidad aceptora BTD en **P2** produce un desplazamiento (19 nm) hacia menor longitud de onda en su máximo de absorción con respecto a su homólogo sin sustituir, **P1**. Este efecto fue explicado en términos de una mayor estabilización del nivel energético HOMO (0.09 eV) con respecto al

LUMO (0.03 eV) tras la fluoración, dando lugar a un aumento del HOMO-LUMO$_{gap}$ con respecto al polímero de partida, **P1**.

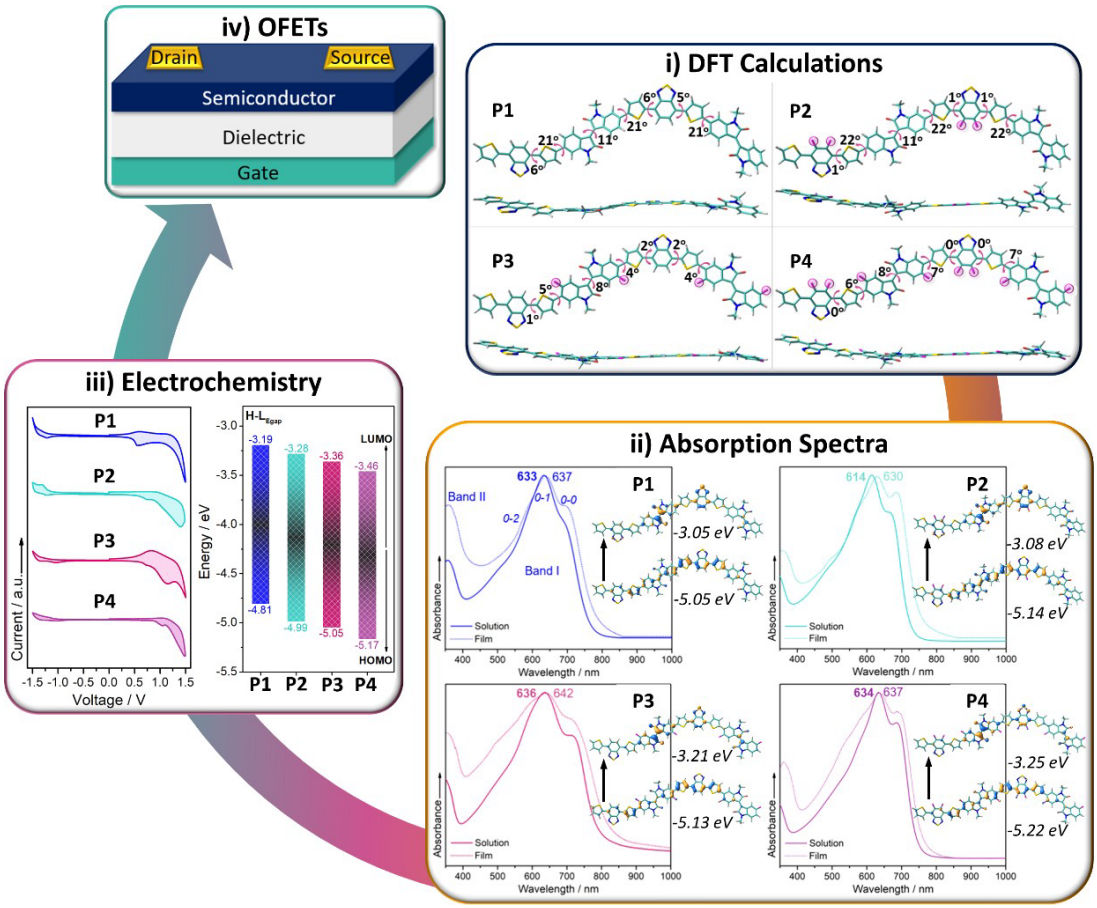

Figura 5.11. Esquema de la caracterización llevada a cabo para los polímeros **P1-P4**, antes de su implementación en dispositivos electrónicos.

Nótese que las topologías tanto de HOMO como de LUMO presentan contribuciones significativas en las unidades IIG y BTD, lo que explica la estabilización de ambos orbitales tras la fluoración. Por otro lado, la introducción de átomos de flúor en la unidad IIG, en **P3,** causa un ligero desplazamiento batocrómico (3 nm) en su máximo de absorción con respecto al del polímero sin sustituir **P1**, debido a una disminución del HOMO-LUMO$_{gap}$ como consecuencia de una mayor estabilización del LUMO (0.16 eV) que del HOMO (0.08 eV). Curiosamente, estos dos efectos independientes causados por la difluoración en

diferentes posiciones del esqueleto polimérico son cooperativos en **P4**, tal y como muestra el nulo desplazamiento espectral observado con respecto al material de partida **P1**.

Se registraron a su vez los espectros de absorción de láminas delgadas, lo que nos permitió entender que la planaridad del esqueleto π-conjugado de estos polímeros mejora en estado sólido como consecuencia de interacciones efectivas entre cadenas cercanas. Además, el aumento gradual del número de átomos de flúor promueve la planarización del sistema polimérico de acuerdo con los resultados calculados teóricamente, siendo este aspecto especialmente destacable para los polímeros en los que la unidad IIG está fluorada (**P3** y **P4**).

Por otra parte, medidas de voltametría cíclica mostraron picos de oxidación bien definidos y reversibles para todos los polímeros, así como niveles de HOMO inferiores a -4.80 eV. Esto, junto con los bajos niveles de LUMO (menores a -3.30 eV) y picos de reducción casi reversibles observados para los polímeros fluorados, los hacen buenos candidatos a semiconductores ambipolares. Tomando como base estos resultados, dichos materiales fueron implementados en OFETs con configuración de contacto-superior, puerta-inferior (bottom-gate top-contact, BG-TC). Como se puede ver en la Figura 5.12, una baja movilidad de huecos ($\sim$1x10^{-5} cm^{2}V^{-1}s^{-1}) fue obtenida para el polímero de partida **P1**. Esto puede relacionarse con la distorsión estructural observada en su esqueleto π-conjugado, lo cual puede dificultar el solapamiento entre orbitales y, por lo tanto, un acoplamiento electrónico bajo. No obstante, la sucesiva fluoración del esqueleto π-conjugado mejora tanto la planaridad como la afinidad electrónica de estos sistemas, disminuyendo progresivamente la barrera de inyección electrónica. Consecuentemente, las propiedades eléctricas de estos polímeros cambian desde un bajo transporte de huecos a otro efectivo de carácter ambipolar al pasar de **P1** a **P4**, siendo el polímero **P3** el que muestra un mayor y mejor equilibrado transporte de carga ambipolar, con movilidades de huecos y electrones de 0.15 y 0.11 cm^{2}V^{-1}s^{-1}, respectivamente.

Cabe destacar que estas movilidades son alrededor de 2 (1) órdenes de magnitud mayores que las del polímero **P2** (**P4**). Este hecho puede parecer inconsistente dada la mayor

planaridad y estabilización de los niveles energéticos observada para el polímero **P4** con respecto a **P3**, lo que sugiere que otros factores como la morfología en estado sólido puede influir en las propiedades de transporte de carga.

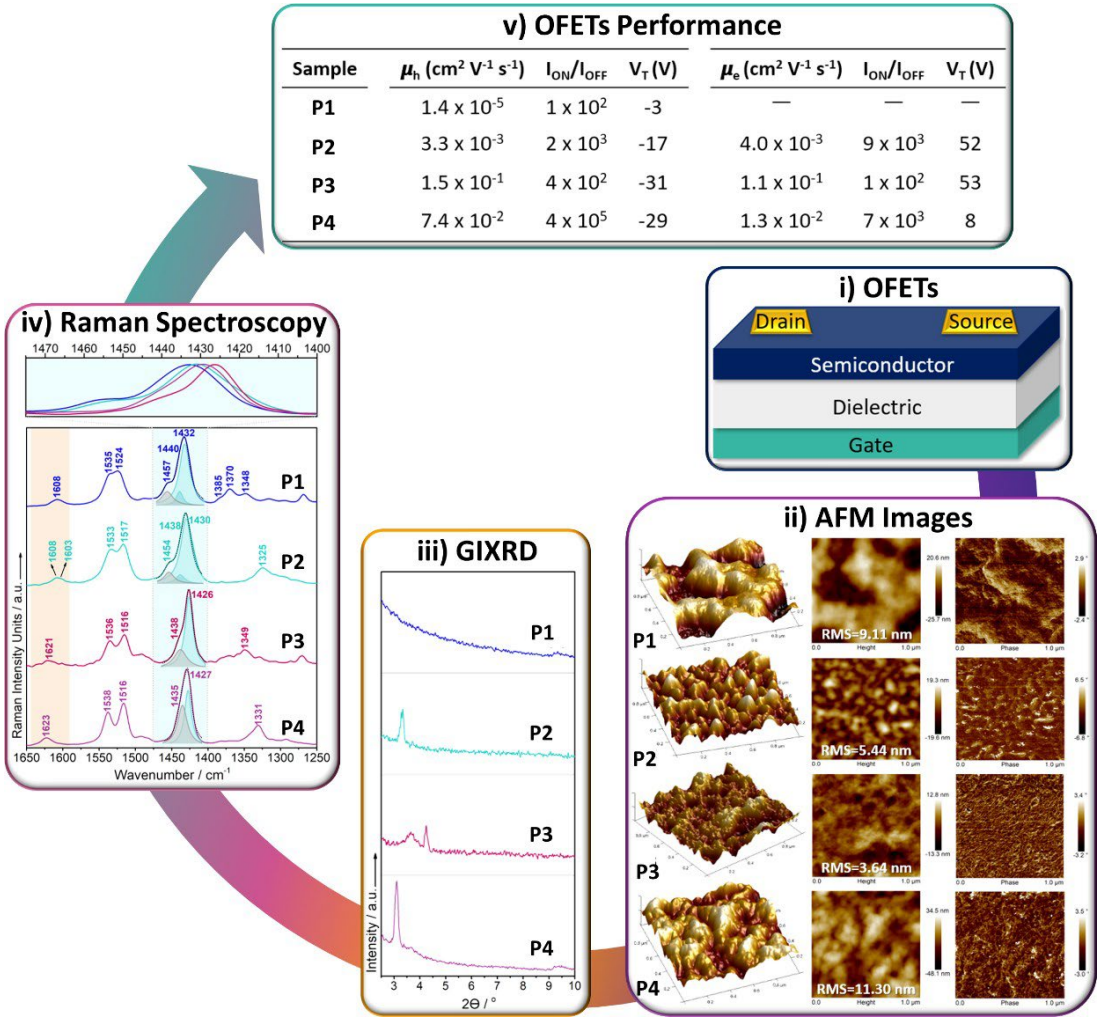

Figura 5.12. Resumen de los principales parámetros eléctricos obtenidos en los OFETs fabricados con los polímeros bajo estudio, así como la caracterización de la lámina semiconductora.

La caracterización de las películas delgadas mediante AFM y GIXRD reveló que la fluoración afecta notablemente las interacciones entre cadenas poliméricas. En este contexto, la cristalinidad está directamente relacionada con el porcentaje de fluoración del esqueleto, lo que se atribuye al incremento de barreras torsionales entre las subunidades,

limitando así la rotación y reforzando la planaridad del esqueleto conjugado. Sin embargo, una pobre uniformidad así como una interconexión ineficiente de los dominios cristalinos fue observada para las láminas de **P4**, pudiendo ser esta la razón de las menores movilidades medidas para este polímero en comparación con **P3**.

Dado que mediante GIXRD solo pueden analizarse dominios cristalinos, la espectroscopia Raman fue utilizada para explorar tanto fases ordenadas como fases desordenadas puesto que ambas son cruciales en el rendimiento final del dispositivo. De acuerdo con esto, la espectroscopía Raman demostró la presencia de fases tanto desordenadas como ordenadas en los polímeros **P1** y **P2**. Por otro lado, la introducción de átomos de flúor en la unidad IIG resultó en la presencia de una única fase ordenada como consecuencia de una efectiva planarización del esqueleto polimérico en **P3** y **P4**. Por lo tanto, la espectroscopía Raman confirma que la fluoración selectiva de la fracción BTD no es suficiente para aumentar significativamente el orden supramolecular dentro del material, siendo necesaria la fluoración en la unidad IIG para lograr una planaridad del esqueleto efectiva.

5.5. Conclusiones generales

Finalmente, en esta sección se intenta proporcionar una visión general de la relación estructura-propiedad analizada para cada uno de los sistemas que componen esta memoria, así como su impacto final en el rendimiento de los dispositivos sobre los que han sido implementados.

En base a los resultados obtenidos durante el estudio de las propiedades de autoensamblaje de sistemas con forma de disco basados en la plataforma de triindol y diazatruxenona (Capítulo I), se pueden extraer las siguientes conclusiones:

Se ha demostrado con la ayuda de cálculos DFT que la funcionalización periférica de las plataformas basadas en triindol y diazatruxenona ejerce un impacto poco significativo sobre su estructura molecular. Del mismo modo, medidas de absorción UV-Vis y Raman

junto con medidas electroquímicas predicen una leve mejora en la deslocalización electrónica de las plataformas π-conjugadas tras la funcionalización, siendo este efecto más relevante para los sistemas sustituidos con grupos aceptores de electrones. Sin embargo, la distinta naturaleza de los grupos periféricos influye enormemente sobre las propiedades de autoensamblaje de estos sistemas, mostrando ser de crucial importancia a la hora de evaluar su aplicabilidad en dispositivos electrónicos como OFETs. De hecho, movilidades tipo p de 2×10^{-2}, 1×10^{-3} y 3×10^{-5} $cm^2V^{-1}s^{-1}$ fueron medidas para los triindoles sin sustituir, sustituido con grupos metoxilo dadores de electrones o con grupos acetilo aceptores de electrones, respectivamente. Esta tendencia sigue el sentido inverso con respecto a la eficiencia de la π-conjugación intramolecular previamente observada a lo largo de la serie, lo cual ha sido atribuido a un pobre solapamiento entre las funciones de onda HOMO y HOMO-1 de los triindoles funcionalizados como consecuencia de la extensión de las mismas sobre las ramas periféricas sin solapamiento π-π. Por otro lado, debido a la anisotropía intrínseca de los semiconductores basados en diazatruxenona, movilidades de huecos de 3×10^{-5} $cm^2V^{-1}s^{-1}$ pudieron ser medidas únicamente para el sistema sustituido con grupos nitro mediante la técnica SCLC (del inglés, "Space Charge Limited).

Curiosamente, la inserción de un grupo cetónico en la plataforma de diazatruxenona produce un doble efecto. Por un lado, mejora la planaridad y la deslocalización electrónica del esqueleto π-conjugado con respecto a su análogo basado en triindol. Por otro lado, el carácter intrínseco dador-aceptor de las moléculas basadas en diazatruxenona no sólo las convierte en materiales ambipolares, sino que también les confiere un importante momento dipolar que puede ser modulado en función de la naturaleza de los sustituyentes periféricos. De hecho, los derivados sustituidos con grupos aceptores de electrones, con valores de momento dipolar doble con respecto al del resto de sistemas que componen la serie, forman mesofases estables gracias a interacciones dipolo-dipolo fuertes.

Considerando los resultados obtenidos en el Capítulo II, con respecto al efecto que produce tanto la inserción de distintos puentes π-conjugados como la posición de enlace de

los mismos en las propiedades optoelectrónicas de polímeros microporosos, se pueden establecer las siguientes conclusiones:

Tanto los resultados obtenidos experimentalmente (absorción UV-Vis, emisión y Raman) como resultados computacionales apuntan al hecho de que la unión covalente de las unidades de truxeno a través de las posiciones 2, 7, 12 produce una mayor extensión de la conjugación electrónica con respecto a los isómeros conectados en posiciones 3,8, 13. El mismo enfoque experimental-teórico ha demostrado que la inserción de grupos fenilo entre las unidades con simetría C_3 apenas afecta las propiedades optoelectrónicas de estos polímeros, mientras que la inserción de grupos BTD implica un aumento significativo en la deslocalización π-electrónica como consecuencia de la inherente naturaleza dador-aceptor de estos sistemas. Curiosamente, ambas modificaciones estructurales han demostrado ser especialmente útiles para el diseño de polímeros orgánicos porosos con capacidad de detección de compuestos nitroaromáticos. En este sentido, se ha demostrado que la eficiencia de detección puede ser notablemente mejorada al conectar las unidades de truxeno a través de espaciadores π-conjugados (fenilo o BTD) en las posiciones 3,8,13.

Además, en base al estudio puramente teórico llevado a cabo para un total de 27 polímeros bidimensionales diferentes basados en plataformas con simétria C_3, podemos afirmar que existe un amplio abanico de modulación en las propiedades estructurales (geometría y tamaño de poro) y electrónicas (band gap y dispersión de bandas) en estos polímeros gracias a la adecuada selección de la plataforma π-conjugada (truxeno, triindol o truxenona), la naturaleza (fenilo o alquino) y posición de los espaciadores π-conjugados (-*meta*, -*para* o la combinación de ambos). De hecho, una disminución significativa del valor de *band-gap* ha sido observada al pasar de polímeros basados en truxeno a triindol y truxenona, cambiando la posición de enlace de -*meta* a -*para*, aumentando el número de uniones de 3 a 6 unidades en **T2,3** o mediante la inserción de grupos espaciadores alquino, sugiriendo así una conjugación más efectiva para **A-To2,3**. Además, las conectividades entre las plataformas con simetría C_3 son determinantes de la estructura de bandas del polímero

final. En este sentido, mientras que la inherente simetría Kagome propia de polímeros trisustituidos **T2** y **T3** con simetría C_3 conduce a la presencia de bandas electrónicas planas indeseables de cara a un efectivo transporte de carga intralaminar, el aumento de las uniones covalentes entre las unidades con simetría C_3 en T2,3 resulta en bandas dispersas con bajas masas efectivas. Interesantemente, también se espera que el apilamiento entre láminas afecte positivamente a los acoplamientos electrónicos de las unidades C_3, tal y como se ha visto para **Ph-Tr2**.

A la vista de los resultados obtenidos en el estudio químico-físico del Capítulo III para los sistemas basados en **NDI** y **PDI**, algunas pautas importantes sobre la relación estructura-propiedad han sido determinadas. De esta manera, se pueden establecer las siguientes conclusiones:

De acuerdo a medidas de absorción UV-Vis y cálculos químico-cuánticos, mientras que la sustitución lateral de estos sistemas con grupos ricos en electrones tiene un impacto insignificante en la estructura molecular, sus propiedades fotofísicas se ven enormemente afectadas. En efecto, solo los derivados sustituidos con grupos de triarilamina **NDI-1** y **PDI-1** muestran transferencia de carga intramolecular en sus espectros de absorción, resultando además en un menor valor de HOMO-LUMO gap. Aparentemente, la extensión del fragmento central en los derivados de **PDI** produce dos efectos contrarios: por un lado, se observa un aumento en la conjugación electrónica así como una mayor facilidad para acomodar cargas negativas en su estructura molecular, mientras que al mismo tiempo se rompe notablemente la planaridad del esqueleto π-conjugado con respecto al de los sistemas basados en **NDI**. Como resultado, el rendimiento eléctrico de OFETs preparados con estos semiconductores depende en gran medida de la naturaleza de la unidad central, con movilidades de electrones para los sistemas basados en **PDI** en torno a dos órdenes de magnitud menores que las de sus análogos **NDI** (movilidades tipo n de 0.3 $cm^2V^{-1}s^{-1}$ fueron medidas para **NDI-1**). Este efecto fue adscrito a la estructura molecular significativamente distorsionada de los sistemas **PDI**, lo que dificulta el ordenamiento en estado sólido en línea con los mayores dominios cristalinos observados en los dispositivos basados en **NDI**.

Además, un mayor grado de cristalinidad en semiconductores sustituidos lateralmente con grupos trifenilamina en comparación con sus análogos sustituidos con grupos fenil-carbazol respalda las mayores movilidades electrónicas observadas en **NDI-1** y **PDI-1** con respecto a **NDI-2** y **PDI-2**.

Por último, los resultados del Capítulo IV nos han ayudado a comprender el efecto de la fluoración sobre las propiedades de transporte de carga de una familia de polímeros, cabiendo destacar las siguientes conclusiones:

Gracias al uso de medidas electroquímicas, absorción UV-Vis y cálculos químico-cuánticos hemos demostrado que la introducción de átomos de F en las unidades IIG y BTD no solo es una estrategia efectiva para modular los niveles de energía de los orbitales frontera, sino que también mejora la planaridad de las cadenas poliméricas como resultado de interacciones no covalentes S•••F. Esto se refleja en las propiedades eléctricas de estos sistemas, en donde la progresiva fluoración cambia las propiedades eléctricas de estos polímeros desde bajos valores de movilidades de huecos ($\sim$1x10^{-5} cm^{2}V^{-1}s^{-1}) para **P1** a un efectivo transporte de carga ambipolar (con movilidades de hasta 0.1 cm^{2}V^{-1}s^{-1} para **P3**) para **P2**-**P4**. Curiosamente, tanto la planaridad como las propiedades optoelectrónicas de estos polímeros dependen claramente de la sección molecular donde se introducen los átomos de flúor, siendo insuficiente la fluoración de la unidad BTD para mejorar de forma efectiva el orden interno de la cadena polimérica, tal y como indica la espectroscopía Raman.

A nivel supramolecular, medidas de GIXRD para láminas delgadas de estos polímeros mostraron que la cristalinidad está directamente relacionada con el porcentaje de fluoración del esqueleto polimérico. Sin embargo, medidas AFM mostraron una interconexión ineficiente de los dominios cristalinos para la lámina delgada fabricada con el polímero **P4**, lo cual puede ser la razón de las menores movilidades observadas para este material con respecto a **P3**.

5.6. Referencias

[1] Keyes, R. W., Physical limits of silicon transistors and circuits. *Reports on Progress in Physics* **2005,** 68, (12), 2701.

[2] Thompson, S. E.; Parthasarathy, S., Moore's law: the future of Si microelectronics. *Materials Today* **2006,** 9, (6), 20-25.

[3] Li, Y.; Sun, H.; Shi, Y.; Tsukagoshi, K., Patterning technology for solution-processed organic crystal field-effect transistors. *Science and Technology of Advanced Materials* **2014**.

[4] Jiang, C.; Chellappan, V.; Goh, W.; Zhang, J., Investigating coating method induced vertical phase distribution in polymer-fullerene organic solar cells. *Solar Energy Materials and Solar Cells* **2018,** 179, 241-246.

[5] Jiang, Z.-Q.; Poriel, C.; Leclerc, N., Emerging organic electronics. *Materials Chemistry Frontiers* **2020,** 4, (9), 2497-2498.

[6] Cornil, J.; Verlaak, S.; Martinelli, N.; Mityashin, A.; Olivier, Y.; Van Regemorter, T.; D'Avino, G.; Muccioli, L.; Zannoni, C.; Castet, F., Exploring the energy landscape of the charge transport levels in organic semiconductors at the molecular scale. *Accounts of Chemical Research* **2013,** 46, (2), 434-443.

[7] Kaiser, W.; Albes, T.; Gagliardi, A., Charge carrier mobility of disordered organic semiconductors with correlated energetic and spatial disorder. *Physical Chemistry Chemical Physics* **2018,** 20, (13), 8897-8908.

[8] Schön, J. H.; Kloc, C.; Batlogg, B., Universal crossover from band to hopping conduction in molecular organic semiconductors. *Physical Review Letters* **2001,** 86, (17), 3843.

[9] Haneef, H. F.; Zeidell, A. M.; Jurchescu, O. D., Charge carrier traps in organic semiconductors: A review on the underlying physics and impact on electronic devices. *Journal of Materials Chemistry C* **2020,** 8, (3), 759-787.

[10] Malagoli, M.; Brédas, J., Density functional theory study of the geometric structure and energetics of triphenylamine-based hole-transporting molecules. *Chemical Physics Letters* **2000,** 327, (1-2), 13-17.

[11] Brédas, J.-L.; Beljonne, D.; Coropceanu, V.; Cornil, J., Charge-Transfer and Energy-Transfer Processes in π-Conjugated Oligomers and Polymers: A Molecular Picture. *Chemical Reviews* **2004,** 104, (11), 4971-5004.

[12] Coropceanu, V.; Cornil, J.; da Silva Filho, D. A.; Olivier, Y.; Silbey, R.; Brédas, J.-L., Charge Transport in Organic Semiconductors. *Chemical Reviews* **2007,** 107, (4), 926-952.

[13] Liu, B.; Wang, Y.; Sun, H.; Gámez-Valenzuela, S.; Yan, Z.; Feng, K.; Uddin, M. A.; Koh, C.; Zhou, X.; López Navarrete, J. T.; Ruiz Delgado, M. C.; Meng, H.; Niu, L.; Woo, H. Y.; Ponce Ortiz, R.; Guo, X., Backbone Configuration and Electronic Property Tuning of Imide-Functionalized Ladder-Type Heteroarenes-Based Polymer Acceptors for Efficient All-Polymer Solar Cells. *Advanced Functional Materials* **2022,** 32, (21), 2200065.

[14] Sun, H.; Autschbach, J., Electronic Energy Gaps for π-Conjugated Oligomers and Polymers Calculated with Density Functional Theory. *Journal of Chemical Theory and Computation* **2014,** 10, (3), 1035-1047.

[15] Park, S. K.; Jackson, T. N.; Anthony, J. E.; Mourey, D. A., High mobility solution processed 6, 13-bis (triisopropyl-silylethynyl) pentacene organic thin film transistors. *Applied Physics Letters* **2007,** 91, (6), 063514.

[16] Seo, J.; Park, D.; Cho, S.; Kim, C.; Jang, W.; Whang, C.; Yoo, K.-H.; Chang, G.; Pedersen, T.; Moewes, A., Buffer layer effect on the structural and electrical properties of rubrene-based organic thin-film transistors. *Applied Physics Letters* **2006,** 89, (16), 163505.

[17] Lee, E. K.; Lee, M. Y.; Park, C. H.; Lee, H. R.; Oh, J. H., Toward environmentally robust organic electronics: approaches and applications. *Advanced Materials* **2017,** 29, (44), 1703638.

[18] Anthony, J. E.; Facchetti, A.; Heeney, M.; Marder, S. R.; Zhan, X., n-Type organic semiconductors in organic electronics. *Advanced Materials* **2010,** 22, (34), 3876-3892.

[19] Sutton, C.; Marshall, M. S.; Sherrill, C. D.; Risko, C.; Brédas, J.-L., Rubrene: The Interplay between Intramolecular and Intermolecular Interactions Determines the Planarization of Its Tetracene Core in the Solid State. *Journal of the American Chemical Society* **2015,** 137, (27), 8775-8782.

[20] Mas-Torrent, M.; Rovira, C., Role of Molecular Order and Solid-State Structure in Organic Field-Effect Transistors. *Chemical Reviews* **2011,** 111, (8), 4833-4856.

[21] Li, C.; Wang, Y.; Zou, Y.; Zhang, X.; Dong, H.; Hu, W., Two-dimensional conjugated polymer synthesized by interfacial Suzuki reaction: towards electronic device applications. *Angewandte Chemie* **2020,** 132, (24), 9489-9493.

[22] Gámez-Valenzuela, S.; Benito-Hernández, A.; Echeverri, M.; Gutierrez-Puebla, E.; Ponce Ortiz, R.; Ruiz Delgado, M. C.; Gómez-Lor, B., Functionalized Crystalline N-Trimethyltriindoles: Counterintuitive Influence of Peripheral Substituents on Their Semiconducting Properties. *Molecules* **2022,** 27, (3), 1121.

[23] García-Frutos, E. M.; Gutierrez-Puebla, E.; Monge, M. A.; Ramírez, R.; Andrés, P. d.; Andrés, A. d.; Gómez-Lor, B., Crystal structure and charge-transport properties of N-trimethyltriindole: Novel p-type organic semiconductor single crystals. *Organic Electronics* **2009,** 10, (4), 643-652.

6 Appendices

Table of contents

6.1. Acronyms and symbols

Acronyms

HMO	Hückel Molecular Orbitals	**NIR**	Near Infrared
HOMO	Highest Occupied Molecular Orbital	**OFET**	Organic Field Effect Transistor
LUMO	Lowest Unoccupied Molecular Orbital	**FT**	Fourier Transform
H-L_{gap}	HOMO-LUMO energy gap	**TD**	Time Dependent
DOS	Density Of States	**HF**	Hartree-Fock
ET	Electron Transfer	**COFs**	Covalent Organic Frameworks
UV-Vis	Ultraviolet-Visible	**D-A**	Donor-Acceptor
IIG	Isoindigo	**OTS**	Octadecyltrichlorosilane
DPP	Diketopyrrolopyrrole	**DFT**	Density Functional Theory
TIPS	Triisopropylsilylethynyl	**HMDS**	Hexamethyldisiloxane
BTBT	Benzothieno[3,2-b][1]benzothiophene	**C8**	Octyl
COFs	Covalent Organic Frameworks	**Ph**	Phenylene
NDI	Naphthalenediimide	**CMO**	Complementary Metal Oxide
PDI	Perylenediimide	**BT**	Benzothiadiazole
OLED	Organic Light-Emitting Diode	**TPA**	Triphenylamine
OPV	Organic Photovoltaic Cells	**FMOs**	Frontier Molecular Orbitals
BG-BC	Bottom Gate-Bottom Contacts	**RMS**	Root-Mean-Square
BG-TC	Bottom Gate-Top Contact	**AFM**	Atomic Force Microscopy
TG-BC	Top Gate-Bottom Contact	**TG-TC**	Top Gate-Top Contact
GIXRD	Grazing Incidence X-Ray Diffraction	**BLA**	Bond Length Alternation
NICS	Nucleus Independent Chemical Shift	**RT**	Room Temperature
ICT	Intramolecular Charge Transfer	**CV**	Cyclic Voltammetry
LCAO	Linear Combination of Atomic Orbitals	**Tx**	Truxene
SCLC	Space Charge-Limited Current	**Tr**	Triindole
CMP	Conjugated Microporous Polymer	**To**	Truxenone
PBC	Periodic Boundary Conditions	**2D**	Bidimensional

Acronyms

VB	Valence Band	**3D**	Tridimensional
CB	Conduction Band	**DNT**	Dinitrotoluene
DRS	Diffuse Reflectance Spectroscopy	**NB**	p-Nitrobencene
PET	Photoinduced Electron Transfer	**NBN**	p-Nitrobenzonitrile
GIAO	Gauge-Independent Atomic Orbital	**POM**	Polarized Optical Microscopy

Symbols

S_0	Ground electronic state	P_{ij}	Bond order between 2 atoms
S_n	Electronic excited state "n"	σ	Electrical conductivity
$I_{on}/_{off}$	Intensities on/off ratio	W_F	Work function of an electrode
a.u.	Arbitrary units	ϕ_B	Injection barrier
m_h^*	Hole effective mass	λ_h	Hole reorganization energy
m_e^*	Electron effective mass	λ_e	Electron reorganization energy
μ_e	Electron field-effect mobility	t_h	Hole transfer integral
[Q]	Concentration of quencher	t_e	Electron transfer integral
K_{SV}	Stern−Volmer constant	Ψ	Wavefunction
I_o/I	Fluorescence intensity ratio	λ_{exc}	Excitation wavelength
ϕ	Inter-ring rotation degree	**D**	Debye
Θ	Rotation degree	ε	Dielectric constant
μ_h	Hole field-effect mobility	V_{GS}	Gate-source electric potential
λ_{max}	Absorption maxima wavelength	V_{DS}	Drain-source electric potential
I_{DS}	Drain-source current	V_T	Threshold voltage
R_q	Root mean square deviation	E_{onset}	Potential Onset
E_c	Cohesive energy	E_{VBM}	Valence Band Maximum
E_g^{el}	Electrochemical HOMO-LUMO gap	E_g^{opt}	Optical HOMO-LUMO gap

6.2. DFT Calculations: Effect of the functionals used

6.2.1. Chapter I

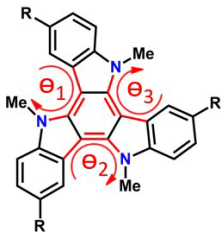

a)

	Neutral state			Radical Cation		
	Θ_1	Θ_2	Θ_3	Θ_1	Θ_2	Θ_3
1	6º	6º	6º	6º	12º	3º
2	6º	6º	6º	7º	11º	3º
3	6º	7º	6º	8º	10º	2º

b)

	Neutral state			Radical Cation		
	Θ_1	Θ_2	Θ_3	Θ_1	Θ_2	Θ_3
1	6º	6º	6º	7º	1º	11º
2	6º	6º	6º	7º	1º	12º
3	6º	6º	6º	7º	1º	10º

Figure 6.1. DFT-calculated dihedral angles values along the conjugated backbone for the triindole systems on their neutral and radical cation states at the (a) B3LYP/6-31G** and (b) M06-2X/6-31G** level of theory.

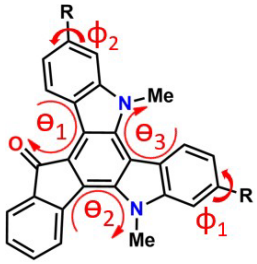

a)

	Θ_1	Θ_2	Θ_3	ϕ_1	ϕ_2
4	0º	9º	6º	36º	39º
5	1º	9º	6º	36º	39º
6	0º	9º	6º	34º	38º
7	1º	10º	6º	34º	37º

b)

	Θ_1	Θ_2	Θ_3	ϕ_1	ϕ_2
4	1º	10º	6º	37º	39º
5	1º	9º	6º	37º	39º
6	1º	10º	6º	36º	39º
7	2º	10º	6º	36º	39º

Figure 6.2. DFT-calculated dihedral angles values along the conjugated backbone for the diazatruxenones at the (a) B3LYP/6-31G** and (b) M06-2X/6-31G** level of theory.

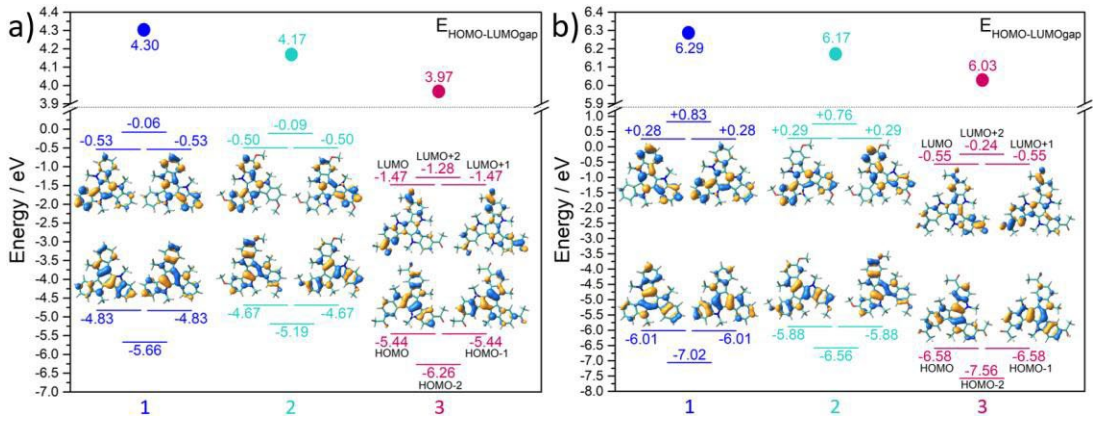

Figure 6.3. DFT-calculated molecular orbital energies for triindoles **1**-**3** at the (a) B3LYP/6-31G** and (b) M06-2X/6-31G** level of theory. The HOMO and LUMO topologies are also shown.

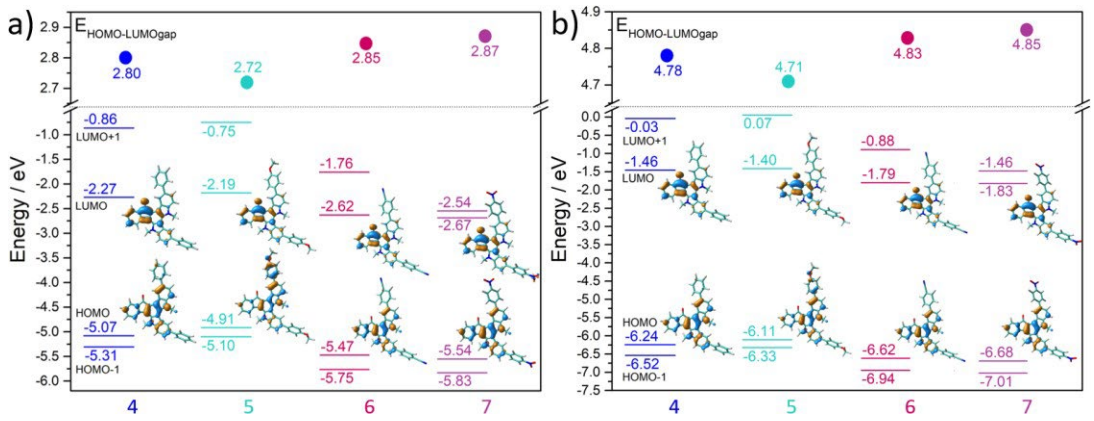

Figure 6.4. DFT-calculated molecular orbital energies for diazatruxenones **4**-**7** at the (a) B3LYP/6-31G** and (b) M06-2X/6-31G** level. The HOMO and LUMO topologies are also shown.

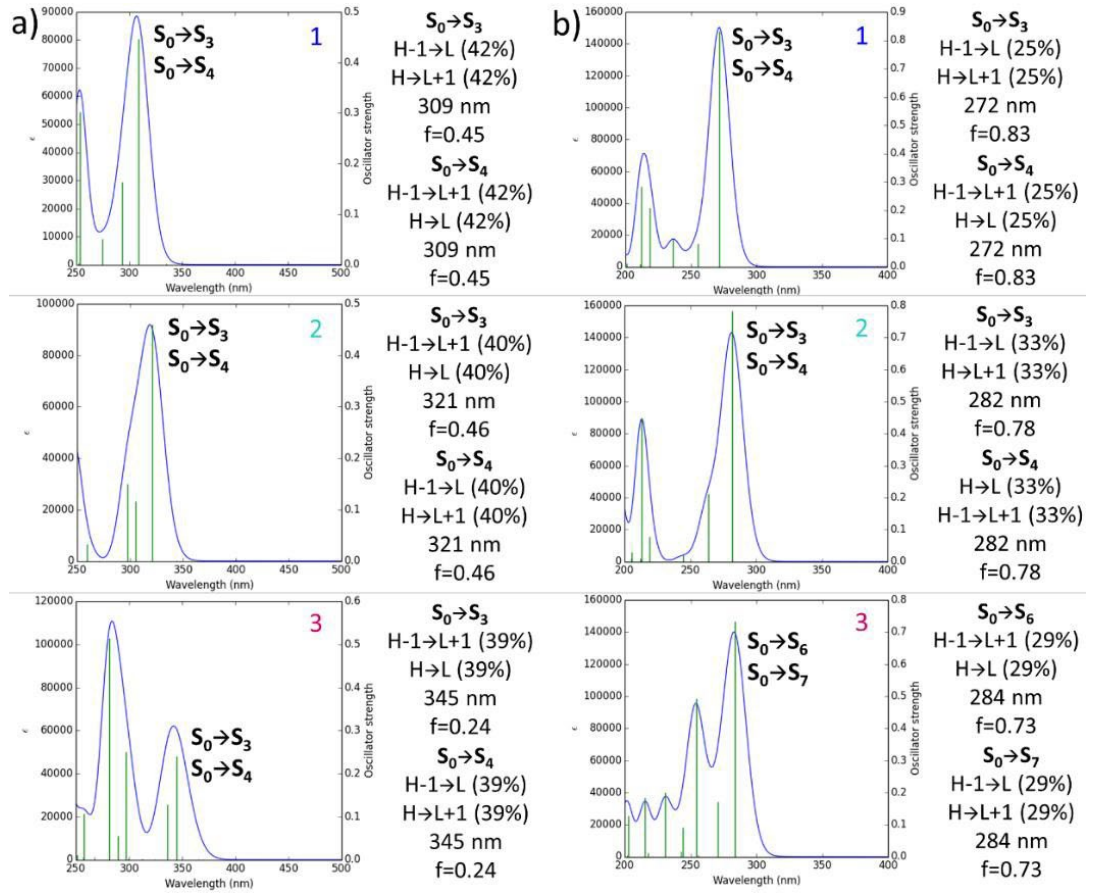

Figure 6.5. Simulated absorption spectra and main excitations (shown as vertical bars) for triindoles **1**-**3** at the (a) B3LYP/6-31G** and (b) M06-2X/6-31G** level of theory.

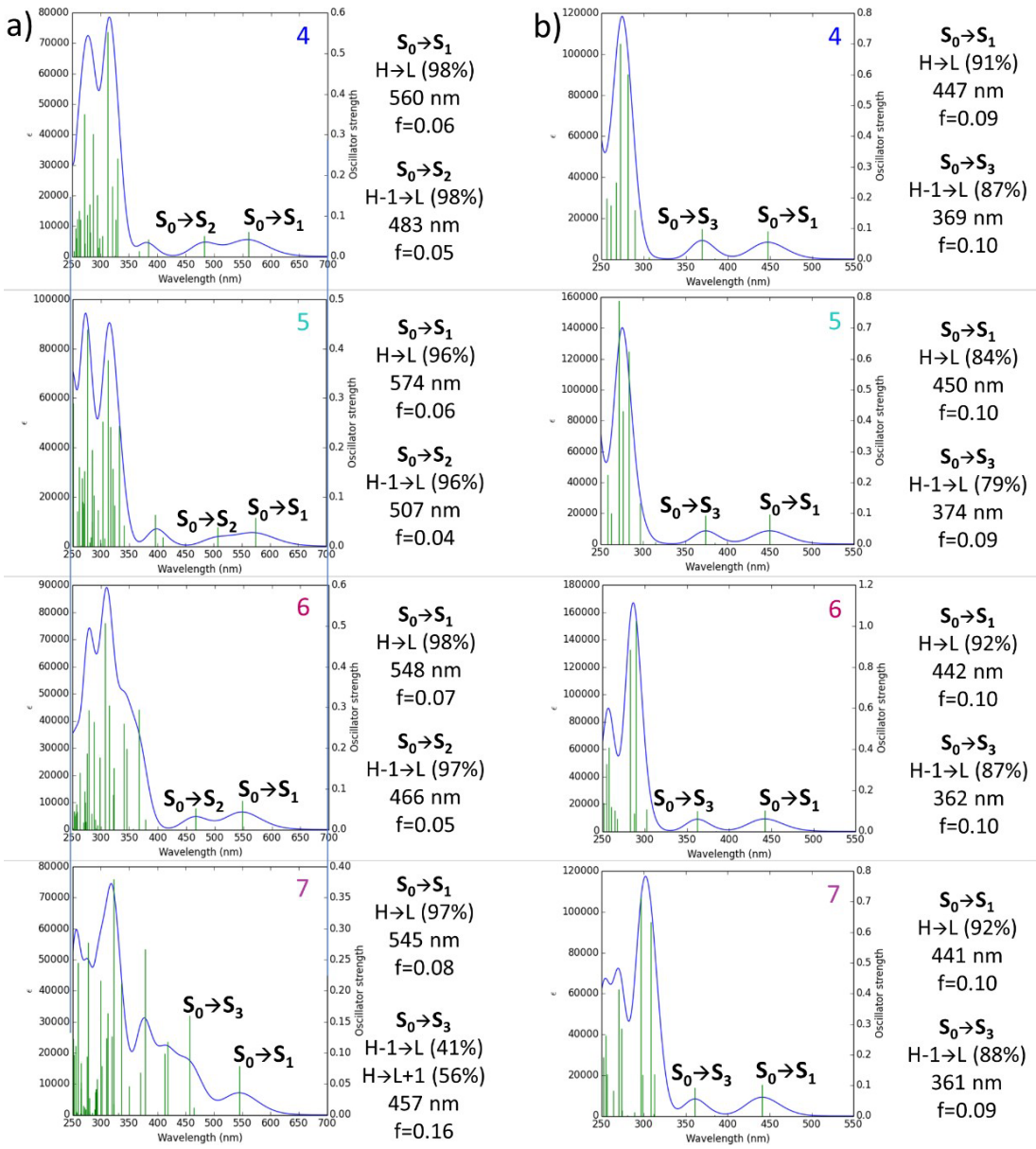

Figure 6.6. Simulated absorption spectra and main excitations (shown as vertical bars) for diazatruxenones **4**-**7** at the (a) B3LYP/6-31G** and (b) M06-2X/6-31G** level of theory.

6.2.2. Chapter III

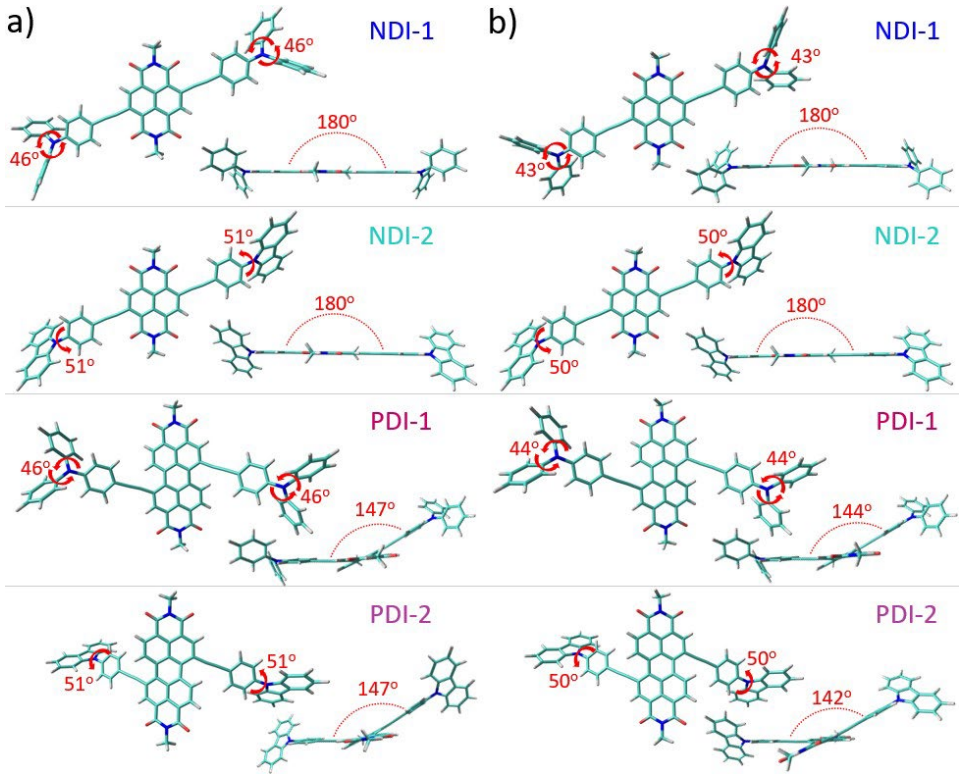

Figure 6.7. Top and lateral views of the optimized geometries for **NDI-1**, **NDI-2**, **PDI-1** and **PDI-2** molecules at the (a) B3LYP/6-31G** and (b) M06-2X/6-31G** level of theory.

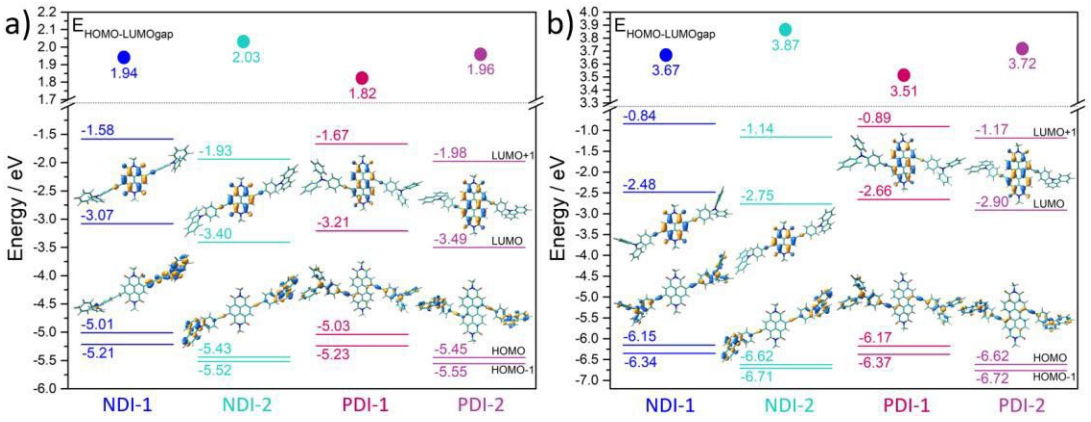

Figure 6.8. DFT-calculated molecular orbital energies for **NDI-1**, **NDI-2**, **PDI-1** and **PDI-2** molecules at the (a) B3LYP/6-31G** and (b) M06-2X/6-31G** level of theory. The HOMO and LUMO topologies are also shown

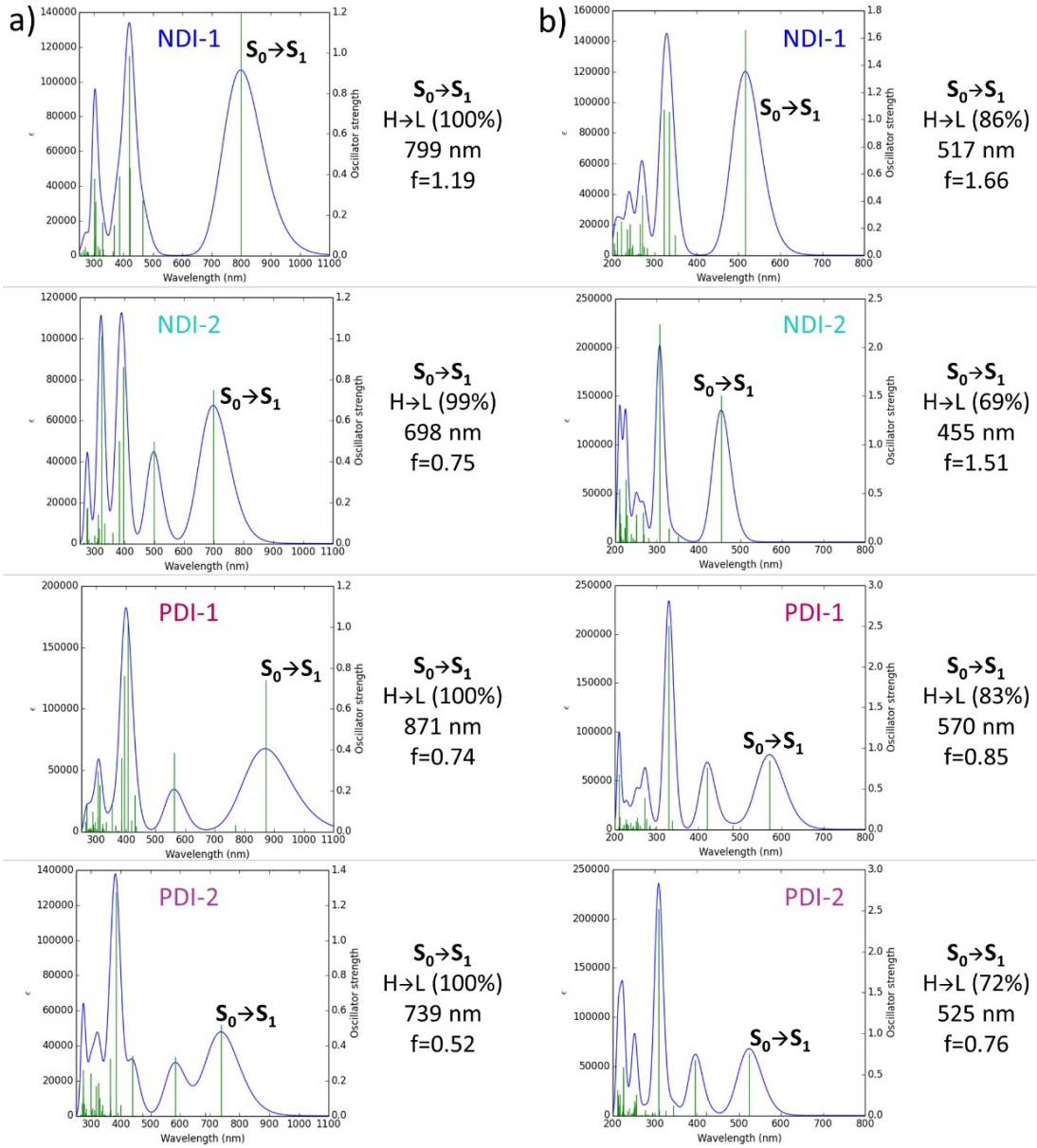

Figure 6.9. Simulated absorption spectra and main excitations (shown as vertical bars) for **NDI-1**, **NDI-2**, **PDI-1** and **PDI-2** molecules at the (a) B3LYP/6-31G** and (b) M06-2X/6-31G** level of theory.

6.2.3. Chapter IV

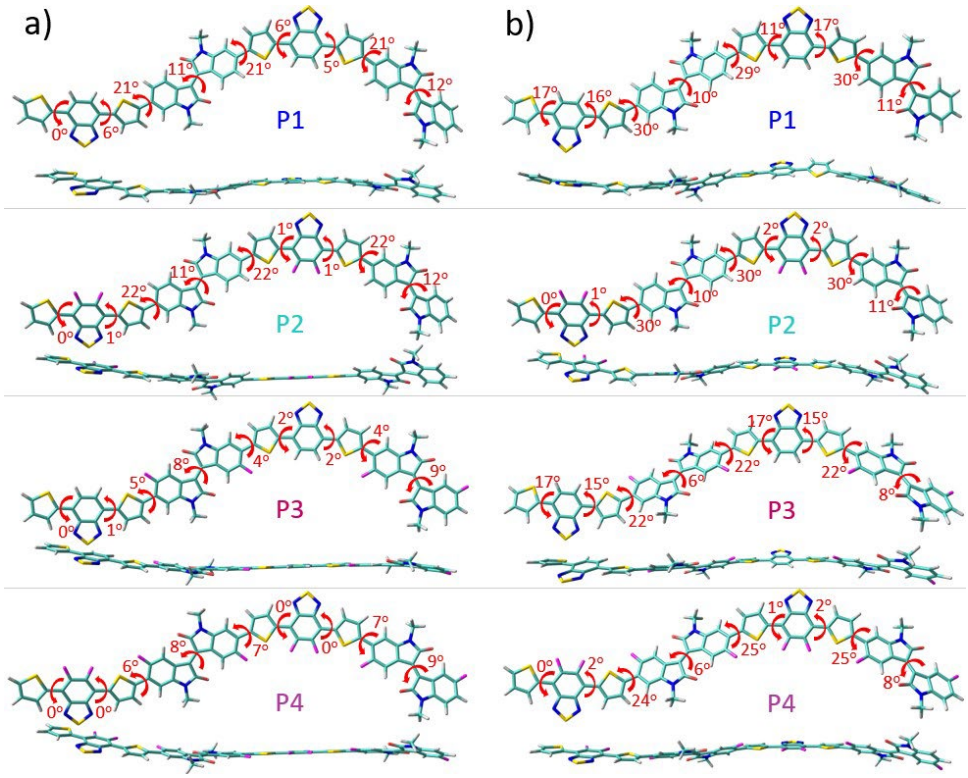

Figure 6.10. Top and lateral views of the optimized geometries for dimeric models of **P1**-**P4** polymers at the (a) B3LYP/6-31G** and (b) ωB97X-D/6-31G** level of theory. The dihedral angles values between selected rings are also shown

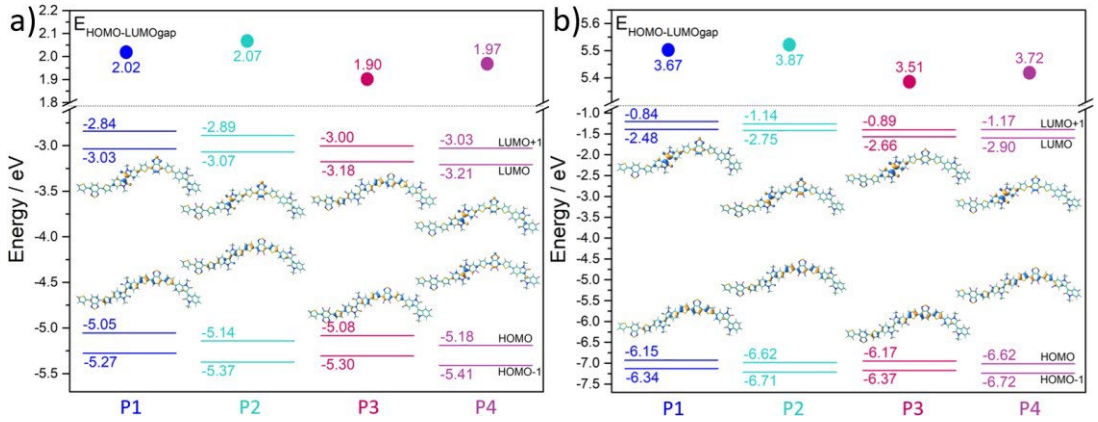

Figure 6.11. DFT-calculated molecular orbital energies for dimeric models of **P1**-**P4** polymers at the (a) B3LYP/6-31G** and (b) ωB97X-D/6-31G** level of theory. The HOMO and LUMO topologies are also shown

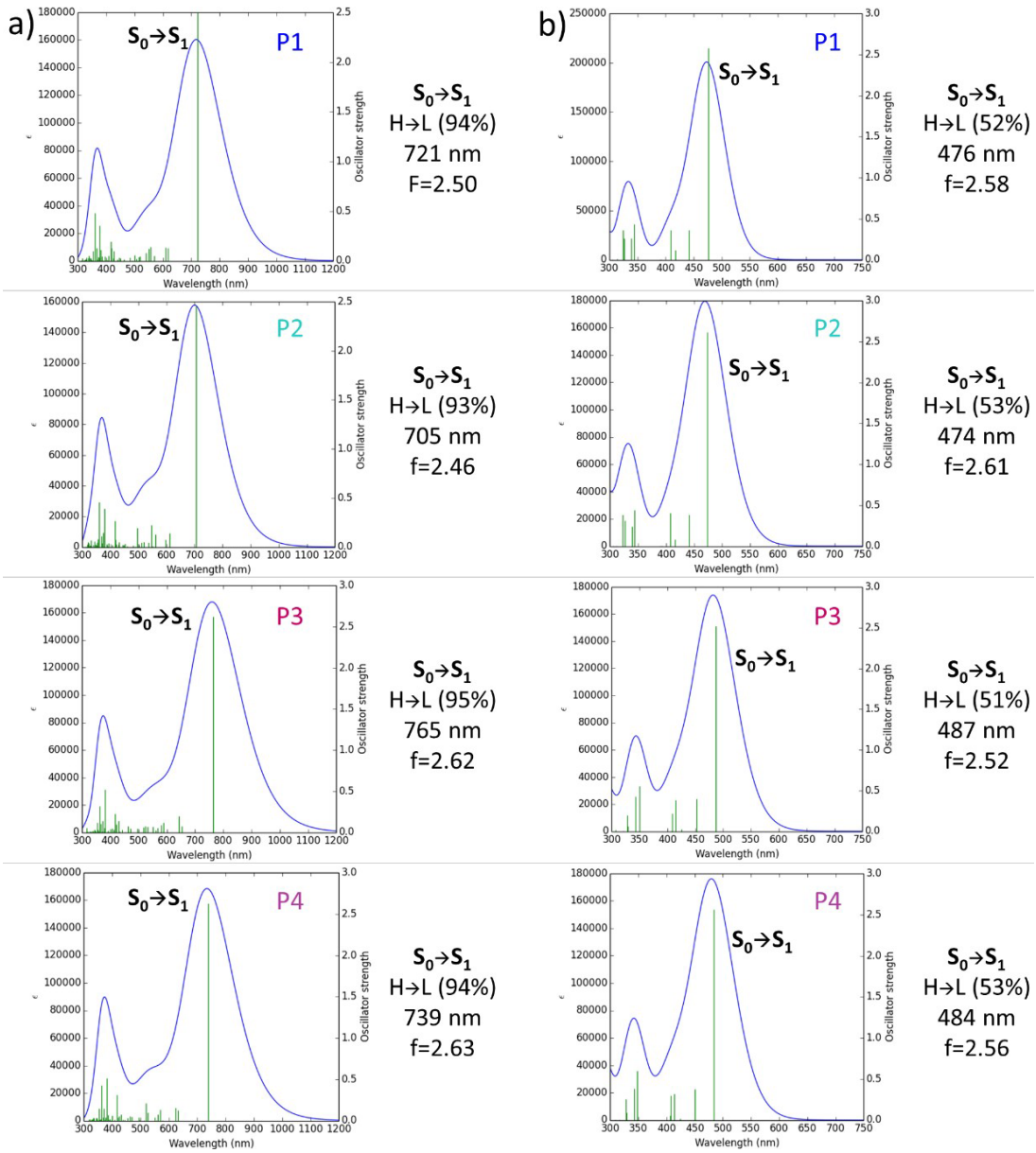

Figure 6.12. Simulated absorption spectra and main excitations (shown as vertical bars) for dimeric models of **P1**-**P4** polymers at the (a) B3LYP/6-31G** and (b) ωB97X-D/6-31G** level of theory.

6.3. OFETs performance optimization

6.3.1. Chapter I

Table 6.1. OFET electrical data of **1** measured at room conditions. Average and the best (in parenthesis) values are shown. The average values were obtained from data of at least 6 devices.

Substrate treatment	Substrate temperature	μ_h in $cm^2 V^{-1} s^{-1}$	I_{ON}/I_{OFF}	V_T in V
OTS	60ºC	2.2×10^{-2} (2.8×10^{-2})	1×10^{7} (3×10^{7})	-11 (-17)
	25ºC	2.0×10^{-5} (3.5×10^{-5})	5×10^{3} (2×10^{4})	-3 (0)
HMDS	60ºC	3.2×10^{-4} (3.6×10^{-4})	1×10^{5} (2×10^{5})	-11 (-6)
	25ºC	1.2×10^{-4} (1.3×10^{-4})	3×10^{4} (9×10^{4})	-14 (-8)
No treatment	60ºC	1.9×10^{-5} (2.8×10^{-5})	3×10^{3} (1×10^{4})	8 (6)
	25ºC	5.9×10^{-6} (6.5×10^{-6})	2×10^{2} (3×10^{2})	-2 (0)

Table 6.2. OFET electrical data of **2** measured at room conditions. Average and the best (in parenthesis) values are shown. The average values were obtained from data of at least 6 devices.

Substrate treatment	Substrate temperature	μ_h in $cm^2 V^{-1} s^{-1}$	I_{ON}/I_{OFF}	V_T in V
OTS	60ºC	2.2×10^{-5} (5.1×10^{-5})	2×10^{2} (3×10^{2})	3 (3)
	25ºC	1.9×10^{-4} (2.0×10^{-4})	9×10^{5} (2×10^{5})	-5 (-5)
	80ºC	9.3×10^{-4} (1.3×10^{-3})	3×10^{3} (6×10^{3})	13 (-2)
	90ºC	1.4×10^{-3} (1.6×10^{-3})	6×10^{3} (1×10^{4})	-4 (-8)
HMDS	60ºC	5.8×10^{-6} (6.6×10^{-6})	6×10^{1} (2×10^{2})	-7 (-5)
	25ºC	8.2×10^{-6} (9.8×10^{-6})	1×10^{2} (3×10^{2})	-10 (-7)
	80ºC	7.5×10^{-6} (8.3×10^{-6})	1×10^{3} (6×10^{3})	4 (-8)
No treatment	60ºC	1.9×10^{-5} (2.8×10^{-5})	3×10^{3} (1×10^{4})	8 (6)
	25ºC	5.9×10^{-6} (6.5×10^{-6})	2×10^{2} (3×10^{2})	-2 (0)
	80ºC	1.8×10^{-6} (2.1×10^{-6})	9 (1×10^{1})	20 (10)

Table 6.3. OFET electrical data of **3** measured at room conditions. Average and the best (in parenthesis) values are shown. The average values were obtained from data of at least 6 devices.

Substrate treatment	Substrate temperature	μ_h in $cm^2 V^{-1} s^{-1}$	I_{ON}/I_{OFF}	V_T in V
OTS	25ºC	1.0×10^{-5} (2.2×10^{-5})	8×10^{1} (2×10^{2})	-14 (-29)
	65ºC	1.3×10^{-5} (1.7×10^{-5})	9×10^{1} (2×10^{2})	-12 (-29)
	120ºC (post annealing)	3.1×10^{-5} (4.5×10^{-5})	2×10^{2} (3×10^{2})	-17 (-21)
HMDS	25ºC	1.7×10^{-5} (2.2×10^{-5})	4×10^{2} (1×10^{3})	-18 (-26)
	65ºC	1.5×10^{-5} (1.7×10^{-5})	2×10^{2} (2×10^{2})	-19 (-12)
	120ºC (post annealing)	1.8×10^{-5} (2.2×10^{-5})	1×10^{2} (2×10^{2})	-13 (-23)
No treatment	25ºC	6.4×10^{-6} (9.9×10^{-6})	6×10^{1} (1×10^{2})	-8 (-11)
	65ºC	6.5×10^{-6} (7.8×10^{-6})	4×10^{1} (7×10^{1})	-3 (-5)
	120ºC (post annealing)	1.0×10^{-6} (7.8×10^{-6})	1×10^{1} (2×10^{1})	18 (7)

6.3.2. Chapter III

Table 6.4. OFET electrical data of **NDI-1** measured under vacuum. Average and the best (in parenthesis) values are shown. The average values were obtained from data of at least 6 devices.

Substrate treatment	Substrate temperature	μ_e in $cm^2V^{-1}s^{-1}$	I_{ON}/I_{OFF}	V_T in V
OTS	90ºC	1.9×10^{-1} (2.3×10^{-1})	2×10^{5} (5×10^{5})	42 (27)
	25ºC	3.1×10^{-1} (3.2×10^{-1})	1×10^{5} (2×10^{5})	40 (36)
	120ºC, 2 hours (post annealing)	9.6×10^{-2} (1.2×10^{-1})	1×10^{5} (2×10^{5})	31 (23)
HMDS	90ºC	2.2×10^{-1} (3.1×10^{-1})	2×10^{5} (4×10^{5})	39 (31)
	25ºC	1.9×10^{-1} (2.3×10^{-1})	9×10^{4} (1×10^{5})	42 (38)
	120ºC, 2 hours (post annealing)	1.1×10^{-1} (1.3×10^{-1})	9×10^{4} (2×10^{5})	40 (34)
No treatment	90ºC	(1.4×10^{-4})	(2×10^{4})	(27)
	25ºC	1.7×10^{-4} (2.4×10^{-4})	2×10^{2} (3×10^{2})	23 (28)
	120ºC, 2 hours (post annealing)	9.0×10^{-5} (4.7×10^{-5})	9×10^{1} (1×10^{2})	12 (10)

Table 6.5. OFET electrical data of **NDI-2** measured under vacuum. Average and the best (in parenthesis) values are shown. The average values were obtained from data of at least 6 devices.

Substrate treatment	Substrate temperature	μ_e in $cm^2 V^{-1} s^{-1}$	I_{ON}/I_{OFF}	V_T in V
OTS	60ºC	7.1×10^{-2} (1.0×10^{-1})	3×10^4 (4×10^4)	55 (50)
	25ºC	7.9×10^{-2} (1.2×10^{-1})	2×10^4 (4×10^4)	61 (55)
	150ºC, 2 hours (post annealing)		---	
HMDS	60ºC	2.5×10^{-2} (3.5×10^{-2})	2×10^4 (3×10^4)	38 (33)
	25ºC	7.3×10^{-2} (1.0×10^{-1})	2×10^4 (4×10^4)	44 (37)
	150ºC, 2 hours (post annealing)		---	
No treatment	60ºC	5.7×10^{-2} (7.3×10^{-2})	3×10^4 (6×10^4)	42 (38)
	25ºC	5.6×10^{-2} (9.0×10^{-2})	2×10^4 (3×10^4)	40 (33)
	150ºC, 2 hours (post annealing)		---	

Table 6.6. OFET electrical data of **PDI-1** measured under vacuum. Average and the best (in parenthesis) values are shown. The average values were obtained from data of at least 6 devices.

Substrate treatment	Substrate temperature	μ_e ($cm^2 V^{-1} s^{-1}$)	I_{ON}/I_{OFF}	V_T(V)
OTS	25ºC	3.2×10^{-3} (4.5×10^{-3})	5×10^2 (1×10^3)	58 (55)
	150ºC, 2 hours (post annealing)	3.9×10^{-3} (4.9×10^{-3})	9×10^2 (1×10^3)	50 (44)
HMDS	25ºC	1.3×10^{-3} (1.5×10^{-3})	2×10^4 (1×10^5)	49 (42)
	150ºC, 2 hours (post annealing)	1.4×10^{-4} (1.9×10^{-3})	8×10^1 (1×10^2)	49 (39)
No treatment	25ºC	8.0×10^{-5} (1.1×10^{-4})	4×10^1 (6×10^1)	27 (14)
	150ºC, 2 hours (post annealing)		---	

Table 6.7. OFET electrical data of **PDI-2** measured under vacuum. Average and the best (in parenthesis) values are shown. The average values were obtained from data of at least 6 devices.

Substrate treatment	Substrate temperature	μ_e ($cm^2 V^{-1} s^{-1}$)	I_{ON}/I_{OFF}	V_T(V)
OTS	80ºC	3.2×10^{-3} (4.0×10^{-3})	3×10^3 (8×10^3)	33 (9)
	25ºC	3.0×10^{-3} (4.0×10^{-3})	3×10^3 (4×10^3)	17 (3)
	120ºC, 2 hours (post annealing)	1.9×10^{-4} (2.4×10^{-4})	2×10^2 (4×10^2)	-4 (-12)
HMDS	80ºC	5.0×10^{-4} (7.3×10^{-4})	7×10^2 (1×10^3)	6 (3)
	25ºC	5.3×10^{-4} (6.9×10^{-4})	5×10^2 (1×10^3)	4 (-1)
	120ºC, 2 hours (post annealing)	4.9×10^{-4} (6.1×10^{-4})	5×10^2 (2×10^3)	0 (-2)
No treatment	80ºC		---	
	25ºC		---	
	120ºC, 2 hours (post annealing)	3.0×10^{-5} (4.0×10^{-5})	3×10^1 (5×10^1)	10 (6)

6.3.3. Chapter IV

Table 6.8. OFET electrical data of **P1** measured under vacuum. Average and the best (in parenthesis) values are shown. The average values were obtained from data of at least 6 devices.

Substrate treatment	Substrate temperature	μ_h in $cm^2 V^{-1} s^{-1}$)	I_{ON}/I_{OFF}	V_T in V
OTS	25ºC	1.4×10^{-5} (2.20×10^{-5})	3×10^1 (4×10^1)	8 (5)
	100ºC, 2h (post annealing)	6.3×10^{-6} (1.53×10^{-5})	4 (6)	31 (24)
	150ºC, 2h (post annealing)	1.1×10^{-5} (1.43×10^{-5})	8×10^1 (1×10^2)	4 (-3)
HMDS	25ºC	5.7×10^{-6} (9.52×10^{-6})	2×10^1 (6×10^1)	22 (0)
	100ºC, 2h (post annealing)	8.6×10^{-6} (1.11×10^{-5})	1×10^1 (2×10^1)	24 (7)
	150ºC, 2h (post annealing)	1.0×10^{-5} (1.30×10^{-5})	5×10^1 (1×10^2)	3 (1)
No treatment	25ºC		--	
	150ºC, 2h (post annealing)		--	

Table 6.9. OFET electrical data of **P2** measured under vacuum. Average and the best (in parenthesis) values are shown. The average values were obtained from data of at least 6 devices.

Substrate treatment	Substrate temperature	μ_e in $cm^2 V^{-1} s^{-1}$	I_{ON}/I_{OFF}	V_T in V	μ_h in $cm^2 V^{-1} s^{-1}$	I_{ON}/I_{OFF}	V_T in V
OTS	25ºC	4.1×10^{-4} (6.29×10^{-4})	1×10^3 (2×10^3)	49 (43)	3.0×10^{-4} (4.24×10^{-4})	2×10^3 (3×10^3)	-10 (-17)
	150ºC, 2h (post annealing)	3.8×10^{-3} (4.03×10^{-3})	4×10^3 (9×10^3)	58 (52)	2.9×10^{-3} (3.32×10^{-3})	1×10^3 (2×10^3)	-1 (-17)
	200ºC, 2h (post annealing)	1.1×10^{-3} (1.45×10^{-3})	3×10^2 (4×10^2)	56 (49)	1.2×10^{-3} (1.65×10^{-3})	1×10^3 (1×10^3)	-35 (-42)
HMDS	25ºC	--			6.5×10^{-6} (7.40×10^{-6})	1×10^3 (6×10^3)	-12 (-21)
	100ºC, 2h (post annealing)	--			2.3×10^{-6} (3.56×10^{-6})	1×10^1 (5×10^1)	9 (4)
	150ºC, 2h (post annealing)	--			1.2×10^{-5} (1.93×10^{-5})	2×10^3 (6×10^3)	-13 (-18)
	200ºC, 2h (post annealing)	--			2.9×10^{-5} (3.25×10^{-5})	7×10^1 (1×10^2)	-19 (-20)
No treatment	25ºC	--			--		
	150ºC, 2h (post annealing)	--			--		

Table 6.10. OFET electrical data of **P3** measured under vacuum. Average and the best (in parenthesis) values are shown. The average values were obtained from data of at least 6 devices.

Substrate treatment	Substrate temperature	μ_e in $cm^2 V^{-1} s^{-1}$	I_{ON}/I_{OFF}	V_T in V	μ_h in $cm^2 V^{-1} s^{-1}$	I_{ON}/I_{OFF}	V_T in V
OTS	25ºC	5.3×10^{-2} (7.9×10^{-2})	9×10^1 (1×10^2)	48 (36)	7.0×10^{-2} (9.7×10^{-2})	1×10^2 (3×10^2)	-13 (-18)
	100ºC, 2h (post annealing)	7.5×10^{-2} (8.0×10^{-2})	9×10^1 (2×10^2)	49 (45)	7.4×10^{-2} (8.2×10^{-2})	1×10^2 (2×10^2)	-14 (-19)
	200ºC, 2h (post annealing)	9.7×10^{-2} (1.1×10^{-1})	8×10^1 (1×10^2)	57 (53)	1.2×10^{-1} (1.5×10^{-1})	2×10^2 (4×10^2)	-26 (-31)
HMDS	25ºC	7.1×10^{-2} (7.8×10^{-2})	3×10^1 (3×10^1)	37 (33)	8.8×10^{-2} (1.0×10^{-1})	3×10^1 (4×10^1)	-20 (-24)
	100ºC, 2h (post annealing)	5.9×10^{-2} (7.5×10^{-2})	2×10^1 (2×10^1)	31 (27)	6.4×10^{-2} (8.4×10^{-2})	2×10^1 (3×10^1)	-16 (-19)
	150ºC, 2h (post annealing)	9.4×10^{-2} (1.0×10^{-1})	3×10^1 (5×10^1)	35 (27)	1.2×10^{-1} (1.4×10^{-2})	4×10^1 (5×10^1)	-23 (-28)
	200ºC, 2h (post annealing)	9.4×10^{-2} (1.0×10^{-1})	1×10^1 (1×10^1)	28 (26)	1.1×10^{-1} (1.1×10^{-1})	1×10^1 (1×10^1)	-12 (-13)
No treatment	25ºC	--			--		
	150ºC, 2h (post annealing)	--			--		

Table 6.11. OFET electrical data of **P4** measured under vacuum. Average and the best (in parenthesis) values are shown. The average values were obtained from data of at least 6 devices.

Substrate treatment	Substrate temperature	μ_e in $cm^2 V^{-1} s^{-1}$	I_{ON}/I_{OFF}	V_T in V	μ_h in $cm^2 V^{-1} s^{-1}$	I_{ON}/I_{OFF}	V_T in V
OTS	25ºC	1.1×10^{-2} (1.3×10^{-2})	2×10^{3} (7×10^{3})	17 (8)	1.3×10^{-2} (1.6×10^{-2})	7×10^{5} (3×10^{6})	-21 (-29)
	150ºC, 2h (post annealing)	2.1×10^{-2} (2.4×10^{-2})	9×10^{1} (2×10^{2})	13 (7)	3.3×10^{-2} (7.4×10^{-2})	1×10^{5} (4×10^{5})	-11 (-29)
	200ºC, 2h (post annealing)	1.4×10^{-2} (1.9×10^{-2})	1×10^{3} (2×10^{3})	37 (32)	6.1×10^{-2} (1.1×10^{-1})	3×10^{4} (4×10^{4})	-17 (-29)
HMDS	25ºC	8.0×10^{-3} (1.1×10^{-2})	2×10^{2} (3×10^{2})	27 (23)	9.3×10^{-3} (1.2×10^{-2})	4×10^{4} (1×10^{5})	-16 (-25)
	100ºC, 2h (post annealing)	6.0×10^{-3} (7.0×10^{-3})	5×10^{1} (7×10^{1})	33 (21)	8.4×10^{-3} (8.8×10^{-3})	9×10^{3} (1×10^{4})	-26 (-28)
	150ºC, 2h (post annealing)	1.2×10^{-2} (1.4×10^{-2})	1×10^{2} (1×10^{2})	27 (24)	1.3×10^{-2} (1.4×10^{-2})	5×10^{6} (1×10^{7})	-16 (-21)
	200ºC, 2h (post annealing)	2.7×10^{-2} (3.4×10^{-2})	5×10^{1} (9×10^{1})	33 (31)	3.3×10^{-2} (4.3×10^{-2})	7×10^{4} (1×10^{5})	-24 (-33)
No treatment	25ºC	3.4×10^{-5} (4.2×10^{-5})	7×10^{1} (1×10^{2})	7 (1)	6.4×10^{-4} (7.5×10^{-4})	6×10^{2} (1×10^{3})	-22 (-27)
	100ºC, 2h (post annealing)	1.1×10^{-4} (1.7×10^{-4})	4×10^{2} (1×10^{3})	26 (18)	9.4×10^{-4} (2.0×10^{-3})	1×10^{3} (1×10^{3})	-21 (-38)
	150ºC, 2h (post annealing)	8.1×10^{-5} (1.0×10^{-4})	2×10^{2} (2×10^{2})	32 (18)	7.3×10^{-4} (1.0×10^{-3})	9×10^{2} (2×10^{3})	-27 (-30)
	200ºC, 2h (post annealing)	7.7×10^{-4} (1.4×10^{-3})	1×10^{2} (2×10^{2})	49 (22)	2.4×10^{-3} (3.3×10^{-3})	1×10^{3} (1×10^{3})	-38 (-44)

6.4. List of publications

The research work developed during the present Ph.D. Thesis has resulted in 14 publications, 4 of them directly linked to the development of the Thesis and 10 additional papers from parallel investigations. In addition, 3manuscripts are either submitted or in preparation.

- Publications directly linked to the present Ph.D. Thesis:

1. **Gámez-Valenzuela, S.**; Benito-Hernández, A.; Echeverri, M.; Gutierrez-Puebla, E.; Ponce Ortiz, R.; Ruiz Delgado, M. C.; Gómez-Lor, B., Functionalized Crystalline N-Trimethyltriindoles: Counterintuitive Influence of Peripheral Substituents on Their Semiconducting Properties. Molecules **2022**, 27, (3), 1121-1135.
2. **Gámez-Valenzuela, S.**; Benito-Hernández, A.; Ponce Ortíz, P.; Golemme, A.; Termine, R.; Ruiz Delgado, M. C.; Gómez-Lor. B., Role of peripheral substitution on electronics and self-assembly of discotic semiconductors: the case of diazatruxenone. *Submitted.*
3. Echeverri, M.; **Gámez-Valenzuela, S.**; González-Cano, R. C.; Guadalupe, J.; Cortijo-Campos, S.; López Navarrete, J. T.; Iglesias, M.; Ruiz Delgado, M. C.; Gómez-Lor, B., Effect of the Linkage Position on the Conjugation Length of Truxene-Based Porous Polymers: Implications for Their Sensing Performance of Nitroaromatics. Chemistry of Materials **2019**, 31, (17), 6971-6978.
4. **Gámez-Valenzuela, S.**; Echeverri, M.; Gómez-Lor, B.; Martínez, J. I.; Ruiz Delgado, M. C., In silico design of 2D polymers containing truxene-based platforms: insights into their structural and electronic properties. Journal of Materials Chemistry C **2020**, 8, (43), 15416-15425.
5. **Gámez-Valenzuela, S.**; Echeverri, M.; Ruiz Delgado, M. C.; Gómez-Lor, B., Donor-Acceptor Truxene-based Porous Polymers for Defense Applications. *In preparation*.
6. **Gámez-Valenzuela, S**.; Torres-Moya, I.; Sánchez, A.; Donoso, B.; López Navarrete, J. T.; Ruiz Delgado, M. C.; Prieto, P.; Ponce Ortiz, R., Extended π-conjugation and structural planarity effects of novel symmetrical D-π-A-π-D naphthalene and perylene diimide semiconductors on n-type electrical properties. *In preparation.*
7. **Gámez-Valenzuela, S**.; Comí, M.; Rodríguez González, S.; Ruiz Delgado, M. C.; Al-Hashimi, M.; Ponce Ortiz, R., The fluorination effect: importance of backbone planarity in achieving high performance ambipolar field effect transistors. Journal of Materials Chemistry C **2023***, Accepted.* (DOI https://doi.org/10.1039/D2TC05073K)

molecules

MDPI

Article

Functionalized Crystalline *N*-Trimethyltriindoles: Counterintuitive Influence of Peripheral Substituents on Their Semiconducting Properties

Sergio Gámez-Valenzuela [1], Angela Benito-Hernández [2], Marcelo Echeverri [2], Enrique Gutierrez-Puebla [2], Rocío Ponce Ortiz [1], Maria Carmen Ruiz Delgado [1,*] and Berta Gómez-Lor [2,*]

[1] Department of Physical Chemistry, University of Málaga, Campus de Teatinos s/n, 29071 Málaga, Spain; sergiogamez@uma.es (S.G.-V.); rocioponce@uma.es (R.P.O.)
[2] Instituto de Ciencia de Materiales de Madrid-Consejo Superior de Investigaciones Científicas (ICMM-CSIC), Sor Juana Inés de la Cruz 3, Cantoblanco, 28049 Madrid, Spain; angelabenitohernandez@gmail.com (A.B.-H.); marceloeche525@hotmail.com (M.E.); egutierrez@icmm.csic.es (E.G.-P.)
* Correspondence: carmenrd@uma.es (M.C.R.D.); bgl@icmm.csic.es (B.G.-L.)

Abstract: Three crystalline *N*-trimethyltriindoles endowed with different functionalities at 3, 8 and 13 positions (either unsubstituted or with three methoxy or three acetyl groups attached) are investigated, and clear correlations between the electronic nature of the substituents and their solid-state organization, electronic properties and semiconductor behavior are established. The three compounds give rise to similar columnar hexagonal crystalline structures; however, the insertion of electron-donor methoxy groups results in slightly shorter stacking distances when compared with the unsubstituted derivative, whereas the insertion of electron-withdrawing acetyl groups lowers the crystallinity of the system. Functionalization significantly affects hole mobilities with the triacetyl derivative showing the lowest mobility within the series in agreement with the lower degree of order. However, attaching three methoxy groups also results in lower hole mobility values in the OFETs (0.022 vs. 0.0014 $cm^2 V^{-1} s^{-1}$) in spite of the shorter stacking distances. This counterintuitive behavior has been explained with the help of DFT calculations performed to rationalize the interplay between the intramolecular and intermolecular properties, which point to lower transfer integrals in the trimethoxy derivative due to the HOMO wave function extension over the peripheral methoxy groups. The results of this study provide useful insights into how peripheral substituents influence the fundamental charge transport parameters of chemically modified triindole platforms of fundamental importance to design new derivatives with improved semiconducting performance.

Keywords: triindole; organic semiconductors; DFT-calculations; OFETs; Raman

Citation: Gámez-Valenzuela, S.; Benito-Hernández, A.; Echeverri, M.; Gutierrez-Puebla, E.; Ponce Ortiz, R.; Ruiz Delgado, M.C.; Gómez-Lor, B. Functionalized Crystalline *N*-Trimethyltriindoles: Counterintuitive Influence of Peripheral Substituents on Their Semiconducting Properties. *Molecules* **2022**, 27, 1121. https://doi.org/10.3390/molecules27031121

Academic Editors: Roberto Termine and Agostina-Lina Capodilupo

Received: 27 December 2021
Accepted: 5 February 2022
Published: 8 February 2022

1. Introduction

In the last few years, the heptacyclic molecule 10,15- dihydro-5*H*-diindolo[3,2-*a*:3′,2′-*c*] carbazole (also known in the literature as triindole or triazatruxene) has been identified as a highly promising *p*-type organic semiconductor in the construction of electronic and opto-electronic devices. Owing to its excellent hole-transporter ability, numerous triindole-based materials have been successfully incorporated in OFETs [1–4] and dye-sensitized [5–7] or perovskite-based [8,9] solar cells exhibiting excellent performances. On the other hand, their favorable optical properties have been successfully exploited in the fabrication of efficient OLEDs [10–14], waveguiding materials [15] and photoconductors [16]. In addition, the triindole core, has been identified as an excellent aromatic core in the construction of high mobility *p*-type semiconducting discotic liquid crystals. By attaching a number of peripheral flexible chains to this molecule, it is possible to induce in this heptacyclic platform columnar mesomorphism giving rise to liquid crystalline materials that exhibit excellent hole mobilities values and can be easily processed from solution or melt [17–19].

CHEMISTRY OF MATERIALS
Cite This: Chem. Mater. 2019, 31, 6971−6978
Article
pubs.acs.org/cm

Effect of the Linkage Position on the Conjugation Length of Truxene-Based Porous Polymers: Implications for Their Sensing Performance of Nitroaromatics

Marcelo Echeverri,[†] Sergio Gámez-Valenzuela,[‡] Rafael C. González-Cano,[‡] Jordy Guadalupe,[†,§] Sandra Cortijo-Campos,[†] Juan Teodomiro López Navarrete,[‡] Marta Iglesias,*[,†] M. Carmen Ruiz Delgado,*[,‡] and Berta Gómez-Lor*[,†]

[†]Instituto de Ciencia de Materiales de Madrid, CSIC, C/Sor Juana Inés de la Cruz 3, Cantoblanco, Madrid 28049, Spain
[‡]Department of Physical Chemistry, University of Malaga, Campus de Teatinos s/n, 29071 Malaga, Spain

Supporting Information

ABSTRACT: Four highly porous truxene-based organic polymers have been synthesized via C−C cross coupling methodologies (under Yamamoto and Suzuki−Miyaura conditions) starting from two different brominated hexamethyltruxene isomers (2,7,12- and 3,8,13-tribromohexamethyltruxene). We have found that the linkage position in these polymers has a strong influence not only on the porosity but also on the absorption and light emitting properties of the final materials. We have performed a joint theoretical and experimental investigation to shed light on the role of the positional isomeric effect of the monomers on the degree of π-conjugation of the final materials. Our study indicates that the 2,7,12 linkage significantly enhances the electronic communication between the covalently linked building units, thus strongly influencing the conjugation length and the position of the energy levels of the final materials. The result of this work provides us with a new design tool to fine-tune the electronic properties of conjugated porous polymers with important implications for their potential applications, as demonstrated by their sensing performance for the detection of nitroaromatic compounds.

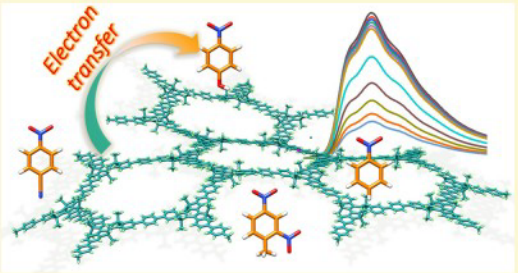

INTRODUCTION

In recent years, considerable attention has been paid to the design and synthesis of porous organic materials, built up from organic building units covalently linked. These materials have found utilities in fields such as adsorption, separation, or catalysis by virtue of their high thermal and chemical stability and permanent surface area.[1,2] On the other hand, the combination of the porous character of these polymers with the inherent functionality of the organic building blocks has enormously broadened their potential applications. Representative examples are porous π-conjugated polymers[3,4] that have emerged as promising candidates for organic electronics,[5] photocatalysis,[6] sensing,[7−13] or energy applications[14] by taking advantage of the light emitting or semiconducting properties of the constituent monomers and of the extended three-dimensional conjugation of the resultant polymers. Multiple synthetic protocols ranging from metal-mediated couplings (Suzuki−Miyaura, Yamamoto, Sonogashira, Heck, etc.) to acid- or base-catalyzed polycondensation reactions or trimerizations have been used for the generation of conjugated porous polymers,[3] allowing for great control of the nature of the linker groups and of the effective conjugation length of the resultant polymers. However, while many efforts have been provided to modulate the electronic properties of these polymers through the convenient choice of the bridging connectors,[15,16] the effect of the linker position on such properties has been very scarcely investigated.[17−19]

Among the plethora of π-conjugated molecules with light emitting or semiconducting properties that have been used as monomers in the construction of conjugated porous polymers, we and others have recently become interested in heptacyclic truxene, which can be considered as a 1,3,5-triphenylbenzene planarized through three bridging methylenes.[20,21] These methylene groups give rise to three additional fused five-membered rings (Scheme 1), thus enhancing the delocalization of the π-system, which confers upon this molecule interesting photoactive properties and excellent electron donating capabilities.[22] Curiously, in contrast to the structurally related 1,3,5-triphenylbenzene, truxene has been very scarcely explored as a building block in the construction of porous organic polymers.

Special Issue: Jean-Luc Bredas Festschrift

Received: April 11, 2019
Revised: July 1, 2019
Published: July 2, 2019

DOI: 10.1021/acs.chemmater.9b01432
Chem. Mater. 2019, 31, 6971−6978

Journal of Materials Chemistry C

ROYAL SOCIETY OF CHEMISTRY

PAPER

View Article Online
View Journal

Cite this: DOI: 10.1039/d0tc03139a

In silico design of 2D polymers containing truxene-based platforms: insights into their structural and electronic properties†

Sergio Gámez-Valenzuela,[a] Marcelo Echeverri,[b] Berta Gómez-Lor,*[b] José I. Martínez*[b] and M. Carmen Ruiz Delgado*[a]

Received 2nd July 2020,
Accepted 10th September 2020

DOI: 10.1039/d0tc03139a

rsc.li/materials-c

In the present work, we investigate two-dimensional (2D) conjugated polymers based on C_3-symmetric truxene-based cores at the density functional theory (DFT) level. In total, 27 different 2D polymers have been exhaustively studied with the aim to explore the impact of the following effects on the electronic and charge-transport properties: (i) the nature of the conjugated platform, going from electron-rich truxene (**Tx**) and triindole (**Tr**) units to electron-deficient truxenone (**To**) cores, (ii) the spacing of the cores with different bridges, *i.e.*, phenylene (**Ph**) or ethynylene (**A**) units, (iii) the linker position (2,7,12-substitution in the $\mathbf{T_2}$ polymers and 3,8,13-substitution in $\mathbf{T_3}$ polymers), and (iv) the increased number of π-bridges connecting the cores, from three linkers in $\mathbf{T_2}$ and $\mathbf{T_3}$ to six linkers in $\mathbf{T_{2,3}}$. To this end, we have carried out a large battery of DFT calculations on fragments extracted from the 2D polymers (dimers and trimers) as well as on the corresponding periodic 2D structures (infinite monolayers and self-assembled monolayers) using periodic boundary conditions. Our results show that simultaneous manipulation of the pore surface size and band-gap engineering together with charge-transport parameters can be achieved in these truxene-based 2D polymers by fine-tuning their structural features. The contributions of this study to the overall understanding of the structure–electronic property relationships of these semiconducting polymers and its correlation with available experimental work are highlighted. Our results provide interesting guidelines to design novel 2D materials with applications ranging from sensing to photocatalysis or electronics.

Introduction

After three decades of enormous research effort, the field of organic semiconductors is currently a mature workbench that has already reached the market.[1–3] Advances in this area have been closely related to the continuous improvement in the ability of organic semiconductors to transport charge carriers (holes or electrons), which is quantified by their charge carrier mobility μ. While the highest mobilities are usually observed in crystalline or liquid crystalline materials, in the pursuit of an optimal balance between mobility and processability, semiconducting polymers are the preferred candidates.[4] These materials are usually constituted by conjugated one-dimensional (1D) chains and offer continuous electronic delocalization along the chain axis, and favor the efficient one-dimensional migration of charge carriers. However, hopping of charge carriers between chains is significantly hindered, thus resulting in slow down.

Expanding the π-conjugation has emerged as an efficient strategy to address the aforementioned drawback; this expansion permits the achievement of equally efficient electron delocalization in two dimension (2D) or three dimension (3D). This possibility has focused increasing attention on 2D organic polymers as semiconducting materials with enhanced transport dimensionality.[5]

2D covalent organic frameworks (COFs) are porous crystalline solids obtained by the polymerization of organic building blocks functionalized with reactive groups that predetermine their growth along two or more directions through dynamic covalent chemistry.[6,7] This design strategy gives rise to well-defined, high-surface-area materials whose final properties, topologies and porosities can be conveniently tuned by the choice of monomers and linking groups and by the position of the reactive groups, which determines the growth direction.

[a] Department of Physical Chemistry, University of Malaga, Campus de Teatinos s/n, 29071, Malaga, Spain. E-mail: carmenrd@uma.es
[b] Instituto de Ciencia de Materiales de Madrid, CSIC. C/Sor Juana Inés de la Cruz 3, Cantoblanco, Madrid 28049, Spain. E-mail: bgl@icmm.csic.es, joseignacio.martinez@icmm.csic.es

† Electronic supplementary information (ESI) available: Theoretical methods and computational details; chemical structures of the molecular fragments studied theoretically and Study of 2D conjugated polymer networks. See DOI: 10.1039/d0tc03139a

Journal of
Materials Chemistry C
Materials for optical, magnetic and electronic devices
Accepted Manuscript

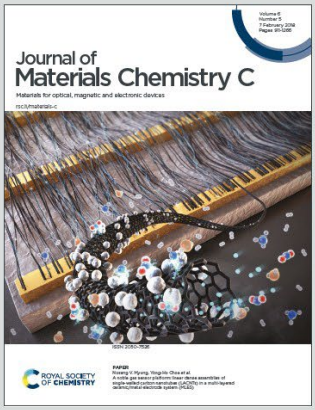

ROYAL SOCIETY OF CHEMISTRY

rsc.li/materials-c

- Other publications related with the Thesis:

8. Wang, D.; Capel Ferron, C.; Li, J.; **Gámez-Valenzuela, S.**; Ponce Ortiz, R.; Lopez Navarrete, J. T.; Hernandez Jolin, V.; Yang, X.; Pena Alvarez, M.; Garcia Baonza, V.; Hartl, F.; Ruiz Delgado, M. C.; Li, H., New Multiresponsive Chromic Soft Materials: Dynamic Interconversion of Short 2, 7-Dicyanomethylenecarbazole-Based Biradicaloid and the Corresponding Cyclophane Tetramer. Chemistry–A European Journal **2017**, 23, (55), 13776-13783.

9. Benincori, T.; **Gámez-Valenzuela, S.**; Goll, M.; Bruchlos, K.; Malacrida, C.; Arnaboldi, S.; Mussini, P. R.; Panigati, M.; Navarrete, J. T. L.; Delgado, M. C. R., Electrochemical studies of a new, low-band gap inherently chiral ethylenedioxythiophene-based oligothiophene. Electrochimica Acta **2018**, 284, 513-525.

10. Malacrida, C.; Habibi, A. H.; **Gámez-Valenzuela, S.**; Lenko, I.; Marqués, P. S.; Labrunie, A.; Grolleau, J.; López Navarrete, J. T.; Ruiz Delgado, M. C.; Cabanetos, C.; Blanchard, P.; Ludwigs, S., Impact of the Replacement of a Triphenylamine by a Diphenylmethylamine Unit on the Electrochemical Behavior of Pentaerythritol-Based Push-Pull Tetramers. ChemElectroChem **2019**, 6, (16), 4215-4228.

11. Rothe, C.; Neusser, D.; Hoppe, N.; Dirnberger, K.; Vogel, W.; **Gámez-Valenzuela, S.**; Navarrete, J. T. L.; Villacampa, B.; Berroth, M.; Delgado, M. C. R., Push–pull thiophene chromophores for electro-optic applications: from 1D linear to β-branched structures. Physical Chemistry Chemical Physics **2020**, 22, (4), 2283-2294.

12. Echeverri, M.; Ruiz, C.; **Gámez-Valenzuela, S.**; Martín, I.; Ruiz Delgado, M. C.; Gutiérrez-Puebla, E.; Monge, M. Á.; Aguirre-Díaz, L. M.; Gómez-Lor, B., Untangling the Mechanochromic Properties of Benzothiadiazole-Based Luminescent Polymorphs through Supramolecular Organic Framework Topology. Journal of the American Chemical Society **2020**, 142, (40), 17147-17155.

13. Echeverri, M.; Ruiz, C.; **Gámez-Valenzuela, S.**; Alonso-Navarro, M.; Gutierrez-Puebla, E.; Serrano, J. L.; Ruiz Delgado, M. C.; Gómez-Lor, B., Stimuli-Responsive Benzothiadiazole Derivative as a Dopant for Rewritable Polymer Blends. ACS Applied Materials & Interfaces **2020**, 12, (9), 10929-10937.

14. Malacrida, C.; Lu, Y.; Dirnberger, K.; **Gámez-Valenzuela, S.**; Ruiz Delgado, M. C.; Ludwigs, S., Towards highly conducting bicarbazole redox polymer films with plateau-like conductivities. Journal of Materials Chemistry C **2020**, 8, (43), 15393-15405.

15. **Gámez-Valenzuela, S.**; Alonso, J. A.; Santoro, G.; Martínez, J. I., Structure, stability, and optical absorption spectra of small TinCx clusters: a first-principles approach. Monthly Notices of the Royal Astronomical Society **2021**, 508, (4), 5074-5091.

16. **Gámez-Valenzuela, S.**; Neusser, D.; Benitez-Martin, C.; Najera, F.; Guadix, J. A.; Moreno-Yruela, C.; Villacampa, B.; Ponce Ortiz, R.; Ludwigs, S.; Andreu, R.; Ruiz Delgado, M. C., V-shaped pyranylidene/triphenylamine-based chromophores with enhanced photophysical, electrochemical and nonlinear optical properties. Materials Advances **2021**, 2, (13), 4255-4263.

17. Liu, B.; Wang, Y.; Sun, H.; **Gámez-Valenzuela, S.**; Yan, Z.; Feng, K.; Uddin, M. A.; Koh, C.; Zhou, X.; López Navarrete, J. T.; Ruiz Delgado, M. C.; Meng, H.; Niu, L.; Woo, H. Y.; Ponce Ortiz, R.; Guo, X., Backbone Configuration and Electronic Property Tuning of Imide-Functionalized Ladder-Type Heteroarenes-Based Polymer Acceptors for Efficient All-Polymer Solar Cells. Advanced Functional Materials **2022**, 32, (21), 2200065.

ChemPubSoc Europe

DOI: 10.1002/chem.201702659

CHEMISTRY A European Journal Full Paper

Biradicals

New Multiresponsive Chromic Soft Materials: Dynamic Interconversion of Short 2,7-Dicyanomethylenecarbazole-Based Biradicaloid and the Corresponding Cyclophane Tetramer

Deliang Wang,[a] Cristina Capel Ferrón,[b] Jie Li,[a] Sergio Gámez-Valenzuela,[b] Rocio Ponce Ortiz,[b] Juan T. López Navarrete,[b] Víctor Hernández Jolín,[b] Xiaodi Yang,[c] Miriam Peña Álvarez,[d] Valentín García Baonza,[d] František Hartl,*[e] M. Carmen Ruiz Delgado,*[b] and Hongxiang Li*[a]

Abstract: This work reports on a quinodimethane-type molecule, 2,7-dicyanomethylene-9-(2-ethylhexyl)carbazole (**1**), one of the shortest π-conjugated biradicaloids reported to be stable in solution under ambient conditions. This carbazole-based quinoidal precursor is able to form a macrocyclic σ-bonded tetramer (**2**). The resolved single-crystal X-ray structure of tetramer **2** shows that four molecules of **1** are linked together through four long $(CN)_2C–C(CN)_2$ bonds (1.631 Å) resulting from coupling of the unpaired electrons in biradicaloid **1**. Dynamic interconversion between monomer **1** and cyclophane tetramer **2** is achieved by reversible cleavage and recovery of the four $(CN)_2C–C(CN)_2$ bonds upon soft external stimuli (light absorption, temperature and pressure), which is accompanied by significant color changes. These novel photo-, thermo-, and mechanochromic properties expand the versatility of π-conjugated biradicaloid compounds as novel functional materials that, in combination with spin chemistry and dynamic covalent chemistry, can be relevant in molecular machines, sensors, and switches.

Introduction

π-Conjugated biradical compounds, featuring unique unsaturated valences and radical centers in the ground state, are fundamentally important for understanding the nature of chemical bonds and the fundamental physical and chemical properties of π-conjugated molecules, and have potential applications in material science.[1–3] However, most of the π-conjugated biradical compounds exhibit high reactivity, easily decomposing or polymerizing under ambient experimental conditions, which preclude the investigation of their properties and applications. Recently, significant progress has been achieved in this field, as some stable π-conjugated biradicals were prepared through increasing the conjugation length and/or introducing bulky substituents at the radical centers.[4–11]

Nonetheless, π-conjugated biradicals existing under ambient conditions are still scarce. Therefore, rational design and facile syntheses of novel stable biradical, or significantly spin–spin interacting biradicaloid compounds to explore their bonding situation, physical properties, and pertinent applicability, constitute a longstanding prominent challenge. Note that the stability of the biradicaloid compounds depends on which of the resonant structures, the open-shell biradical or the closed-shell quinoidal form, contributes more to the ground state structure.

Dynamic covalent chemistry (DCC) has attracted great attention because it provides an efficient strategy to prepare complex assemblies.[12,13] The building block that can dynamically form covalent bonds is the key for the success of DCC. π-Conjugated mono- and biradicals are potential building blocks in DDC because they can selectively construct macrocyclic or staircase oligomers or polymers by self-assembly processes. For instance, triphenylamine and carbazole units substituted with dicyanomethyl radicals have been reported to form mac-

[a] D. Wang, J. Li, Prof. H. Li
Key Laboratory of Synthetic and Self-assembly Chemistry for Organic Functional Materials, Shanghai Institute of Organic Chemistry
Chinese Academy of Sciences, No. 345 Lingling Rd.
Shanghai, 200032 (P. R. China)
E-mail: lhx@mail.sioc.ac.cn

[b] Dr. C. Capel Ferrón, S. Gámez-Valenzuela, Dr. R. Ponce Ortiz, Prof. J. T. López Navarrete, Prof. V. Hernández Jolín, Prof. M. C. Ruiz Delgado
Department of Physical Chemistry, University of Malaga
Campus de Teatinos s/n, 229071, Malaga (Spain)
E-mail: carmenrd@uma.es

[c] Prof. X. Yang
Laboratory of Advanced Materials, Fudan University
No. 200 Handan Rd., Shanghai, 200438 (P. R. China)

[d] Dr. M. Peña Álvarez, Prof. V. García Baonza
MALTA-Consolider Team, Department of Physical Chemistry
Complutense University of Madrid, 28040 Madrid (Spain)

[e] Prof. F. Hartl
Department of Chemistry, University of Reading
Whiteknights, Reading RG6 6AD (UK)
E-mail: f.hartl@reading.ac.uk

Supporting information (including full experimental details, absorption spectra, Raman spectra, DFT calculations, and X-ray analysis data) and the ORCID identification numbers for the authors of this article can be found under https://doi.org/10.1002/chem.201702659.

Electrochimica Acta 284 (2018) 513–525

Contents lists available at ScienceDirect

Electrochimica Acta

journal homepage: www.elsevier.com/locate/electacta

Electrochemical studies of a new, low-band gap inherently chiral ethylenedioxythiophene-based oligothiophene

Tiziana Benincori [a], Sergio Gámez-Valenzuela [b], Miriam Goll [c], Kirsten Bruchlos [c], Claudia Malacrida [c], Serena Arnaboldi [d], Patrizia Romana Mussini [d], Monica Panigati [d, e], Juan T. López Navarrete [b], M. Carmen Ruiz Delgado [b, **], Giulio Appoloni [a, ***], Sabine Ludwigs [c, *]

[a] Dipartimento di Scienza e Alta Tecnologia, Università degli Studi dell'Insubria, Via Valleggio 11, 22100 Como, Italy
[b] Department of Physical Chemistry, University of Málaga, 29071 Málaga, Spain
[c] IPOC-Functional Polymers, Institute of Polymer Chemistry, University of Stuttgart, Pfaffenwaldring 55, 70569 Stuttgart, Germany
[d] Dipartimento di Chimica, Università degli Studi di Milano, Via Golgi 19, 20133 Milano, Italy
[e] Istituto per lo Studio delle Macromolecole, Consiglio Nazionale delle Ricerche (ISMAC-CNR), Via E. Bassini 15, 20133 Milano, Italy

ARTICLE INFO

Article history:
Received 16 March 2018
Received in revised form
19 July 2018
Accepted 20 July 2018
Available online 24 July 2018

Keywords:
Low-band gap monomer
bisEDOT
Self-rigidification
Cyclic oligomers
Mixed valence conductivity

ABSTRACT

In the present paper, the synthesis and characterization of 2,2′-bis{bi[2,2′-(3,4-ethylenedioxy)thiophen-5-yl]}-3,3′-bithianaphthene, nicknamed BT_2E_4, is reported. We show that electrooligomerization of BT_2E_4 leads to electroactive films which are evaluated by cyclic voltammetry (CV), UV/vis spectroelectrochemistry and CV coupled with *in-situ* conductance measurements. Direct comparisons to the properties of the oligomers obtained from the atropisomeric all-thiophene analogue BT_2T_4 show that the introduction of EDOT leads to a strong reduction of the band-gap, an overall red-shifted absorption spectrum and a rigidification of the structure. Finally, DFT and TD-DFT calculations were performed in parallel to investigate and to compare the electronic and molecular structures of neutral and charged monomer and oligomer species.

1. Introduction

Since the discovery of organic semiconductors, polythiophenes have been deeply investigated and frequently used in organic electronic devices as active components. They have been principally employed as electron-donor layers in light-emitting diodes (OLEDs), field-effect transistors (OFETs) and bulk heterojunction organic solar cells (BHJSC).

The most popular materials are poly-(3,4-ethylenedioxythiophene) (PEDOT) [1–5] and regioregular poly-(3-hexylthiophene) (P3HT) [6,7,43], which are, at least for the moment, the sole examples of commercially available thiophene-based materials on large scale.

In parallel to the development of polythiophene materials, Garnier [8,9] demonstrated in 1989 that also shorter oligomers, such as α-sexithiophene, can act as active semiconductor organic layers in transistor devices.

Some years ago, we synthesized the 2,2′-bis(2,2′-bithiophene-5-yl)-3,3′-bithianaphthene (**1**), nicknamed BT_2T_4, a new, non-planar, intrinsically chiral sexithiophene, which was chemically or electrochemically oxidized to give well organized electroactive films characterized by perfect regio- and stereo-regularity [10].

BT_2T_4 represents the first member of a new class of chiral oligothiophenes structurally different from those described in literature where the stereogenic elements responsible for monomer and, consequently, polymer chirality, are stereogenic centres, external to the polyconjugated electroactive backbone [11]. Furthermore, only few examples of chiral electroactive materials derived from the electrodeposition of EDOT monomers functionalized with side chains including carbon stereogenic centres are known in literature [12,13].

The racemate of BT_2T_4 was resolved through chiral HPLC into

* Corresponding author.
** Corresponding author.
*** Corresponding author.
E-mail addresses: tiziana.benincori@uninsubria.it (T. Benincori), carmenrd@uma.es (M.C. Ruiz Delgado), sabine.ludwigs@ipoc.uni-stuttgart.de (S. Ludwigs).

https://doi.org/10.1016/j.electacta.2018.07.147
0013-4686/

PCCP

ROYAL SOCIETY OF CHEMISTRY

PAPER

View Article Online
View Journal | View Issue

Cite this: *Phys. Chem. Chem. Phys.*, 2020, **22**, 2283

Push–pull thiophene chromophores for electro-optic applications: from 1D linear to β-branched structures†

Christian Rothe,[a] David Neusser,[a] Niklas Hoppe,[b] Klaus Dirnberger,[a] Wolfgang Vogel,[b] Sergio Gámez-Valenzuela,[c] Juan T. López Navarrete,[c] Belén Villacampa,[d] Manfred Berroth,[b] M. Carmen Ruiz Delgado *[c] and Sabine Ludwigs *[a]

Received 16th October 2019,
Accepted 30th December 2019

DOI: 10.1039/c9cp05640h

rsc.li/pccp

We report the synthesis and characterization of a novel series of push–pull chromophores bearing 1D linear and β-branched thiophenes as π-conjugated spacers between a 2,2,4,7-tetramethyl-1,2,3,4-tetrahydroquinoline electron donor unit and dicyano- and tricyanovinylene electron acceptor groups. The effect of the introduction of β-thiophenes on the linear and nonlinear (NLO) optical properties as well as electrochemical and thermal data is studied in detail by performing a comparative study between the branched and 1D linear systems. In addition, a parallel DFT computational study is used to evaluate structure–property relationships. The non-linear optical behavior of the molecules both in solution and in solid state as electro-optic (EO) films using a guest–host approach shows very promising performance for electro-optic applications with high molecular first hyperpolarizabilities ($\mu\beta$) of 4840 × 10^{-48} esu and electro-optic coefficients r_{33} reaching 650 pm V^{-1}. One highlight is that the electro-optic films of the β-branched chromophores are superior in terms of thermal stability in device operation as measured by a transmissive modified reflective Teng-Man method. This work provides guidelines for the design of improved electro-optic materials including β-branched chromophores which could be useful for practical EO applications, where both enhanced β and r_{33} values together with chemical and thermal stability are necessary.

Introduction

The substantial demand for higher data rates[1] and thus the need in the domain of communications for more potent photonic devices such as frequency converters, modulators or optical switches has led to strong research activities during the past years. Meanwhile, devices including electro-optic (EO) components which are based on non-linear optical (NLO) materials and films are used for modern optical transmitters. As alternative to the classically used lithium niobate modulators, organic compounds have found their way into so-called silicon-organic hybrid (SOH) approaches where an integrated silicon photonics platform is combined with electro-optic organic films.[2] Modulator-bandwidths of up to 500 GHz have been demonstrated recently.[3] In the SOH platform the EO-films are mainly prepared using a guest–host approach, which means that organic compounds with a highly asymmetric structure and high dipole moment are macroscopically oriented in polymer matrices (such as poly(methylmethacrylate)) by electric field poling.[4] SOH-modulators provide high interaction of the optical signal with the electro-optic film, typically using the Pockels effect. The molecular first hyperpolarizability β of the chromophore is the main physical quantity for the Pockels effect on the molecular scale, which allows a change in the refractive index Δn of the materials by application of weak external electric fields.[5] The electro-optic coefficient r_{33} is the most specific characteristic parameter of the poled EO-film and can be measured by the Teng-Man method,[6] which gives the bulk coefficient of the material. In SOH devices, the result may be different for the same material due to the thin films and sub-micron structures.

[a] *IPOC-Functional Polymers, Institute of Polymer Chemistry, University of Stuttgart, Pfaffenwaldring 55, 70569 Stuttgart, Germany. E-mail: sabine.ludwigs@ipoc.uni-stuttgart.de*
[b] *Institute of Electrical and Optical Communications Engineering, University of Stuttgart, Pfaffenwaldring 47, 70569 Stuttgart, Germany*
[c] *Department of Physical Chemistry, University of Málaga, 29071 Málaga, Spain. E-mail: carmenrd@uma.es*
[d] *Departamento de Física de la Materia Condensada, Escuela de Ingeniería y Arquitectura – Universidad de Zaragoza, C/María de Luna, 3, 50018, Zaragoza, Spain*

† Electronic supplementary information (ESI) available: Synthetic details, thermal properties; experimental absorption maxima of all cromophores in different solvents; cyclic voltammograms and differential-pulsed cyclovoltammograms; details of DFT-calculations; experimental and calculated nonlinear optical properties of all chromophores; details of NLO-measurements (PDF). See DOI: 10.1039/c9cp05640h

ChemPubSoc Europe

DOI: 10.1002/celc.201900565

CHEMELECTROCHEM Articles

Impact of the Replacement of a Triphenylamine by a Diphenylmethylamine Unit on the Electrochemical Behavior of Pentaerythritol-Based Push-Pull Tetramers

Claudia Malacrida,[a] Amir Hossein Habibi,[b] Sergio Gámez-Valenzuela,[c] Illia Lenko,[b] Pablo Simón Marqués,[b] Antoine Labrunie,[b] Jérémie Grolleau,[b] Juan T. López Navarrete,[c] M. Carmen Ruiz Delgado,[c] Clément Cabanetos,*[b] Philippe Blanchard,*[b] and Sabine Ludwigs*[a]

The synthesis of a tetra-functionalized pentaerythritol core decorated with *N*-methyl-*N*,*N*-diphenylamine-based push-pull chromophores and its electropolymerization to 3D push-pull networks are described. The electrochemical and absorption behaviors of the tetramer are compared with the one of two reference linear push-pull compounds, carrying triphenylamine (TPA) or methyldiphenylamine (MeDPA) donor groups, a thienyl linker and a dicyanovinyl acceptor group (DCV). We found that substituting the outer phenyl with a methyl group causes important differences in the radical cation stability, such that MeDPA chromophore generates stable dimers and TPA is reversibly oxidized. Interestingly, DFT calculations suggest that steric hindrance and electrostatic interactions dominate the radical cation reactivity.

1. Introduction

Triphenylamine (TPA) and more generally arylamine derivatives, constitute outstanding building blocks for the preparation of electroactive materials for opto-electronic applications.[1–3] In particular, D-π-A push-pull molecules, in which the electron-donating group (D) derived from an arylamine is connected to an electron-withdrawing group (A) through a π-conjugated spacer, have been extensively investigated as efficient donor materials for organic photovoltaics (OPV)[4–10] and electro-optical applications.[11,12] On the other hand, arylamine derivatives may exhibit a peculiar electrochemical behavior resulting in the molecule dimerization triggered by their chemical oxidation.[13–16] The electrochemically generated electroactive benzidine-based dimers, endowed with a biphenyl bond, are also generally soluble and diffuse from the working electrode to the electrolyte solution.[17] Electropolymerizable arylamine containing monomers can be achieved by exploiting the dimerization ability of two or more unsubstituted arylamine units connected to a central core, for example in star-bust or multimeric systems. Different examples of electropolymerization of arylamine derivatives to produce modified electrodes are indeed reported in the literature,[18–23] and have shown promising results when employed as electroactive polymer layers in electrochromic devices.[20–24] Another attractive approach for the obtainment of functionalized triarylamine electroactive surface, as an alternative to electrodeposition from monomer solution, exploits the dimerizing ability of arylamine units just in a post deposition step of pre-deposited films. In this case the triarylamine unit is present for example as a redox-active pendant covalently bound to a polymer backbone, acting as a cross-linker unit upon oxidative triggering, and generating polymer films crosslinked with redox-active tetraphenylbenzidine (TPB) moieties.[1,25–27]

While the redox behavior of simple arylamines upon oxidation is known and well-characterized, their functionalization by π-conjugated blocks, such as in the case of D-π-A push-pull molecules, results in an enhanced charge delocalization of the radical-cation species that might lead to a different electrochemical behavior. In this general context, we previously showed that the simple and synthetically accessible TPA-based push-pull molecule **1** (2-((5-(4-(diphenylamino)phenyl)thiophen-2-yl)methylene)malononitrile) (Scheme 1) exhibited good absorption properties in the visible spectrum and interesting photovoltaic properties as donor material combined with C_{60}[10,28,29] or its soluble analogue [6,6]-phenyl-C_{61}-butyric acid methyl ester ($PC_{61}BM$) as acceptors.[30] More recently, following a "multimer" approach, the related pentaerythritol based push-pull tetramer **Tetra-1** was shown to give promising and higher power conversion efficiencies (*PCEs*) when blended with $PC_{71}BM$ in bulk heterojunction solar cells.[31] In addition, the substitution of one terminal phenyl ring of the TPA unit of molecule **1** by a methyl group affording **2** (2-((5-(4-(methyl(phenyl)amino)phenyl)thiophen-2-yl)methylene)malononitrile), induced a 50-

[a] C. Malacrida, Prof. S. Ludwigs
IPOC-Functional Polymers, Institute of Polymer Chemistry, University of Stuttgart, Pfaffenwaldring 55, 70569 Stuttgart, Germany
E-mail: sabine.ludwigs@ipoc.uni-stuttgart.de
[b] A. H. Habibi, I. Lenko, P. S. Marqués, A. Labrunie, J. Grolleau, C. Cabanetos, P. Blanchard
MOLTECH-Anjou, UMR 6200, UNIV Angers, CNRS, 2 bd Lavoisier, 49045 ANGERS Cedex, France
E-mail: clement.cabanetos@univ-angers.fr
philippe.blanchard@univ-angers.fr
[c] S. Gámez-Valenzuela, J. T. López Navarrete, M. C. Ruiz Delgado
Department of Physical Chemistry, University of Málaga, 29071 Málaga, Spain

Supporting information for this article is available on the WWW under https://doi.org/10.1002/celc.201900565

An invited contribution to a Special Issue on Organic Electrosynthesis.

JACS
JOURNAL OF THE AMERICAN CHEMICAL SOCIETY
pubs.acs.org/JACS
Article

Untangling the Mechanochromic Properties of Benzothiadiazole-Based Luminescent Polymorphs through Supramolecular Organic Framework Topology

Marcelo Echeverri, Constanza Ruiz, Sergio Gámez-Valenzuela, Irene Martín, M. Carmen Ruiz Delgado, Enrique Gutiérrez-Puebla, M. Ángeles Monge, Lina M. Aguirre-Díaz,* and Berta Gómez-Lor*

Cite This: J. Am. Chem. Soc. 2020, 142, 17147−17155
Read Online

ABSTRACT: Two new luminophore polymorphs of 4-bromo-7-(4-nonylphenyl)benzo[*c*][1,2,5]thiadiazole (**1α** and **1β**) exhibiting different color emissions, which switch into each other in response to shear force and solvent vapors, are presented and their X-ray structure is determined. Supramolecular organic framework topology (SOFT) studies on the two polymorphic structures led us to conclude that the mechanochromic phase transformation can be explained on the basis of modifications in their respective topological nets: **mab** and **pcu** for **1α** and **1β**, respectively, as a result of the breaking and restoration of a number of weak supramolecular interactions. The color changes accompanying this transformation have been rationalized with the help of time-dependent density functional theory. We firmly believe that our findings will inspire future research on the design of novel stimuli-responsive organic materials with switchable properties based on their supramolecular interactions by establishing clear SOFT-property relationships.

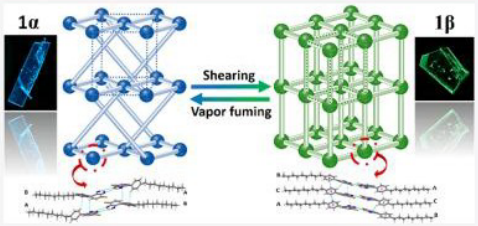

INTRODUCTION

Mechanochromic materials, possessing solid-state light-emitting properties that vary upon mechanical grinding or pressing, arouse much interest in recording or sensing applications that involve luminescent detection. A number of metal complexes and purely organic compounds have been found to exhibit this interesting phenomenon;[1−6] however, only in a few of them is the underlying mechanism properly understood, despite the obvious importance of such knowledge in the development of new mechanochromic compounds. In this context, the emission switching between polymorphs is especially interesting.[7−15] By allowing the understanding of how molecules are self-associated in the solid state through a deep supramolecular analysis, we can use single crystals to help us realize how intermolecular interactions operate among each other, either separately or cooperatively, thus providing accurate information on the key factors that govern the correspondig solid-state light-emitting properties.[6,16−19] Unfortunately, although several mechanochromic luminophores have been reported to date, in most examples crystal-to-amorphous transitions originate in the differences of color observed.

Topological analysis of crystalline structures provide an excellent tool to assess the origin of intermolecular interactions operating in crystals. The construction of a topological net is carried out considering the initial geometrical data, as well as the chemically relevant interactions of the material under study; so, as the reliability of the information increases, the resulting net can be the strongest topological reference for the structure.[20] To date, topological analysis has been extensively applied to simplify complex inorganic and hybrid covalent and supramolecular frameworks,[21−24] but its application to purely organic crystals is only very incipient.[25−28] On the other hand, although previous work has already unveiled the line from spectroscopy to property passing through synthon and crystal structure recognition within synthons,[29−31] the use of topological analysis to explain in a simple manner the correlation between the supramolecular framework and the physical properties for a specific system has not yet been realized.

Chalcogen bondings, that is, the interaction between group VI elements (O, S, Se, Te, and Po) and a Lewis-base partner atom,[32] has emerged as a key motif for controling supramolecular frameworks growth. The close contact of chalcogens and oxygen or nitrogen atoms is observed in many organic crystals, where this interaction enhances the intermolecular ordering and play important roles in determining the

Received: July 27, 2020
Published: September 11, 2020

https://dx.doi.org/10.1021/jacs.0c08059
J. Am. Chem. Soc. 2020, 142, 17147−17155

ACS APPLIED MATERIALS & INTERFACES

www.acsami.org Research Article

Stimuli-Responsive Benzothiadiazole Derivative as a Dopant for Rewritable Polymer Blends

Marcelo Echeverri, Constanza Ruiz, Sergio Gámez-Valenzuela, Matias Alonso-Navarro, Enrique Gutierrez-Puebla, José L. Serrano, M. Carmen Ruiz Delgado,* and Berta Gómez-Lor*

Cite This: ACS Appl. Mater. Interfaces 2020, 12, 10929−10937 Read Online

ACCESS | Metrics & More | Article Recommendations | Supporting Information

ABSTRACT: A new rod-shaped benzothiadiazole fluorophore, namely, 4,7-di-(4-nonylphenyl)benzo[*c*][1,2,5]thiadiazole, which strongly emits fluorescence both in solution and in solid state has been synthesized, and its photophysical properties were rationalized with the help of density functional theory calculations. This molecule crystallizes in two distinct light-emitting crystalline phases, which can be interconverted in response to pressure, temperature, and solvent vapors. Powder X-ray diffraction indicates that in both polymorph, molecules adopt a lamellar packing, the different interlayer spacing being the main difference between the two structures. Single-crystal analysis of one of the polymorphs allows us to identify weak interaction planes, which presumably facilitates the polymorphic transformation through mechanically or thermally induced sliding processes. The polymorphic transformation and the origin of the switchable fluorescence have been rationalized through a spectroscopic and theoretical study. This study suggests that the different colors observed are due to different intermolecular aromatic interactions owing to the displacement of the molecules with respect to the layer normal. Interestingly, blending this molecule with a biodegradable polymer such as poly(vinyl alcohol) gives rise to a thermally activated reversible switchable fluorescent system, which entitles this material as an attractive candidate for technological applications, such as thermal sensors, security inks, or rewritable paper.

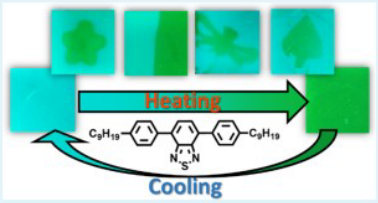

KEYWORDS: *mechanochromism, thermochromism, fluorescence, polymorphism, benzothiadiazole, phase transformation*

INTRODUCTION

Smart materials which switch their optical spectroscopic properties (i.e., color and fluorescence) upon physical external stimulation (i.e., pressure and temperature) arouse enormous interest and have found applications in fields such as sensing,[1,2] construction,[3,4] recording,[5,6] display technologies,[7,8] or rewritable paper.[9,10] Although highly efficient inorganic and metal-based chromogenic and fluorogenic materials[5,11−13] have been developed, the enormous structural diversity of organic chromophores and fluorophores gives these materials a privileged place in the area.[1−3,14,15] Particularly, the ready tunability of their optical properties together with their high compatibility with different flexible substrates makes these materials especially interesting for technological applications.

In the quest for efficient chromogenic compounds, benzothiadiazole (BTD) has emerged as an attractive moiety. This electron-deficient heterocycle presents high fluorescence quantum efficiencies both in solution and in solid state, properties that have been utilized for applications such as organic electronics[16,17] and bioimaging.[18,19] Recently, some BTD-based compounds that switch their emission color upon mechanical stress or thermal stimuli have been reported,[20−27] but in most of them, the origin of the color transformation is crystal to-amorphous transition. This fact prevents an in-depth study of the mechanism behind this process and limits the rational development of new chromophores with predesigned properties.

Herein, we present a new BTD derivative, namely, 4,7-di-(4-nonylphenyl)benzo[*c*][1,2,5]thiadiazole, which crystallize as a mixture of a blue-emitting (polymorph A) and green-emitting polymorph (polymorph B). Polymorph A can be readily converted to polymorph B in response to external stimuli (pressure and temperature). Vapor fuming provides the opposite transformation probably because of a solution recrystallization process to form the metastable phase. Interestingly, heating above the melting temperature of both polymorphs gives rise to a smectic mesophase (SmA) that upon cooling yields only polymorph B.

In this molecule, the BTD moiety is flanked by two phenyl groups substituted with long flexible chains, which make the assembly of these molecules into layers possible, as could be confirmed by single-crystal analysis of one of the two polymorphs. A combined spectroscopic and theoretical study has been performed in order to get an insight into the

Received: November 21, 2019
Accepted: February 11, 2020
Published: February 11, 2020

https://dx.doi.org/10.1021/acsami.9b21209
ACS Appl. Mater. Interfaces 2020, 12, 10929−10937

Journal of Materials Chemistry C

ROYAL SOCIETY OF CHEMISTRY

PAPER

View Article Online
View Journal

Cite this: DOI: 10.1039/d0tc03090b

Towards highly conducting bicarbazole redox polymer films with plateau-like conductivities†

Claudia Malacrida,[a] Yushi Lu,[a] Klaus Dirnberger,[a] Sergio Gámez-Valenzuela,[b] M. Carmen Ruiz Delgado [b] and Sabine Ludwigs *[a]

Chemical doping of redox polymer films based on triphenylamine (PVTPA), phenylcarbazole (PVPhCbz) and carbazole (PVCbz) pendant redox units is performed with different concentrations of $FeCl_3$ solutions. Analogies to *in situ* electrochemical doping show that stable crosslinked dimer containing redox polymer films are created. The conductivity behavior of the doped films is analyzed and the charge carrier species are identified by UV-Vis-NIR spectroscopy. In particular the behavior of PVCbz upon doping is unique: transparent films with conductivities as high as 2×10^{-2} S cm^{-1} are found over a large range of $FeCl_3$ concentrations. Such plateau-like conductivity – also encountered upon electrochemical doping – is a phenomenon, usually only found for conjugated polymers such as poly(3-hexylthiophene). PVTPA and PVPhCbz on the other hand show bell-shape behavior with maximum conductivities reaching 10^{-3} S cm^{-1} for a limited range of dopant concentrations. The stability (induced by crosslinking) and the transparency make the layers applicable as transparent electrodes or hole-transport layers in opto-electronic devices. The observed results are discussed in the context of mixed valence conductivity with high conductivities only accessible when a certain amount of dications coexists with radical cation species. While PVTPA and PVPhCbz follow the classical findings of the model, a favorable π-stacking tendency of bicarbazole dimers seems to strongly improve efficient communication between the redox sites in the three dimensionally connected redox polymer films. Our results indicate that the nature of charge propagation of redox and conjugated polymers is closer than usually discussed in the literature which can be mainly attributed to intermolecular interactions throughout the films. Last but not least we want to highlight the strength of *in situ* electrochemical techniques to identify charged species and potential-dependent conductivity regions which help targeting optimized chemical doping.

Received 30th June 2020,
Accepted 3rd September 2020

DOI: 10.1039/d0tc03090b

rsc.li/materials-c

Introduction

The intrinsic electronic conductivity upon chemical and electrochemical doping combined with their solution processability, lightweight and synthetic versatility has made conducting polymers very appealing candidates in a wide number of applications including thermoelectric devices, transparent electrodes as well as in energy storage applications.[1–5]

Based on the nature of charge propagation conducting polymers can be subdivided into two main groups, namely redox and conjugated polymers.[6] In the case of redox polymers, electronic conductivity is sustained by electron hopping, which is essentially an electron exchange reaction between localized redox active units, whereas for conjugated polymers the motion of delocalized electrons occurs in intra and inter conjugated chains. Mechanisms of conductivity, and in particular, correlations with the redox state of the polymers have been the subject of studies since decades;[7,8] a useful technique for this purpose, with Murray[9,10] and Zotti[11] as pioneers, is *in situ* conductance coupled to cyclic voltammetry. Despite several studies in the literature,[7,8,12] a general mechanism for describing the potential-dependent conductivity behavior of conducting polymers has not yet been found. A mixed-valence conductivity model can be successfully employed for describing the conductivity profile of pure redox systems which is typically characterized by narrow potential regions of conductivity with a characteristic peak or bell-shape.[7,8,10,13,14] Experimentally it remains non-trivial to find the optimum doping level to reach maximum conductivities, furthermore conductivities typically remain rather low.[8]

Conjugated systems such as poly(3-hexylthiophene) and poly(ethylenedioxythiophene) are on the other hand characterized

[a] IPOC-Functional Polymers, Institute of Polymer Chemistry, University of Stuttgart, Pfaffenwaldring 55, 70569 Stuttgart, Germany. E-mail: sabine.ludwigs@ipoc.uni-stuttgart.de
[b] Department of Physical Chemistry, University of Málaga, 29071 Málaga, Spain

† Electronic supplementary information (ESI) available. See DOI: 10.1039/d0tc03090b

Monthly Notices of the ROYAL ASTRONOMICAL SOCIETY

MNRAS **508,** 5074–5091 (2021) https://doi.org/10.1093/mnras/stab2735
Advance Access publication 2021 September 24

Structure, stability, and optical absorption spectra of small $Ti_n C_x$ clusters: a first-principles approach

Sergio Gámez-Valenzuela,[1] Julio A. Alonso [2], Gonzalo Santoro [3] and José I. Martínez [3]★

[1] *Department of Physical Chemistry, University of Malaga, Campus de Teatinos s/n, E-29071 Malaga, Spain*
[2] *Department of Theoretical and Atomic Physics and Optics, University of Valladolid, E-47011 Valladolid, Spain*
[3] *ESISNA Group, Institute of Materials Science of Madrid (ICMM-CSIC), E-28049 Madrid, Spain*

Accepted 2021 September 20. Received 2021 August 16; in original form 2021 June 8

ABSTRACT

Titanium carbide molecular clusters are thought to form in the circumstellar envelopes of carbon-rich asymptotic giant branch (AGB) stars but, to date, their detection has remained elusive. To facilitate the astrophysical identification of those clusters in AGB and post-AGB environments, the molecular structures and optical absorption spectra of small Ti_nC_x clusters, with $n = 1$–4 and $x = 1$–4, and some selected larger clusters, Ti_3C_8, Ti_4C_8, Ti_6C_{13}, Ti_7C_{13}, Ti_8C_{12}, Ti_9C_{15}, and $Ti_{13}C_{22}$, have been calculated. The density functional formalism, within the B3LYP approximation for electronic exchange and correlation, was used to find the lowest energy structures. Except the clusters having a single Ti atom, the rest exhibit three-dimensional structures. Those are formed by a Ti fragment surrounded in general by carbon dimers. The optical spectra of Ti_nC_x, computed by time-dependent density functional theory, using the corrected CAM-B3LYP functional, show absorption features in the visible and near-infrared regions which may help in the identification of these clusters in space. In addition, most of the clusters have sizable electric dipole moments, allowing their detection by radioastronomical observations.

Key words: astrochemistry – molecular data – methods: numerical – stars: AGB and post-AGB – stars: carbon – circumstellar matter.

1 INTRODUCTION

Titanium carbide (TiC) dust is predicted to form in the inner regions of the circumstellar envelopes (CSEs) of carbon-rich (C-rich) asymptotic giant branch (AGB) stars (Agúndez et al. 2020). Due to its high refractory nature, TiC is considered to be the first condensate in the atmosphere of C-rich AGBs and may act as seed for the heterogeneous nucleation of dust. The identification of TiC crystals embedded in graphite spherules extracted from the Murchinson meteorite supports this prediction (Bernatowicz et al. 1991, 1996) but, to date, the detection of molecules comprised of titanium and carbon that may serve as precursors for the formation of TiC dust has remained elusive.

In the inner regions of the CSE of AGBs, titanium is in atomic form presenting fairly low abundances. The reaction of Ti with acetylene (C_2H_2) has been suggested as a possible pathway for the formation of stoichiometric TiC molecules (Chigai, Yamamoto & Kozasa 1999; Gail & Sedlmayr 2013), and chemical equilibrium calculations of AGB atmospheres show that the depletion of atomic Ti starts at stellar radii in which most carbon is locked into C_2H_2. However, the predicted abundance of the diatomic molecule TiC is too low and the high stability of large clusters such as Ti_8C_{12}, which might be formed through the reaction of smaller Ti_nC_x clusters, suggests that it is a reasonable candidate as molecular precursor of TiC dust. Indeed, chemical equilibrium calculations show that Ti_8C_{12} replaces atomic Ti as the main Ti reservoir at 2–3 stellar radii (Agúndez et al. 2020).

On the other hand, TiC nanocrystals were suggested as carriers of the 21 μm emission feature in C-rich protoplanetary nebulae (PPNe) (Helden et al. 2000). However, the low abundance of Ti in these environments is not consistent with this carrier (Chigai et al. 2003; Zhang, Jiang & Li 2009) and the possibility of a hydrocarbon-based carrier has been considered instead, although coated TiC grains could circumvent the constrains imposed by the Ti abundance in post-AGB environments (Sloan et al. 2014).

The solid-state phase diagram of the Ti-C alloy (Okamoto 1998) shows a very stable compound centred at $Ti_{55}C_{45}$ with a wide composition range. This compound has a high melting temperature of 3066°C. These features reveal that the formation of strong Ti-C bonds is favourable, and this is also the case for Ti–C nanoclusters, which exhibit highly stable structures at particular stoichiometries.

Three decades ago, by reacting metal vapours with hydrocarbons, Castleman and coworkers discovered a class of highly stable cage-like clusters with formula M_8C_{12}, the metallocarbohedrenes, or metcars (Guo, Kerns & Castleman 1992a; Guo et al. 1992b; Wei et al. 1992; Rohmer, Bénard & Poblet 2000), where M denotes an early transition metal (mainly, Ti, V, Zr, Nb, Hf, Mo, Cr, and Fe). Later on, Yu, Huber & Froben (1995) performed similar experiments by reacting laser-vaporized Ti with CH_4, and observed the formation of Ti_8C_{12} along with several other clusters including Ti_nC_{2n} stoichiometries. The mass spectrometric studies of anionic $Ti_nC_x^-$ clusters performed by Wang, Ding & Wang (1997) and Wang

★ E-mail: joseignacio.martinez@icmm.csic.es

Materials Advances

ROYAL SOCIETY OF CHEMISTRY

PAPER

View Article Online
View Journal

Check for updates

Cite this: DOI: 10.1039/d1ma00415h

V-shaped pyranylidene/triphenylamine-based chromophores with enhanced photophysical, electrochemical and nonlinear optical properties†

Sergio Gámez-Valenzuela,[a] David Neusser,[b] Carlos Benitez-Martin,[cd] Francisco Najera,[cd] Juan A. Guadix,[de] Carlos Moreno-Yruela,[fg] Belén Villacampa,[h] Rocío Ponce Ortiz,[a] Sabine Ludwigs,[b] Raquel Andreu *[f] and M. Carmen Ruiz Delgado *[a]

Received 6th May 2021,
Accepted 24th May 2021

DOI: 10.1039/d1ma00415h

rsc.li/materials-advances

We report the synthesis and comprehensive study of two chromophores based on 4*H*-pyranylidene moiety as a part of the π-conjugated spacer. Triphenylamine (TPA) acts as donor and tricarbonitrile-based electron-accepting groups complete these V-shaped D–A–D architectures (A, acceptor; D, donor). Their electrochemical, photophysical and nonlinear optical properties are analyzed in detail by using a joint experimental and theoretical approach. The two chromophores exhibit near-infrared fluorescence, large Stokes shift, enhanced emission in tetrahydrofuran/water mixtures and good photostability. Additionally, the dimerization of triphenylamine groups to tetraphenylbenzidine (TPB) takes place upon electrochemical and chemical oxidation showing their peculiar electrochemical behavior and film formation capabilities. Interestingly, high molecular first hyperpolarizabilities and two-photon absorption cross-sections were found, highlighting their potential applications in electro-optical devices. Overall, our work demonstrates that these near-infrared (NIR) fluorescent chromophores are versatile materials with a myriad of applications ranging from optoelectronics to biological applications.

Introduction

Organic push–pull molecules represent a subclass of π-conjugated systems that are end-capped with electron donor(s) and electron acceptor(s). The D–π–A arrangement allows the direct interaction of the donor (D) and the acceptor (A) through the π-system, so-called intramolecular charge transfer (ICT). Their versatility and well-defined and tunable structures, which give rise to predictable properties, represent a main advantage keeping them into focus for different applications: nonlinear optics (NLO),[1] dye-sensitized solar cells (DSSCs),[2] bulk-heterojunction solar cells (BHJSCs),[3] organic light-emitting diodes (OLEDs),[4] two-photon absorbers,[5] or near-infrared absorbing dyes (NIR).[6]

In addition to the ordinary linear D–π–A systems, push–pull chromophores may also adopt quadrupolar (D–π–A–π–D or A–π–D–π–A), tripodal ($D–(π–A)_3$ or $A–(π–D)_3$) or even more extraordinary arrangements, which may be pictured as uppercase letters (molecules with shape similar to H, V, X or Y).[7] As far as the field of NLO is concerned, non-centrosymmetry is an imperative requirement for applications based on second order processes.[8] On the other hand, for two-photon absorption (2PA) (a third order process) a high degree of π conjugation is desirable. Following the arrangements above mentioned, branching donors and acceptors

[a] Department of Physical Chemistry, University of Malaga, Campus de Teatinos s/n, 29071, Malaga, Spain. E-mail: carmenrd@uma.es
[b] IPOC – Functional Polymers, Institute of Polymer Chemistry, University of Stuttgart, Pfaffenwaldring 55, D-70569 Stuttgart, Germany
[c] Departamento de Química Orgánica, Universidad de Málaga-IBIMA, Campus de Teatinos s/n, Málaga 29071, Spain
[d] Centro Andaluz de Nanomedicina y Biotecnología-BIONAND, Parque Tecnológico de Andalucía, c/Severo Ochoa, 35, 29590 Campanillas, Málaga 29071, Spain
[e] Departamento de Biología Animal, Facultad de Ciencias, Universidad de Málaga-IBIMA, Campus de Teatinos s/n, Málaga 29071, Spain
[f] Instituto de Nanociencia y Materiales de Aragón (INMA)-Departamento de Química Orgánica, CSIC-Universidad de Zaragoza, Zaragoza 50009, Spain. E-mail: randreu@unizar.es
[g] Center for Biopharmaceuticals & Department of Drug Design and Pharmacology, Faculty of Health and Medical Sciences, University of Copenhagen, Universitetsparken 2, DK-2100 Copenhagen, Denmark
[h] Instituto de Nanociencia y Materiales de Aragón (INMA)-Departamento de Física de la Materia Condensada, CSIC-Universidad de Zaragoza, Zaragoza 50009, Spain

† Electronic supplementary information (ESI) available: Experimental and theoretical details, synthesis, DFT-calculations, photostability, spectroelectrochemistry and chemical doping and 2P-fluorescence spectra/imaging. See DOI: 10.1039/d1ma00415h

RESEARCH ARTICLE

Check for updates
ADVANCED FUNCTIONAL MATERIALS
www.afm-journal.de

Backbone Configuration and Electronic Property Tuning of Imide-Functionalized Ladder-Type Heteroarenes-Based Polymer Acceptors for Efficient All-Polymer Solar Cells

Bin Liu, Yingfeng Wang, Huiliang Sun, Sergio Gámez-Valenzuela, Zhenglong Yan, Kui Feng, Mohammad Afsar Uddin, Changwoo Koh, Xin Zhou, Juan Teodomiro López Navarrete, María Carmen Ruiz Delgado, Hong Meng, Li Niu, Han Young Woo, Rocío Ponce Ortiz,* and Xugang Guo**

Electron-deficient ladder-type π-conjugated systems are highly desired for constructing polymer acceptors due to their unique electronic properties. Herein, two series of polymer acceptors PBTIn-(F)T (n = 1–4) based on imide-functionalized ladder-type heteroarenes (BTIn) with tunable conjugation length are synthesized. Effects of their backbone configuration and electronic properties on film morphology and performance of all-polymer solar cells (all-PSCs) are systematically investigated through theoretical computation, Raman spectroscopy, grazing incidence wide-angle X-ray scattering, etc. It is found that the ladder-type heteroarene size extension and polymer backbone fluorination gradually lower the frontier molecular orbital energy levels, leading to progressive bandgap narrowing with more efficient exciton dissociation. Furthermore, the centrosymmetric and axisymmetric characteristics of BTIn result in distinct backbone configuration with varied self-aggregation and crystalline phases, hence determining the blend film morphology. The highest efficiencies in these two series are attained from PBTI3-T and PBTI3-FT with a curved backbone configuration. PBTI4-(F)T with further extended heteroarenes shows linear backbone, negatively affecting film morphology and efficiency. This study provides fundamental material structure-device performance correlations for ladder-type heteroarenes-based polymer acceptors for the first time and demonstrates that more extended ladder-type backbones do not necessarily improve the device performance, offering guidelines for designing polymer acceptors to maximize all-PSC performance.

1. Introduction

All-polymer solar cells (all-PSCs), which are composed of a p-type polymer as electron donor and a n-type polymer as electron acceptor, have attracted considerable attention due to their pronounced advantages over other type of organic solar cells (OSCs), including excellent mechanical flexibility/durability and superior device performance stability.[1] Extensive studies focusing on polymer donors have greatly enhanced the power conversion efficiencies (PCEs) of OSCs. In contrast, the development of polymer acceptors lags largely behind, hence more efforts of developing polymer acceptors are urgently needed to improve all-PSC performance and leverage their advantages. To date, the reported polymer acceptors with PCE of >8% in all-PSCs are exclusively dominated by naphthalene diimide, perylene diimide, and B←N bridged bipyridine-based polymers,[2] except for recently reported cyano-functionalized polymers.[3] The development of all-PSCs in turn lags behind the state-of-the-art small-molecule acceptor (SMA)-based counterparts.[4]

B. Liu, Y. Wang, Z. Yan, K. Feng, X. Zhou, X. Guo
Department of Materials Science and Engineering
Southern University of Science and Technology
Shenzhen, Guangdong 518055, China
E-mail: guoxg@sustech.edu.cn
B. Liu, H. Meng
School of Advanced Materials
Peking University Shenzhen Graduate School
Peking University
Shenzhen, Guangdong 518055, China

The ORCID identification number(s) for the author(s) of this article can be found under https://doi.org/10.1002/adfm.202200065.

DOI: 10.1002/adfm.202200065

H. Sun, L. Niu
Center for Advanced Analytical Science
School of Chemistry and Chemical Engineering
Guangzhou University
Guangzhou, Guangdong 510006, China
E-mail: huiliang@gzhu.edu.cn
S. Gámez-Valenzuela, J. T. López Navarrete, M. C. Ruiz Delgado, R. Ponce Ortiz
Department of Physical Chemistry
University of Málaga
Campus de Teatinos s/n, Málaga 29071, Spain
E-mail: rocioponce@uma.es
M. A. Uddin, C. Koh, H. Y. Woo
Department of Chemistry
College of Science
Korea University
Seoul 136-713, Republic of Korea